This is to certify that the

dissertation entitled

Nucleon Structure Functions from

Deep Inelastic Charged Current Neutrino Scattering

presented by

William Gilbert Cobau

has been accepted towards fulfillment
of the requirements for

Ph.D. degree in Physics

Raymond Brock
Major professor

Date July 20, 1992

NUCLEON STRUCTURE FUNCTIONS
FROM
DEEP INELASTIC CHARGED CURRENT
NEUTRINO SCATTERING

By

William Gilbert Cobau

A THESIS

Submitted to
Michigan State University
in partial fulfillment of the requirements
for the degree of

DOCTOR OF PHILOSOPHY

Department of Physics and Astronomy

1992

Abstract

Nucleon Structure Functions from Deep Inelastic Charged Current Neutrino Scattering

By

William Gilbert Cobau

From a large data set of charged current neutrino–nucleon interactions, double differential cross sections and nucleon structure functions have been measured. In addition, the Quantum Chromodynamics parameter Λ_{QCD} has been measured from the Q^2 evolution of the extracted structure functions.

For Márcia,

who fills my life with love and energy.

ACKNOWLEDGEMENTS

This thesis would not have been possible without the effort of many people besides myself.

First, I would like to thank my wife Márcia Maria Campos Torres for putting up with me and encouraging me to finish this thesis, as quickly as possible.

Without the efforts of my fellow E733 graduate students, this work would not have been possible. Special thanks go to my fellow hunchbacks, George Perkins and Robert Hatcher with whom I spent many 12 hour owl shifts. E733 was not an example of "Too many Scientists and not Enough Hunchbacks." Three Hunchbacks were sufficient. Elizabeth Gallas' work on the flux file has been essential to this work.

My Advisor Raymond Brock deserves special credit for believing that I could earn my PhD and then giving me the freedom to explore my own ideas and for telling me when I was too far-a-field. While spending time at Fermilab, Stuart Fuess has served as my Pseudo-Advisor. Both Chip and Stu have spent large amounts of time discussing all parts of this analysis and giving me critical feedback on both the analysis and the actual thesis.

I would also like to thank "Supertech" Ron Olsen for much help in running the experiment. Ron was the Lab C technician during E733. There were few problems that Ron could not deal with quickly and efficiently.

Finally, I would like to thank my parents, John and Arlene Cobau, for their love and support. Special thanks go to my father for helping with the proof reading of this thesis–not an easy task for a non-scientist.

Table of Contents

Appendices

List of Tables

List of Figures

Chapter 1

Introduction and Theory

1.1 Introduction

The structure of the world around us is a recurring theme in mankind's search for knowledge. The ancient Greeks first gave man the concepts of elements and atoms as the building blocks of matter. In the past century, our understanding of the building blocks of matter has increased greatly. Atoms have gone from theoretical constructs to real physical objects that we can manipulate. We also know that atoms have a structure that we can describe and explain using Quantum Mechanics. At the center of the atom is the nucleus, which consists of nucleons–protons and neutrons.

The structure of these nucleons is the topic of this thesis. In the past thirty years, elementary particle physicists have come to believe that the nucleons are not elementary particles but are composites, like the nucleus and atom. The constituents of the nucleons have been named quarks and gluons or, in general, partons. Quarks are strongly interacting particles which carry a charge of ⅓ or ⅔ the electron charge. Gluons are the carriers of the strong force and are uncharged. The theory of Quantum Chromodynamics (QCD) describes the interactions of strongly interacting particles such as quarks and gluons.

This thesis presents measurements of the structure of the nucleon and of a fundamental constant of QCD, Λ_{QCD}.

Measurements of the nucleon structure are done in scattering experiments. The nucleon is probed by the scattering of high energy particles such as the electron, the neutrino, or the pion. By examining the results of the high energy collisions, one can

gather information about the internal structure of the struck object. The energy of the probe being used determines the size of the structures that can be observed, the higher the energy of the probe, the finer the structure that can be observed.

Scattering experiments, such as the one presented in this thesis, have discovered the structure of the atom, then the structure of the nucleus, and now are probing the structure of the nucleon. In the future, it is possible that scattering experiments will find that the partons that we now believe are fundamental are themselves composed of some new set of particles.

This thesis presents an analysis of charged current neutrino–nucleon scattering. Neutrino–nucleon scattering experiments belong to a larger group of scattering experiments termed Deep Inelastic Scattering (DIS) experiments. These experiments include Electron–Nucleon, Muon–Nucleon and Neutrino–Nucleon scattering experiments. The Feynman Diagram for these processes are shown in Figure 1.1. The experiments are termed Deep Inelastic Scattering because one looks for inelastic events with large momentum transfers to the nucleon system. The large momentum transfers probe deeply into the internal structure of the struck nucleon.

1.1.1 Why Neutrino Scattering?

Neutrino experiments are inherently difficult because neutrino beams are difficult to produce and the cross sections for neutrino interactions are very small compared to that for electron or muon interactions. Then the reader may wonder: *"Why bother? Why not use electrons and muons exclusively to probe the structure of the nucleon?"* The answer to this question is that neutrino–nucleon scattering provides additional and complementary information. Electron–nucleon or muon–nucleon scattering is predominantly an electromagnetic process using the virtual photon as the probe of the nucleon. Electromagnetic interactions conserve parity. In contrast, neutrino–nucleon scattering is strictly a weak process using the virtual W (or Z) to probe the nucleon. Parity is not

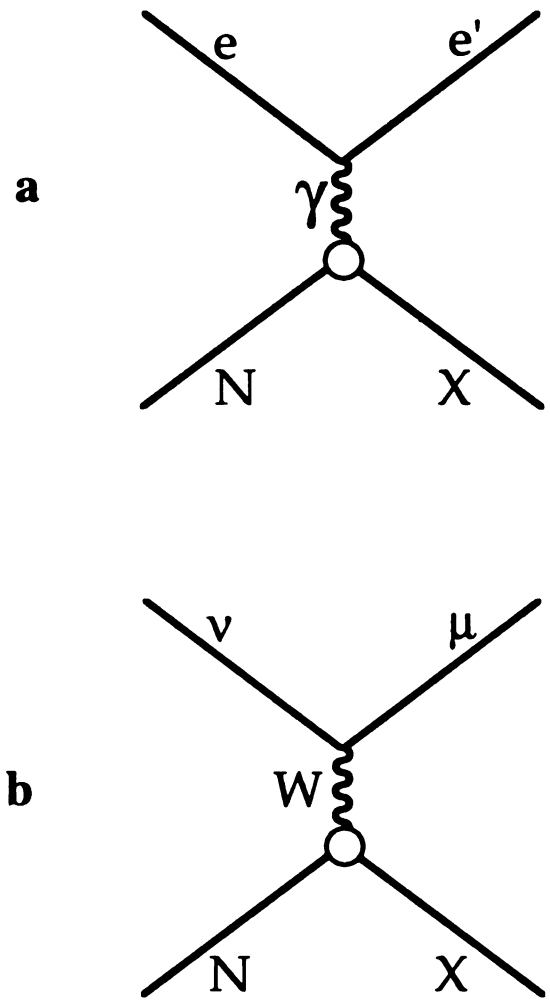

Figure 1.1. eN and νN Scattering Feynman Diagrams. Shown are the Feynman Diagrams for electron–nucleon scattering and charged current neutrino–nucleon scattering. Diagram (a) describes the electron–nucleon scattering. The incoming electron, e, emits a virtual photon, γ, resulting in the outgoing e'. The virtual photon strikes the nucleon, N, destroying the nucleon. The resulting debris is denoted by X. This same diagram can be used to describe μN scattering. Diagram (b) describes neutrino–nucleon scattering. This diagram is very similar to the diagram above. The incoming neutrino, ν, emits a virtual W and the outgoing lepton is a muon, μ. The W strikes the nucleon, N, and the destroyed nucleon continues on as the hadron system, X.

conserved in weak interactions. Thus neutrino–nucleon interactions are sensitive to the parity violating parts of the nucleon structure which are not available in charged particle scattering. As we will see, this makes neutrino scattering sensitive to both the valence and quantum sea parts of the nucleon and allows one to separate the valence part of the nucleon from the quantum sea.

1.1.2 This Chapter

This Chapter will present an overview of the theory of Neutrino–Nucleon scattering and the Quark–Parton Model. There will then be some preliminary discussion of the data and analysis presented in this thesis. Finally, the contents of this thesis will be outlined.

1.2 Theory

The theory of DIS, in general, and neutrino–nucleon scattering, specifically, is well understood. This thesis does not pretend to give a comprehensive review of the theory of DIS. There are many excellent text books (such as, Halzen and Martin 1984; Leader and Predazzi 1983; Quigg 1983; and Cheng and Li 1984) with large sections devoted to DIS and the Quark–Parton Model. This section will provide an overview of neutrino–nucleon scattering and try to look at weak interactions in the context of the Quark–Parton Model.

Using Lorentz Invariance and the known structure of Weak interactions, one can derive the form of the differential neutrino–nucleon cross section, This derivation is model independent. It is in this context that structure functions have a profound importance because they will allow a description of the structure of the nucleon without resorting to complex theoretical interpretations.

A discussion of the Quark–Parton Model follows. The Quark–Parton Model provides a foundation in which to interpret the structure function results that were obtained previously. The Quark–Parton Model provides a context in which we will

examine the neutrino–quark scattering. The theory of Weak interactions allows one to calculate the cross section for neutrino–free quark scattering in the same way one might calculate neutrino–electron scattering. From the results of neutrino–quark scattering, one will construct the differential cross sections for neutrino–nucleon scattering and determine, using the derived cross sections, the correspondence between the structure functions and the quark distributions.

1.2.1 The Theory of Neutrino–Nucleon Scattering

One can use the methods of Lorentz Invariance and the structure of weak interactions (see Cheng and Li 1984 or Halzen and Martin 1984) to calculate the cross section for the inclusive process,

$$\nu(k) + N(p) \rightarrow l(k') + X(P'). \tag{1.1}$$

This approach has the advantage that it is somewhat model independent. One begins with the Feynman diagram shown in Figure 1.1b and defines the standard Lorentz Invariants,

$$q = k - k' \tag{1.2}$$

$$\nu = p \cdot q / M. \tag{1.3}$$

The effective Lagrangian for Figure 1.1 can be written as,

$$\mathcal{L}_{\text{eff}} = -\frac{G_F}{\sqrt{2}} J_\lambda^\dagger J^\lambda + \text{h.c.} \tag{1.4}$$

where,

$$J^\lambda = J_l^\lambda + J_h^\lambda. \tag{1.5}$$

In Equation 1.5, we break the charge–charge current into lepton and hadron pieces. The lepton piece J_l^λ shows the standard V–A behavior of the Weak Interaction with the form,

$$J_l^\lambda = \overline{\nu}_e \gamma^\lambda (1 - \gamma_5) e + \overline{\nu}_\mu \gamma^\lambda (1 - \gamma_5) \mu + \ldots \tag{1.6}$$

One can then calculate the amplitude of the interaction as,

$$T_n^{(\nu)} = \frac{G_F}{\sqrt{2}}\bar{u}_l(k')\gamma_\lambda(1-\gamma_5)u_\nu(k)\langle n|J_h^\lambda|p\rangle. \tag{1.7}$$

The differential cross section can then be calculated from the amplitude, $T_n^{(\nu)}$ as,

$$d\sigma_n^{(\nu)} = \frac{1}{\nu}\frac{1}{2M}\frac{1}{2E}\frac{d^3k'}{(2\pi)^3 2k_0'}\frac{d^3P'}{(2\pi)^3 2P_0}$$
$$\times\frac{1}{2}\sum_{\text{spins}}\left|T_n^{(\nu)}\right|^2(2\pi)^4\delta(k+p-k'-P'). \tag{1.8}$$

which we can then simplify into the expression,

$$\frac{d\sigma^\nu}{d|q^2|d\nu} = \frac{G_F^2}{32\pi E^2}\mathbf{l}^{\alpha\beta}\mathbf{W}_{\alpha\beta} \tag{1.9}$$

Now the structure of the interaction is contained in the two matrices, $\mathbf{l}_{\alpha\beta}$ and $\mathbf{W}_{\alpha\beta}$. The lepton matrix, $\mathbf{l}_{\alpha\beta}$, is determined by the Weak Interaction and has the form,

$$\mathbf{l}_{\alpha\beta} = 8\left\{k_\alpha k'_\beta + k'_\alpha k_\beta - k\cdot k' g_{\alpha\beta} + i\varepsilon_{\alpha\beta\gamma\delta}k'^\gamma k^\delta\right\}. \tag{1.10}$$

The hadron matrix, $\mathbf{W}_{\alpha\beta}$ is much less well defined. There is no theoretical basis to dictate the form of $\mathbf{W}_{\alpha\beta}$, so one chooses the most general form possible:

$$\begin{aligned}\mathbf{W}_{\alpha\beta}(p,q) = &-\mathrm{W}_1 g_{\alpha\beta} + \mathrm{W}_2 p_\alpha p_\beta/M^2 - i\mathrm{W}_3\,\varepsilon_{\alpha\beta\gamma\delta}p^\delta q^\gamma/M^2 \\ &+\mathrm{W}_4 q_\alpha q_\beta/M^2 + \mathrm{W}_5\left(p_\alpha q_\beta + q_\alpha p_\beta\right)/M^2 \\ &+i\mathrm{W}_6\left(p_\alpha q_\beta - q_\alpha p_\beta\right)/M^2,\end{aligned} \tag{1.11}$$

Where the W_i are Lorentz-invariant functions of ν and q^2, commonly called structure functions.

Now, we can calculate the cross section,

$$\frac{d\sigma^\nu}{d|q^2|d\nu} = \frac{G_F^2}{2\pi}\left(\frac{E'}{E}\right)\left[2\mathrm{W}_1\sin\frac{\theta}{2} + \mathrm{W}_2\cos^2\frac{\theta}{2} + \frac{(E+E')}{M}\sin^2\frac{\theta}{2}\mathrm{W}_3\right]. \tag{1.12}$$

The W_4, W_5, and W_6 are zero in the limit that $m_l = 0$. In the anti-neutrino case, sign of the W_3 term is reversed.

To make the conversion to a modern notation based on the concepts of scaling and the parton model, we make the following redefinitions of the structure functions,

$$M W_1(\nu, Q^2) \equiv F_1(x) \tag{1.13}$$

$$\nu W_2(\nu, Q^2) \equiv F_2(x) \tag{1.14}$$

$$\nu W_3(\nu, Q^2) \equiv F_3(x) \tag{1.15}$$

where,

$$Q^2 = -q^2 \tag{1.16}$$

$$x \equiv \frac{-q^2}{p \cdot q} = \frac{Q^2}{2M\nu} \tag{1.17}$$

This leads to the recasting of the cross section in the form,

$$\frac{d^2\sigma^{\nu,\bar{\nu}N}}{dxdy} = \frac{G_F^2 S}{2\pi}\left[y^2 x F_1 + \left(1 - y + \tfrac{Mxy}{2E_\nu}\right)F_2 \pm \left(y - \tfrac{1}{2}y^2\right)x F_3\right] \tag{1.18}$$

where,

$$y \equiv \frac{p \cdot q}{p \cdot k} = \frac{\nu}{E_\nu} \tag{1.19}$$

We can make a final simplification, by using the Callan–Gross relationship (1969),

$$2x F_1(x) = F_2(x) \tag{1.20}$$

giving,

$$\frac{d^2\sigma^{\nu,\bar{\nu}N}}{dxdy} = \frac{G_F^2 S}{2\pi}\left[\left(1 - y + \tfrac{1}{2}y^2\right)F_2 \pm \left(y - \tfrac{1}{2}y^2\right)x F_3\right]. \tag{1.21}$$

In Equation 1.21 we have neglected the term $\frac{Mxy}{2E_\nu}$ because it is small and decreases as the neutrino energy increases. From this modern form, in the next section, we will be able to make direct associations between these new structure functions and the quarks in the quark–parton model.

1.2.2 Quark–Parton Model

To account for the baffling array of "elementary" particles discovered during the years following World War II, Gell-Mann (1964) and Zweig (1964) suggested that one might account for the properties of the observed baryons and mesons by an underlying structure of particles which Gell-Mann named quarks. Quarks were thought to be strongly interacting, spin ½, particles of charges $-\frac{1}{3}e$ and $\frac{2}{3}e$, where e is the magnitude

of the charge of the electron. The quarks also carried quantum numbers such as isospin and "strangeness." The baryons were thought to be combinations of three quarks (or anti-quarks) and mesons combinations of a quark with an anti-quark. This Quark Model was successful in providing a framework for examining hadron spectroscopy and explaining the observed resonances but was initially considered more of an accounting scheme than a model of some structure underlying the seen spectrum of baryons and mesons.

Starting in 1967, a group of physicists from MIT and SLAC, lead by R.E. Taylor, J.I. Friedman, and H.W. Kendall, conducted a series of deep inelastic electron–proton and electron–deuterium scattering experiments at SLAC (See review article by Friedman and Kendall, 1972.) The theoretical expectations in 1967 were that the inelastic spectra would decrease rapidly as a function of increasing four-momentum transfer, Q^2. Contrary to the theoretical expectations, is was found that the inelastic cross section had only a weak dependence on Q^2 beyond the dependence on Q^4 dictated by the photon propagator of Quantum Electrodynamics. This independence of the four-momentum transfer has come to be known as "scaling."

At the end of the sixties, it was suggested by Feynman (1969) and Bjorken and Paschos (1969) that the unexpected scaling seen in the SLAC inelastic electron–proton scattering data was due to the scattering of the electron off of partons, constituents of the proton. In the parton picture, the momentum of struck hadrons is distributed between the partons that make up the particular hadron. Each parton carries a fraction of the hadron's momentum, x, where,

$$x \equiv \frac{Q^2}{p \cdot q}. \tag{1.22}$$

Summing x over all the partons yields,

$$\sum_{\text{partons}} x_i \equiv 1. \tag{1.23}$$

With the 1974 discovery of the charm quark in the form of the J/ψ, the quark

model suddenly went from an accounting mechanism to the model of the underlying structure of hadrons. Quarks were now considered one of the building blocks of hadrons.

1.2.3 Quantum Chromodynamics

The Quark Model described above is successful at describing the known hadronic resonances but at the cost of the Pauli Exclusion Principle. States such as the Δ^{++}, which is the combination of three spin-up u quarks, violate the Pauli Exclusion Principle. In an effort to maintain the Exclusion Principle, it was proposed that quarks carried an additional quantum number (dubbed "*color*.") To allow states such as the Δ^{++}, there must be three colors. Results from the measurement of the cross section for $e^-e^+ \rightarrow q\bar{q}$ show that the cross section is 3 times greater than that expected for color-less quarks from the measurement of the cross section for $e^-e^+ \rightarrow \mu\bar{\mu}$. Thus color is real degree of freedom for quarks that does not exist for leptons. Quantum Chromodynamics describes (as its name implies) the interactions of colored particles.

Quantum Chromodynamics (QCD) is a theory of strong interactions. There are a number of similarities between Quantum Electrodynamics (QED) and QCD. In QED, the force is mediated by photons. Whereas, in QCD, the strong force is mediated by bosons call gluons. In QED, photons couple only to charged particles. In QCD, the quarks carry color which is similar to charge in that gluons only interact with colored particles. At this point, the two theories, QED and QCD, begin to diverge.

Figure 1.2 shows some primitive Feynman vertices from QED and QCD. It is possible to reduce all Feynman diagrams a combination of these primitive vertices. Figure 1.2a shows the basic vertex of QED, a charged particle emits (or absorbs) a photon (either real or virtual) and continues on. From this basic vertex, one constructs all the diagrams of QED. Since the photon is uncharged, the charge of the scattered particle remains the same. Figure 1.2b shows a similar diagram for QCD. In this vertex, a colored particle (a

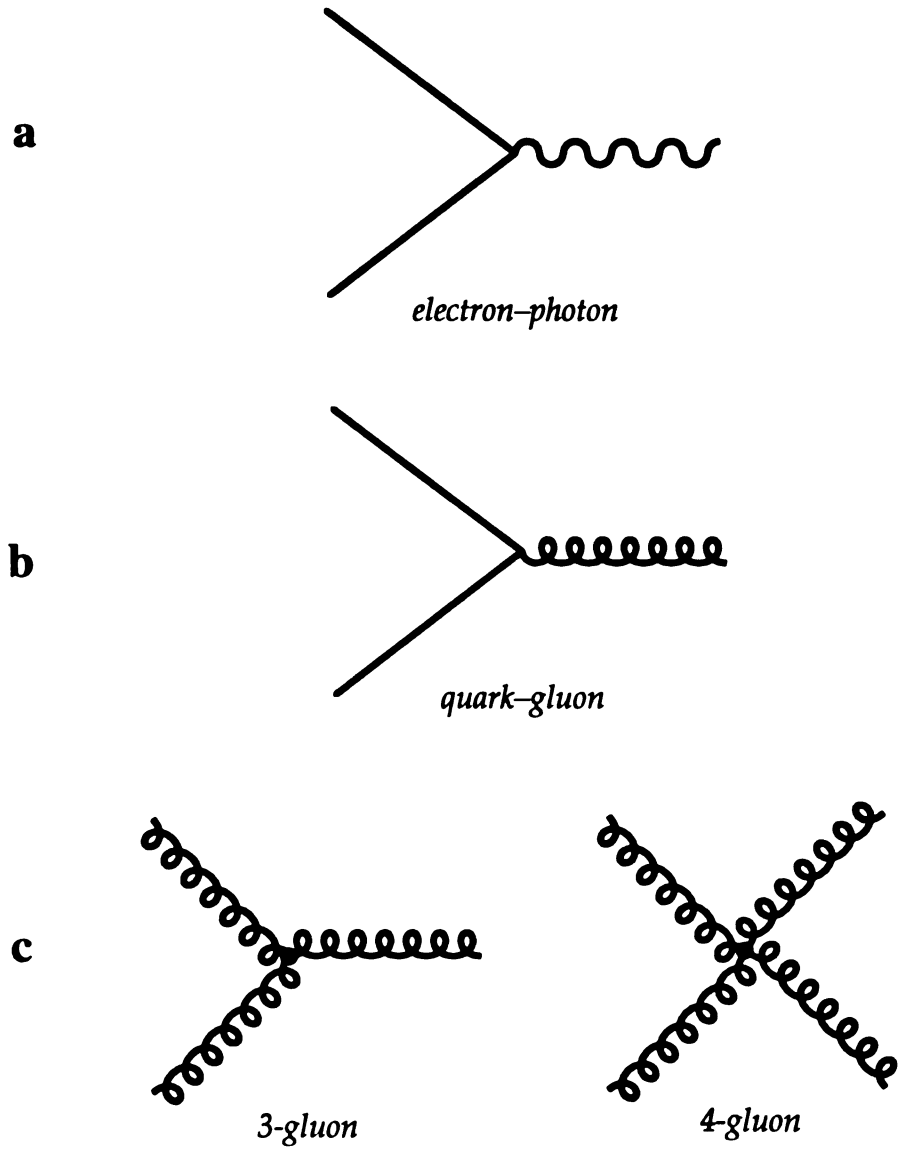

Figure 1.2. Primitive Vertices for QED and QCD. Shown are the vertices from which all Feynman Diagrams for QED and QCD can be constructed. Diagram (a) shows the only type of vertex in QED, the interaction of a photon with a charged particle such as an electron. Diagram (b) shows a similar vertex in QCD, the interaction of a colored quark with a gluon. Diagrams (c) show vertices unique to QCD. The 3-gluon and 4-gluon vertices are a result of the fact that gluons are colored.

quark) emits or absorbs a gluon. The difference between this vertex and and the QED vertex is that while the photon is uncharged, the gluon is color "charged" or colored (or more accurately bicolored). So in Figure 1.2b, for example, a blue quark emits a blue-$\overline{\text{red}}$ gluon and continues on as a red quark. The fact that gluons are bicolored leads to gluon–gluon interactions which have no analog in QED. The gluon–gluon interactions lead to two additional primitive vertices beyond Figure 1.2b which are shown in Figure 1.2c.

The self-interaction of the gluons leads to very different properties for QCD when compared with QED. At low energies, the strong coupling constant, α_s, is of order unity whereas $\alpha = 1/137$ so the perturbative techniques used in QED were thought to be unusable. The self-interaction diagrams of QCD cause a screening effect that makes α_s shrink as a function of the 4-momentum transfer, Q^2. This "running" of the coupling constant means that at high energies α_s is small enough to apply perturbative techniques.

There is an additional property of QCD called confinement. Confinement is the experimental fact that one never observes colored particles. This is presumably because as one tries to separate two quarks, the energy required to separate the two quarks is more than is required to produce a $q\bar{q}$ pair.

While QCD describes how the quarks are held together in a hadron, QCD makes no predictions about x distributions of the constituent partons of a hadron. QCD does make explicit predictions about the how the parton distributions evolve with Q^2. The determination of the parton distributions is left to experimenters.

1.2.4 Neutrino–Nucleon Scattering From a Quark–Parton Model Perspective.

As a beginning, let us calculate the differential cross section for the process,

$$\nu_\mu(k) + e(p) \rightarrow \mu(k') + \nu_e(p'). \tag{1.24}$$

The Feynman Diagram for the process is shown in Figure 1.3. The calculation of the cross section for $\nu_\mu e$ scattering is straight forward because all of the particles involved

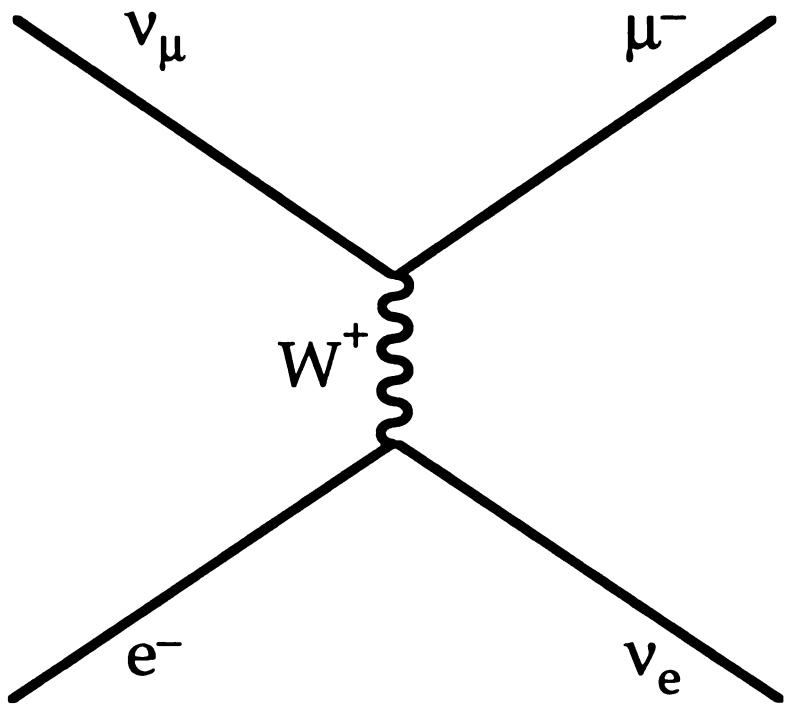

Figure 1.3. Feynman Diagrams For $\nu_\mu e$ Scattering. The figure shows the Feynman Diagram for $\nu_\mu e$ scattering. The incoming muon neutrino, ν_μ, emits a virtual W^+ becoming the outgoing muon, μ^-. The W^+ interacts with the electron, e^- which becomes an electron neutrino, ν_e.

are point-like. The cross section for this process is simply,

$$\frac{d\sigma}{dy} = \frac{G_F^2 s}{\pi}. \tag{1.25}$$

This is almost the same diagram as for neutrino–quark scattering. (See Figure 1.4.) For free quarks, the differential cross section would be that shown in Equation 1.25. In the case of neutrino–anti-quark scattering, there is the additional complication of the helicity suppression of the interaction. This yields (for free quarks),

$$\frac{d\sigma^{\nu\bar{q}}}{dy} = \frac{G_F^2 s}{\pi}(1-y)^2. \tag{1.26}$$

The above cross sections ignore the fact that one never scatters off of free quarks. The struck quark is always confined within a nucleon. We can extend the cross section formulas accounting for the fact that the struck quark does not carry the full momentum of the nucleon. The first addition necessary to account for confinement of the quark is that since $s_{\text{nucleon}} \neq s_{\text{quark}}$, one must use s_{quark}. One can calculate s_{quark},

$$s_{\text{quark}} \equiv \left(k + p_{\text{quark}}\right)^2 \cong -2k \cdot p_{\text{quark}} = -2k \cdot xp_{\text{nucleon}} = xs_{\text{nucleon}}, \tag{1.27}$$

and then substitute s_{quark} (or xs) for the s in Equations 1.25 or 1.26. The probability that a quark carries momentum xp must also be included in the cross section. One can define a parton distribution function (PDF) such that the probability that a quark carries momentum xp is $q(x)dx$. This gives the double differential cross sections in term of the parton distribution functions:

$$\frac{d^2\sigma^{\nu q}}{dxdy} = \frac{G_F^2 s}{\pi} x\,q(x) \tag{1.28}$$

$$\frac{d^2\sigma^{\nu\bar{q}}}{dxdy} = \frac{G_F^2 s}{\pi}(1-y)^2 x\,\bar{q}(x) \tag{1.29}$$

From Equations 1.28 and 1.29 and charge conservation, one can construct the double differential cross section for neutrino–proton (neutron) or anti-neutrino–proton scattering as shown,

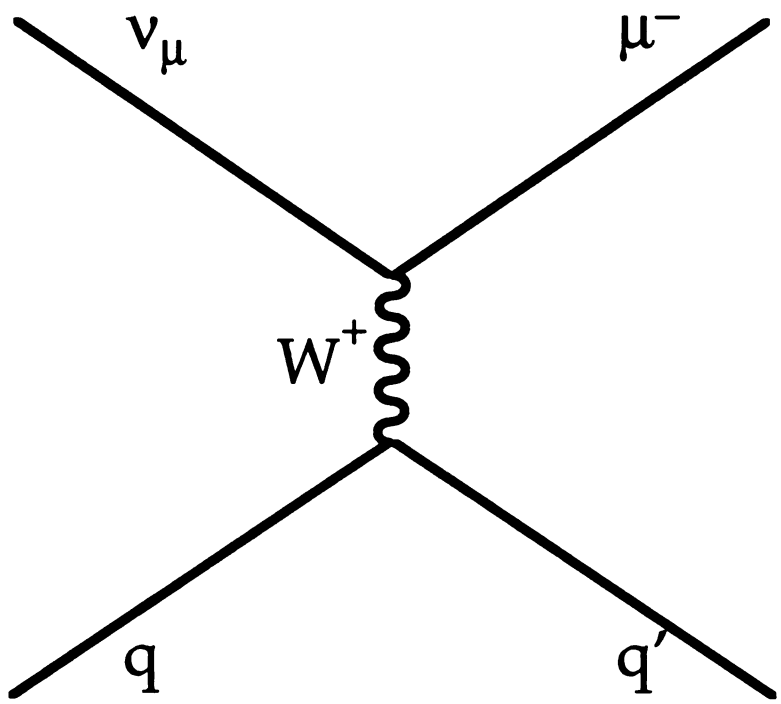

Figure 1.4. Feynman Diagrams For $\nu_\mu q$ Scattering. The figure shows the Feynman Diagram for $\nu_\mu q$ scattering. The incoming neutrino, ν_μ, emits a virtual W becoming the outgoing muon, μ. The W then interacts with the quark, q resulting in the outgoing quark, q′.

$$\frac{d^2\sigma^{\nu p}}{dxdy} = \frac{G_F^2 s}{\pi} x\left[d(x) + (1-y)^2\,\bar{u}(x) + s(x) + (1-y)^2\,\bar{c}(x)\right] \qquad (1.30)$$

$$\frac{d^2\sigma^{\bar{\nu}p}}{dxdy} = \frac{G_F^2 s}{\pi} x\left[(1-y)^2\,\bar{d}(x) + u(x) + (1-y)^2\,\bar{s}(x) + c(x)\right] \qquad (1.31)$$

where u, d, s, and c are the parton distribution functions for the up, down, strange and charm quarks respectively and $\bar{u}$, $\bar{d}$, $\bar{s}$, and $\bar{c}$ are the PDFs for the anti-quarks. Equations 1.30 and 1.31 apply equally well for the neutron if one uses the PDFs for the neutron. It is customary to treat the proton and neutron as an isospin doublet and to assume that when one writes the PDF $d(x)$, one means $d_{proton}(x)$ which is the same as $u_{neutron}(x)$. The non-valence distributions are assumed to be identical for the proton and the neutron.

For this thesis, it will be useful to consider the neutrino–nucleon cross section. By nucleon, one refers to the average of the proton and neutron cross sections. The FMMF target is almost isoscalar, i.e. has equal number of protons and neutron, so the target approximates a nucleon target. Using the above convention of the PDFs, one finds the differential neutrino–nucleon cross section is,

$$\begin{aligned}\frac{d^2\sigma^{\nu N}}{dxdy} &= \frac{1}{2}\left\{\frac{d^2\sigma^{\nu p}}{dxdy} + \frac{d^2\sigma^{\nu n}}{dxdy}\right\} \\ &= \frac{G_F^2 s}{2\pi} x\left\{u(x) + d(x) + 2(1-y)^2\,\bar{u}(x) + 2s(x) + 2(1-y)^2\,\bar{c}(x)\right\}, \qquad (1.32) \\ &= \frac{G_F^2 s}{2\pi} x\left\{u(x) + d(x) + s(x) + \bar{s}(x) + (1-y)^2\left[\bar{u}(x) + \bar{d}(x) + c(x) + \bar{c}(x)\right]\right\}\end{aligned}$$

Where we have used the relationships that $\bar{u}(x) = \bar{d}(x)$, $s(x) = \bar{s}(x)$, and $c(x) = \bar{c}(x)$. Next, we regroup the PDFs, giving,

$$\begin{aligned}\frac{d^2\sigma^{\nu N}}{dxdy} = \frac{G_F^2 s}{2\pi} x\Big\{&\left(1 - y + \tfrac{1}{2}y^2\right)\left[u(x) + d(x) + s(x) + c(x) + \bar{u}(x) + \bar{d}(x) + \bar{s}(x) + \bar{c}(x)\right] \\ &+\left(y - \tfrac{1}{2}y^2\right)\left[u(x) + d(x) + 2s(x) - \bar{u}(x) - \bar{d}(x) - 2\bar{c}(x)\right]\Big\} \qquad (1.33)\end{aligned}$$

Comparing Equation 1.33 with Equation 1.21, one can make the immediate correspondence between the quark distributions and the structure functions F_2 and xF_3. For F_2, one finds,

$$F_2^{\nu N} = x\mathrm{u} + x\mathrm{d} + x\mathrm{s} + x\mathrm{c} + x\bar{\mathrm{u}} + x\bar{\mathrm{d}} + x\bar{\mathrm{s}} + x\bar{\mathrm{c}}$$
$$= xq + x\bar{q} = F_2^{\bar{\nu}N}, \qquad (1.34)$$

where $q(x)$ and $\bar{q}(x)$ are now the sums of the quark and anti-quark distributions. Equation 1.34 shows that F_2 is the same for neutrinos and anti-neutrinos and that F_2 can be regarded as the sum of the quark and anti-quark distributions.

For xF_3, the correspondence between the quark distributions and xF_3 differ between the cases of νN and $\bar{\nu}N$ scattering. Comparison between Equations 1.21 and 1.33 gives,

$$xF_3^{\nu N} = x\mathrm{u} + x\mathrm{d} + 2x\mathrm{s} - x\bar{\mathrm{u}} - x\bar{\mathrm{d}} - 2x\bar{\mathrm{c}} \approx xq - x\bar{q}. \qquad (1.35)$$

for the case of νN scattering. The same analysis for $\bar{\nu}N$ scattering shows,

$$xF_3^{\bar{\nu}N} = x\mathrm{u} + x\mathrm{d} + 2x\mathrm{c} - x\bar{\mathrm{u}} - x\bar{\mathrm{d}} - 2x\bar{\mathrm{s}} \approx xq - x\bar{q}. \qquad (1.36)$$

To first-order, the structure functions are the same but when one includes the strange and charm sea in the calculation, one finds that,

$$xF_3^{\nu N} \neq xF_3^{\bar{\nu}N}. \qquad (1.37)$$

It will be necessary to correct for the differences in xF_3, when one calculates F_2.

1.2.5 Structure Function Evolution

In the parton model, the parton distribution and structure function are constants as a function of Q^2. QCD makes no prediction about the form of the quark or parton distributions but it does predict that the parton distributions are not just functions of x but are functions of Q^2. The prediction of QCD goes beyond simply saying that the parton distributions are functions of Q^2, it quantitatively predicts the dependence of the parton distributions on Q^2. From the evolution of the the parton distributions, one can measure the parameter, Λ_{QCD}.

The vertices shown in Figure 1.2 result in the quark and gluon distributions changing as a function of Q^2. The higher the Q^2, the shorter the distances probed and the higher the probability that one will separately resolve the quark and the soft gluon it

has emitted. Thus as Q^2 grows, the average x of the struck parton decreases and the parton distributions and structure functions evolve with Q^2.

QCD makes a quantitative prediction about the Q^2 evolution of the structure functions and parton distributions. The evolution of the structure functions is described by the Altarelli–Parisi equations (Altarelli and Parisi 1977):

$$\frac{dF_{NS}}{d\log Q^2} = \frac{\alpha_s(Q^2)}{2\pi}\int_x^1 \frac{dz}{z}\left[P_{qq}\left(\tfrac{x}{z},Q^2\right)F_{NS}(z,Q^2)\right] \quad (1.38a)$$

$$\frac{dF_S}{d\log Q^2} = \frac{\alpha_s(Q^2)}{2\pi}\int_x^1 \frac{dz}{z}\left[P_{qq}\left(\tfrac{x}{z},Q^2\right)F_S(z,Q^2) + P_{qG}\left(\tfrac{x}{z},Q^2\right)G(z,Q^2)\right] \quad (1.38b)$$

$$\frac{dG}{d\log Q^2} = \frac{\alpha_s(Q^2)}{2\pi}\int_x^1 \frac{dz}{z}\left[P_{GG}\left(\tfrac{x}{z},Q^2\right)G(z,Q^2) + P_{Gq}\left(\tfrac{x}{z},Q^2\right)F_S(z,Q^2)\right] \quad (1.38c)$$

where F_{NS} is the non-singlet structure function, F_S is the singlet structure function and G is the gluon structure function. F_{NS} corresponds to the valence quark distributions which is simply xF_3. F_S corresponds to the valence and sea quark distributions which is F_2. P_{qq}, P_{qG}, and P_{GG} are "splitting functions" and have the form. The splitting functions describe the two contributions to the Q^2 evolution of the structure function (or parton distributions) at a given x_0:

- A higher x quark emits a gluon and now carries momentum x_0p.
- A quark carrying momentum x_0p emits a gluon and now is a lower x quark.

These contributions result in the number of low x partons growing as a function of Q^2 while the number of high x partons shrinks. As we have seen the structure functions are simply the sum and differences of parton distributions and thus exhibit the same Q^2 behavior as the parton distributions. To examine the evolution of F_{NS}, one must first regularize the Altarelli–Parisi Equation 1.38a. The regularization yields:

$$\frac{3\pi}{\alpha_s(t)}\frac{\partial F_{NS}(x,t)}{\partial t} =$$

$$\left[3+4\log(1-x)\right]F_{NS}(x,t)+2\int_x^1\frac{dz}{1-z}\left[\left(1-z^2\right)F_{NS}(x/z,t)-2F_{NS}(x,t)\right], \quad (1.38)$$

where $t=\log\left(Q^2/\Lambda^2\right)$. Now the evolution of the non-singlet structure function is a direct function of t. Using Equation 1.38, it is possible to measure Λ_{QCD}.

1.3 This Thesis

The thesis reports on the measurement of Neutrino–Nucleon Structure Functions by a collaboration of Michigan State University, Fermi National Accelerator Laboratory (Fermilab), Massachusetts Institute of Technology and the University of Florida (the FMMF collaboration) in a series of experiments conducted at Fermilab during the 1980s.

The FMMF collaboration is a group of approximately 40 physicists. The collaborators are listed in Appendix A.

Fermilab is a United States Government Laboratory located in Batavia, Illinois, approximately 45 kilometers west of Chicago. Fermilab was constructed in the late 1960s. The main purpose of Fermilab is the operation of a Proton-Synchrotron which provides high energy particle beams for use by elementary particle physics experiments. By the beginning of the 1980s, the Fermilab Main Ring provided 400 GeV protons to experimental areas. Between 1982 and 1984, the accelerator complex at Fermilab was upgraded by the installation of a new Proton-Synchrotron constructed of high field superconducting magnets. The new accelerator (dubbed the TeVatron) is located in the same tunnel as the older Main Ring and is capable of delivering 800 GeV protons to the Fixed Target Areas.

In the late 1970s, the FMMF collaboration constructed a detector at Fermilab which consisted of an extremely fine grained target–calorimeter and a muon spectrometer. From 1980 to 1988 the detector was exposed to neutrino beams created using protons

extracted from Fermilab's Main Ring and Tevatron. The series of experiments are described in detail in Chapter 2. Chapter 2 continues with a description of how individual events are measured. Chapter 3 describes the Monte Carlo used in the correction of the data for acceptance and smearing. Chapter 4 discusses the extraction of the double differential cross sections, $\frac{d^2\sigma}{dxdy}$, and the structure functions, F_2 and xF_3, and presents the measured cross sections and structure functions. Chapter 5 compares the FMMF structure functions presented in Chapter 4 with those measured by other DIS experiments. In Chapter 5, a measurement of Λ_{QCD} will also be discussed. A number of Appendices are also included at the end of the thesis to provide more detailed explanation of the analysis used in this thesis.

Chapter 2

The Experiment

2.1 Introduction

The FMMF detector was located in Lab C at Fermi National Accelerator Laboratory. Lab C is located at the end of the Neutrino Center beam line. Neutrino Center serviced experimental areas for up to 4 experiments, all of which could be run simultaneously. The FMMF detector was exposed to neutrino beams during 3 separate periods, in 1982, 1985 and 1987–88 (referred to as 1987). The data from each of these runs is included in this thesis. This chapter initially describes the individual exposures, briefly describing the neutrino beam characteristics, the trigger (or triggers) used and any differences in the detector instrumentation. The neutrino beams and the FMMF detector are then discussed in detail. A discussion of event measurement follows. The chapter concludes with a discussion of the final data sample.

This thesis covers data taken over six years and an experimental effort (including construction, data taking and analysis) that required more than ten years. Appendix A gives the names and affiliation of all of the scientists involved in the building, the operation and/or the analysis of the data taken using the FMMF detector.

2.2 The Exposures

This section summarizes the three exposures, including the neutrino beams and differences in the instrumentation of the FMMF detector.

2.2.1 1982, Experiment 594.

During 1982, the FMMF detector was exposed to a narrow band DiChromatic beam. The DiChromatic beam is described in detail below. For the DiChromatic beam, 400 GeV protons were used to create a secondary beam of pions (π's) and kaons (K's) which were then sign and momentum selected and allowed to decay into a beam of neutrinos that passed through the FMMF detector. The momentum selection resulted in a strong correlation between neutrino energy and beam radius. For this thesis, data from 4 secondary momentum settings were used, –165 GeV/c, +165 GeV/c, +200 GeV/c and +250 GeV/c. When positive (negative) secondaries were selected, a beam of neutrinos (anti-neutrinos) was produced.

The standard trigger used in 1982 for the FMMF detector is based on energy deposited in the target-calorimeter. This trigger was 50% efficient for a 5 GeV energy deposition and fully efficient for 10 GeV. This standard trigger is referred to as the PTH trigger.

During the 1982 running, the muon spectrometer was instrumented using a charge division read-out scheme.

2.2.2 1985, Experiment 733, Part 1.

In 1985, the FMMF detector was exposed to a wide band beam produced with 800 GeV protons from the Tevatron. The beam is described as the Quad-Triplet beam (QTB) because of its optics and it is also described below. The primary feature of this beam is its high energy (due to the use of 800 GeV incident protons) and the lack of secondary momentum selection, which results in a large neutrino flux and a beam of neutrinos and anti-neutrinos.

In 1985, a much more complicated trigger scheme was used. The goal of the new triggering scheme was to maximize the number of dimuon and the high Q^2 events observed while attempting to maintain as large a minimum bias set as possible. To supplement the PTH trigger, two special triggers designed to enhance the number of

dimuon and high Q^2 events were built. To accommodate competition among the rare process triggers while ensuring at least one trigger per spill, the neutrino spill was divided into two parts, a "beam gate" and "tail gate" (See Figure 2.1.) The beam gate was the first part of the neutrino spill and was devoted to the triggers designed to isolate special physics signals. The tail gate followed the beam gate was devoted to the minimal trigger with the purpose of maximizing the amount of data taken over the course of the run.

The first of these special triggers was the HiE trigger. The HiE trigger was designed to enhance the sample of high Q^2 events. The HiE trigger was simply the PTH trigger with a higher threshold. The HiE trigger was fully efficient for 100 GeV energy depositions. Figure 2.2 shows the measured trigger threshold of the HiE trigger.

The second of these special triggers was the 2MU trigger. It was designed to enhance the sample of events with two (or more) muons. The 2MU trigger was also based on the PTH trigger. When a PTH trigger was observed, the spectrometer planes were interrogated as to how many hits were recorded. It was required that 3 out of the 8 spectrometer planes have more than two hits. Because of the time required to interrogate the spectrometer planes, the 2MU trigger was delayed relative to the PTH and HiE triggers. The 2MU trigger events were not used in this thesis because the acceptance of the 2MU trigger was not well understood.

In addition to the previously mentioned triggers, there was a Quasi-Elastic trigger. The Quasi-Elastic trigger events were not used in this thesis.

The beam gate was designed for use with the special triggers that enhanced the dimuon and high Q^2 signals. To this end, during the beam gate, any HiE or 2MU trigger was taken (assuming that another trigger had not been honored previously). The PTH trigger was prescaled by a factor of ten or eleven (i.e. only every tenth or every eleventh PTH trigger was taken.) The Quasi-Elastic trigger was also prescaled by three. This triggering scheme resulted in approximately equal live-times for all four triggers during the beam gate.

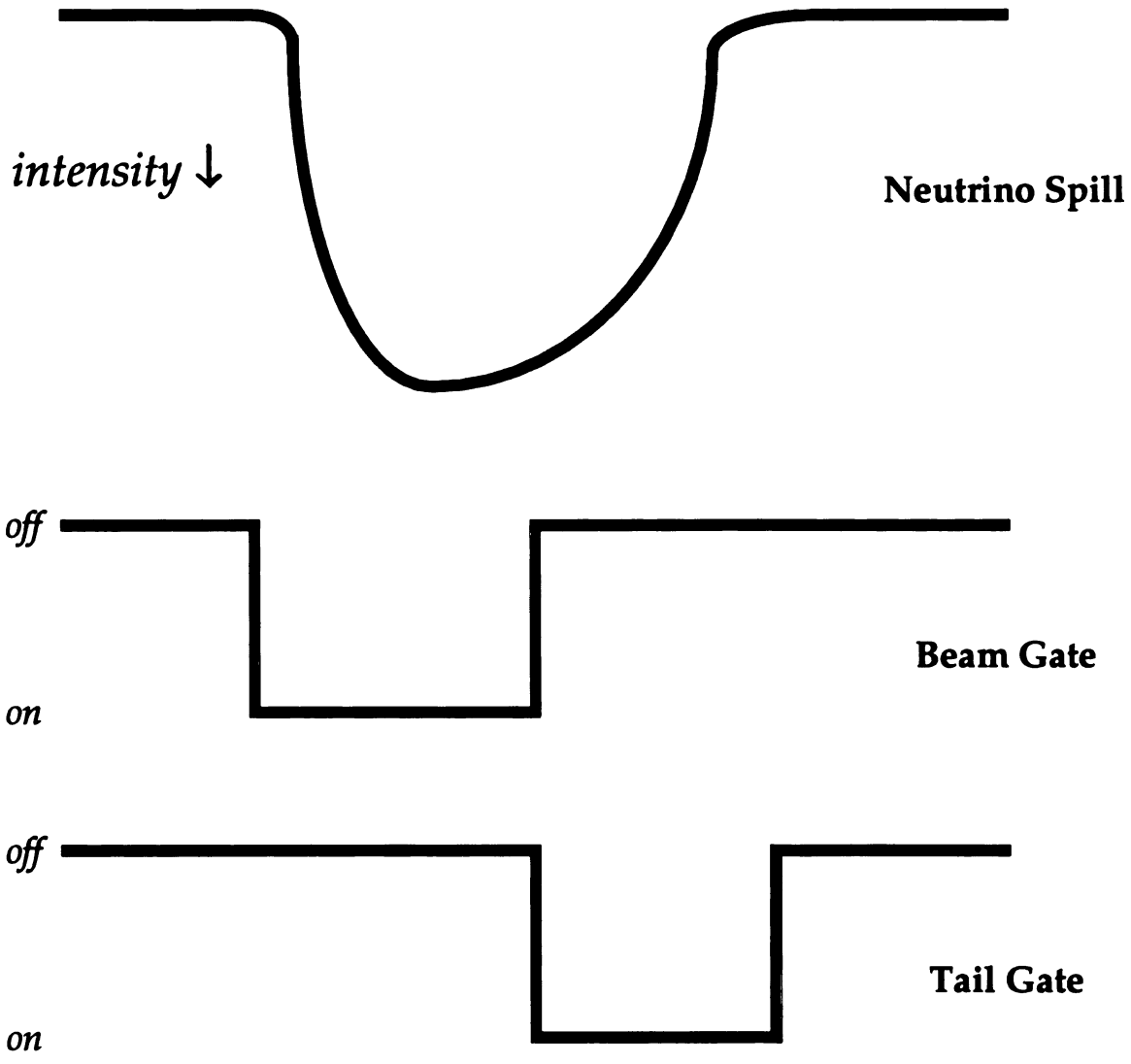

Figure 2.1. Neutrino Gate Structure. Shown is a schematic of the neutrino beam spill and the neutrino gates. The top graph shows the intensity of neutrinos as a function of time. The middle graph shows the "beam gate." The bottom graph shows the "tail gate." The width of the neutrino spill was 2–3 milliseconds. The beam gate covers the first part of the neutrino spill while the tail gate involves the last part of the neutrino spill. During the beam gate, the triggers for rare processes were given preference. If no trigger was taken during the beam gate, any available trigger was taken during the tail gate. This scheme was adopted to maximize the number of rare triggers taken while still maintaining a trigger rate of 1 trigger per neutrino spill.

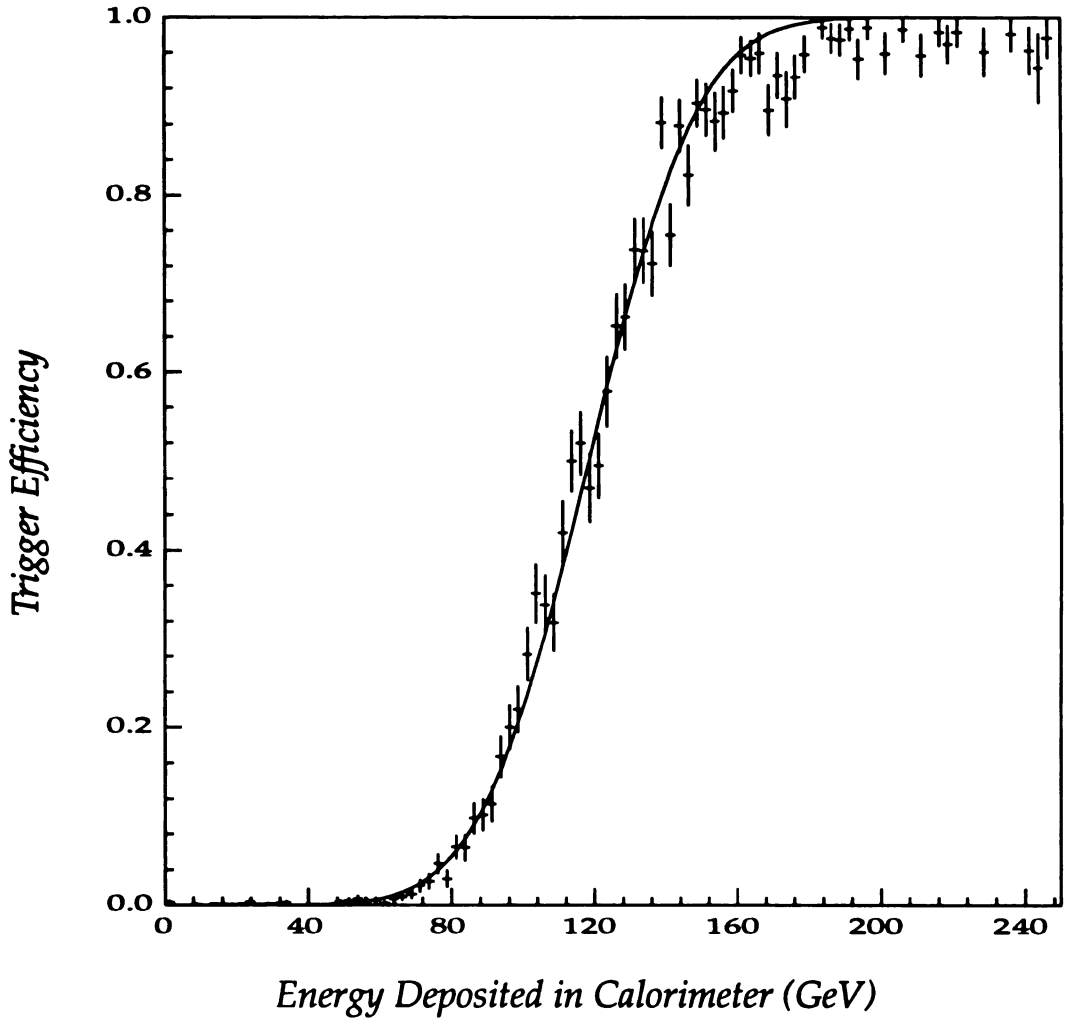

Figure 2.2. HiE Trigger Turnon. The threshold of the HiE trigger as a function of energy deposited in the calorimeter is shown as measured in the data. A fit to the turnon is also shown.

The tail gate was designed to maximize the size of the complete data set by ensuring that at least one trigger was taken during every neutrino spill. During the tail gate, the PTH trigger was no longer prescaled, which allowed any minimum bias event that occurred in the tail gate to be taken.

The experimenters adjusted the relative widths of the beam and tail gates, based on neutrino beam intensity, to maximize the number of rare triggers while maintaining a high event to spill ratio.

Between the 1982 and 1985 exposures, the muon spectrometer was upgraded from the previous charge division read-out to a drift read-out. This change substantially improved the position resolution of the spectrometer. For the higher energy muons produced by the Tevatron Quad-Triplet beam, the improved position resolution was essential.

2.2.3 1987, Experiment 733, Part 2.

From April 1987 through the end of January 1988, the FMMF detector was again exposed to neutrinos from the Quad-Triplet beam. During this exposure, the triggering scheme was much simpler than in 1985. As in 1982, the PTH trigger became the primary trigger. The prescaling of the PTH trigger was eliminated along with the 2MU and HiE triggers. A new second trigger, the CC trigger, was added. The CC trigger was designed to capture charged current events. The CC trigger required that a muon penetrate into the spectrometer, traverse 205 cm of iron and hit the second timing counter located in the fourth gap of the spectrometer. (See Figure 2.7) Approximately half of the data for this thesis came from this exposure.

2.3 Beams

The two separate neutrino beams to which the FMMF detector was exposed differed dramatically. The DiChromatic beam from the 400 GeV era at Fermilab was a low flux, relatively low energy neutrino beam with a very well defined neutrino energy (E_ν)

versus radius (R) relationship. The Quad-Triplet beam was a high energy, high flux neutrino beam with much less correlation between E_ν and R.

2.3.1 DiChromatic Narrow Band Beam

The DiChromatic beam is described in great detail elsewhere (Edwards and Sciulli 1976). 400 GeV protons were incident on a one interaction length beryllium-oxide target. The secondary π's and K's were momentum-selected by the helical DiChromatic magnet train. Finally, the secondaries were allowed to decay in a 300 m evacuated decay space. To reduce the background of wide band neutrinos, the beam is designed so that the momentum vector of the secondaries never pointed in the direction of the detector until the secondaries reached the decay space. A schematic of the beam is shown in Figure 2.3.

The momentum-selection of the DiChromatic train results in a secondary momentum spread of approximately 10%. This small momentum bite and the kinematics of the dominant two-body decays of the secondary mesons gives the beam its well defined E_ν versus R relation. Figure 2.4 shows a scatter plot of E_ν versus R for accepted charged current events at one of the neutrino settings. One can see the two well defined narrow bands of neutrino energy versus radius corresponding to decays from π's and K's. This two parent structure is typical of neutrino beams. What is not typical of other wide band neutrino beams is how strongly correlated E_ν and R are in the DiChromatic beam. The penalty one pays for this excellent E_ν versus R relationship is an order of magnitude reduction in neutrino flux.

2.3.2 Quad-Triplet Wide Band Beam

The Quad-Triplet beam contrasts markedly from the DiChromatic beam. The Tevatron QTB has a higher mean energy, much higher maximum energy and much higher instantaneous flux. There is no attempt to select the sign or momentum of the secondaries. The lack of sign selection results in a beam that contains both neutrinos and

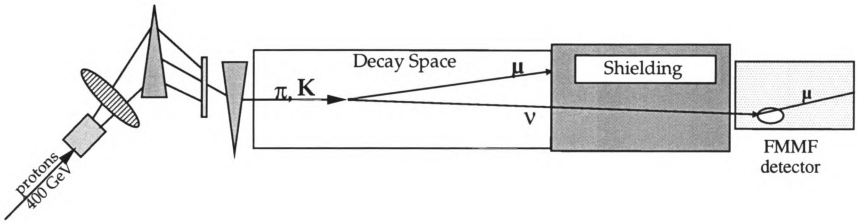

Figure 2.3. DiChromatic Beam Schematic. 400 GeV protons are incident on a target creating π's and K's which are then sign and momentum selected, focused, and allowed to decay. A few of the resulting 10^9 neutrinos per accelerator cycle then interact in the FMMF detector. Drawing is not to scale.

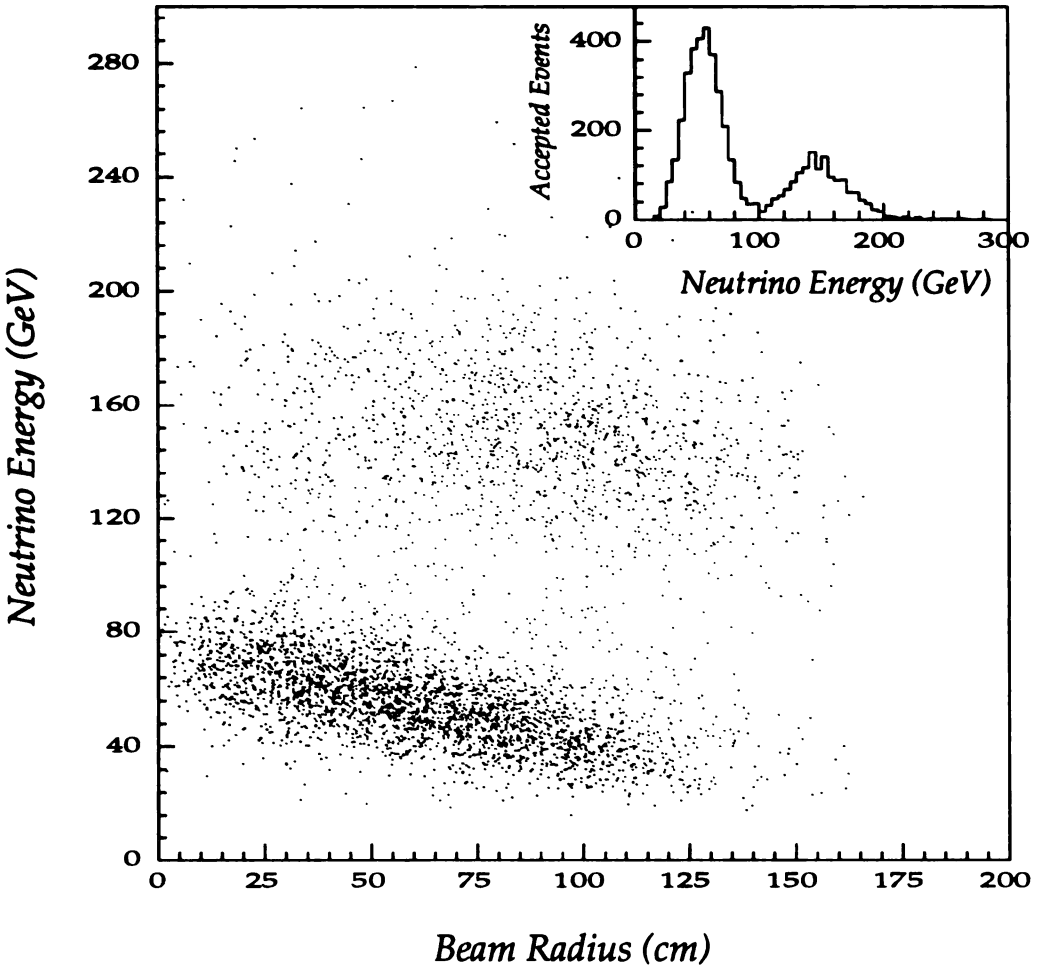

Figure 2.4. Neutrino Energy Versus Beam Radius for DiChromatic Beam. Shown is a scatter plot of reconstructed neutrino energy versus beam radius for accepted events from the data for the +165 setting. One can note the two bands from pion and kaon decay. The inset in the upper right-hand corner shows the projection of the neutrino energy distribution.

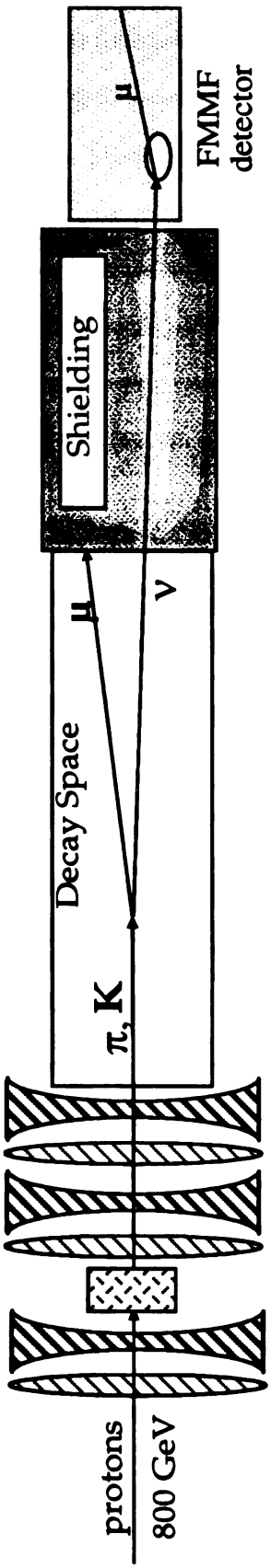

Figure 2.5. Quadrupole Triplet Beam Schematic. 800 GeV protons are incident on a target creating π's and K's which are then focused and allowed to decay. A few of the resulting 10^9 neutrinos per proton pulse then interact in the FMMF detector. Drawing is not to scale.

anti-neutrinos, with integral anti-neutrino flux being approximately 30% of the total flux. The wide range in momenta of the secondaries broadens the E_ν versus R bands for each of the parents. Details on this beam are available elsewhere (Stutte 1985). As one can see in Figure 2.5, the beam is extremely simple. 800 GeV protons were pointed at the neutrino detectors and then struck a one interaction length beryllium-oxide target. The secondaries are then focused in a point-to-parallel fashion by 4 sets of 2" × 2" quadrupoles. The focusing is optimized for a secondary momentum of 300 GeV/c. An example of the E_ν versus R relationship for the Quad-Triplet beam is showed in Figure 2.6.

2.4 Detector

The FMMF detector is described in great detail elsewhere (Bogert et al. 1982; Tartaglia 1984; Brock et al. 1992; Strongin 1988). A schematic of the detector is shown in Figure 2.7. The detector was composed of a target-calorimeter followed by a muon spectrometer. A veto was used at the upstream end of the detector to eliminate non-neutrino background in triggering. This section will briefly describe the parts of the FMMF detector relevant to this thesis. Differences between the detector configuration during different exposures will also be noted.

2.4.1 Front Veto Configuration

During all three exposures, a veto system was used at the front of the detector to reject events caused by incoming charged particles. The most common cause of these charged particles was the interaction of neutrinos in the material (or other detectors) upstream of the FMMF detector. The veto was then made part of the trigger (i.e. TRIGGER = TRIGGER CONDITION • $\overline{\text{VETO}}$).

During the 1982 run, a set of liquid scintillator tanks with photo-multiplier tubes (PMT's) for read-out was used as a veto wall. Due to the low instantaneous rate of the DiChromatic beam, the activity in this veto configuration was minimal.

For the 1985 run, a single veto wall of 8 5'×8'×1" acrylic scintillator counters with

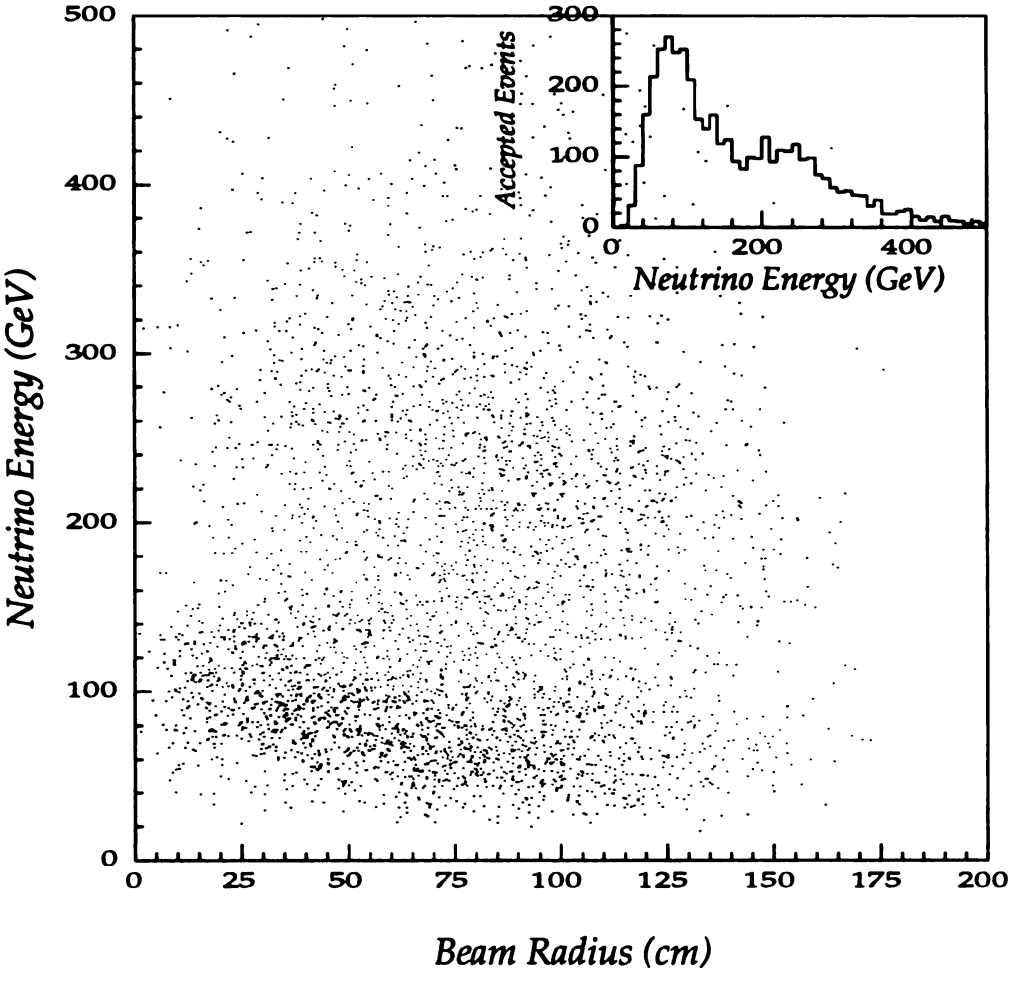

Figure 2.6. Neutrino Energy Versus Beam Radius for Quadrupole-Triplet Beam. Shown is a scatter plot of reconstructed neutrino energy versus beam radius for accepted events from a portion of the 1987 data. Note that the two bands from pion and kaon decay are still present but the bands are much less distinct when compared to the DiChromatic beam. The inset in the upper right-hand corner shows the projection of the neutrino energy distribution.

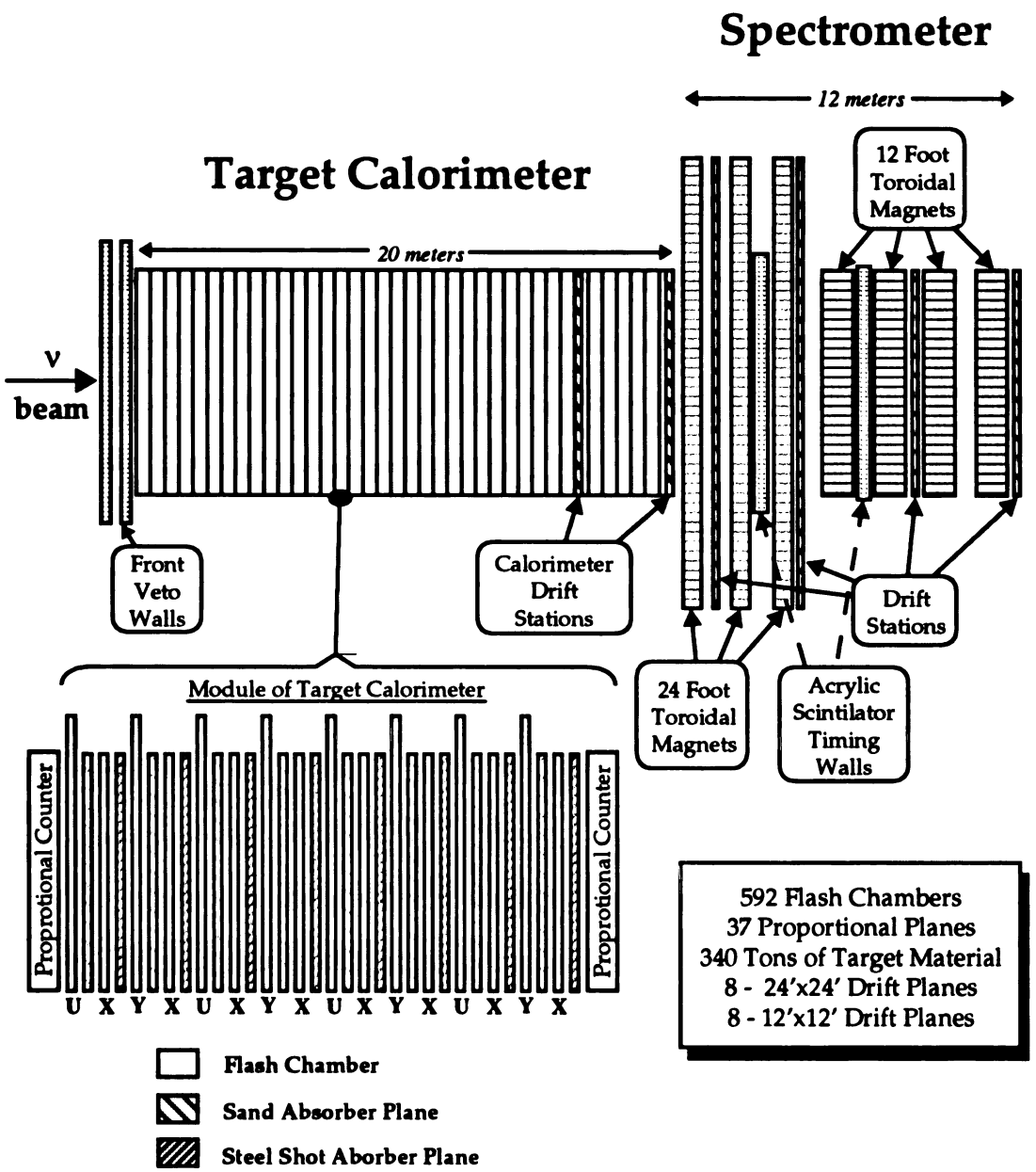

Figure 2.7. FMMF Detector Schematic. The construction of the FMMF detector is shown.The upstream end of the detector consists of the target–calorimeter with its two types of detectors: proportional planes, and flash chambers. Downstream of the target–calorimeter is the muon spectrometer with its toroidal magnets, and its position measurement stations. This figure shows the detector in its 1987 configuration.

wave-shifter to PMT read-out was built. Within the first few minutes of running, it was discovered that the single veto wall was insufficient. The QTB created a "sky-shine" of soft neutrons that caused an extremely high incoherent singles rate resulting in a 100% dead-time. To resolve this problem, a new veto was quickly assembled using the first two calorimeter proportional planes and an existing set of liquid scintillator tanks that formed a plane located between bays 1 and 2. The proportional planes and liquid scintillator plane were run in coincidence to form an effective veto while avoiding the dead time problems of the single wall. Any interaction in Bay 1 was vetoed, eliminating Bay 1 from the fiducial volume of the detector.

For the 1987 run, a set of double acrylic scintillator walls was constructed at Michigan State University. These walls were constructed in a modular fashion and hung in the front of the detector on a structure of UNISTRUT™. The two separate walls were then run in coincidence to provide an effective low rate-veto. The new double veto wall preformed flawlessly.

2.4.2 Target-Calorimeter

The target-calorimeter served three purposes:

- Target material for neutrino interactions.
- Tracker for measuring the paths of outgoing muons.
- Calorimeter for measuring the energy transferred to the nucleon system by the neutrino interactions.

The target-calorimeter was built from 2 types of detectors and 2 different target-absorber planes. The detectors used in the calorimeter were 592 (608, in 1982) roughly 4.5 m × 4.5 m flash chambers in 3 views and 37 12' × 12' proportional tube planes in 2 views. The flash chambers are binary devices made of corrugated plastic which provided extremely fine position resolution for single particle tracking and calorimetry information. The proportional planes were standard gas–wire proportional devices used for both the triggering of the detector and in calorimetry. The target-absorber planes were constructed

of Plexiglass tubes filled with either sand or steel shot. The target-calorimeter was constructed in 37 sub-units called modules. The standard module (see Figure 2.7) consisted of 4 "beams" of flash chamber detectors and absorber followed by a proportional plane. A beam consisted of a flash chamber followed by a sand absorber plane followed by a second flash chamber followed by a steel shot absorber plane. The pattern was repeated so that the beam consisted of 4 flash chambers and 4 absorber planes. The complete module contained 16 flash chambers, 8 sand absorber planes, 8 steel shot absorber planes and 1 proportional tube plane.

The total target-calorimeter had a mass of approximately 300 metric tons with about 100 metric tons in the fiducial region. The density of the calorimeter was 1.35 g/cm^3. Table 2.1 gives a complete list of the target-calorimeter properties.

2.4.2.1 Flash Chambers

The flash chambers provide the extremely fine sampling and segmentation of the FMMF detector. There were 592 (608 in 1982) flash chambers sampling every 0.22 radiation lengths and 0.04 interaction lengths. Many of the details of the construction and operation of the flash chamber are ignored or only superficially covered in this section. The reader desiring more detail is directed to the references mentioned above or the theses of J.A. Slate (1985) or G.J. Perkins (1992).

The flash chambers were constructed of approximately 4.5 m long pieces of corrugated polypropylene with cells running the length of the corrugated sheet. Figure 2.8 shows a schematic of an individual flash chamber. Flash chamber cells were 5 mm × 5 mm × 4.5 m. The cells were filled with a gas mixture of 90% Helium and 10% Neon. Aluminum foil electrodes covered both sides of each chamber. When an interaction was detected in the detector and a trigger was executed, an approximately 4.5 kV pulse was delivered to one electrode in approximately 60 nanoseconds while the other was maintained at ground. This was called the "flash". If there was any ionization left in a cell (by the passage of one or more charged particles), this rapid high voltage pulse resulted in

Table 2.1

Calorimeter Properties

Property	Detector Average	Flash Chamber Sampling	Proportional Plane Sampling
Density, ρ	1.35 g/cm^3	4.2 g/cm^2	67.5 g/cm^2
Radiation Length, X_o	14 cm	0.22 X_o	3.5 X_o
Interaction Length, λ	85 cm	0.04 λ	0.59 λ
Protons per Nucleus, Z	9.8	—	—
Neutrons per Nucleus, N	10.4	—	—
Nucleons per Nucleus, A	20.2	—	—
Non-isoscalarity, δ	2.97%	—	—

Table 2.1. Average Properties of Target and Detector Sampling. Listed are the average properties of the FMMF target and the sampling fractions of the calorimeter detectors.

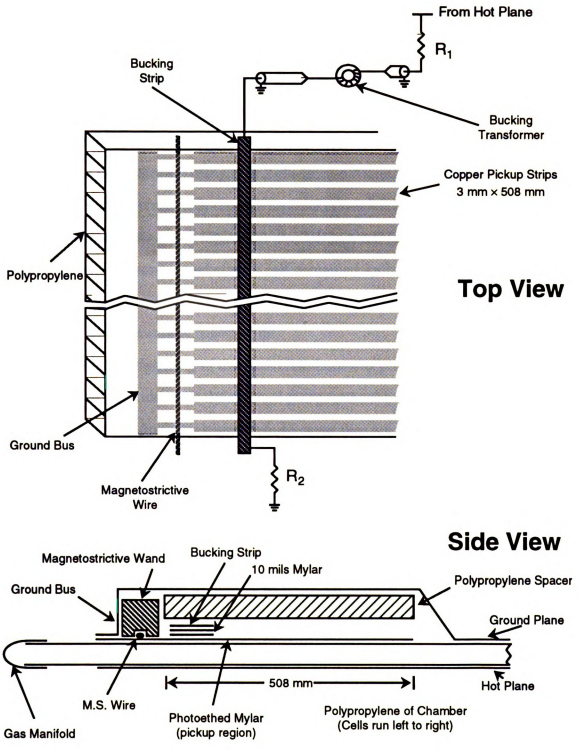

Figure 2.8. Flash Chamber Schematic. The figure shows the construction of a flash chamber. The pickup region is shown in detail.

the formation of a plasma in the cell. The plasma rapidly filled the entire length of the cell. The plasma was detected through the capacitive coupling of the plasma to copper read-out fingers. The entire chamber was read-out using a single magnetostrictive wire which was excited by the current flow in the read-out fingers. The advantage of this type of chamber and read-out system was that large number of cells could be read out (over 700 cells per chamber) using only 2 electronics channels per chamber. The disadvantage was that one could only detect if ionization was left in a cell or not. There was no way to determine how much ionization was left in a cell (as in an analog device). Because one could detect only whether a cell contained ionization, the flash chamber is often referred to as a digital device or more properly as a binary device. The detection of plasma in a cell is commonly called a "hit."

The rapid retriggering of the flash chambers was problematic. It was necessary to wait for a few seconds while the residual charge recombined. Any residual ionization left in a cell from the previous trigger would cause that cell to "refire". The recombination of charge was extremely slow because charge would collect on the walls of cells and the plastic insulator provided no path to ground. During 1982, the flash chambers were not retriggered more often than once every 10 seconds. In 1985 and 1987, it was found that it was possible with the careful control of the electronegative components in the recirculating gas to retrigger as quickly as every 3.5 seconds with minimal refire.

A schematic of a module is also shown in Figure 2.7. The chambers were oriented in three separate views; X, which provided a vertical sampling, and U and Y, which provided horizontal sampling in two separate views, ±10° from vertical in stereo. The ordering of the flash chambers and absorber planes within a beam was U chamber, sand plane, X chamber, steel shot plane, Y chamber, sand plane, X chamber and steel shot plane. Each module consisted of four beams.

In 1982, there were an additional 16 flash chambers which were located at the extreme downstream end of the detector. The first two modules in bay 8 and and the last

two in bay 9 were removed between the 1982 and 1985 runs for the installation of a calorimeter drift system which was extremely important in the alignment of the detector, in particular the alignment of the spectrometer.

2.4.2.2 Proportional Planes

The 37 proportional planes were positioned between flash chamber modules (16 chambers) and were aligned alternately either horizontally or vertically. The planes were spaced every 3.5 radiation lengths and every 0.59 interaction lengths. The proportional planes were constructed of 1" × 8" × 12' aluminium extrusions. 18 extrusions combined to form a single plane and create an active area of 12' × 12'. Extrusions were divided by thin aluminium webs into approximately 1" square tubes, 12' long. 50 μm gold plated wires were strung down the length of the tubes. The tubes were filled with a mixture of 90% Argon and 10% Methane. Positive 1750 V was applied to the wire and the tubes were run in proportional mode. The planes were read out by ganging the signals from 4 tubes together and amplifying the combined signal. This resulted in 36 channels per plane and a lateral sampling of 4".

The primary purpose of the proportional planes was for triggering the detector, since the flash chambers are passive devices and require some sort of trigger. The first step in forming a trigger was for the pulse height in any two planes to exceed a very low threshold. Upon observation of this pre-trigger condition, the total pulse heights from all the proportional planes in the fiducial volume were combined and if this pulse height exceeded a pre-determined level, the trigger was satisfied. The standard trigger (known as the PTH trigger) discussed above was found by test beam studies to be 50% efficient for 5 GeV of energy deposited in the calorimeter and 100% for 10 GeV.

In addition to providing the trigger, in 1985 and 1987, it proved useful to use the proportional planes to augment the flash chamber calorimetry. At the higher energies of the QTB, the flash chambers saturate due to their binary nature, resulting in a constant fractional resolution for higher energies, in contrast the proportional tubes' fractional

resolution improves as the energy deposited increases.

Calorimetry will be discussed in detail in a later section of this chapter and in great detail in Appendix B.

2.4.3 Spectrometer

The muon spectrometer was used to measure the momentum and charge of the muon. The momentum is required to reconstruct the muon energy, and the charge of the muon "tags" the event as a neutrino or anti-neutrino event.

The spectrometer consisted of 7 iron-core toroidal magnets and 4 muon position stations. The magnets were of two types. The spectrometer consisted of the three 24' magnets, followed by the four 12' magnets. The 24' magnets in the upstream part of the spectrometer were 24' in diameter and 60 cm thick while the 12' magnets in the downstream part of the spectrometer were 12' in diameter and 125 cm thick. The total length in the z (beam) direction of the spectrometer was approximately 1200 cm, of which 680 cm was iron.

There were four stations for the measurement of muon position. These were located in the gap between the first and second 24' magnets, between the third 24' magnet and the first 12' magnet, between the second and third 12' magnet and after the last 12' magnet. All the stations were constructed in the same manner as the proportional planes, using an aluminium extrusion similar to that used in proportional planes. The extrusion used contained two layers with cells offset by one half a cell width. Stations consisted of four layers, two measuring horizontal position and two measuring vertical position. The layers with the same orientation in a station were offset from each other by half a wire spacing (0.5 inches). The first two stations were shaped like crosses. These stations were 24' tall and wide but the wings of the crosses were only 12' wide. The last two stations were 12' × 12' planes. As with the proportional planes, 50 μm gold plated wires were strung in the middle of each cell. Positive high voltage was applied to each

wire.

In 1982, the planes in each station were run in a "charge division" mode using 90% Argon and 10% Methane, which gave no better than the 1" cell-size spatial resolution. For 1985 and 1987, the planes were run in a drift configuration using 90% Argon and 10% Ethane, which gave a 2 mm resolution. The drift configuration required an additional acrylic scintillator plane for timing of the drift electrons. The two different configurations are described in detail below.

2.4.3.1 Charge Division

The charge division scheme is describe in the thesis of Juan Bofill (1984). In the charge division scheme, same ends of 8 (16 for the first station) adjacent wires were resistively connected. The charge was collected by two amplifiers on opposite ends of this resistive network. The more charge collected on a given amplifier, the closer the wire hit is to that amplifier. The hit wire is determined by the ratio

$$\Delta = \frac{q_1 - q_2}{q_1 + q_2},$$

where q_1 and q_2 are the charge collected by the two amplifiers. From Δ, one can determine which wire was hit. This simple scheme results in a single plane resolution of 8.7 mm.

2.4.3.2 Drift

In a drift system, a charge particle (in our case, a muon) traverses a cell producing ionization that drifts towards the anode (the wire) or cathode (cell walls) due to the applied electric field. By measuring the length of time for the ionization to reach the anode wire and knowing the drift velocity of the gas, one can determine the distance of closest approach of the charged particle. In the FMMF spectrometer, the time of traversal of the charge particle was determined by the coincidence of two acrylic scintillator planes. The scintillator planes were located in the gap between the second and third 24' toroids and the gap between the first and second 12' toroids.

If there were two back to back (separate layers, but adjacent wires) clean, isolated, drifted hits in a given drift station, these hits were combined for a position resolution of 2 mm. This combination was done within the muon fitting process because one needs a rough fit of the charged particle to resolve the left/right ambiguity. (See Figure 2.9.)

2.4.4 Event Display

Figure 2.10 shows an event display of a charged-current event from the 1987 run. The neutrino beam is incident on the detector from the left. The left side of the display shows the calorimeter elements. The flash chamber hits for the three separate views are shown in the three larger panels. The two views of the proportional planes are shown above and below the flash chamber displays. One can clearly see the neutrino interaction vertex, the hadronic shower, and the outgoing muon in both the flash chambers and the proportional planes. The two views of the spectrometer are depicted at the right side of the display. The rectangular outlines show the positions of the toroidal magnets while a hit in the drift system is displayed as "+." Hits that are grouped together as a cluster of hits are indicated by a surrounding circle. The fit of the muon in the spectrometer is indicated by the curved line connecting the spectrometer clusters. One can see how one measures a charged-current event using the FMMF detector. The energy transferred to the hadron system is measured in the calorimeter. The angle through which the lepton was scattered is inferred using the trajectory of the muon in the calorimeter. The energy of the muon is measured in the spectrometer. From these three measurements, one can fully reconstruct the event kinematics. The next section discusses, in detail, how one measures an event.

2.5 Event Reconstruction and Measurement

To fully reconstruct the kinematics of a deep inelastic neutrino event, one needs to measure three quantities; the energy transfer, ν, the energy of the muon (i.e. outgoing lepton) E_μ and the polar angle of the outgoing muon relative to the incoming neutrino,

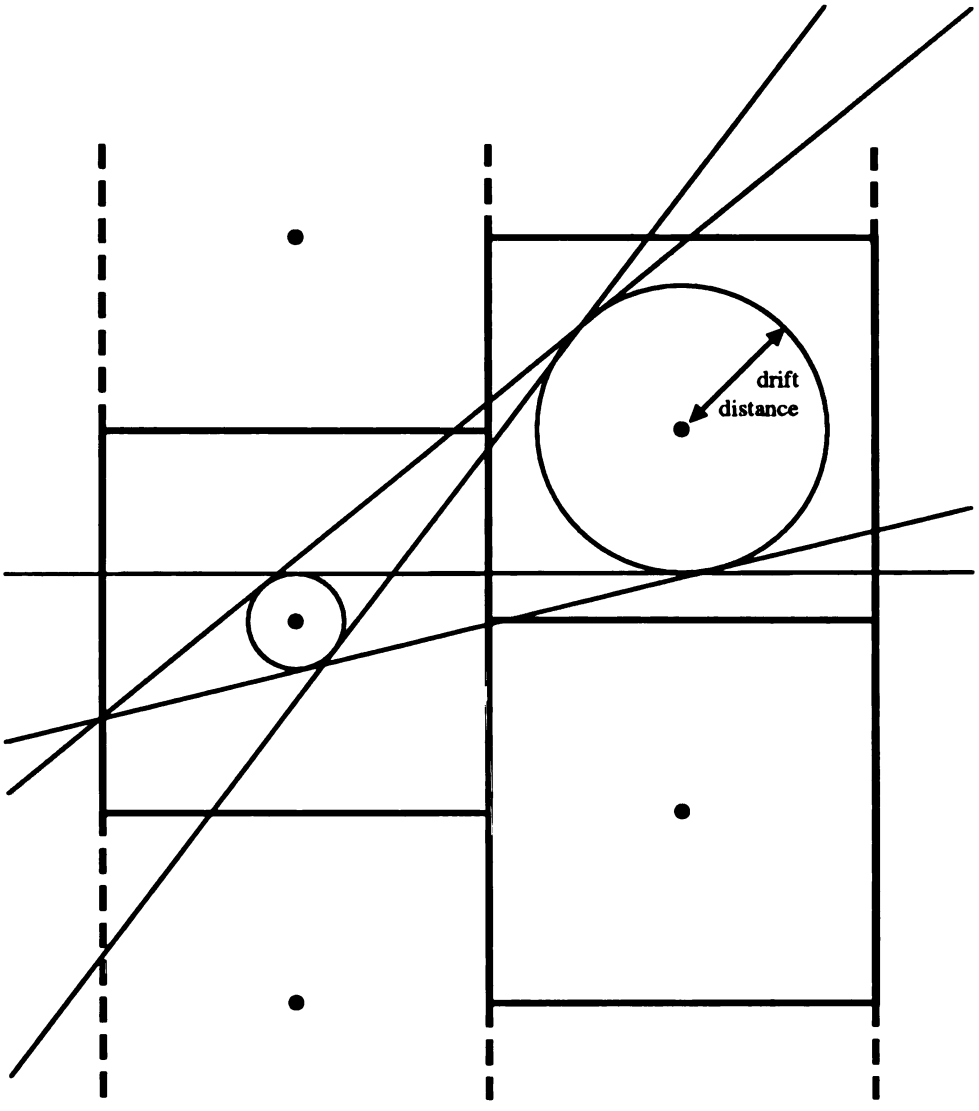

Figure 2.9. Left/Right Ambiguity. Drift systems with only two layers suffer from an ambiguity in hit position. The drift time corresponds to the closest approach to the sense wire.The figure shows two hit cells and the corresponding "drift distance" and the four possible trajectories through the two cells which in turn correspond to four different positions at center wall between the two drift layers. The ambiguity is resolved in the fitting process.

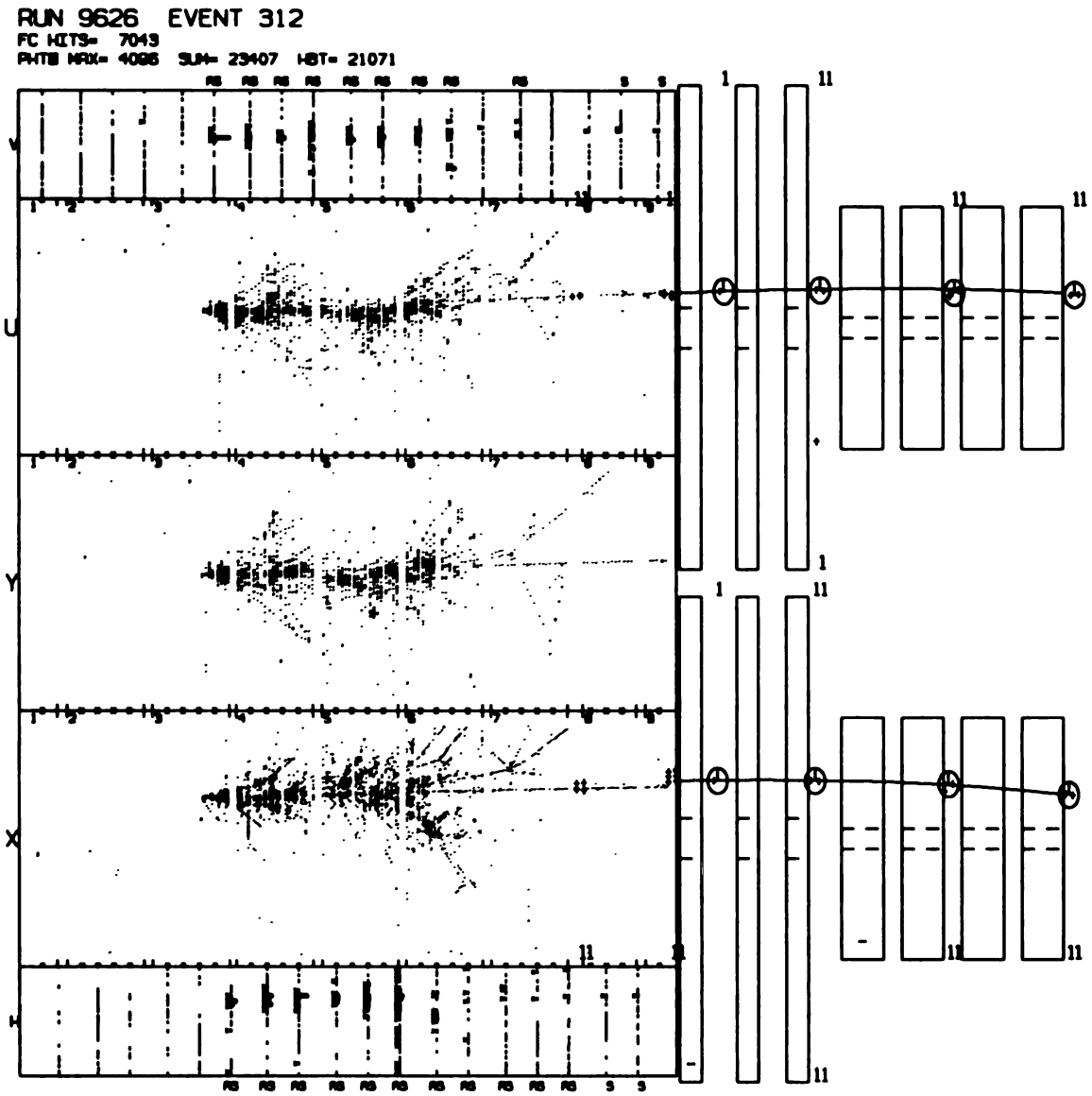

Figure 2.10. Event Display. The figure shows a charged-current event from the 1987 run. The left side of the display shows the displays of the flash chamber hits and the proportional plane pulse height. The right side of the display shows the two views of the spectrometer. One clearly sees the vertex of the neutrino interaction, the resulting hadronic debris, and the track of the outgoing muon in the calorimeter. The spectrometer hits of the muon are shown along with the fit of the muon in the spectrometer.

θ_μ. From these three "measurables," one can reconstruct the physics variables: the neutrino energy (E_ν), the fraction of the lepton's energy transferred to the nucleon system (y), the fraction of the nucleon's momentum carried by the struck parton (x) and the square of the four-momentum transfer (Q^2). To reconstruct the kinematics of a deep inelastic event, one must determine any three of the physics variables. In practice, one always reconstructs all four and then uses the appropriate variable for a given analysis. These four variables are discussed in detail in chapter 1. Reconstruction of E_ν and y is straight forward. By definition, $E_\nu = \nu + E_\mu$ and $y = \frac{\nu}{E_\nu}$. For reconstruction of Q^2, one uses the relationship,

$$Q^2 \cong 4E_\nu E_\mu \sin^2\left(\tfrac{1}{2}\theta_\mu\right),$$

which neglects the muon mass. Finally, x is reconstructed by the relationship,

$$x = \frac{Q^2}{2M\nu},$$

where M is the mass of the struck nucleon and we have assumed the nucleon is at rest.

The analysis chain for this thesis involves a number of preliminary steps before the event can be "measured". A flow chart for this analysis chain is shown in Figure 2.11. The first of these preliminary steps is to find and reconstruct the event interaction vertex. Once the event vertex is found, a search light algorithm is employed to find muon candidates. The calorimeter flash chamber tracks of the muon candidates are then fit to a straight line. The fit to the calorimeter track gives the muon angle. The calorimeter tracks are also used as the input to the fitting of the muon in the spectrometer. The fit in the spectrometer measures the muon energy and charge. The calorimeter is then used to measure the energy transferred to the nucleon system, ν.

The next sections discuss vertex finding, muon finding and the techniques used to measure E_μ, θ_μ and ν.

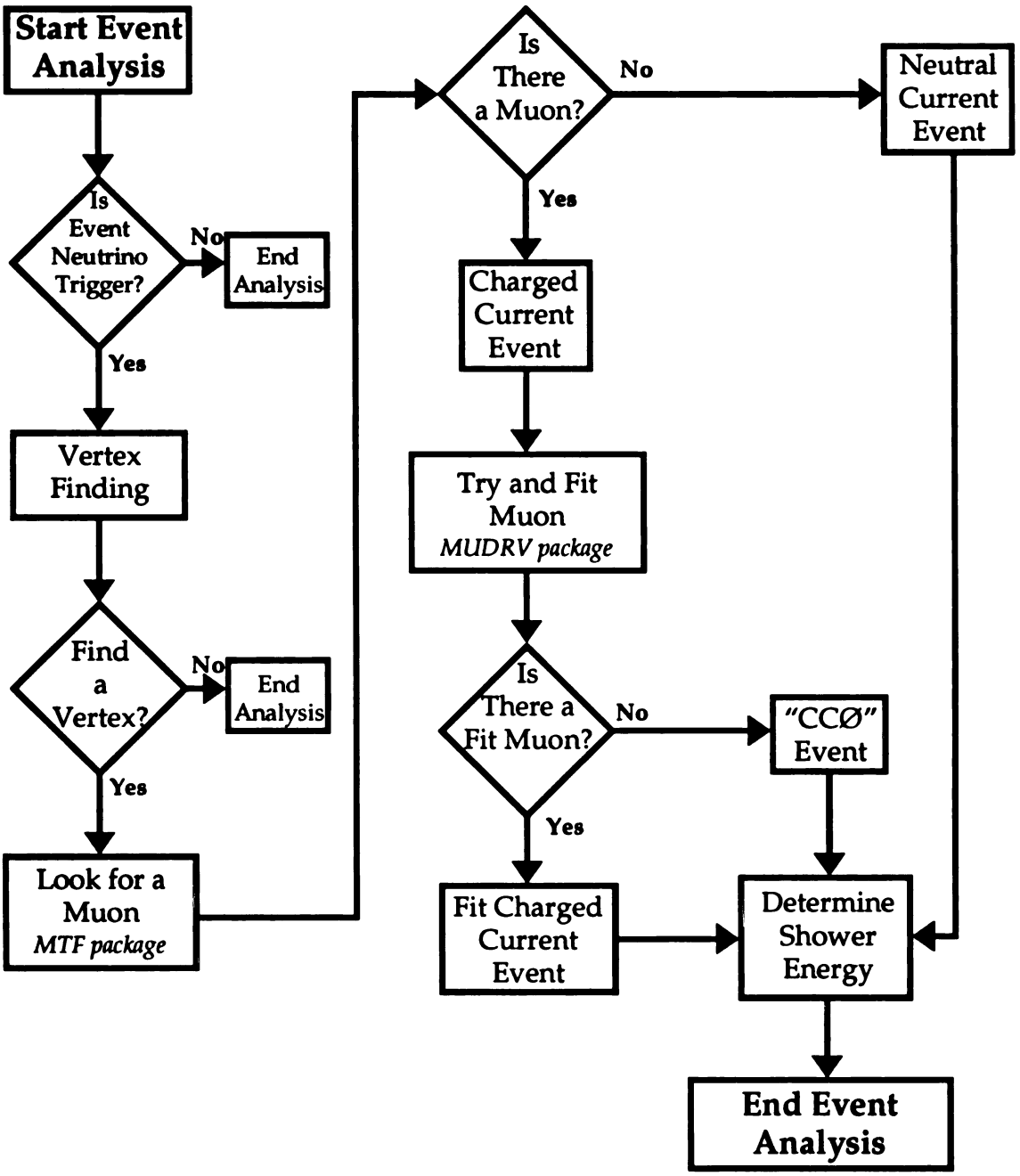

Figure 2.11. Event Analysis Diagram. The figure shows the event analysis chain in the form of a flow chart. Included are all of the required branches. Optional branches such choice of fiducial volume are ignored.

2.5.1 Vertex Finding.

The vertex finding algorithm is based on energy deposited in the calorimeter. The algorithm starts by searching for a hadron shower in the calorimeter using the proportional planes. Searching with the proportional planes has two virtues: the coarser segmentation of the proportional planes allows a more efficient search for the shower and the flash chambers are susceptible to effects of ionization left behind by previous events, untriggered upon events, cosmic rays or other "out of time" events which would confuse the vertex finding. The algorithm uses the latches of the proportional plane and finds a shower by looking for at least two proportional planes in a row with latches on. An estimate of the z position of the vertex is made using the z position of the most upstream proportional plane of the most upstream group of planes with latches on. Once the hadron shower is found by the proportional planes, a search for the vertex is made independently in each of the three flash chamber views. The search in flash chambers starts at the downstream end of the shower and "walks" towards the front of the detector until the beginning of the shower is found and the algorithm has located the lateral vertex position. Once the vertex has been found in each view, the final result is constrained to be a single point in three-space.

The vertex finding routine has been found to be greater than 99% efficient at finding a vertex for events with $\nu > 10$ GeV (Mattison 1986; Mukherjee 1986).

2.5.2 Muon Finding and Fitting

The muon track finding is done by a software package call the MTF (Muon Track Finding) package. The muon finding and fitting is done in a three step process: segments in individual views are found, the segments from the separate views are then combined into tracks and finally the muon candidates are selected and fit. In each flash chamber view, a search is made for long tracks originating from the vertex. The search is done using angular bins that originate at the vertex. In the angular bins that contain a

potential muon candidate, hits are combined to form continuous segments which originate at the vertex. The segments in the individual views are then "3-view-matched" to form a track. To be considered a muon candidate, a track must travel 5 meters in the z (beam) direction before exiting the calorimeter (either out the back or one of the sides). Finally, the track is fit to a line using a least-squares technique.

2.5.3 θ_μ

The muon angle measurement results directly from muon calorimeter fit. Assuming that the neutrino was traveling parallel to the z axis, the muon momentum polar angle, θ_μ, is the angle through which the lepton was scattered. The angular resolution is estimated from Monte Carlo studies to be,

$$\sigma_{\theta_\mu} \approx \frac{74 \text{ mR} - \text{GeV}}{E_\mu},$$

which is consistent with previous estimates made in studies using cosmic ray muons.

2.5.4 E_μ

The muon energy is measured in the muon spectrometer and then corrected for $\frac{dE}{dx}$ loss in the target-calorimeter. The spectrometer fitting algorithm projects trajectories for different muon energies (and charge) into the spectrometer based on the calorimeter fit of the muon. The calculation of the trajectory includes the mean muon $\frac{dE}{dx}$ in the spectrometer iron. These trajectories are then used to select the correct combination of hits in the spectrometer and to estimate the muon momentum. The projection process is then repeated and the χ^2 for each of the projected momentum is calculated and the χ^2 surface is fit to a parabola. The minimum of the parabola defines the fit momentum. Greater detail on the muon fitting can be found elsewhere (Strongin 1989; Hatcher 1993; Brock 1992).

The calorimeter energy loss is accounted for by an "integration" calculation using the muon momentum entering the spectrometer as measured as the starting point.

The calorimeter muon track is divided into steps. The algorithm starts where the muon exited the calorimeter and adds to the measured muon energy the calculated mean $\frac{dE}{dx}$ for the step based on energy of the muon as it leaves the step. The algorithm then steps back to the vertex to calculate the final muon energy. The calorimeter correction to the spectrometer fit is shown in Figure 2.12. The mean correction is 3.1 GeV and is directly correlated the amount of calorimeter material traversed and thus with the vertex z position.

Monte Carlo studies using a full simulation of the muon spectrometer and including parameterizations of the cross sections for discrete energy loss mechanisms (See Chapter 3 for details) such as nuclear bremsstrahlung and pair production show that the fractional resolution in E_μ is,

$$\frac{\sigma_{p_\mu}}{p_\mu} = 14\%,$$

for $E_\mu > 50$ GeV. The resolution worsens at low energies due to multiple scattering in the iron toroids.

2.5.5 ν

The energy transfer from the lepton to the hadron system, ν (nu not to be confused with neutrino) is measured directly in the calorimeter. As we saw in Chapter 1, ν is defined as,

$$\nu \equiv E_\nu - E_\mu.$$

ν is sometimes referred to as E_h (or E_{hadron}) but E_h is really the energy part of the outgoing hadron system 4-vector, $P' = \left(E_h, \vec{P}\right)$. One often finds in the literature statements such as, $E_\nu = E_h + E_\mu$ or $y = \frac{E_h}{E_\nu}$. Obviously, in this context, ν and E_h are being used synonymously, albeit incorrectly. In a neutrino target-calorimeter, one measures the kinetic energy transferred to the nucleon system. (The rest mass of the struck nucleon is undetectable because baryon number conservation requires that one baryon still remain after the interaction.) This is simply ν.

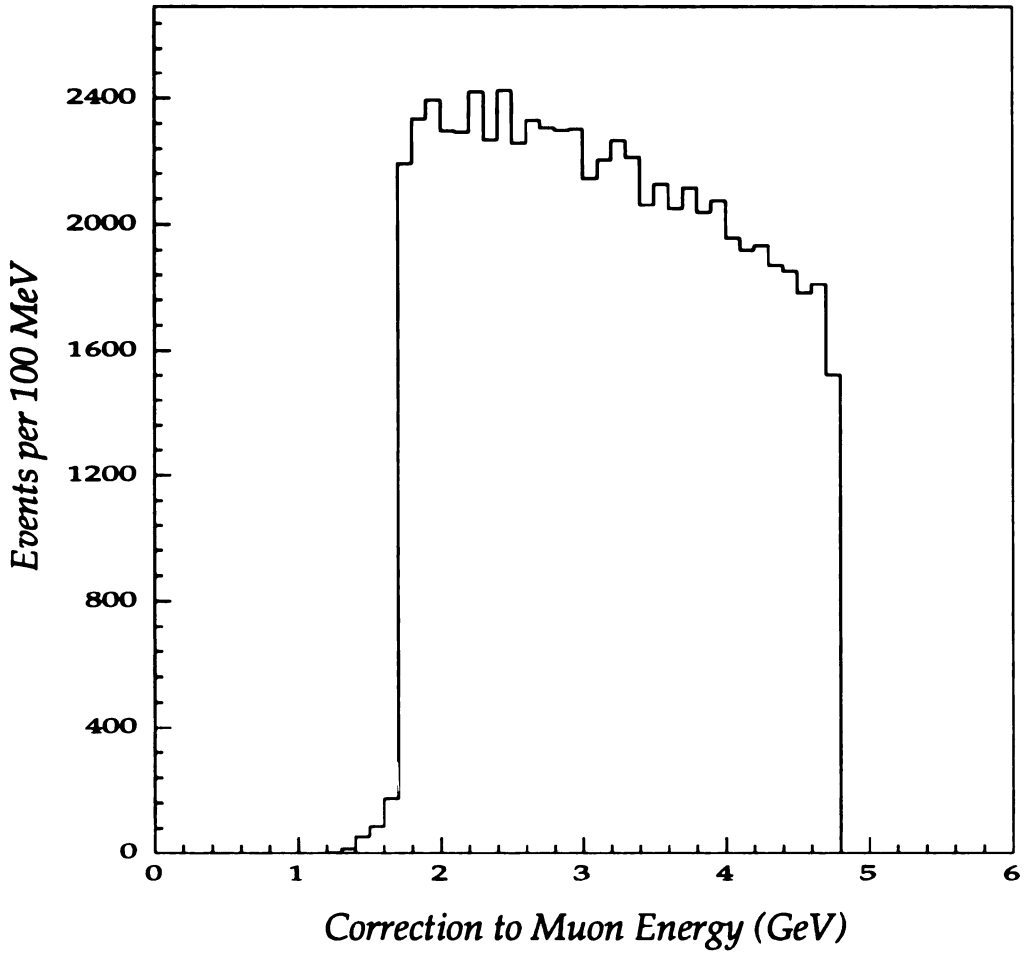

Figure 2.12. Calorimeter Energy Loss Correction to Fit Muon Energy. Plotted is the distribution of the difference between the final reconstructed muon energy and the result of the spectrometer fit. The sharp edges of the distribution are due to the fiducial volume requirements imposed in the data analysis.

The FMMF detector is unusual in that it contains two separate detectors in its calorimeter, the flash chambers and the proportional planes. As discussed above, these two different detectors have very different properties.

The primary advantages of the flash chambers are their very fine granularity and sampling. The primary disadvantage is that at higher energies the chambers are subject to saturation. The finer sampling in principle should lead to intrinsically better resolution for the flash chamber when compared to the proportional planes but saturation results in a severe degradation of the resolution, especially at higher energies.

In contrast, the proportional planes sample much more coarsely than the flash chambers, but, being sampling analog devices, their resolution shows the typical $1/\sqrt{\nu}$ proportionality.

In addition to the above problems, all large detectors can be sensitive to environmental effects. The QTB data runs involved the gathering of data over periods of eight to nine months. The analysis for this thesis required a stable, known calibration of the calorimeter over an entire eight or nine month exposure. Both the flash chambers and proportional planes showed time-dependent behavior. These time dependent behaviors are much better understood and handled with the proportional planes than with the flash chambers because of the well understood nature of proportional detectors and the self monitoring hardware built into the proportional plane system (Tartaglia 1984; Tartaglia et. al. 1985).

The one final problem that requires mentioning is that of calibrating a device as large as the FMMF detector. During both the 1985 and 1987 runs, a test beam of pions, kaons and protons of a known momentum was continuously brought into Lab C and used to calibrate the FMMF detectors. This was extremely useful in understanding the detector, but at the same time was extremely limited because the calibration beam was only incident on the front of the detector.

For E594, an algorithm (SHOWER) was developed that corrected the flash chamber

response for saturation and variation in detector response in a microscopic fashion. This algorithm was then recalibrated using the E_ν versus radius of the DiChromatic narrow band neutrino beam (Mattison 1986). The SHOWER ν scale was used as is for the 1982 data. In 1982, no attempt was made to combine the flash chamber calorimetry with that of the proportional planes. For the QTB data, it was found that the SHOWER algorithm was unstable over the long exposures. In addition, at the higher energies of the QTB beam, saturation was a much more important effect.

For all of the above reasons, it was necessary for the 1985 and 1987 data to develop a new method of measuring ν and insuring the stability of the calibration. The requirements for a new method were:

- Long Term Stability - the calibration must be consistent over an entire exposure.
- Detector-Wide Uniformity - the calibration must be consistent over the entire fiducial volume of the detector.
- Sensible Functional Form - the final calibration must have a smooth functional form that is sensible, for example, a quadratic in some form of corrected hits.
- Inclusion of the Proportional Planes - for the better resolution of the proportional planes at high energies.

A new calibration method was developed based on the above principles.

The new calibration algorithm used an innovative scheme for measuring and then compensating for the variation of the response of the flash chambers. Using the proportional planes, showers in a small range of energies were selected from the neutrino data. This data set was used to measure the response of each flash chamber module using the shower transition curves. The measured response was used to correct the "raw" hits observed in a given module. A scale for the "corrected raw" hits was then obtained using the test beam data and later adjusted using the charged current neutrino data set and the neutrino Monte Carlo. Finally, the flash chamber measurement was then combined with proportional plane measurement based on the measured resolutions. This method is described in detail in Appendix B.

The fractional resolution of the flash chambers and proportional planes and of the combined measurement is shown in Figure 2.13. As one can see the proportional planes exhibit the typical behavior with a fractional resolution of $3\% + 116\%/\sqrt{\nu}$ whereas the flash chambers exhibit large effects of saturation with constant fractional resolution above 100 GeV. The final combined fractional resolution is consistent with,

$$\frac{\sigma_\nu}{\nu} \approx 6\% + \frac{47\%}{\sqrt{\nu}}.$$

2.6 Final Event Sample

The final event sample for this thesis consists of fully reconstructed charged current events, which requires a found vertex, a found and momentum analyzed muon and a measured ν. Additional cuts are made to insure that the event is well measured and that the acceptance is well understood. The cuts applied and the resultant event sample are discussed in this section.

2.6.1 Cuts

The cuts were of three types, acceptance cuts, measurement quality cuts and physics cuts. The acceptance cuts are made to compensate for effects such as trigger and algorithm inefficiencies. Measurement quality cuts are made to eliminate events which are questionably measured. Physics cuts are made for various reasons such as insuring that an event is a deep inelastic event or for comparing the data to Monte Carlo only in kinematic regimes that are well understood theoretically.

2.6.1.1 Acceptance Cuts

There are a number of standard acceptance cuts: a requirement that the event vertex be within a defined fiducial volume, the requirement that $\nu > 10$ GeV and a complicated requirement on the calorimeter track of the fit muon.

The fiducal volume was defined as $32 <$ LVEST < 401 ($8 <$ LVEST < 401 for 1982 data) and CCEDGE > 250.0. The first cut is on the z position of the vertex based on the flash

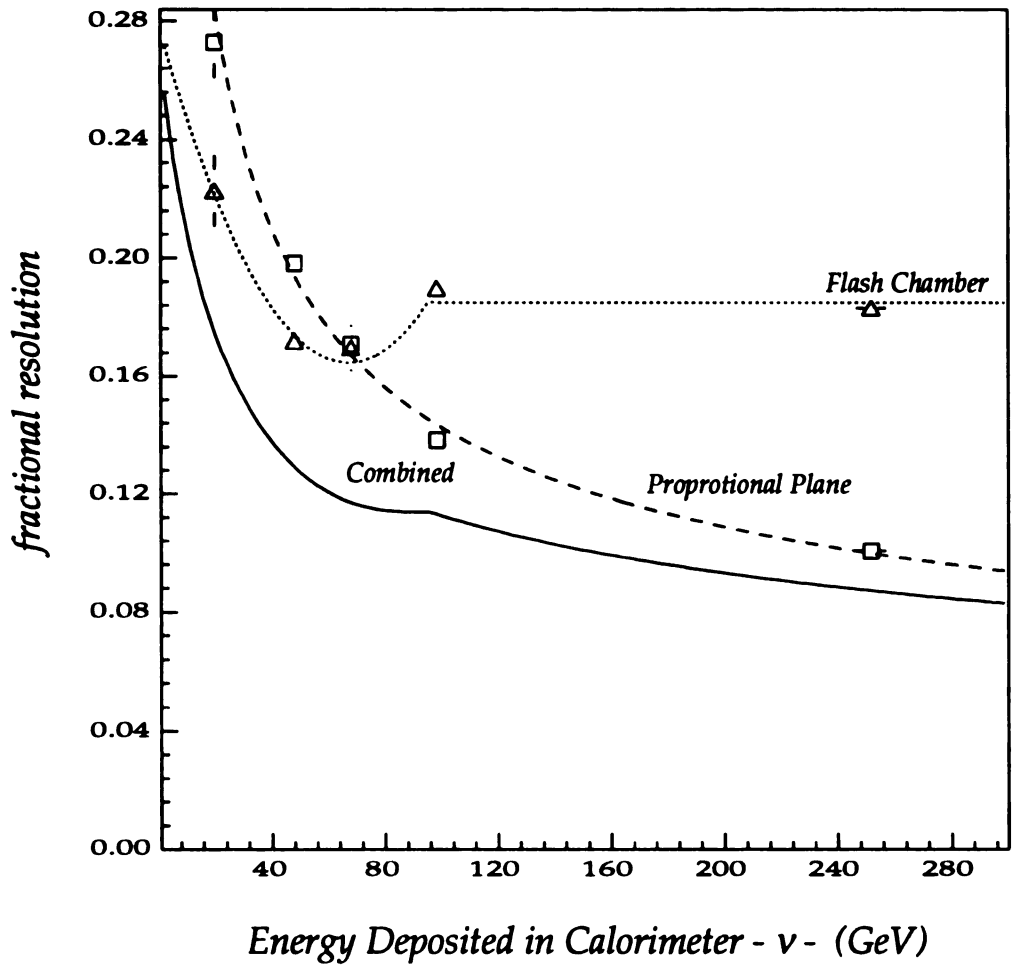

Figure 2.13. Fractional ν Resolution as Function of ν. Plotted is the ν resolution as a function of ν as measured in the test beam. The fractional resolutions, $\frac{\sigma_\nu}{\nu}$, for the Flash Chambers, the Proportional Plane and the combined measurement are shown. The open squares show the measured fractional resolution for the flash chambers with the dotted line showing the fit functional form. The open triangles show the measured fractional resolution for the proportional planes with the dashed line showing the fit of the resolutions. The solid line shows the combination of the fractional resolutions of the flash chambers and the proportional planes.

chamber of the found vertex, LVEST. The second cut is on the transverse position of the vertex and requires that the event vertex be no less than 25 inches (125 cm) from the detector edge in any flash chamber view.

The ν cut is based on the standard PTH trigger. The trigger has been measured to be fully efficient at 10 GeV. As no attempt has been made to model the trigger efficiency, a hard 10 GeV cut has been imposed.

The HiE trigger introduces a second threshold. For the HiE trigger, the trigger turn-on was measured using PTH triggers from the 1985 run. The measured ν distribution for all PTH triggers was plotted and the same distribution was plotted for the PTH triggers that were also HiE triggers. The ratio of these two distributions gave the trigger turnon shown in Figure 2.2. This function was then fit to the integral of a Gaussian where the width and mean of the Gaussian are the free parameters. This function is simply the error function. The form was chosen because the trigger is based on the amount of energy seen by the proportional planes and if the amount of energy deposited is above threshold the trigger is taken. Since there are resolution effects, the integral of a Gaussian is the appropriate form. The error function gives a good fit to the distribution as shown in Figure 2.2. The fit was then used in modeling the HiE trigger in the Monte Carlo.

The MTF package has been found to be excellent at finding tracks. The MTF package was originally written to enable simple Monte Carlo simulation. For this reason, the package uses two simple criteria (only one of which is important for this analysis) to determine which tracks are those of muons. A track is classified as a muon, if the track is 10 meters or longer in z, or if a track exits the calorimeter and the track is 5 meters or longer in z. The first criterion is relevant for stopping tracks and is thus not important for this thesis. The second criterion is obviously relevant for this thesis. The problem is the definition of "exiting" the calorimeter. Exiting through the rear of the detector is easy to define but exiting the sides is more difficult to define. The problem is that the software must determine which chamber was the last chamber hit before exiting and from this

chamber the z traversed is determined This is a difficult pattern recognition exercise. Chamber inefficiencies, phantom hits from cosmic rays and other instrumental problems cause inconsistencies in the application of the criterion. For this reason, an additional cut is imposed on the muon track to insure the same criterion is used for both the data and the Monte Carlo. This cut involves projecting the exit point of the muon from the calorimeter using the muon's fit trajectory and requiring that the z position of this projected exit point be 5.5 meters downstream of the vertex z position. This is an easy requirement to implement in software and it eliminates uncertainty in the muon calorimeter acceptance.

Finally, the acceptance of the spectrometer is modeled by a full detector simulation of the muon spectrometer. This simulation will be discussed in the next chapter.

2.6.1.2 Measurement Quality Cuts

Measurement quality cuts are applied to the fit muons. The standard cuts were:

- The muon must traverse at least 175 centimeters of spectometer toroidal magnet iron.
- The muon charge must be consistent with the expected neutrino in the 1982 exposure.

These cuts insure that the muon momentum was well measured.

2.6.1.3 Physics Cuts

There are two standard physics cuts. The cuts are applied for different reasons but are closely related.

The first of these cuts is on the square of the hadron system invariant mass, W^2. W^2 is defined as,

$$W^2 = P'^2 = (P+q)^2 = M^2 + 2P\cdot q + q^2 = M^2 + 2M\nu - Q^2.$$

For this cut, an event is required to have $W^2 > 2.5\,\mathrm{GeV}^2$. This cut is made to insure that the event is a true deep inelastic event, not the quasi-elastic excitation of a nucleon resonance.

The second of these cuts is on the square of the 4-momentum transfer, Q^2. This

cut is used only for comparisons between data and Monte Carlo because the quark distributions used as input for the Monte Carlo are derived from data with a $Q^2 > 5$ GeV^2 and the evolution of the quark distributions to low 4-momentum transfers ($Q^2 <$ 5.0 GeV^2) is not well understood theoretically.

2.6.2 Sample

The final data sample for this thesis includes data from the three exposures previously discussed. This data set consists of roughly 110,000 reconstructed, accepted charged current events. Approximately one half of the data was taken during the 1987 exposure. The other half of the data was split somewhat evenly between the 1982 narrow band data, the 1985 low bias events (the low-bias event sample consisted of PTH in the beam gate and the PTH, HiE and 2MU events in the tail gate) and 1985 HiE events (only in the beam gate). Table 2.1 gives event sums for each of the individual data sets and other useful information.

Table 2.2.

Event Statistics

Data Set	Triggers	Reconstructed Events	In Fidicial Volume	Charged Current Events	Fit Charged Current Events	Final Event Sample
+165 NBB	33,510	26,830	12,317	8,540	7,257	5,345
−165 NBB	44,263	24,718	9,926	5,347	4,741	2,803
+200 NBB	31,810	22,455	10,323	6,848	5,788	4,544
+250 NBB	29,066	19,400	8,430	5,525	4,641	3,790
1985 Low Bias	75,078	35,661	32,050	23,482	20,925	17,682
1985 HiE	60,115	28,691	25,941	25,941	16,263	16,004
1987 Low Bias	239,187	118,866	112,183	112,183	75,209	60,441

Table 2.2. Event Statistics. The table shows the numbers of triggers, reconstructed events, events in the fiducial volume, charged current events, charged current events with a fit, and events in the final sample and how they are partioned between the three exposures and various setting and triggers. For an event to be reconstructed, the vertex must be found. This requirement along with the fiducial volume requirement eliminates any contamination from cosmic rays. *Charged Current Events* are events where a muon was found. *Fit Charged Current Events* are events where the muon was found and fit in the spectrometer. For an event to be part of the final event sample it must have passed all the previous cuts and had $W^2 > 2.5\ \mathrm{GeV}^2$ and $\nu > 10\ \mathrm{GeV}$. The final data sample contains 110,609 events.

Chapter 3

Monte Carlo Simulation

3.1 Introduction

To correct the data for acceptance and smearing, a means of calculating the complicated effects of the experimental resolutions and the acceptance is needed. This complicated calculation is done using Monte Carlo techniques. The VLIB Monte Carlo Simulation used for this analysis consists of four parts: the neutrino beam simulation, the interaction simulation, the event simulation and the event analysis simulation. Each of these parts of the Monte Carlo simulation is discussed below.

3.2 Beam Simulation

The neutrino beam simulation starts with the parameterization of the Atherton production spectrum (Atherton et al. 1980) by Malensek (1981) adapted for 800 GeV (or 400 GeV) protons on beryllium oxide. The beam line simulation program DECAY TURTLE (Carey, Brown, and Iselin 1982) propagates, and decays the produced pions and kaons through the simulated optics of the beam lines. When a pion or kaon decays, the simulation determines the kinematics of the decay and calculates the trajectory of the neutrino produced. From the trajectory of the neutrino, the program calculates the neutrino position in the FMMF detector and creates E_ν vs radius histograms for the various parents, and, in the case of kaons, various decays. Beam files are formed from the saved histograms along with information about relative fluxes of the neutrinos from each type of decay. A beam file consists of a list of neutrinos with their radial positions in the detector (the z position is chosen later), their energies, and their parentage. The interaction

portion of the Monte Carlo then takes the appropriate beam files as input.

The beam simulation is extremely detailed. The interested reader is directed to the thesis of E. Gallas (1992).

3.3 Interaction Simulation

The interaction simulation consists of two primary sections, a simulation of the Fermi-motion of nucleons within the complex nuclei that make up the FMMF target calorimeter and the actual simulation of the neutrino–nucleon interaction.

3.3.1 Fermi-Motion Simulation

The simulation of the Fermi-motion of the nucleons follows the method of Bodek and Ritchie (1981). To properly simulate the Fermi-motion of the nucleons, one first randomly selects the nucleus of the struck nucleon and whether the nucleon is a neutron or a proton. Based on the choice of nucleon and nucleus, the kinetic energy of the nucleon is thrown according to the prescription of Bodek and Ritche. Then the motion of the nucleon is randomly oriented in space. The average kinetic energy of a nucleon is approximately 250 MeV. Figure 3.1 shows the thrown kinetic energy distribution.

The Fermi-motion simulation determines the motion of the nucleon in the laboratory frame but to properly use the theoretical framework described in Chapter 1, the nucleon must be at rest. Thus, before the simulation of the neutrino–nucleon interaction, one selects a neutrino in the laboratory frame and then Lorentz boosts the neutrino–nucleon system into the nucleon rest frame. Then one simulates the interaction and the resulting system is Lorentz boosted back into the laboratory frame.

Fermi-motion smears the reconstructed x distribution particularly, at high x, because one assumes that the nucleon is at rest in laboratory. Figure 3.2 shows the effects of reconstructing the x distribution of including the motion of the nucleon versus making the assumption that the nucleon is at rest. As one can see, Fermi-motion results in

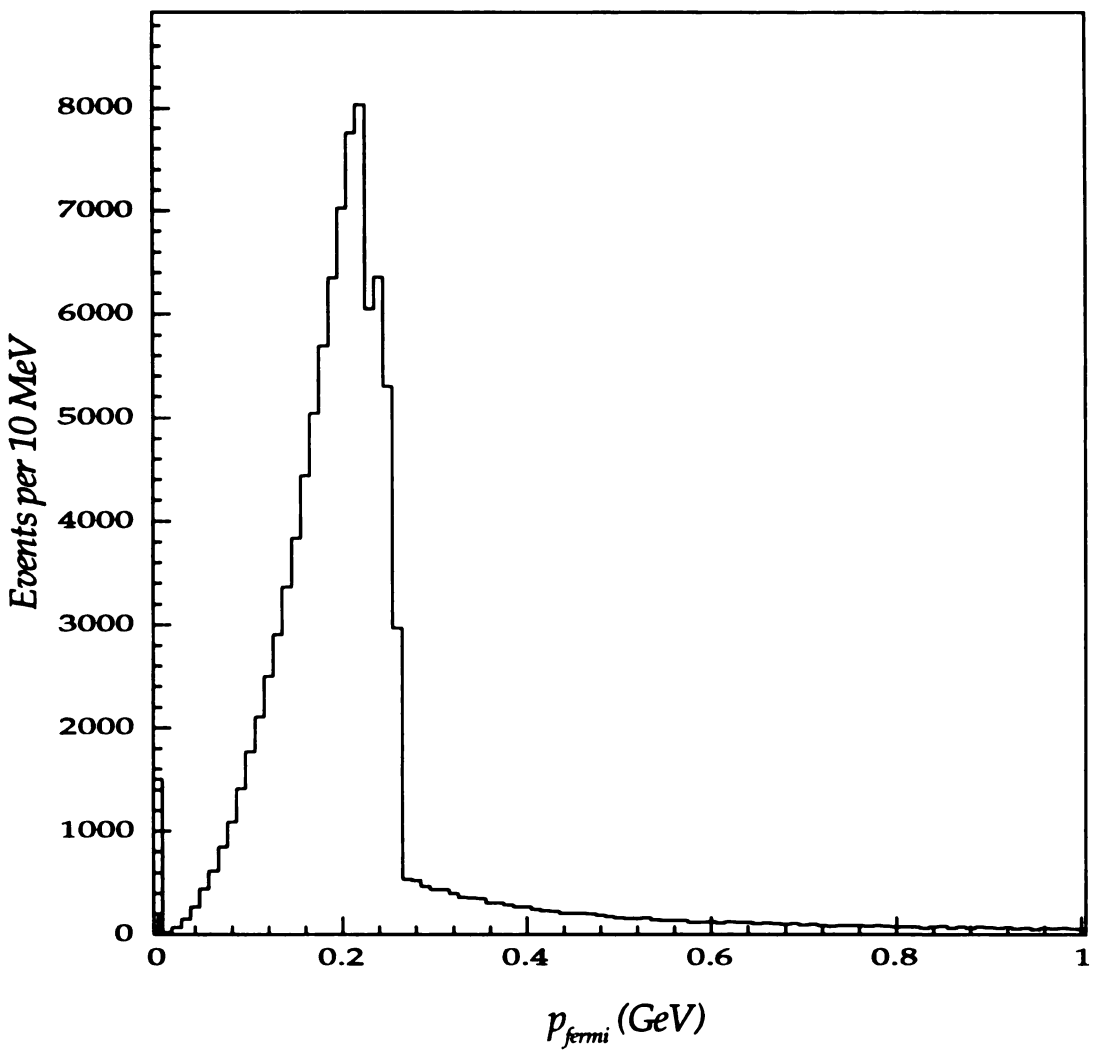

Figure 3.1. Fermi Momentum Distribution. The figure shows the generated distribution of $|\vec{p}_{\text{fermi}}|$ for the nucleons in the target calorimeter. Note the narrow peak at $\vec{p}_{\text{fermi}}$=0 due to the presence of hydrogen (which has no Fermi-motion) in the target. The integral of the figure is normalized to 100,000 events.

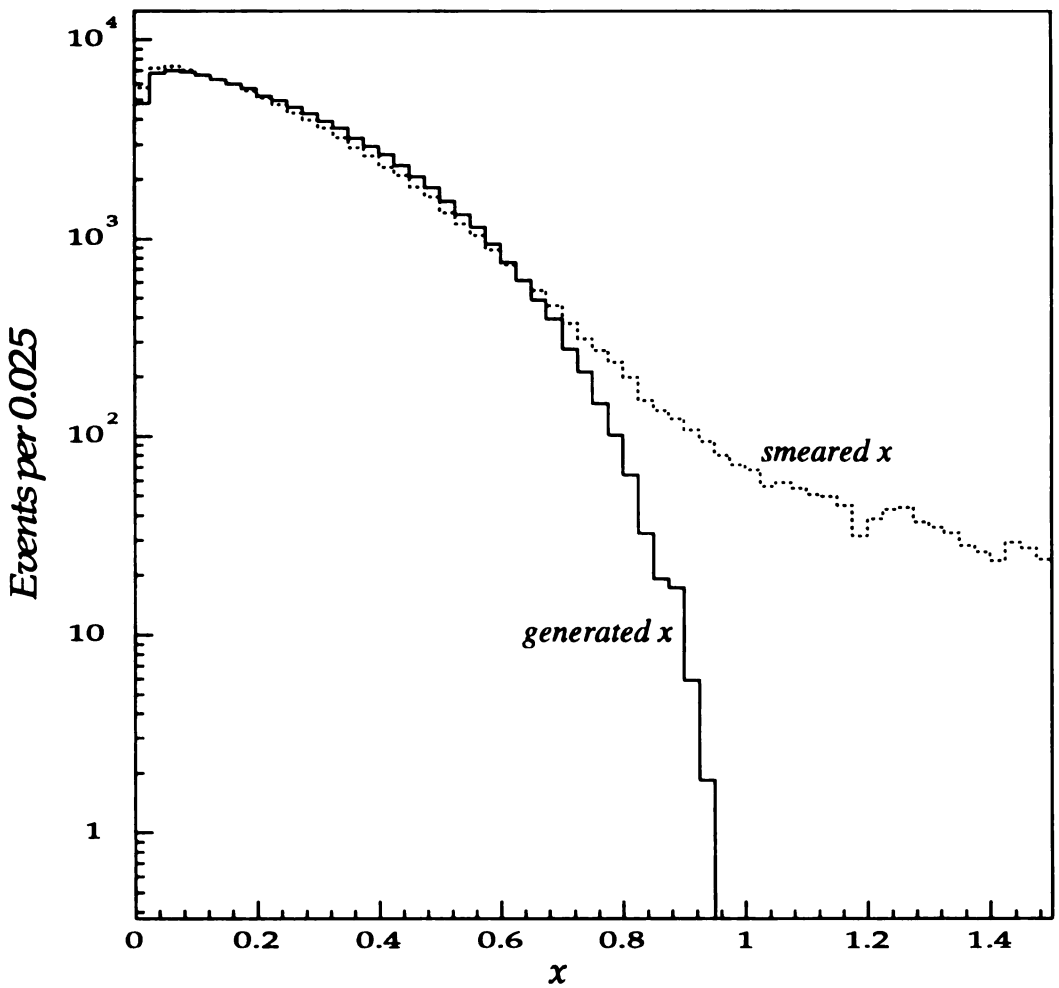

Figure 3.2. Effects of Fermi-Motion on Perceived x Distribution. The figure shows a comparison of the generated x and "Fermi-motion smeared" x distributions. The solid line shows the generated x distribution. The dotted line shows the "Fermi-motion smeared" distribution. The Fermi-motion smeared x is calculated in the laboratory frame assuming that the nucleon is at rest. The integral of the figure is normalized to 100,000 events. Note the logarithmic scale.

reconstruction of x's greater than 1.0.

3.3.2 Neutrino–Nucleon Interaction

The interaction simulation uses a leading-order quark based cross section. The cross section is calculated based on the species of the struck nucleon. The cross section calculation does the radiative and slow rescaling corrections but does not include beyond leading-order QCD diagrams such as quark–quark or quark–gluon effects. Appendix C gives the details of the physical cross section calculation, radiative corrections and the slow rescaling correction.

The interaction simulation starts in the rest frame of the nucleon. The invariants x and y are selected. The selected x and y, the boosted neutrino energy and a set of quark distributions are then used to calculate the νp or νn differential cross section. Based on the cross section and the weight of the selected x and y, the event is rejected or accepted.

If the event is accepted, an additional muon leg radiative correction is made by generating a photon to be lost by the muon, which is presumed to be emitted collinearly to the muon. The momentum four-vector of the photon is then absorbed into the hadron system and correspondingly removed from the muon. Finally, the four-vectors of the final state are Lorentz boosted back into the laboratory frame.

3.4 Event Simulation

The interaction part of the Monte Carlo generates the final state, which consists of the muon four-vector and the hadron system four-vector in the laboratory frame. The VLIB software package simulates the event from these two four-vectors.

Whether an event becomes a part of the final event sample is determined almost solely on the characteristics of that event's muon and the geometry of the FMMF detector. If one wished to parameterize the muon acceptance, it would be a function of the vertex position, the muon angle, the muon energy, the charge of the muon, and possibly other factors. While it might be possible to determine such a parameterization, it is likely that

the parameterization would still be insufficient or too complicated to allow its use in making the acceptance corrections necessary for this analysis. In sharp contrast, the event acceptance effects of the hadron shower are straight-forward and a simple parameterization of the shower energy resolutions allows one to adequately make the acceptance corrections.

For these reasons, VLIB divides the simulation of the event into a muon simulation and a hadron simulation. For the muon simulation, VLIB does a complete detector simulation of the muon tracking and fitting. In contrast, VLIB bases the hadron shower simulation on resolutions measured from the test beam data.

This section concentrates on the exact simulation of the muon. The next section will discuss the simulation of the event measurement including both the measurement of the hadron system and the muon.

3.4.1 Muon Simulation

The muon simulation consists of two distinct parts: calorimeter tracking and the spectrometer tracking. In both parts, VLIB divides the muon track into small steps in z. In each step, VLIB calculates the energy loss and the multiple scattering. At the end of each step, the muon's energy is reduced and its direction altered appropriately.

VLIB divides energy loss into two parts. Losses greater than 1 MeV are treated as discrete processes while losses less than 1 MeV are treated in a statistical fashion using the limited Bethe-Bloch formula (Particle Data Group 1990). VLIB simulation of discrete energy losses includes four processes: knock on electrons (δ rays), nuclear bremsstrahlung, pair production, and nuclear interactions. For the last three processes, VLIB uses the parameterizations of the cross section by VanGinnekin (1986). Figure 3.3 shows the probabilities of a muon experiencing an energy loss of T in an interval dx, $\frac{dN}{dxdT}$, due to one of the loss mechanisms mentioned above. For small losses, δ rays dominate. The three other processes have cross sections that do not fall as rapidly and these processes

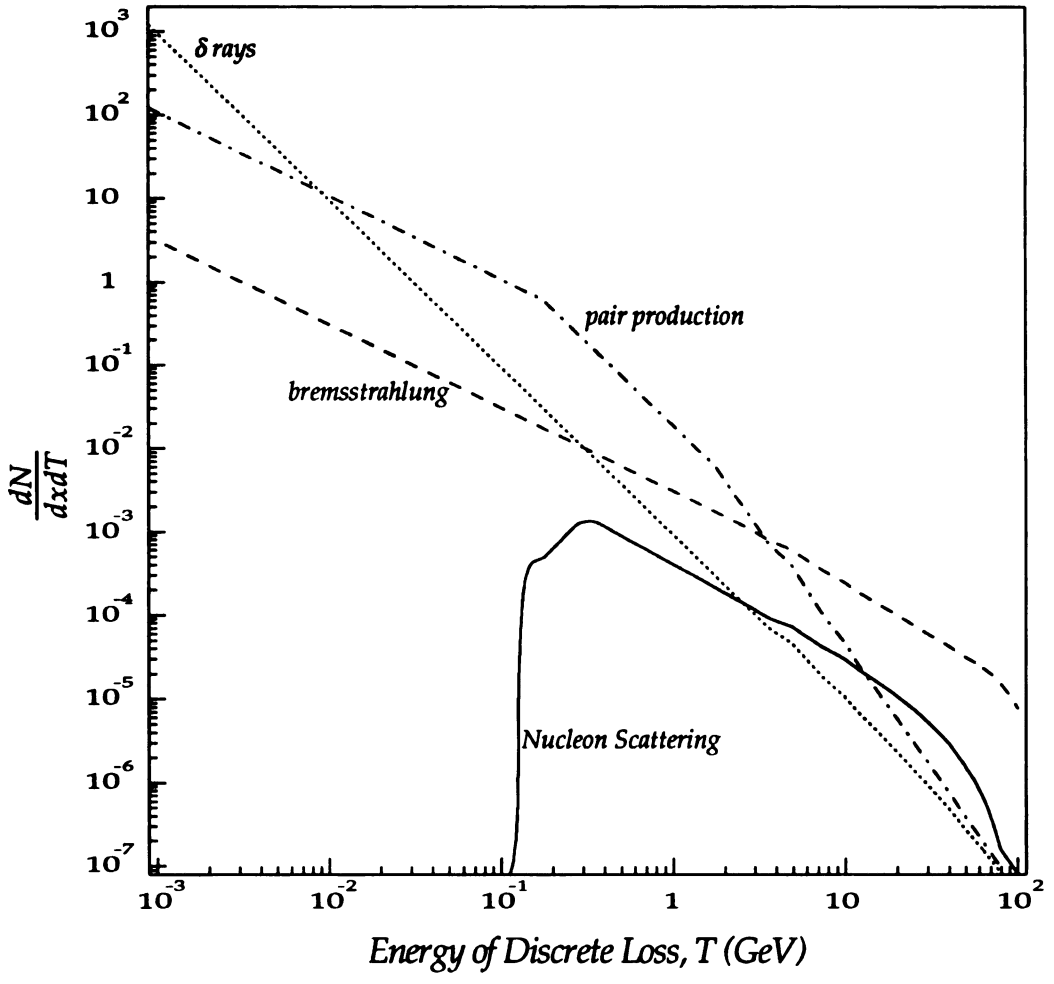

Figure 3.3. Differential Cross Sections for δ Rays, Bremsstrahlung, Pair Production and Inelastic Nucleon Scattering for 100 GeV Muon Traversing Iron. The figure shows the calculation of the differential cross sections, $\frac{dN}{dxdT}$ for δ rays (dotted line), bremsstrahlung (dashed line), pair production (dashed/dotted line), and Nucleon Scattering (solid line). The cross sections are plotted as a function of the energy of lost by the muon (T).

dominate at large discrete losses. These large energy losses can cause serious resolution problems.

To simulate the discrete loss of energy by a muon in each step through a material, VLIB calculates the probability that the muon undergoes a discrete loss due to each mechanism. Then, based on the calculated cross section, VLIB determines whether the muon underwent a discrete loss. Finally, if the muon underwent a discrete loss, VLIB determines the energy of the loss.

Once VLIB determined the amount of energy lost due to discrete processes, it calculates the energy lost due to the limited $\frac{dE}{dx}$ and then reduces the muon energy appropriately. This process results in an energy loss distribution exemplified by Figure 3.4. The statistical treatment of losses below 1 MeV results in the sharp lower edge while the simulation of the discrete processes results in the extremely long high loss tail.

High energy discrete losses create an asymmetric resolution function for the muon energy as seen in Figure 3.5. One should also note the long tails in the distribution which result in extremely poorly measured events. The distribution also has a very non-Gaussian shape. For this reason, the importance of the simulation of the discrete loss processes can not be underestimated.

3.4.1.1 Calorimeter Tracking

For purposes of propagating the muon through the target calorimeter, VLIB treats the calorimeter as a homogeneous volume with the average properties of the target calorimeter. VLIB makes no attempt to model the response of the flash chambers or the proportional planes to the passage of the muon. The energy loss and multiple scattering of the muon is treated as described above. The routine propagating the muon through the calorimeter saves the muon's initial (vertex) position and momentum and its final position and momentum. For the calorimeter tracking, VLIB defines the final muon position as the point where the muon stops or exits the calorimeter.

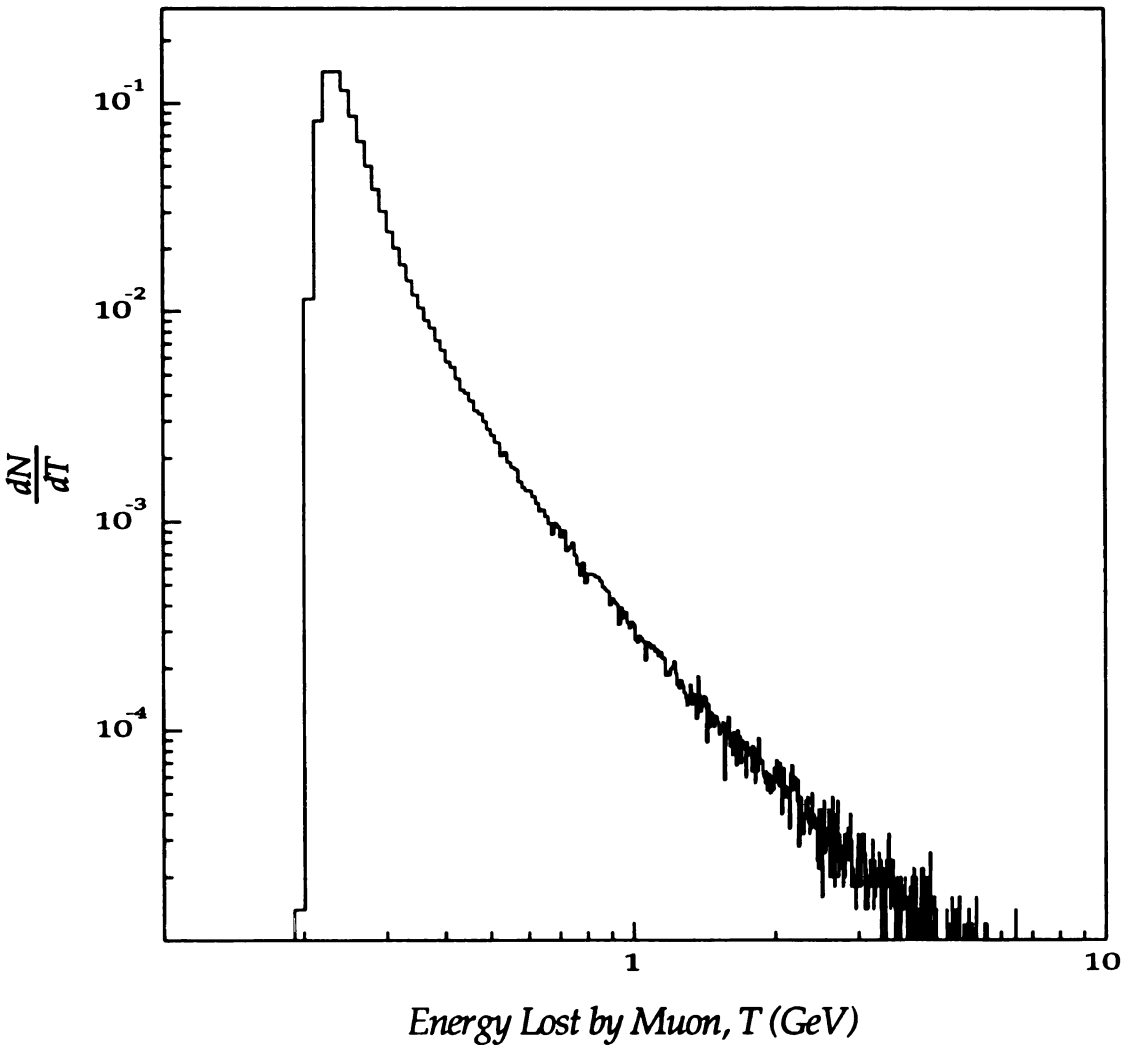

Figure 3.4. Spectrum of Energy Lost by 100 GeV Muon Traversing 20 cm of Iron. Using method outlined in text, this figure shows the Monte Carlo calculation of the spectrum of energy lost (T) by 100 GeV muons as they traverse 20 cm of iron. The bin size is 1 MeV.

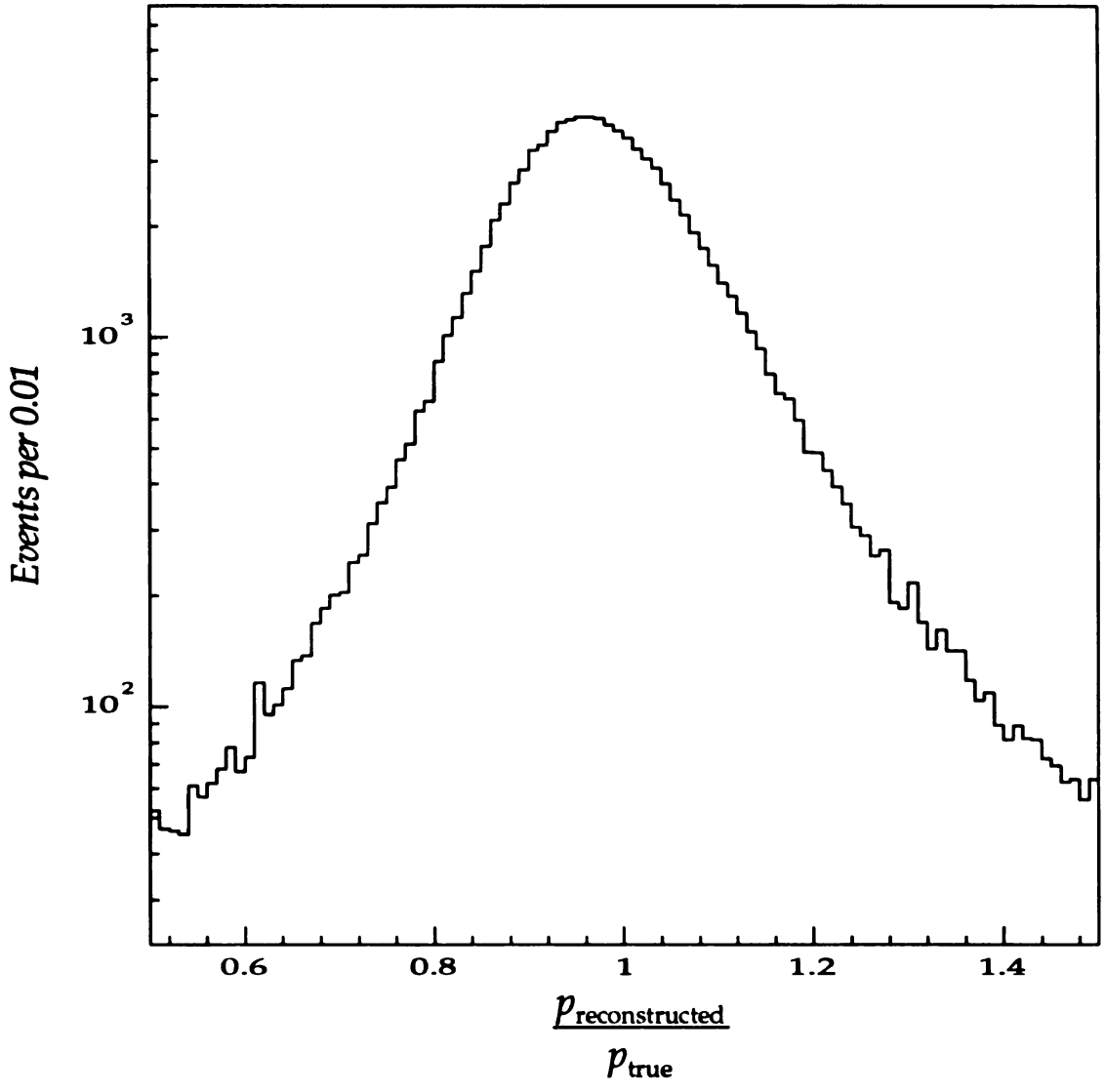

Figure 3.5. Monte Carlo Muon Momentum Resolution. The figure shows the distribution of reconstructed muon energy to true muon energy for 1987 Monte Carlo events. Note the long non-Gaussian tails typical of muon resolution functions. The integral of the distribution has been normalized to 100,000 events.

3.4.1.2 Spectrometer Simulation

A unique feature of this analysis is the full simulation of the muon spectrometer and the muon fitting. To this end, the simulation of the spectrometer is much more complicated than that of the calorimeter.

VLIB continues the propagation of the muon through the spectrometer if the muon exits the calorimeter and if it hits the front face of the first 24' toroidal magnet. The spectrometer simulation is much more complex than that of the calorimeter. Initially, VLIB propagates the muon through the spectrometer in the same manner as used in the calorimeter but with the additional complication of the toroidal field in the magnet iron. The routine used to propagate the muon through the spectrometer is also used in the muon fitting package used to analyze the data, but for event generation, multiple scattering and discrete energy losses are thrown. VLIB tracks the muon as it passes through the iron and field of the magnets, the air gaps, the lead shot (used to fill the holes of the toroidal magnets), and the position measurement stations. The tracking routine saves the position and momentum of the muon at each position measurement station.

After tracking the muon through the spectrometer, the hits in the spectrometer are simulated. VLIB simulates the hits based on information obtained from the data. For the simulation, the efficiency of each measurement station was studied using the data. The typical measurement station (a pair of back-to-back planes) was 98–99% efficient. The spectrometer studies also included the frequency and resolution of back-to-back drifted hit clusters as opposed to single hits clusters or multiple hit clusters. The frequency and distribution of noise hits were also measured. The frequency of noise hits varied by as much as 35% between measurement stations with the 24' planes being the most susceptible to noise. From this information VLIB simulates the response of each of the muon measurement stations. As a cross-check, after analyzing the muon as discussed below, we repeated the efficiency, resolution and noise measurements made for the data on the Monte Carlo and compared the results. The Monte Carlo reasonably

simulates the behavior of each of the actual measurement stations. Figure 3.6 shows a comparison of spectrometer hit distributions from the data and Monte Carlo.

3.5 Analysis of Monte Carlo Events

As discussed above, the simulation of muons in VLIB differs greatly from the simulation of the hadrons. As discussed in Chapter 2, for each neutrino interaction one must first determine if the interaction was a charge current interaction and then attempt to measure the muon angle, charge and momentum along with the energy transfer ν. Let us examine the simulation of the event measurement.

3.5.1 Event Classification and Muon Angle

In the data, the muon track finding (MTF) package does the initial classification of the event by searching for muons. If one or more muons are found, we classify the event as a charged current event. The MTF package has a set of criteria that it applies to any track it finds to determine if the track is as a muon. For this analysis, a track must traverse 5 meters of calorimeter along the beam direction to be classified as a muon. VLIB simulates this behavior by imposing the same requirement on thrown muons using the true vertex and the true exit position.

One reconstructs the muon angle from the found slopes of the muon in two perpendicular views. In the data, the MTF package fits the average trajectory of the muon over the entire length of the muon's track. To simulate the averaging of the trajectory of the track, VLIB uses the line connecting the vertex and the end point of the muon track as the "average" trajectory of the muon. The slope of the "average" trajectory in each view is then smeared by the resolution of the least-squares fitting algorithm.

3.5.2 Muon Fitting

Once MTF finds a muon, the reconstruction program attempts to fit the muon in the spectrometer. Analysis of the data and Monte Carlo uses the exact same fitting package with the Monte Carlo using the previously generated hits. If the muon is fit

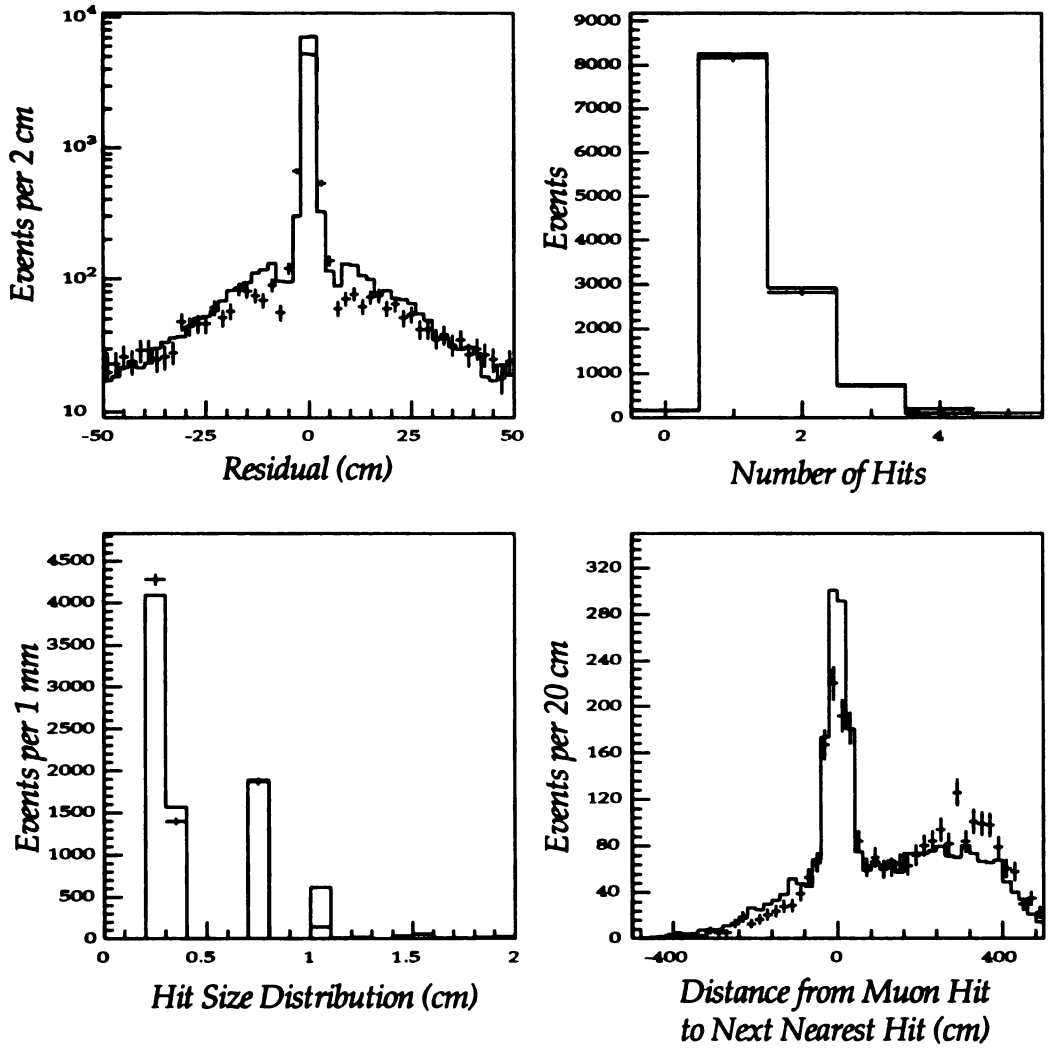

Figure 3.6. Comparison of Data and Monte Carlo Drift Hit Distributions. The figure shows comparison of the typical drift hit distributions from 1987 data and Monte Carlo. In all four plots, the data is shown as the points with error bars while the Monte Carlo is shown as the solid outline. Upper left corner shows the fit residual (i.e. hit position – fit position) for all hits. Upper right corner shows the distribution of the number of hits. Lower left shows the hit size distribution. Hit size varies based on whether a hit is formed from a clean back-to-back hit, single hit or a group of hits. Lower right shows signed distance from hit used in muon fit to next nearest hit. Noise results in the asymmetry seen in the distribution.

successful, the fitting package (after correction for energy loss in the calorimeter) returns the muon's measured energy and charge. From the measured charge of the muon, we determine whether a neutrino or anti-neutrino interaction occurred.

3.5.3 Hadron Energy

VLIB simulates the reconstruction of the energy transfer by use of the resolutions presented in Chapter 2. Using the true ν, VLIB calculates the resolutions of the both the flash chambers and proportional calorimetry. From the calculated resolution, VLIB determines the response of both types of calorimetry. The responses are combined in the same manner as the data to produce the measured ν.

3.5.4 Comparison of Accepted Integral Distributions of Data and Monte Carlo

To complete this chapter, let us compare some distributions from the data to the same distributions for the Monte Carlo. Figures 3.7–3.10 show comparisons for the ν, E_μ, θ_μ, and E_ν distributions for 4 different data sets. In addition, it is instructive to examine the distribution of the iron traversed by fit muons which is shown in Figure 3.11. The comparisons involve an additional cut beyond the standard cuts described in the previous chapter. In general, low Q^2 physics is not well understood theoretically and the theory presented in Chapter 1 is no exception. For this reason, for the comparison between data and Monte, one makes an additional requirement that the reconstructed Q^2 is greater than 5.0 GeV^2. This moves the Monte Carlo out of the region of theoretical uncertainty.

The agreement between data and Monte Carlo shown in Figures 3.7–3.11 is very good. In the "iron" distribution, one notes that there seems to be a small discrepancy between the data and Monte Carlo as to the ratio of events that traverse the entire spectrometer to those that exit from the 24' wings. From this discrepancy, one estimates that the Monte Carlo correctly models the acceptance of the detector and cuts to 1.3%. This uncertainty in the knowledge of the acceptance will be included in the systematic errors

presented in the next chapter.

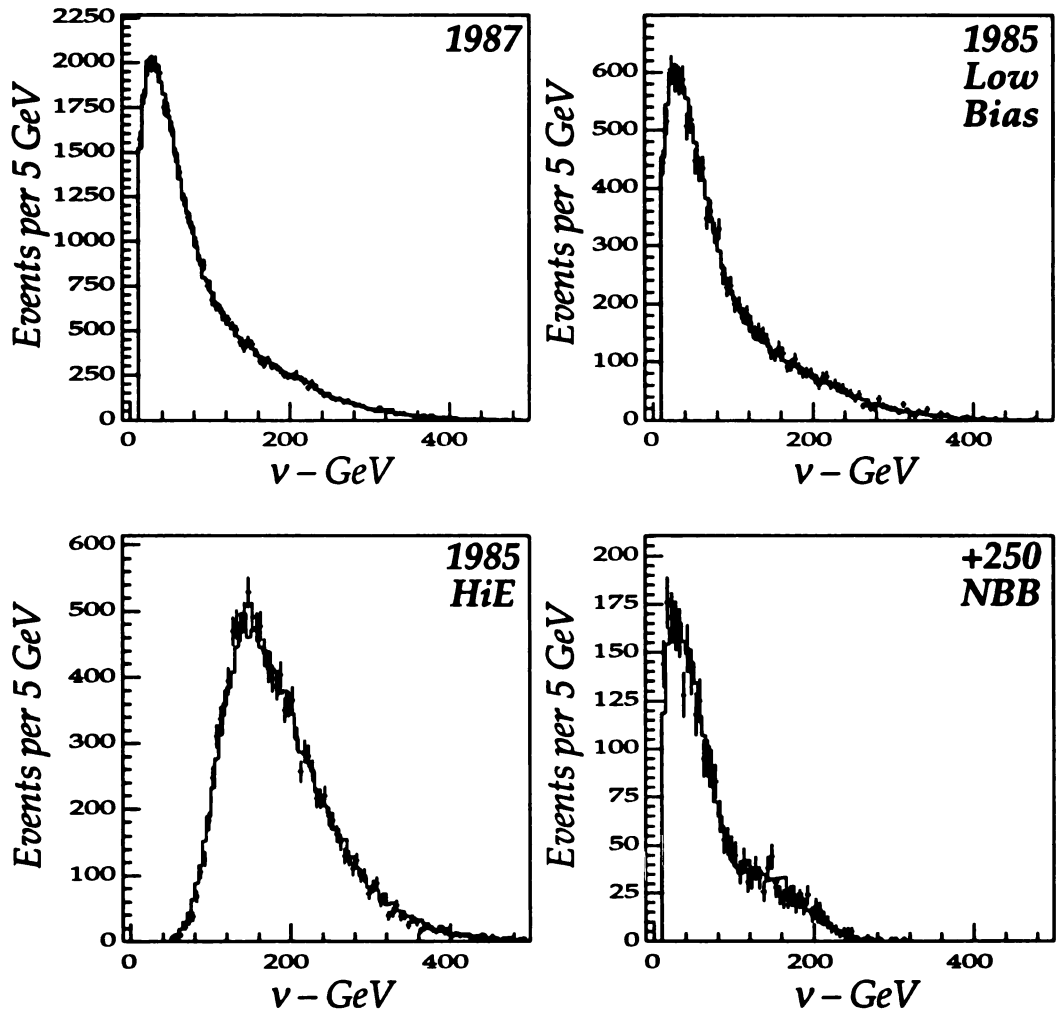

Figure 3.7. Comparison of Data and Monte Carlo ν Distributions. The figure shows the ν distributions for accepted neutrino events from the 1987 (top-left), 1985 low-bias triggers (top-right), 1985 HiE triggers (bottom-left), and 1982 +250 narrow band (bottom-right) data sets. The data is shown as the points with error bars while the Monte Carlo is overlayed as a solid outline. The Monte Carlo is area normalized. The HiE triggers show the effects of the high trigger threshold.

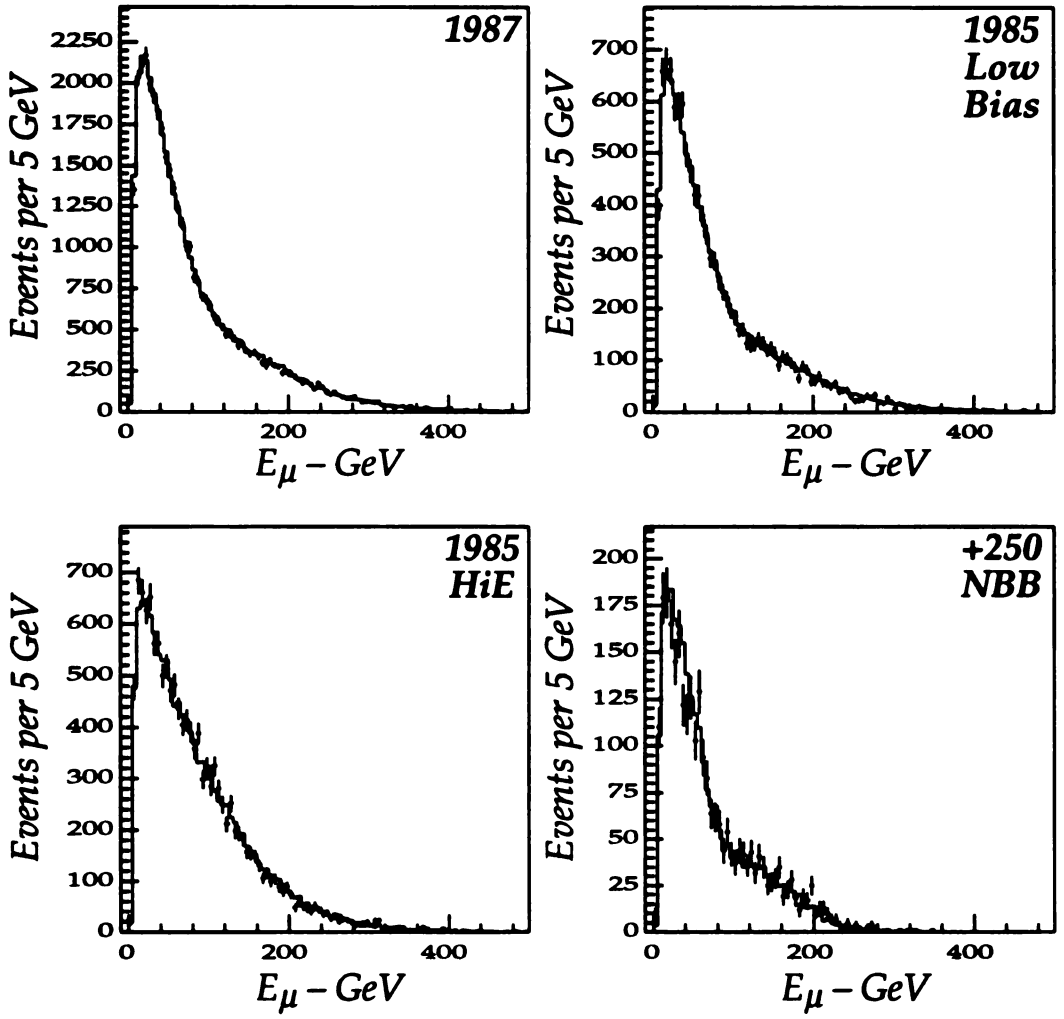

Figure 3.8. Comparison of Data and Monte Carlo E_μ Distributions. The figure shows the E_μ distributions for accepted neutrino events from the 1987 (top-left), 1985 low-bias triggers (top-right), 1985 HiE triggers (bottom-left), and 1982 +250 narrow band (bottom-right) data sets. The data is shown as the points with error bars while the Monte Carlo is overlayed as a solid outline. The Monte Carlo is area normalized.

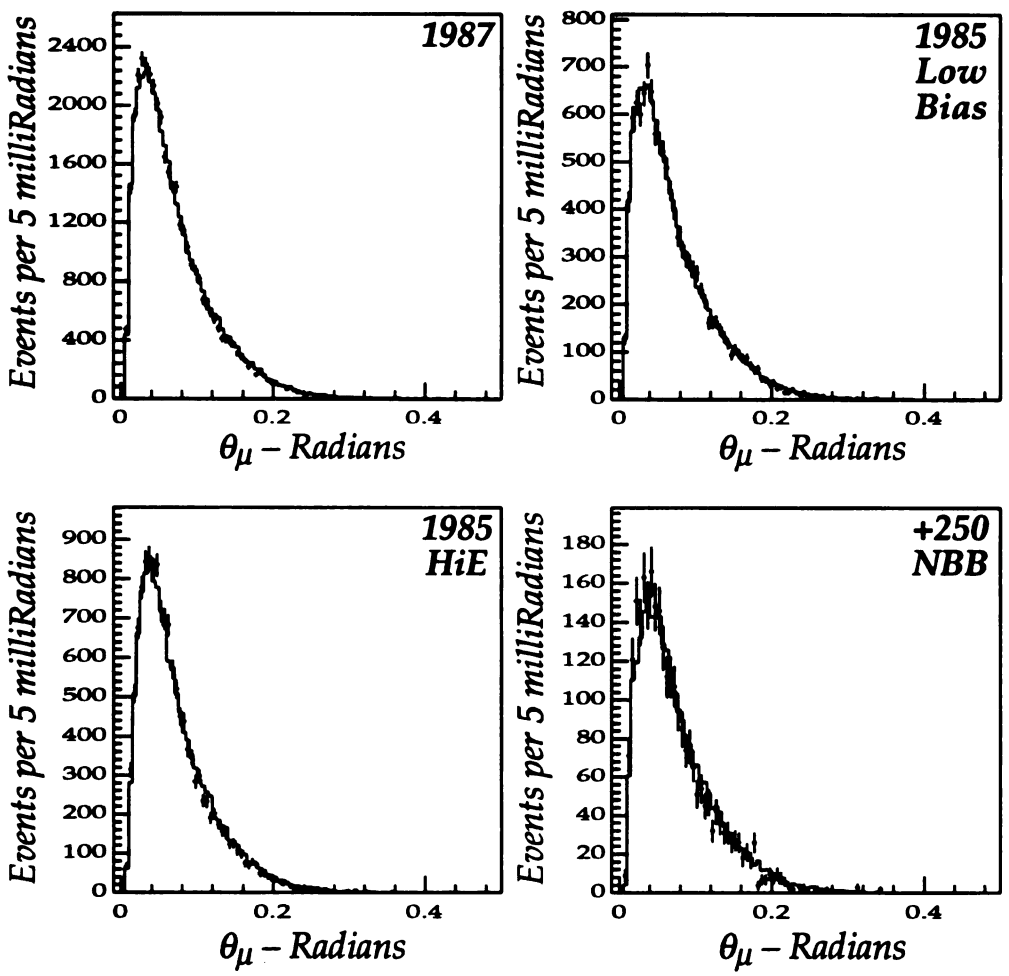

Figure 3.9. Comparison of Data and Monte Carlo θ_μ Distributions. The figure shows the θ_μ distributions for accepted neutrino events from the 1987 (top-left), 1985 low-bias triggers (top-right), 1985 HiE triggers (bottom-left), and 1982 +250 narrow band (bottom-right) data sets. The data is shown as the points with error bars while the Monte Carlo is overlayed as a solid outline. The Monte Carlo is area normalized.

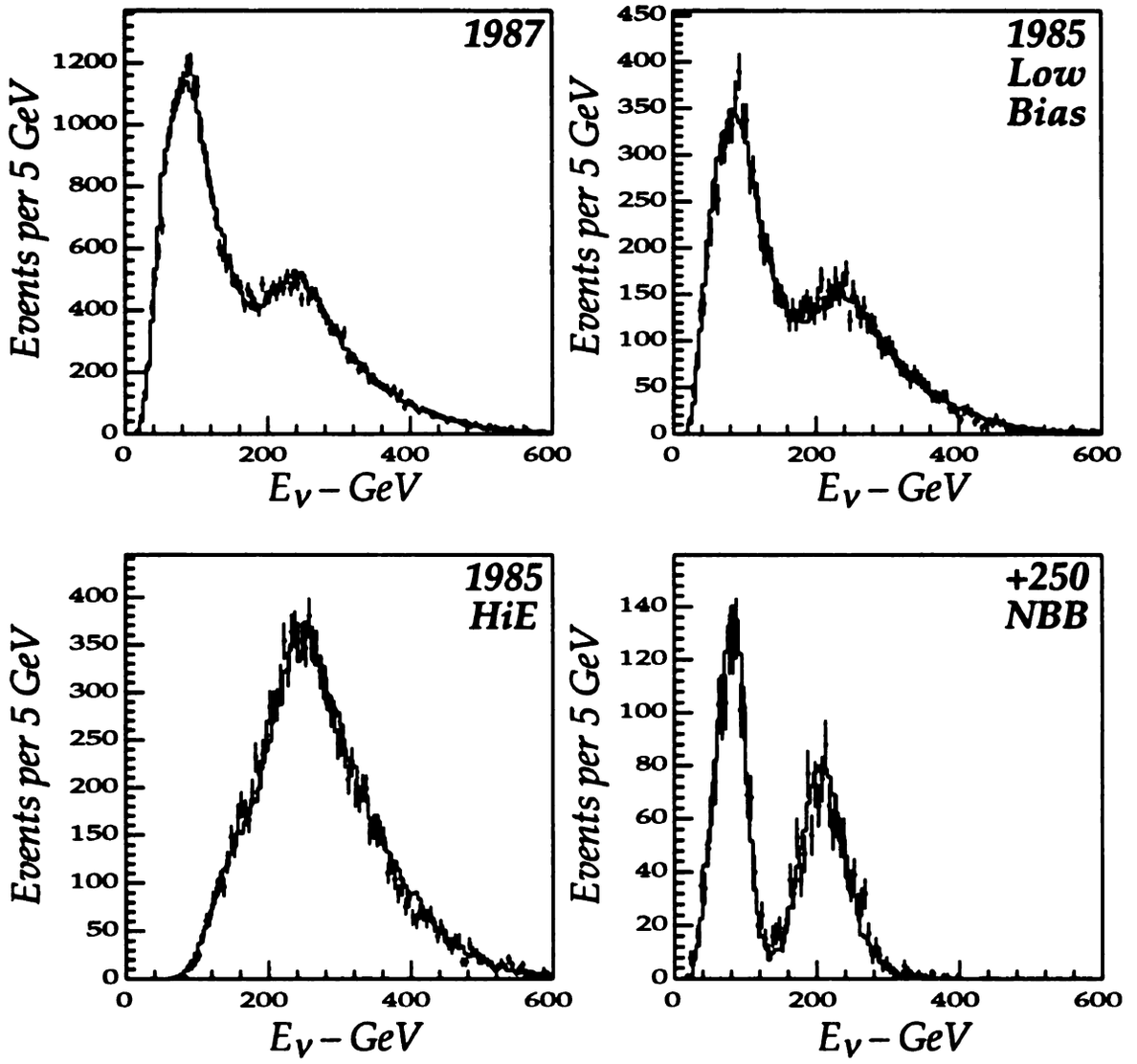

Figure 3.10. Comparison of Data and Monte Carlo E_ν Distributions. The figure shows the E_ν distributions for accepted neutrino events from the 1987 (top-left), 1985 low-bias triggers (top-right), 1985 HiE triggers (bottom-left), and 1982 +250 narrow band (bottom-right) data sets. The data is shown as the points with error bars while the Monte Carlo is overlayed as a solid outline. The Monte Carlo is area normalized. The distributions shows the typical double banded π/K structure. For the HiE triggers, the high ν threshold results in a data set that is almost entirely "kaon" neutrinos.

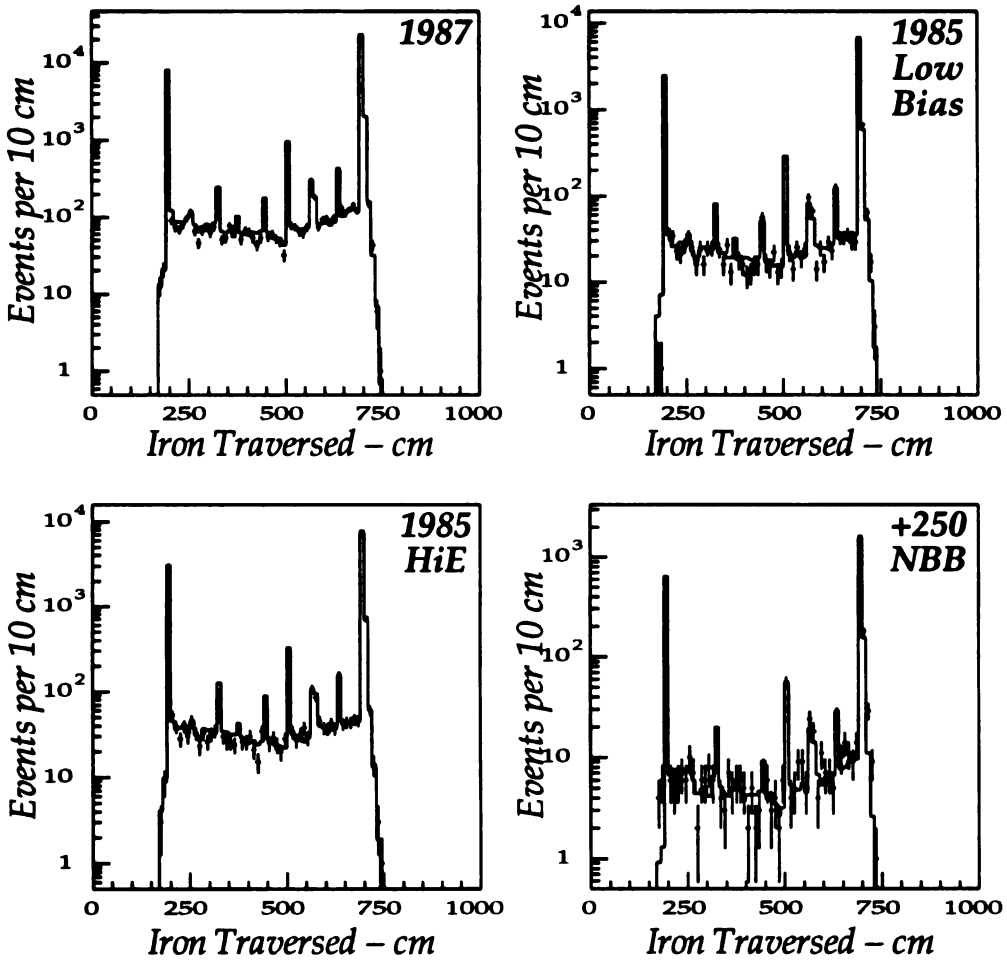

Figure 3.11. Comparison of Data and Monte Carlo Iron Distributions. The figure shows the distributions of iron traversed in spectrometer by the fit muon for accepted neutrino events from the 1987 (top-left), 1985 low-bias triggers (top-right), 1985 HiE triggers (bottom-left), and 1982 +250 narrow band (bottom-right) data sets. The data is shown as the points with error bars while the Monte Carlo is overlayed as the solid outline. Note the logarithmic scales. The Monte Carlo is area normalized.

Chapter 4

Structure Function Extraction

4.1 Introduction

For this thesis, neutrino–nucleon structure functions have been extracted. The analysis presented in this thesis assumes the average of the world's results for the total neutrino–nucleon ($\sigma^{\nu N}$) and anti-neutrino–nucleon ($\sigma^{\bar{\nu}N}$) cross sections. Starting with assumed total cross sections, the double differential cross sections, $\frac{d^2\sigma}{dxdy}$, are measured. The analysis then extracts the structure functions using the measured double differential cross sections and a parameterization of $R(x,Q^2)$. This chapter describes the measurement of the double differential cross sections and structure functions. The method for determining the systematic errors is then discussed. The final section of this chapter presents the measured cross sections and structure functions.

4.2 Differential Cross Section Extraction

To first order, this analysis measures the double differential cross section, $\frac{1}{E_\nu}\frac{d^2\sigma^{\nu N}}{dxdy}$, by assuming the total cross section, $\frac{\sigma^{\nu N}}{E_\nu}$ and calculating the corrections to the data for smearing and acceptance by the Monte Carlo techniques. This procedure has been adopted because there was no monitoring of the flux of secondary particles in the decay region of the Quadrupole Triplet Beam. In neutrino experiments using narrow band neutrino beams, one does extensive monitoring of the number and spectrum of secondaries produced which allows one to directly measure the total cross section. The lack of flux monitoring has necessitated the use of an assumed total cross section. Once the total cross section is known, the double differential cross section (in a given E_ν interval) is measured from the ratio of number events in the appropriate x, y,

E_ν bin to total number of events in the E_ν interval. It can be shown that the differential cross section is,

$$\frac{1}{E_\nu}\frac{d^2\sigma^{\nu N}}{dxdy} = \frac{\sigma^{\nu N}}{E_\nu}\frac{1}{\Delta x\Delta y}\frac{\text{number corrected data events in x,y,E}_\nu\text{ bin}}{\text{number corrected data events in E}_\nu\text{ interval}}$$

$$= \frac{\sigma^{\nu N}}{E_\nu}\frac{1}{\Delta x\Delta y}\frac{\text{DATA}_{ijk}\text{MC}_{ijk}^{True}}{\text{MC}_{ijk}^{Accepted}}\frac{\text{MC}_k^{Accepted}}{\text{DATA}_k\text{MC}_k^{True}} \qquad (4.1)$$

where i, j, k refer to the appropriate x, y, E_ν bin, DATA_{ijk} is the number of accepted data events in the given x, y, E_ν bin, $\text{MC}_{ijk}^{Accepted}$ is the number of accepted Monte Carlo events in the given x, y, E_ν bin, and MC_{ijk}^{True} is the number of thrown Monte Carlo events in the given x, y, E_ν bin. Similarly, DATA_k, $\text{MC}_k^{Accepted}$, and MC_k^{True} refer to the total number of events in the neutrino energy interval. In the above equation, the third fraction is the corrected number of events in the x, y, E_ν bin while the last fraction is the reciprocal of the corrected number of events in the E_ν energy interval.

4.2.1 Total Cross Section

The assumed total cross sections are a combination of the three newest, highest statistics measurements of the total cross sections. The three sets of results from the CCFR (Auchincloss et al. 1990), CDHSW (Berge et al. 1987), and CHARM (Allaby et al. 1988) collaborations are consistent with the total cross sections rising linearly with energy. The mean is $\frac{\sigma^{\nu N(\bar{\nu}N)}}{E_\nu} = 0.6762\pm0.0140\ (0.3332\pm0.0088) \times 10^{-38}\ \text{cm}^2\text{GeV}^{-1}$.

4.2.2 Correction for Target Neutron Excess

The above total cross sections are for scattering off an isoscalar target (i.e. number of protons = number of neutrons). If the target contains more neutrons than protons, the total cross section for neutrinos is enhanced because of the excess number of d valence quarks (as compared to an isoscalar target) while the total cross section for anti-neutrinos is reduced. The FMMF target calorimeter is nearly isoscalar,

$$\delta \equiv \frac{N-Z}{N+Z} = 2.97\%,$$

where N is the average number of neutrons per nucleon and Z is the number of protons per nucleon. For the FMMF detector, $N = 10.2$ and $Z = 9.8$ which should be compared with $N = 29.9$ and $Z = 26$ (with $\delta = 6.89\%$) for the typical iron calorimeter detectors. The slight non-isoscalarity of the FMMF target requires a small correction to total cross sections noted above. Then the calculation of the differential cross sections requires a correction of the opposite sign to account for the differences in the shapes of the valance quark distributions.

If one assumes the simple quark–parton model, it can be shown that the corrections to the total cross sections are of the form,

$$\sigma^{\nu FMMF} = \sigma^{\nu N} + \sigma^{\text{correction}} \tag{4.2a}$$

$$\sigma^{\bar{\nu}FMMF} = \sigma^{\bar{\nu}N} - \sigma^{\text{correction}} \tag{4.2b}$$

where,

$$\sigma^{\text{correction}} = \delta \frac{G_F^2 M E_\nu}{\pi} \int x\big(\mathrm{u}(x) - \mathrm{d}(x)\big) dx dy.^{\dagger} \tag{4.3}$$

This correction, for the FMMF target, to the total neutrino (anti-neutrino) cross section is roughly one (two) percent. One then substitutes $\sigma^{\nu\text{FMMF}}$ in place of $\sigma^{\nu\text{N}}$ in formula 4.1 resulting in,

$$\frac{1}{E_\nu}\frac{d^2\sigma^{\nu FMMF}}{dxdy} = \frac{\sigma^{\nu FMMF}}{E_\nu}\frac{1}{\Delta x \Delta y}\frac{\mathrm{DATA}_{ijk}\mathrm{MC}_{ijk}^{True}}{\mathrm{MC}_{ijk}^{Accepted}}\frac{\mathrm{MC}_k^{Accepted}}{\mathrm{DATA}_k\mathrm{MC}_k^{True}}. \tag{4.4}$$

Now, one must correct for the difference in the shapes of the u and d valance quark distributions. In the same manner as the corrections to the total cross section, one corrects the differential cross section. If one takes the double derivative of equations 4.2, using the definition of $\sigma^{\text{correction}}$ in Equation 4.3, one finds,

---

† The u and d quark distribution referred to here are those measured in the proton. This analysis assumes that the proton and neutron form an isoscalar doublet. From this assumption, one concludes that $u_{\text{neutron}} = d_{\text{proton}}$ and $d_{\text{neutron}} = u_{\text{proton}}$.

$$\frac{d^2\sigma^{\nu N}}{dxdy} = \frac{d^2\sigma^{\nu FMMF}}{dxdy} - \delta\frac{G_F^2 ME_\nu}{\pi}x\left(u(x) - d(x)\right) \qquad (4.5a)$$

$$\frac{d^2\sigma^{\bar{\nu}N}}{dxdy} = \frac{d^2\sigma^{\bar{\nu}FMMF}}{dxdy} + \delta\frac{G_F^2 ME_\nu}{\pi}x\left(u(x) - d(x)\right) \qquad (4.5b)$$

and applies this correction to complete the calculation of the neutrino (anti-neutrino) nucleon double differential cross section.

4.3 Structure Function Measurement

As we saw in Chapter 1, the differential cross section can be expressed in terms of three structure functions,

$$\frac{d^2\sigma^{\nu N,\bar{\nu}N}}{dxdy} = \frac{G_F^2 ME}{\pi}\left\{y^2 xF_1 + \left(1 - y + \frac{Mxy}{2E_\nu}\right)F_2 \pm \left(y - \tfrac{1}{2}y^2\right)xF_3\right\}.$$

To extract xF_3, one takes the difference of the neutrino and anti-neutrino differential cross sections. The difference yields

$$\frac{d^2\sigma^{\nu N}}{dxdy} - \frac{d^2\sigma^{\bar{\nu}N}}{dxdy} = \frac{2G_F^2 ME}{\pi}\left\{y - \tfrac{1}{2}y^2\right\}xF_3\left(x,Q^2\right)$$

The extraction of F_2 requires that one eliminate xF_1 by making an assumption about $R(x,Q^2) \equiv \frac{\sigma_L}{\sigma_T}$. The definition of R yields,

$$\frac{F_2}{2xF_1} = \frac{1+R}{1+\frac{Q^2}{\nu^2}} = \frac{1+R}{1+\frac{4M^2x^2}{Q^2}},$$

allowing one to eliminate xF_1. In this analysis, we use a parameterization of the measurement of R made at SLAC by Dasu et al. (1988). The parameterization given by Dasu et al. is,

$$R\left(x,Q^2\right) = \left[\frac{1.11(1-x)^{3.34}}{\log\left(Q^2/\Lambda^2\right)} + \frac{0.11(1-x)^{-1.94}}{Q^2}\right]$$

where Λ is assumed to be 200 MeV. This parameterization is based on "an empirical parameterization of the perturbative QCD calculations of R" with the addition of a second higher twist term.

To extract F_2, one takes the sum of the neutrino and anti-neutrino differential

cross sections. The sum yields,

$$\frac{d^2\sigma^{\nu N}}{dxdy}+\frac{d^2\sigma^{\bar{\nu}N}}{dxdy}=\frac{2G_F^2ME}{\pi}\left\{1-y+\frac{Mxy}{2E_\nu}+\frac{y^2}{2}\frac{1+\frac{4M^2x^2}{Q^2}}{1+R}+\Delta\right\}F_2(x,Q^2). \quad (4.6)$$

The Δ term in Equation 4.6 corrects for the non-cancellation of xF_3. As we previously saw in Chapter 1, $xF_3^{\nu N} \neq xF_3^{\bar{\nu}N}$ due to the contributions of the sea quarks. One finds that the correction to F_2 is,

$$\Delta = 4\left(y-\tfrac{1}{2}y^2\right)\left(4s(x,Q^2)-4c(x,Q^2)\right).$$

The average x, y, y^2, E_ν, and Q^2 are calculated from the Monte Carlo in the appropriate x, y, E_ν bin and then used to calculate the structure functions from the sums and differences of the double differential cross sections.

After the structure functions are calculated for a given x, y, E_ν bin, in each x bin, one combines the structure functions from y, E_ν bins covering the same Q^2 range.

4.4 Systematic Error Analysis

Systematic errors arise from a number of sources. In this analysis, systematic errors could arise from two general types of errors: an incomplete knowledge of the acceptance of the experiment and errors in the calibration of the scales used in the event measurement.

4.4.1 Acceptance

The acceptance of this analysis has been extensively studied. The acceptance (of a given bin) is simply the ratio of the final number of events accepted in the bin to the total true number of events in the bin. To insure that the acceptance of the analysis is well understood, the Monte Carlo (described in Chapter 3) includes a full simulation of the muon spectrometer and of the mechanisms of catastrophic energy loss from muons traversing matter. The acceptance for a given bin is then calculated from the Monte Carlo simulation as the ratio of the number of Monte Carlo events accepted to the number of Monte Carlo events thrown.

Figures 3.7–3.11 showed comparisons between data and the Monte Carlo simulation of some integral distributions. In general, the agreement between the data and the simulation is impressive. A close examination of the distribution of the iron traversed by fit muons shows a small discrepancy. From this discrepancy one estimates an uncertainty in the knowledge of the acceptance as 1.3% of the acceptance calculated from the Monte Carlo simulation. The error in the knowledge of acceptance results directly in a 1.3% systematic error in cross sections. This systematic error is then added in quadrature with systematic errors from other sources.

4.4.2 Measurement Biases

Systematic errors can also result from errors in the calibration of scales. These types of errors result in measurement biases. From the various calibrations, we have estimated the possible variations in the calibrations.

The possible variation in the ν calibration has two distinct components, a pedestal error, and a scale error. A pedestal error could result from either an incorrect subtraction of the calorimeter noise or improper extrapolation of the calibration scale to low energies. A scale error could be the result of a calibration error due to a mismeasurement of the momentum of the test beam particle or an error in the calibration procedure. From the scale fitting done using the neutrino data (as described in Appendix B), we have conservatively estimated the possible errors in the ν calibration as a pedestal of 1.0 GeV and a scale of 2.0%.

In contrast, the p_μ calibration only has a possible scale error which could be due to the a mismeasurement of the magnetic fields of the toroidal magnets. From a fit of scale similar to those described in Appendix B where one allows p_μ to vary in addition to ν, the error in the p_μ calibration is estimated at 2.0% and is highly correlated with the errors in the calibration of ν. The correlation of the scale errors results from the final part of the calibration procedure where the neutrino energy vs radius relationship is used to

determine the final calibration constants.

A possible error in the θ_μ calibration differs from those in p_μ and ν. One calculates θ_μ from the muon slopes in two orthogonal views. Any error in alignment results in an increase in the resolution but not in a systematic bias. The physical size of the calorimeter and the flash chamber cells (and their spacing) actually sets the θ_μ scale. From the physical size of the calorimeter and limitations in survey techniques in Lab C, one estimates the maximum possible error in the θ_μ scale as 0.05% (1 cm over 20 m). In practice, the size of any possible θ_μ scale bias allows us neglect θ_μ as a source of systematic error.

The systematic errors due to calibration uncertainties have been studied in two similar methods which give comparable results. Both methods involve varying the ν and p_μ measurements and observing the effects on the final cross section and structure function measurements. The primary method involves varying the smeared Monte Carlo values. The second method involves varying the calibration constants for the data. Initially, one varies the calibration constants and does the complete cross section and structure function analysis. Each variation in the calibration constants is treated as a separate experiment. The set of different variations forms an ensemble of experiments. Based on a large number of variations in the calibration constants, one then directly calculates the systematic errors from the variations in the differential cross section or the structure functions. To account for correlations, in addition to varying each of the calibration constants individually, the calibration constants were varied simultaneously. The details of the method of calculating the systematic errors is explained in detail in Appendix D. The systematic errors reported in this thesis were calculated from the simultaneous variation of the scales.

4.5 Scale Errors

As discussed above, this analysis assumes the total cross sections (and the energy dependence) for neutrino nucleon and anti-neutrino nucleon scattering. The assumed total cross section was derived from an average of the world's data on the total cross section. The error for neutrinos is 2.1% and for anti-neutrinos is 2.4%. The results of the propagation of the total cross section errors is presented as a separate scale error for both the differential cross sections and the structure functions.

4.6 Results

To calculate the differential cross sections and structure functions presented in this thesis, data from 1982, 1985, and 1987 were analyzed on an event by event basis as described in Chapter 2. The cuts described therein were applied. The data naturally divided itself into seven different data sets, the four narrow band settings from 1982 (three neutrino settings, and one anti-neutrino), the 1985 low bias triggers, the 1985 High Energy triggers and the 1987 data (all low bias). For each of these data sets, the data was binned into neutrino and anti-neutrino bins, 12 x bins, 5 y bins and 5 neutrino energy bins. The binning is discussed below. For both data and Monte Carlo, the number of accepted events in each x, y, E_ν bin and in each E_ν interval were accumulated. Because the y bins do not cover the entire y interval from 0.0 to 1.0, the sum of the number of events in the x, y bin in an E_ν interval does not equal the total accepted event in an E_ν interval. In addition, for the Monte Carlo, the same sums are accumulated for all throw charged current events using the thrown values of x, y, and E_ν.

Table 4.1 shows the event statistics for both data, Monte Carlo accepted and Monte Carlo thrown. The statistics for the Narrow Band Data sets are combined. Table 4.1 also shows the mean E_ν, and Q^2 for each data set.

In addition, to the bin and interval event sums for the best values of the calibration constants, bin and interval sums are also accumulated for the variations of the

Table 4.1

Final Event Sample

	Data Set	1982 Low Bias	1985 Low Bias	1985 HiE	1987 Low Bias	TOTAL
anti-neutrinos	Data Events	2803	2319	1128	8821	15071
	$\langle E_\nu \rangle$ (GeV^2)	75.6	132.0	240.5	127.1	130.0
	$\langle Q^2 \rangle$ (GeV)	11.0	17.4	37.1	16.0	16.9
	Thrown MC	48995	54778	54778	61904	—
	Accepted MC	27620	34496	3270	40025	—
neutrinos	Data Events	13679	15363	14876	51620	95538
	$\langle E_\nu \rangle$ (GeV)	109.2	165.6	267.4	166.9	174.0
	$\langle Q^2 \rangle$ (GeV^2)	21.4	32.0	64.8	31.7	35.4
	Thrown MC	144675	325823	325823	372613	—
	Accepted MC	106959	225817	52590	264296	—

Table 4.1. Final Event Sample. The table shows the characteristics of the final data set. The statistics have been tabulated for reconstructed events that pass all cuts and divided between neutrinos and anti-neutrinos. The table also shows the average neutrino energy and 4-momentum transfer. In addition, the Monte Carlo Simulation statistics are shown. For the simulation, the numbers of thrown and accepted events are shown. The three 1982 Narrow Band neutrino data settings have been combined and entered as "1982 Neutrino" data set.

calibration constants as described above in the section on systematic errors and in Appendix D. The systematic errors can be calculated from either Monte Carlo or data. The systematic errors presented here are based on the results from the Monte Carlo study but are consistent with those from the data study.

4.6.1 Binning

An unusual binning scheme is chosen for the differential cross section measurement. While for the differential cross section measurement, any y, E_ν scheme would be acceptable, for structure function extraction it will be important that one is able to combine y, E_ν bins. For each x interval, each y, E_ν bin represents a range in Q^2. It is important that the y bin for a given E_ν interval is chosen so that there are y bins in the adjacent E_ν interval that encompass the similar (or better still, the same) Q^2 intervals. For this reason, a logarithmic binning scheme has been chosen so that the same Q^2 interval that is covered by bin (i,j,k) is also covered by bins $(i,j-1,k+1)$ and $(i,j+1,k-1)$. Table 4.2 shows the binning limits for x, y, and E_ν.

4.6.2 Final Cross Section Results

The data for this thesis comes from 7 different data sets. The differential cross sections are calculated for x, y, E_ν bins in each data set. The Monte Carlo statistics are at least a factor of 3 greater than that of the data for all data sets. For data from the 1982 narrow band running, wrong sign events (for example, events with a μ^+ for a neutrino setting) were ignored. Once the differential cross sections were calculated for all appropriate bins as outlined above for each data set, the results were averaged. From the Monte Carlo, one calculates systematic errors (as discussed above), and the mean true y, Q^2, and E_ν (which are required for structure function extraction) for each bin in each data set and then the results are averaged in the same manner as the cross sections. The results for the differential cross sections are shown in Tables 4.3 and 4.4.

4.6.3 Final Structure Function Results

The structure functions are calculated as outlined above from the differential cross sections presented in Table 4.3 and 4.4 and are shown in Table 4.5. In addition to the statistical errors, systematic and scale errors are also presented.

Table 4.2

Binning Limits for Structure Function Extraction

N	x limits	y limits	E_ν limits
0	0.000	0.030	16.0 GeV
1	0.030	0.060	32.0 GeV
2	0.060	0.120	64.0 GeV
3	0.100	0.240	128.0 GeV
4	0.150	0.480	256.0 GeV
5	0.200	0.960	512.0 GeV
6	0.250	—	—
7	0.300	—	—
8	0.400	—	—
9	0.500	—	—
10	0.600	—	—
11	0.700	—	—
12	1.000	—	—

Table 4.2. Binning Limits for Structure Function Extraction. The table shows the limits of the bins used in structure functions extraction. Note the logarithmic binning of y and E_ν.

Table 4.3
Anti-Neutrino Differential Cross Sections

$x = 0.015$

y	E_ν (GeV)	$\frac{1}{E}\frac{d^2\sigma}{dxdy}$	Statistical Error	Systematic Error	Scale Error	Events
0.360	26.2	0.7353	0.2326	0.0628	0.0046	10
0.720	26.1	0.6499	0.1102	0.0319	0.0041	32
0.180	49.6	1.0680	0.2372	0.1454	0.0067	22
0.360	49.6	1.0233	0.0801	0.0509	0.0064	158
0.720	49.5	0.9058	0.0536	0.0281	0.0057	270
0.180	91.1	1.0449	0.1216	0.0992	0.0065	75
0.360	90.3	1.1104	0.0806	0.0477	0.0069	184
0.720	90.7	1.0736	0.0513	0.0352	0.0067	401
0.090	177.8	1.2385	0.2484	0.0779	0.0078	25
0.180	177.1	1.0466	0.1568	0.0617	0.0065	47
0.360	179.0	1.0896	0.1094	0.0392	0.0068	117
0.720	178.7	1.4739	0.0641	0.0424	0.0092	462
0.180	325.8	1.9084	0.4244	0.0593	0.0119	21
0.360	325.7	1.1699	0.2004	0.0412	0.0073	34
0.720	325.6	1.6287	0.1253	0.0698	0.0102	150

Table 4.3. Anti-Neutrino Differential Cross Sections. The table shows the measured differential cross sections, $\frac{1}{E}\frac{d^2\sigma}{dxdy}$, (in units of 10^{-38}cm^2/GeV) for x, y, E_ν bins. For each x bin, the table shows the y, E_ν bin, the differential cross section, the statistical error, the systematic error, the scale error and the number of events in the x, y, E_ν. The cross section measurement and the determination of the systematic and scale errors are discussed in the text.

Table 4.3 continued

Anti-Neutrino Differential Cross Sections

$x = 0.045$

y	E_ν (GeV)	$\frac{1}{E}\frac{d^2\sigma}{dxdy}$	Statistical Error	Systematic Error	Scale Error	Events
0.360	26.0	0.8671	0.2768	0.1105	0.0054	11
0.720	26.2	0.9067	0.1336	0.0232	0.0057	41
0.180	49.6	1.7454	0.2935	0.1430	0.0109	35
0.360	49.6	1.2496	0.0889	0.0610	0.0078	187
0.720	49.6	0.9393	0.0563	0.0238	0.0059	259
0.090	91.7	1.2924	0.4882	0.1575	0.0081	11
0.180	89.9	1.6200	0.1577	0.0943	0.0101	106
0.360	90.1	1.3572	0.0933	0.0347	0.0085	205
0.720	90.4	1.0572	0.0551	0.0418	0.0066	341
0.090	179.3	1.6573	0.2880	0.1121	0.0104	38
0.180	179.1	1.4236	0.1735	0.0589	0.0089	69
0.360	178.5	1.6376	0.1333	0.0335	0.0102	146
0.720	178.9	1.0702	0.0587	0.0373	0.0067	309
0.180	325.9	1.0830	0.3209	0.0768	0.0068	12
0.360	325.7	1.3637	0.2200	0.0319	0.0085	39
0.720	325.5	1.1221	0.1103	0.0716	0.0070	95

Table 4.3 continued

Anti-Neutrino Differential Cross Sections

$x = 0.080$

y	E_ν (GeV)	$\frac{1}{E}\frac{d^2\sigma}{dxdy}$	Statistical Error	Systematic Error	Scale Error	Events
0.360	26.7	0.5386	0.2185	0.1203	0.0034	10
0.720	26.3	0.7391	0.1122	0.0305	0.0046	40
0.180	49.6	1.6923	0.2514	0.1157	0.0106	49
0.360	49.6	1.2677	0.0793	0.0343	0.0079	237
0.720	49.6	0.8627	0.0490	0.0195	0.0054	281
0.090	90.7	1.3271	0.3665	0.1695	0.0083	17
0.180	91.0	1.6057	0.1372	0.0611	0.0100	135
0.360	90.3	1.3167	0.0804	0.0393	0.0082	253
0.720	90.4	0.8549	0.0439	0.0256	0.0054	349
0.090	176.9	1.5483	0.2450	0.0930	0.0097	41
0.180	177.8	2.0598	0.1992	0.0493	0.0129	107
0.360	177.8	1.3106	0.1023	0.0408	0.0082	160
0.720	178.7	0.8144	0.0465	0.0331	0.0051	276
0.090	325.7	1.4266	0.4376	0.1007	0.0089	11
0.180	325.7	1.0507	0.2784	0.0786	0.0066	16
0.360	325.7	0.8926	0.1593	0.0539	0.0056	31
0.720	325.5	0.7209	0.0758	0.0665	0.0045	87

Table 4.3 continued

Anti-Neutrino Differential Cross Sections

$x = 0.125$

y	E_ν (GeV)	$\frac{1}{E}\frac{d^2\sigma}{dxdy}$	Statistical Error	Systematic Error	Scale Error	Events
0.360	26.2	0.8889	0.2293	0.1550	0.0056	16
0.720	26.3	0.5741	0.0965	0.0205	0.0036	32
0.180	49.6	1.6030	0.2262	0.1423	0.0100	49
0.360	49.5	1.0172	0.0650	0.0358	0.0064	225
0.720	49.5	0.6455	0.0390	0.0143	0.0040	247
0.090	91.2	1.2309	0.2970	0.1123	0.0077	18
0.180	91.0	1.3451	0.1087	0.0711	0.0084	150
0.360	90.9	1.0884	0.0645	0.0171	0.0068	269
0.720	89.9	0.5811	0.0323	0.0201	0.0036	304
0.090	179.4	1.4074	0.2130	0.0737	0.0088	57
0.180	178.8	1.5495	0.1491	0.0375	0.0097	105
0.360	177.6	1.0660	0.0823	0.0197	0.0067	159
0.720	179.2	0.5485	0.0334	0.0161	0.0034	242
0.090	325.8	1.4965	0.4144	0.1799	0.0094	13
0.180	325.9	1.3636	0.2681	0.0768	0.0085	27
0.360	325.7	0.9767	0.1398	0.0297	0.0061	47
0.720	325.6	0.5313	0.0561	0.0132	0.0033	81

Table 4.3 continued
Anti-Neutrino Differential Cross Sections

$x = 0.175$

y	E_ν (GeV)	$\frac{1}{E}\frac{d^2\sigma}{dxdy}$	Statistical Error	Systematic Error	Scale Error	Events
0.360	26.2	0.7595	0.2038	0.0699	0.0048	13
0.720	26.1	0.5391	0.1037	0.0148	0.0034	24
0.180	49.6	1.5096	0.2234	0.0895	0.0094	48
0.360	49.5	1.0036	0.0670	0.0198	0.0063	208
0.720	49.6	0.4258	0.0331	0.0128	0.0027	149
0.090	90.9	1.2295	0.3333	0.1348	0.0077	17
0.180	90.8	1.2365	0.1049	0.0435	0.0077	136
0.360	90.7	0.9710	0.0629	0.0211	0.0061	227
0.720	90.1	0.4725	0.0306	0.0093	0.0030	218
0.090	178.2	1.3588	0.2074	0.0650	0.0085	42
0.180	178.4	1.0914	0.1184	0.0417	0.0068	81
0.360	178.0	1.0229	0.0798	0.0254	0.0064	154
0.720	179.1	0.3835	0.0292	0.0089	0.0024	155
0.090	325.9	1.0117	0.3098	0.1327	0.0063	11
0.180	325.9	1.3759	0.3102	0.0931	0.0086	21
0.360	325.7	0.8667	0.1372	0.0291	0.0054	38
0.720	325.4	0.3958	0.0506	0.0303	0.0025	60

Table 4.3 continued

Anti-Neutrino Differential Cross Sections

$x = 0.225$

y	E_ν (GeV)	$\frac{1}{E}\frac{d^2\sigma}{dxdy}$	Statistical Error	Systematic Error	Scale Error	Events
0.360	26.0	0.7443	0.2589	0.0681	0.0047	12
0.720	26.2	0.2888	0.0716	0.0155	0.0018	14
0.180	49.5	0.9464	0.1816	0.0839	0.0059	28
0.360	49.6	0.7212	0.0572	0.0194	0.0045	149
0.720	49.5	0.3082	0.0279	0.0070	0.0019	107
0.090	91.6	0.5440	0.2856	0.1068	0.0034	13
0.180	90.6	1.1168	0.1001	0.0336	0.0070	119
0.360	90.6	0.7276	0.0529	0.0143	0.0046	179
0.720	90.9	0.2648	0.0213	0.0064	0.0017	137
0.090	177.2	1.1913	0.2032	0.0943	0.0075	38
0.180	177.5	0.8455	0.1112	0.0421	0.0053	56
0.360	178.2	0.6116	0.0658	0.0149	0.0038	89
0.720	178.9	0.2356	0.0229	0.0070	0.0015	95
0.090	325.8	2.2550	0.5791	0.1335	0.0141	15
0.180	325.9	0.8411	0.2136	0.0812	0.0053	15
0.360	325.6	0.7384	0.1182	0.0303	0.0046	37
0.720	325.4	0.1932	0.0318	0.0116	0.0012	35

Table 4.3 continued

Anti-Neutrino Differential Cross Sections

$x = 0.275$

y	E_ν (GeV)	$\frac{1}{E}\frac{d^2\sigma}{dxdy}$	Statistical Error	Systematic Error	Scale Error	Events
0.360	26.1	0.7082	0.2221	0.0586	0.0044	11
0.180	49.5	0.7173	0.1494	0.0505	0.0045	22
0.360	49.5	0.6790	0.0573	0.0147	0.0042	129
0.720	49.5	0.2615	0.0268	0.0066	0.0016	85
0.180	90.3	1.1045	0.0981	0.0364	0.0069	121
0.360	91.1	0.5142	0.0454	0.0123	0.0032	121
0.720	90.5	0.2212	0.0211	0.0059	0.0014	99
0.090	179.0	0.6754	0.1333	0.0656	0.0042	26
0.180	178.6	0.7238	0.0993	0.0349	0.0045	51
0.360	178.6	0.5134	0.0579	0.0261	0.0032	78
0.720	179.1	0.2224	0.0215	0.0060	0.0014	93
0.180	325.7	0.8670	0.2075	0.0689	0.0054	18
0.360	325.8	0.5310	0.1065	0.0283	0.0033	26
0.720	325.6	0.1186	0.0251	0.0090	0.0007	19

Table 4.3 continued

Anti-Neutrino Differential Cross Sections

$x = 0.350$

y	E_ν (GeV)	$\frac{1}{E}\frac{d^2\sigma}{dxdy}$	Statistical Error	Systematic Error	Scale Error	Events
0.360	26.0	0.6946	0.1763	0.0636	0.0043	17
0.720	26.1	0.2154	0.0508	0.0105	0.0013	15
0.180	49.6	0.6941	0.1113	0.0343	0.0043	39
0.360	49.5	0.4986	0.0355	0.0182	0.0031	177
0.720	49.5	0.1303	0.0130	0.0036	0.0008	82
0.090	90.9	0.7474	0.1915	0.0639	0.0047	22
0.180	89.8	0.7754	0.0606	0.0455	0.0049	155
0.360	90.2	0.4096	0.0279	0.0178	0.0026	196
0.720	90.4	0.1206	0.0101	0.0031	0.0008	112
0.090	178.4	0.8962	0.1212	0.0579	0.0056	53
0.180	178.3	0.7128	0.0757	0.0262	0.0045	84
0.360	177.9	0.4480	0.0396	0.0149	0.0028	118
0.720	177.4	0.1057	0.0108	0.0031	0.0007	80
0.090	325.7	0.7350	0.2069	0.0556	0.0046	12
0.180	325.7	0.4318	0.0986	0.0513	0.0027	20
0.360	325.6	0.4253	0.0688	0.0176	0.0027	36
0.720	325.4	0.1095	0.0161	0.0045	0.0007	37

Table 4.3 continued

Anti-Neutrino Differential Cross Sections

$x = 0.450$

y	E_ν (GeV)	$\frac{1}{E}\frac{d^2\sigma}{dxdy}$	Statistical Error	Systematic Error	Scale Error	Events
0.180	49.6	0.3062	0.0727	0.0435	0.0019	18
0.360	49.5	0.3014	0.0282	0.0177	0.0019	104
0.720	49.4	0.0558	0.0084	0.0038	0.0003	39
0.090	91.8	0.5049	0.1524	0.0812	0.0032	11
0.180	90.3	0.4891	0.0459	0.0367	0.0031	107
0.360	91.1	0.2676	0.0233	0.0147	0.0017	124
0.720	89.9	0.0586	0.0072	0.0026	0.0004	50
0.090	177.7	0.5523	0.0932	0.0441	0.0035	34
0.180	177.6	0.4067	0.0534	0.0288	0.0025	55
0.360	178.3	0.2080	0.0262	0.0054	0.0013	64
0.720	179.1	0.0524	0.0073	0.0023	0.0003	41
0.090	325.8	0.5684	0.1432	0.1179	0.0036	15
0.360	325.7	0.2535	0.0488	0.0161	0.0016	25
0.720	325.6	0.0642	0.0118	0.0031	0.0004	25

Table 4.3 continued

Anti-Neutrino Differential Cross Sections

$x = 0.550$

y	E_ν (GeV)	$\frac{1}{E}\frac{d^2\sigma}{dxdy}$	Statistical Error	Systematic Error	Scale Error	Events
0.180	49.6	0.1497	0.0512	0.0279	0.0009	10
0.360	49.6	0.1415	0.0186	0.0132	0.0009	54
0.720	49.6	0.0287	0.0061	0.0016	0.0002	16
0.180	90.5	0.2897	0.0323	0.0277	0.0018	78
0.360	89.3	0.1198	0.0139	0.0099	0.0008	70
0.720	90.1	0.0415	0.0057	0.0009	0.0003	42
0.090	178.2	0.2422	0.0595	0.0409	0.0015	16
0.180	178.5	0.1517	0.0292	0.0302	0.0009	31
0.360	179.1	0.1075	0.0166	0.0071	0.0007	39
0.720	178.8	0.0201	0.0042	0.0019	0.0001	17
0.180	325.9	0.2662	0.0729	0.0191	0.0017	14
0.360	325.8	0.1261	0.0341	0.0125	0.0008	16
0.720	325.4	0.0208	0.0054	0.0014	0.0001	14

Table 4.3 continued
Anti-Neutrino Differential Cross Sections

$x = 0.650$

y	E_ν (GeV)	$\frac{1}{E}\frac{d^2\sigma}{dxdy}$	Statistical Error	Systematic Error	Scale Error	Events
0.360	49.6	0.0518	0.0097	0.0078	0.0003	27
0.180	89.6	0.0922	0.0142	0.0106	0.0006	42
0.360	89.8	0.0607	0.0085	0.0037	0.0004	49
0.720	89.9	0.0095	0.0018	0.0005	0.0001	18
0.090	178.0	0.1139	0.0262	0.0140	0.0007	18
0.180	175.7	0.0545	0.0156	0.0207	0.0003	13
0.360	179.4	0.0207	0.0059	0.0054	0.0001	16

$x = 0.850$

y	E_ν (GeV)	$\frac{1}{E}\frac{d^2\sigma}{dxdy}$	Statistical Error	Systematic Error	Scale Error	Events
0.360	49.6	0.0067	0.0010	0.0006	0.0000	41
0.720	49.6	0.0015	0.0004	0.0001	0.0000	10
0.090	91.7	0.0059	0.0033	0.0018	0.0000	10
0.180	88.7	0.0107	0.0016	0.0016	0.0001	47
0.360	91.1	0.0034	0.0005	0.0005	0.0000	45
0.720	90.6	0.0009	0.0002	0.0001	0.0000	16
0.090	178.3	0.0118	0.0033	0.0020	0.0001	14
0.180	179.1	0.0073	0.0016	0.0015	0.0000	20
0.360	179.4	0.0027	0.0006	0.0003	0.0000	22
0.720	179.0	0.0005	0.0001	0.0000	0.0000	11
0.180	325.4	0.0058	0.0024	0.0005	0.0000	11
0.720	325.6	0.0006	0.0001	0.0000	0.0000	17

Table 4.4
Neutrino Differential Cross Sections

$x = 0.015$

y	E_ν (GeV)	$\frac{1}{E}\frac{d^2\sigma}{dxdy}$	Statistical Error	Systematic Error	Scale Error	Events
0.360	26.0	1.2096	0.2352	0.1234	0.0076	27
0.720	26.0	0.9833	0.1029	0.0494	0.0062	89
0.180	49.8	0.6169	0.1225	0.1470	0.0039	39
0.360	49.7	1.2205	0.0710	0.0868	0.0076	291
0.720	49.7	1.1519	0.0491	0.0423	0.0072	534
0.090	92.3	0.4909	0.1894	0.1218	0.0031	15
0.180	92.1	1.3664	0.0919	0.1122	0.0086	222
0.360	91.7	1.4450	0.0621	0.0587	0.0090	533
0.720	91.7	1.4568	0.0409	0.0522	0.0091	1222
0.045	186.7	1.5292	0.4215	0.1893	0.0096	15
0.090	184.9	1.1107	0.1214	0.1407	0.0070	91
0.180	185.9	1.5442	0.0998	0.0650	0.0097	245
0.360	185.9	1.7569	0.0730	0.0622	0.0110	571
0.720	185.7	1.6706	0.0377	0.0491	0.0105	1851
0.045	336.7	1.4856	0.3328	0.1690	0.0093	20
0.090	336.5	1.1487	0.1849	0.0804	0.0072	39
0.180	336.3	2.1238	0.1819	0.0478	0.0133	139
0.360	336.7	1.8061	0.0949	0.0492	0.0113	358
0.720	336.5	1.8567	0.0551	0.0788	0.0116	1077

Table 4.4. Neutrino Differential Cross Sections. The table shows the measured differential cross sections, $\frac{1}{E}\frac{d^2\sigma}{dxdy}$, (in units of $10^{-38}\text{cm}^2/\text{GeV}$) for x, y, E_ν bins. For each x bin, the table shows the y, E_ν bin, the differential cross section, the statistical error, the systematic error, the scale error and the number of events in the x, y, E_ν. The cross section measurement and the determination of the systematic and scale errors are discussed in the text.

Table 4.4 continued

Neutrino Differential Cross Sections

$x = 0.045$

y	E_ν (GeV)	$\frac{1}{E}\frac{d^2\sigma}{dxdy}$	Statistical Error	Systematic Error	Scale Error	Events
0.360	26.1	1.3089	0.2446	0.1488	0.0082	30
0.720	26.1	1.5824	0.1469	0.0525	0.0099	107
0.180	49.7	2.0579	0.2451	0.1645	0.0129	71
0.360	49.7	1.4601	0.0796	0.1021	0.0091	337
0.720	49.7	1.5993	0.0587	0.0597	0.0100	711
0.090	92.7	1.2214	0.2710	0.0991	0.0076	26
0.180	92.2	1.8020	0.1075	0.1233	0.0113	288
0.360	91.8	1.9131	0.0724	0.0728	0.0120	686
0.720	91.9	1.8685	0.0466	0.0754	0.0117	1532
0.090	185.3	1.9157	0.1639	0.1307	0.0120	140
0.180	185.1	2.0241	0.1160	0.0941	0.0127	307
0.360	185.8	2.0551	0.0798	0.0741	0.0129	652
0.720	185.9	2.0309	0.0431	0.0716	0.0127	2079
0.045	336.7	1.3134	0.2874	0.1551	0.0082	22
0.090	336.2	1.6587	0.2236	0.1177	0.0104	59
0.180	336.4	2.1006	0.1762	0.0594	0.0131	142
0.360	336.6	2.2904	0.1100	0.0430	0.0143	427
0.720	336.7	2.2165	0.0611	0.1076	0.0139	1240

Table 4.4 continued

Neutrino Differential Cross Sections

$x = 0.080$

y	E_ν (GeV)	$\frac{1}{E}\frac{d^2\sigma}{dxdy}$	Statistical Error	Systematic Error	Scale Error	Events
0.360	25.9	1.2640	0.2086	0.1138	0.0079	42
0.720	25.9	1.6462	0.1300	0.0462	0.0103	147
0.180	49.8	1.5447	0.1836	0.1104	0.0097	83
0.360	49.7	1.8831	0.0799	0.0808	0.0118	541
0.720	49.7	1.7612	0.0542	0.0536	0.0110	988
0.090	91.3	1.5057	0.2839	0.1113	0.0094	36
0.180	91.8	1.8583	0.0956	0.1247	0.0116	377
0.360	91.8	1.9018	0.0630	0.0601	0.0119	888
0.720	91.9	1.9244	0.0420	0.0653	0.0120	1971
0.045	186.7	1.2751	0.3351	0.1505	0.0080	17
0.090	185.8	1.9775	0.1454	0.1353	0.0124	186
0.180	185.6	2.1692	0.1054	0.0903	0.0136	433
0.360	185.9	2.2055	0.0713	0.0514	0.0138	937
0.720	186.1	2.0315	0.0376	0.0630	0.0127	2677
0.045	336.7	2.1039	0.3430	0.1431	0.0132	43
0.090	335.1	1.9678	0.2132	0.1107	0.0123	90
0.180	335.7	2.2705	0.1627	0.0606	0.0142	215
0.360	336.4	2.1808	0.0945	0.0504	0.0136	524
0.720	336.7	2.0011	0.0503	0.0936	0.0125	1474

Table 4.4 continued

Neutrino Differential Cross Sections

$x = 0.125$

y	E_ν (GeV)	$\frac{1}{E}\frac{d^2\sigma}{dxdy}$	Statistical Error	Systematic Error	Scale Error	Events
0.360	26.0	1.2799	0.2037	0.1105	0.0080	46
0.720	26.0	1.4474	0.1153	0.0324	0.0091	143
0.180	49.8	1.8680	0.1781	0.1109	0.0117	113
0.360	49.7	1.8469	0.0701	0.0608	0.0116	668
0.720	49.7	1.8585	0.0521	0.0423	0.0116	1169
0.090	92.4	1.9448	0.2888	0.1130	0.0122	47
0.180	92.0	1.8731	0.0841	0.0924	0.0117	498
0.360	91.7	1.9517	0.0573	0.0424	0.0122	1134
0.720	91.9	1.8741	0.0378	0.0564	0.0117	2286
0.045	186.7	1.6175	0.3656	0.1583	0.0101	25
0.090	185.2	1.9353	0.1358	0.0654	0.0121	211
0.180	186.0	1.8730	0.0886	0.0465	0.0117	448
0.360	185.7	1.9210	0.0613	0.0447	0.0120	966
0.720	186.0	1.9205	0.0336	0.0428	0.0120	2982
0.045	336.5	1.7663	0.2793	0.1842	0.0111	43
0.090	335.8	1.9441	0.2015	0.1004	0.0122	98
0.180	336.5	1.8198	0.1250	0.0813	0.0114	217
0.360	336.4	2.0339	0.0807	0.0413	0.0127	624
0.720	336.6	1.9523	0.0451	0.0772	0.0122	1725

Table 4.4 continued

Neutrino Differential Cross Sections

$x = 0.175$

y	E_ν (GeV)	$\frac{1}{E}\frac{d^2\sigma}{dxdy}$	Statistical Error	Systematic Error	Scale Error	Events
0.360	26.2	1.5932	0.2476	0.1031	0.0100	45
0.720	26.0	1.8352	0.1557	0.0628	0.0115	129
0.180	49.8	1.5938	0.1706	0.0863	0.0100	92
0.360	49.7	1.8220	0.0727	0.0577	0.0114	612
0.720	49.7	1.7324	0.0524	0.0271	0.0108	1027
0.090	92.7	1.6344	0.2526	0.0991	0.0102	49
0.180	91.8	1.7386	0.0818	0.0517	0.0109	463
0.360	91.8	1.9232	0.0582	0.0363	0.0120	1066
0.720	91.6	1.6636	0.0373	0.0407	0.0104	1893
0.045	187.0	1.5323	0.3322	0.1536	0.0096	23
0.090	185.6	1.7337	0.1277	0.0675	0.0108	190
0.180	186.0	1.9088	0.0925	0.0501	0.0119	428
0.360	185.6	1.7147	0.0584	0.0271	0.0107	856
0.720	186.0	1.7460	0.0334	0.0374	0.0109	2541
0.045	336.7	1.5139	0.2342	0.1385	0.0095	45
0.090	336.2	1.6374	0.1735	0.0915	0.0102	93
0.180	336.4	1.6315	0.1210	0.0527	0.0102	187
0.360	336.0	1.7272	0.0759	0.0396	0.0108	524
0.720	336.6	1.7169	0.0432	0.0575	0.0107	1479

Table 4.4 continued

Neutrino Differential Cross Sections

$x = 0.225$

y	E_ν (GeV)	$\frac{1}{E}\frac{d^2\sigma}{dxdy}$	Statistical Error	Systematic Error	Scale Error	Events
0.360	25.9	1.4644	0.2439	0.0722	0.0092	39
0.720	26.2	1.7409	0.1678	0.0565	0.0109	107
0.180	49.9	1.4423	0.1744	0.0566	0.0090	81
0.360	49.7	1.6614	0.0709	0.0316	0.0104	540
0.720	49.7	1.5672	0.0544	0.0227	0.0098	796
0.090	92.7	1.0182	0.2120	0.1121	0.0064	33
0.180	91.8	1.5380	0.0764	0.0517	0.0096	412
0.360	91.7	1.6106	0.0540	0.0246	0.0101	880
0.720	91.8	1.4526	0.0370	0.0253	0.0091	1490
0.045	186.2	1.2136	0.2904	0.1068	0.0076	22
0.090	184.5	1.4452	0.1160	0.0565	0.0090	164
0.180	185.9	1.5740	0.0817	0.0365	0.0099	376
0.360	186.1	1.5986	0.0575	0.0253	0.0100	775
0.720	186.1	1.4508	0.0316	0.0230	0.0091	2006
0.045	336.3	1.5227	0.2526	0.1349	0.0095	38
0.090	336.6	1.4080	0.1638	0.0787	0.0088	78
0.180	336.2	1.4688	0.1215	0.0779	0.0092	150
0.360	336.7	1.4131	0.0674	0.0534	0.0088	441
0.720	336.7	1.4345	0.0406	0.0469	0.0090	1194

Table 4.4 continued

Neutrino Differential Cross Sections

$x = 0.275$

y	E_ν (GeV)	$\frac{1}{E}\frac{d^2\sigma}{dxdy}$	Statistical Error	Systematic Error	Scale Error	Events
0.360	26.0	1.3213	0.2352	0.0795	0.0083	34
0.720	26.2	1.1280	0.1454	0.0532	0.0071	78
0.180	49.8	1.3536	0.1568	0.0390	0.0085	87
0.360	49.7	1.4444	0.0687	0.0320	0.0090	439
0.720	49.7	1.3479	0.0551	0.0352	0.0084	586
0.090	92.7	0.8982	0.1844	0.0809	0.0056	34
0.180	91.9	1.3372	0.0747	0.0504	0.0084	327
0.360	91.7	1.3614	0.0500	0.0296	0.0085	739
0.720	91.9	1.2699	0.0366	0.0198	0.0079	1184
0.045	186.8	1.4349	0.3355	0.1405	0.0090	23
0.090	186.5	1.3901	0.1194	0.0521	0.0087	144
0.180	185.1	1.3501	0.0769	0.0383	0.0084	319
0.360	185.2	1.2021	0.0493	0.0189	0.0075	606
0.720	185.8	1.2179	0.0301	0.0214	0.0076	1594
0.045	336.5	0.7804	0.1647	0.1166	0.0049	26
0.090	334.1	1.3287	0.1637	0.1512	0.0083	75
0.180	336.5	1.4306	0.1145	0.0570	0.0090	166
0.360	336.1	1.3249	0.0665	0.0344	0.0083	401
0.720	336.6	1.2520	0.0383	0.0287	0.0078	1033

Table 4.4 continued

Neutrino Differential Cross Sections

$x = 0.350$

y	E_ν (GeV)	$\frac{1}{E}\frac{d^2\sigma}{dxdy}$	Statistical Error	Systematic Error	Scale Error	Events
0.360	26.2	1.0577	0.1656	0.0603	0.0066	46
0.720	26.1	1.1470	0.1151	0.0416	0.0072	101
0.180	49.8	1.1251	0.1101	0.0475	0.0070	108
0.360	49.7	1.0115	0.0417	0.0483	0.0063	586
0.720	49.7	0.9945	0.0365	0.0273	0.0062	721
0.090	91.8	0.9053	0.1358	0.0607	0.0057	55
0.180	91.7	1.0661	0.0463	0.0522	0.0067	537
0.360	91.8	1.0094	0.0308	0.0370	0.0063	1067
0.720	91.9	0.9029	0.0231	0.0192	0.0057	1488
0.045	186.6	1.0864	0.1992	0.0691	0.0068	31
0.090	185.7	0.9335	0.0680	0.0352	0.0058	196
0.180	185.9	0.9389	0.0452	0.0432	0.0059	440
0.360	185.7	0.9642	0.0323	0.0374	0.0060	891
0.720	186.0	0.8168	0.0181	0.0160	0.0051	1969
0.045	336.6	0.9782	0.1438	0.1017	0.0061	51
0.090	336.0	0.9412	0.0910	0.1252	0.0059	110
0.180	336.1	0.9968	0.0679	0.0672	0.0062	222
0.360	336.0	0.9521	0.0391	0.0465	0.0060	604
0.720	336.6	0.8152	0.0223	0.0181	0.0051	1288

Table 4.4 continued

Neutrino Differential Cross Sections

$x = 0.450$

y	E_ν (GeV)	$\frac{1}{E}\frac{d^2\sigma}{dxdy}$	Statistical Error	Systematic Error	Scale Error	Events
0.360	26.1	0.5368	0.1241	0.0737	0.0034	20
0.720	26.3	0.3090	0.0766	0.0696	0.0019	33
0.180	49.7	0.7251	0.0851	0.0668	0.0045	78
0.360	49.8	0.6068	0.0327	0.0417	0.0038	356
0.720	49.8	0.5821	0.0315	0.0295	0.0036	360
0.090	92.3	0.7959	0.1394	0.0830	0.0050	42
0.180	91.5	0.6387	0.0356	0.0639	0.0040	337
0.360	91.3	0.5831	0.0235	0.0362	0.0036	644
0.720	91.9	0.4857	0.0179	0.0210	0.0030	753
0.045	187.5	0.6075	0.1464	0.0783	0.0038	22
0.090	185.8	0.6734	0.0544	0.0585	0.0042	164
0.180	185.8	0.5419	0.0344	0.0423	0.0034	257
0.360	185.8	0.5186	0.0232	0.0327	0.0032	519
0.720	185.9	0.4359	0.0138	0.0178	0.0027	1010
0.045	335.5	0.4117	0.0869	0.0595	0.0026	26
0.090	335.5	0.6630	0.0732	0.0574	0.0041	84
0.180	336.4	0.6493	0.0534	0.0459	0.0041	155
0.360	336.5	0.5531	0.0291	0.0357	0.0035	366
0.720	336.7	0.4020	0.0154	0.0163	0.0025	690

Table 4.4 continued

Neutrino Differential Cross Sections

$x = 0.550$

y	E_ν (GeV)	$\frac{1}{E}\frac{d^2\sigma}{dxdy}$	Statistical Error	Systematic Error	Scale Error	Events
0.360	26.0	0.2749	0.0873	0.0351	0.0017	13
0.180	49.7	0.3558	0.0581	0.0546	0.0022	42
0.360	49.7	0.3572	0.0242	0.0366	0.0022	223
0.720	49.7	0.2860	0.0226	0.0234	0.0018	164
0.090	92.4	0.4701	0.0912	0.0652	0.0029	31
0.180	91.6	0.3359	0.0239	0.0423	0.0021	209
0.360	91.6	0.2824	0.0149	0.0284	0.0018	372
0.720	91.4	0.2245	0.0120	0.0136	0.0014	369
0.045	186.5	0.4717	0.1195	0.0577	0.0030	17
0.090	185.1	0.3051	0.0338	0.0456	0.0019	87
0.180	185.4	0.2782	0.0218	0.0268	0.0017	176
0.360	184.8	0.2381	0.0146	0.0243	0.0015	279
0.720	185.8	0.1889	0.0086	0.0131	0.0012	508
0.045	336.3	0.3405	0.0699	0.0597	0.0021	25
0.090	334.3	0.2420	0.0354	0.0309	0.0015	54
0.180	336.5	0.2479	0.0285	0.0300	0.0016	87
0.360	336.6	0.2367	0.0167	0.0184	0.0015	212
0.720	336.5	0.1624	0.0093	0.0085	0.0010	315

Table 4.4 continued

Neutrino Differential Cross Sections

$x = 0.650$

y	E_ν (GeV)	$\frac{1}{E}\frac{d^2\sigma}{dxdy}$	Statistical Error	Systematic Error	Scale Error	Events
0.360	25.8	0.1508	0.0528	0.0217	0.0009	10
0.180	49.9	0.1112	0.0281	0.0241	0.0007	29
0.360	49.8	0.1201	0.0116	0.0141	0.0008	112
0.720	49.7	0.0871	0.0112	0.0099	0.0005	64
0.090	92.5	0.2199	0.0482	0.0306	0.0014	22
0.180	92.0	0.1219	0.0114	0.0210	0.0008	120
0.360	91.4	0.1131	0.0080	0.0119	0.0007	210
0.720	91.5	0.0881	0.0065	0.0065	0.0006	195
0.090	185.3	0.1281	0.0176	0.0197	0.0008	58
0.180	183.3	0.1194	0.0125	0.0162	0.0007	102
0.360	185.6	0.0886	0.0076	0.0102	0.0006	153
0.720	186.0	0.0691	0.0046	0.0067	0.0004	244
0.045	337.4	0.1041	0.0333	0.0223	0.0007	19
0.090	335.4	0.0598	0.0147	0.0227	0.0004	30
0.180	334.8	0.1083	0.0143	0.0160	0.0007	62
0.360	336.2	0.0799	0.0077	0.0100	0.0005	114
0.720	336.4	0.0654	0.0049	0.0033	0.0004	191

Table 4.4 continued

Neutrino Differential Cross Sections

$x = 0.850$

y	E_ν (GeV)	$\frac{1}{E}\frac{d^2\sigma}{dxdy}$	Statistical Error	Systematic Error	Scale Error	Events
0.180	49.7	0.0174	0.0033	0.0027	0.0001	33
0.360	49.7	0.0125	0.0012	0.0019	0.0001	118
0.720	49.8	0.0109	0.0014	0.0012	0.0001	63
0.090	92.5	0.0338	0.0062	0.0037	0.0002	31
0.180	91.1	0.0135	0.0012	0.0025	0.0001	141
0.360	91.4	0.0105	0.0007	0.0013	0.0001	232
0.720	91.9	0.0075	0.0006	0.0006	0.0000	190
0.090	177.0	0.0075	0.0012	0.0017	0.0000	66
0.180	186.1	0.0114	0.0011	0.0019	0.0001	103
0.360	185.4	0.0063	0.0006	0.0010	0.0000	133
0.720	185.5	0.0062	0.0004	0.0006	0.0000	259
0.045	336.7	0.0152	0.0034	0.0028	0.0001	21
0.090	334.0	0.0156	0.0022	0.0018	0.0001	51
0.180	334.0	0.0100	0.0012	0.0013	0.0001	79
0.360	336.0	0.0065	0.0006	0.0010	0.0000	123
0.720	336.5	0.0056	0.0004	0.0005	0.0000	192

Table 4.5

FMMF Structure Functions

x	Q^2	F_2	F_2 Statistical Error	F_2 Systematic Error	F_2 Scale Error	xF_3	xF_3 Statistical Error	xF_3 Systematic Error	xF_3 Scale Error	$\bar{\nu}$	ν
0.015	0.404	0.8788	0.0291	0.0689	0.0040	0.2289	0.0717	0.0368	0.0088	188	809
0.015	0.957	1.1348	0.0281	0.0475	0.0051	0.2131	0.0449	0.0136	0.0076	317	1351
0.015	1.844	1.4395	0.0317	0.0556	0.0064	0.3049	0.0428	0.0141	0.0084	358	1932
0.015	3.642	1.7933	0.0399	0.0605	0.0078	0.1590	0.0499	0.0074	0.0098	224	2209
0.015	6.714	2.0880	0.0803	0.0986	0.0091	0.1566	0.0940	0.0097	0.0106	66	1077
0.045	2.140	1.2061	0.0349	0.0769	0.0055	0.3493	0.0871	0.0371	0.0122	267	1030
0.045	2.877	1.4127	0.0320	0.0504	0.0065	0.4862	0.0506	0.0333	0.0096	303	1763
0.045	5.512	1.6411	0.0350	0.0671	0.0076	0.5544	0.0474	0.0270	0.0100	329	2326
0.045	10.97	1.7685	0.0399	0.0665	0.0083	0.6722	0.0492	0.0242	0.0102	179	2506
0.045	20.15	1.9398	0.0743	0.1144	0.0092	0.7547	0.0869	0.0292	0.0107	38	1240

Table 4.5. FMMF Structure Functions. Tabulated are the Structure Functions extracted from the FMMF data in x, Q^2 bins. (Q^2 is presented in units of GeV^2.) In addition the statistical, systematic and scale errors are tabulated. The final two columns indicate the number of anti-neutrino and neutrino events in the x, Q^2 bin. Please see the text for details on the extraction of the struction functions and the determinations of the errors.

Table 4.5 continued

FMMF Structure Functions

x	Q^2	F_2	F_2 Statistical Error	F_2 Systematic Error	F_2 Scale Error	xF_3	xF_3 Statistical Error	xF_3 Systematic Error	xF_3 Scale Error	$\bar{\nu}$	ν
0.080	3.032	1.2561	0.0309	0.0600	0.0058	0.6311	0.0780	0.0534	0.0130	311	1472
0.080	5.114	1.4636	0.0290	0.0451	0.0068	0.6149	0.0453	0.0277	0.0100	395	2399
0.080	9.802	1.5642	0.0292	0.0529	0.0075	0.7616	0.0397	0.0278	0.0099	364	3123
0.080	19.45	1.5971	0.0325	0.0603	0.0079	0.8616	0.0404	0.0213	0.0097	147	3201
0.080	35.82	1.5699	0.0539	0.1011	0.0079	0.8870	0.0630	0.0231	0.0092	37	1474
0.125	4.738	1.1958	0.0267	0.0530	0.0056	0.7566	0.0678	0.0265	0.0122	314	1794
0.125	7.981	1.3749	0.0248	0.0324	0.0066	0.8481	0.0400	0.0213	0.0100	365	2849
0.125	15.30	1.3854	0.0241	0.0418	0.0069	0.8928	0.0326	0.0257	0.0091	340	3469
0.125	30.49	1.4257	0.0261	0.0367	0.0073	0.9557	0.0322	0.0191	0.0089	127	3606
0.125	55.96	1.4585	0.0429	0.0567	0.0075	0.9907	0.0502	0.0478	0.0088	28	1725
0.175	7.411	1.1705	0.0273	0.0357	0.0054	0.8813	0.0749	0.0400	0.0135	305	1648
0.175	11.15	1.2368	0.0236	0.0254	0.0061	0.9331	0.0383	0.0174	0.0092	275	2614
0.175	21.44	1.2411	0.0236	0.0301	0.0061	0.8141	0.0317	0.0211	0.0080	271	2936
0.175	42.71	1.2468	0.0247	0.0277	0.0065	0.9457	0.0303	0.0226	0.0079	95	3065
0.175	78.33	1.2613	0.0399	0.0560	0.0066	0.9273	0.0467	0.0210	0.0077	29	1479

Table 4.5 continued

FMMF Structure Functions

x	Q^2	F_2	F_2 Statistical Error	F_2 Systematic Error	F_2 Scale Error	xF_3	xF_3 Statistical Error	xF_3 Systematic Error	xF_3 Scale Error	$\bar{\nu}$	ν
0.225	8.835	0.9860	0.0253	0.0247	0.0046	0.9829	0.0710	0.0263	0.0121	227	1436
0.225	14.31	1.0476	0.0222	0.0202	0.0052	0.8931	0.0370	0.0114	0.0082	209	2130
0.225	27.64	1.0021	0.0207	0.0194	0.0052	0.8441	0.0281	0.0131	0.0069	166	2415
0.225	54.88	1.0010	0.0218	0.0194	0.0054	0.8433	0.0268	0.0108	0.0066	60	2447
0.225	100.7	0.9826	0.0311	0.0369	0.0055	0.8772	0.0364	0.0272	0.0064	17	1194
0.275	10.51	0.8369	0.0235	0.0267	0.0039	0.7676	0.0663	0.0261	0.0099	181	1192
0.275	17.40	0.8658	0.0206	0.0232	0.0043	0.7998	0.0361	0.0211	0.0072	158	1719
0.275	33.73	0.8500	0.0197	0.0177	0.0044	0.7295	0.0275	0.0094	0.0060	133	1956
0.275	67.02	0.8633	0.0206	0.0195	0.0046	0.7023	0.0254	0.0104	0.0056	56	1995
0.350	11.75	0.6742	0.0155	0.0324	0.0031	0.5771	0.0447	0.0271	0.0081	288	1711
0.350	22.12	0.6460	0.0131	0.0234	0.0032	0.6066	0.0228	0.0176	0.0053	243	2338
0.350	42.82	0.6152	0.0121	0.0181	0.0032	0.5475	0.0167	0.0124	0.0043	174	2601
0.350	85.15	0.5661	0.0120	0.0143	0.0031	0.5025	0.0146	0.0097	0.0037	61	2573
0.350	156.7	0.5716	0.0169	0.0154	0.0032	0.5073	0.0198	0.0102	0.0037	14	1288

Table 4.5 continued

FMMF Structure Functions

x	Q^2	F_2	F_2 Statistical Error	F_2 Systematic Error	F_2 Scale Error	xF_3	xF_3 Statistical Error	xF_3 Systematic Error	xF_3 Scale Error	$\bar{\nu}$	ν
0.450	16.28	0.4014	0.0120	0.0338	0.0018	0.2859	0.0333	0.0359	0.0042	175	1078
0.450	28.35	0.3803	0.0104	0.0218	0.0019	0.3551	0.0188	0.0202	0.0032	152	1345
0.450	54.90	0.3257	0.0089	0.0157	0.0017	0.3070	0.0126	0.0152	0.0024	84	1427
0.450	109.9	0.3061	0.0089	0.0135	0.0017	0.2737	0.0109	0.0118	0.0020	40	1376
0.550	17.65	0.2205	0.0091	0.0243	0.0010	0.1798	0.0261	0.0222	0.0025	98	553
0.550	34.32	0.1780	0.0066	0.0176	0.0009	0.1798	0.0128	0.0162	0.0016	79	766
0.550	67.32	0.1606	0.0061	0.0110	0.0008	0.1294	0.0086	0.0105	0.0011	62	735
0.550	134.4	0.1320	0.0055	0.0094	0.0007	0.1206	0.0067	0.0082	0.0009	17	720
0.650	25.17	0.0732	0.0028	0.0080	0.0003	0.0584	0.0062	0.0088	0.0007	101	718
0.650	79.52	0.0554	0.0029	0.0055	0.0003	0.0586	0.0043	0.0044	0.0004	24	410
0.850	24.18	0.0089	0.0004	0.0013	0.0000	0.0063	0.0015	0.0016	0.0001	83	427
0.850	52.92	0.0068	0.0003	0.0009	0.0000	0.0072	0.0007	0.0008	0.0001	46	449
0.850	104.3	0.0048	0.0003	0.0005	0.0000	0.0046	0.0004	0.0005	0.0000	38	402

Chapter 5

Results and Conclusions

5.1 Introduction

In Chapter 4 the extraction of differential cross sections and structure functions from the FMMF charged current neutrino–nucleon scattering data was described and the measured cross sections and structure function were presented in a series of tables. This chapter will discuss the structure functions in the context of QCD evolution, make comparisons of the FMMF structure functions with those of other experiments, describe the fitting of a set of parton distribution functions (PDF) based on the FMMF structure functions and finally present a series of measurements of Λ_{QCD} from the Q^2 evolution of the FMMF structure functions.

5.2 Structure Functions Comparisons

In this section, the FMMF structure functions are compared with the qualitative expectations of QCD and with the measured structure functions from other experiments.

5.2.1 Q^2 Evolution

An important prediction of the parton model is that structure functions should be constant instead of falling rapidly as a function of Q^2. This is the phenomenon known as scaling and was an early indication that the nucleon had an internal structure. QCD modifies the predictions of the parton model. QCD predicts that the structure functions should evolve as a function of Q^2. The Altarelli–Parisi equations (Altarelli and Parisi 1977) desribe this Q^2 evolution. The qualitative prediction of QCD is that as Q^2 increases, the observed number of soft (low x) gluons and quarks from the quantum sea

increases. This results in the evolution of the structure functions as a function of Q^2. The low x structure functions will grow as a function of Q^2 while the high x structure functions will shrink and the "intermediate" x structure functions will be constant. Figure 5.1 shows a schematic of the Q^2 evolution of parton distributions.

Figure 5.2 plots the FMMF structure functions and their statistical errors as a function of Q^2 for the various x bins. The structure functions show the behavior expected by QCD. At low x, the structure functions grow as a function of Q^2. At high x, the structure functions decrease as a function of Q^2. As least qualitatively, the measured structure functions agree with the predictions of QCD.

5.2.2 CDHSW

A comparison of the FMMF structure functions and those of CDHSW (Berge et al. 1991) is presented in Figure 5.3. The CDHSW structure functions are derived from an extremely large data set of 640,000 reconstructed and accepted neutrino events and 550,000 anti-neutrino events. The CDHSW data were taken using the CERN SPS magnet horn wide band beam. Since the CERN SPS could deliver only 400 GeV protons, the average energy of the neutrinos from the CERN horn beam was significantly lower than that available at the Tevatron. The horn beam did have the advantage of being a sign-selected beam (i.e. the beam consisted of only neutrinos or anti-neutrinos). This allowed the collection of the large anti-neutrino data set. The CDHSW detector consists of a large magnetized iron scintillator sampling calorimeter with interspersed drift chambers. The muons were immediately focused by the magnetized iron absorber plates and the muon tracks were reconstructed using drift chambers. The CDHSW structure function analysis was done in the same manner as this analysis using assumed total cross sections. The major differences between the two analyses is that CDHSW makes no correction for Fermi-Motion and that CDHSW uses the assumed form of R,

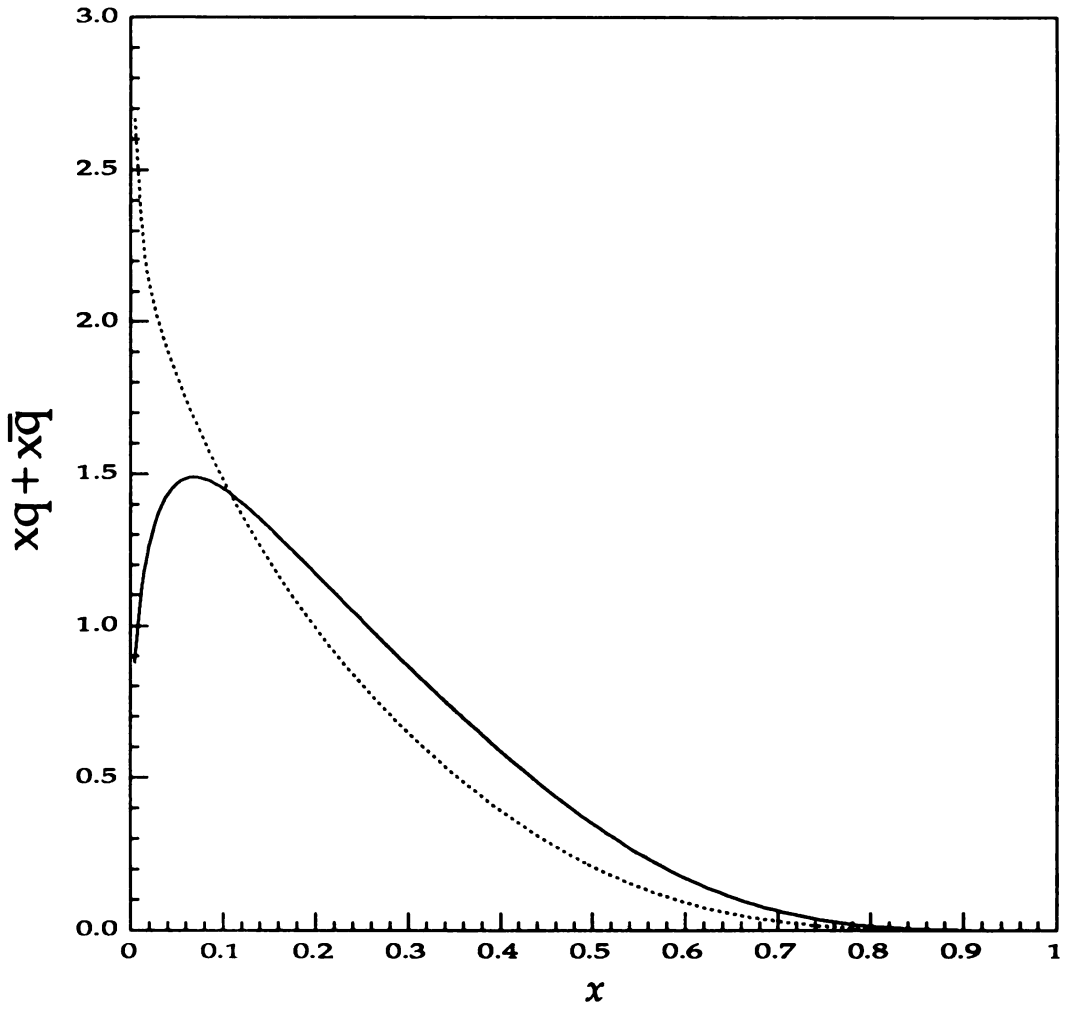

Figure 5.1. Effects of Q^2 Evolution. The figure shows the combined quark and anti-quark distributions, $xq + x\bar{q}$, as a function of x for different values of Q^2. The solid outline shows $xq + x\bar{q}$ for $Q^2 = 5\ GeV^2$. The dotted outline shows $xq + x\bar{q}$ for $Q^2 = 250\ GeV^2$. Note how the sea quarks dominate the high Q^2 distribution. The HMRS–BCDMS parton distributions were used for this figure.

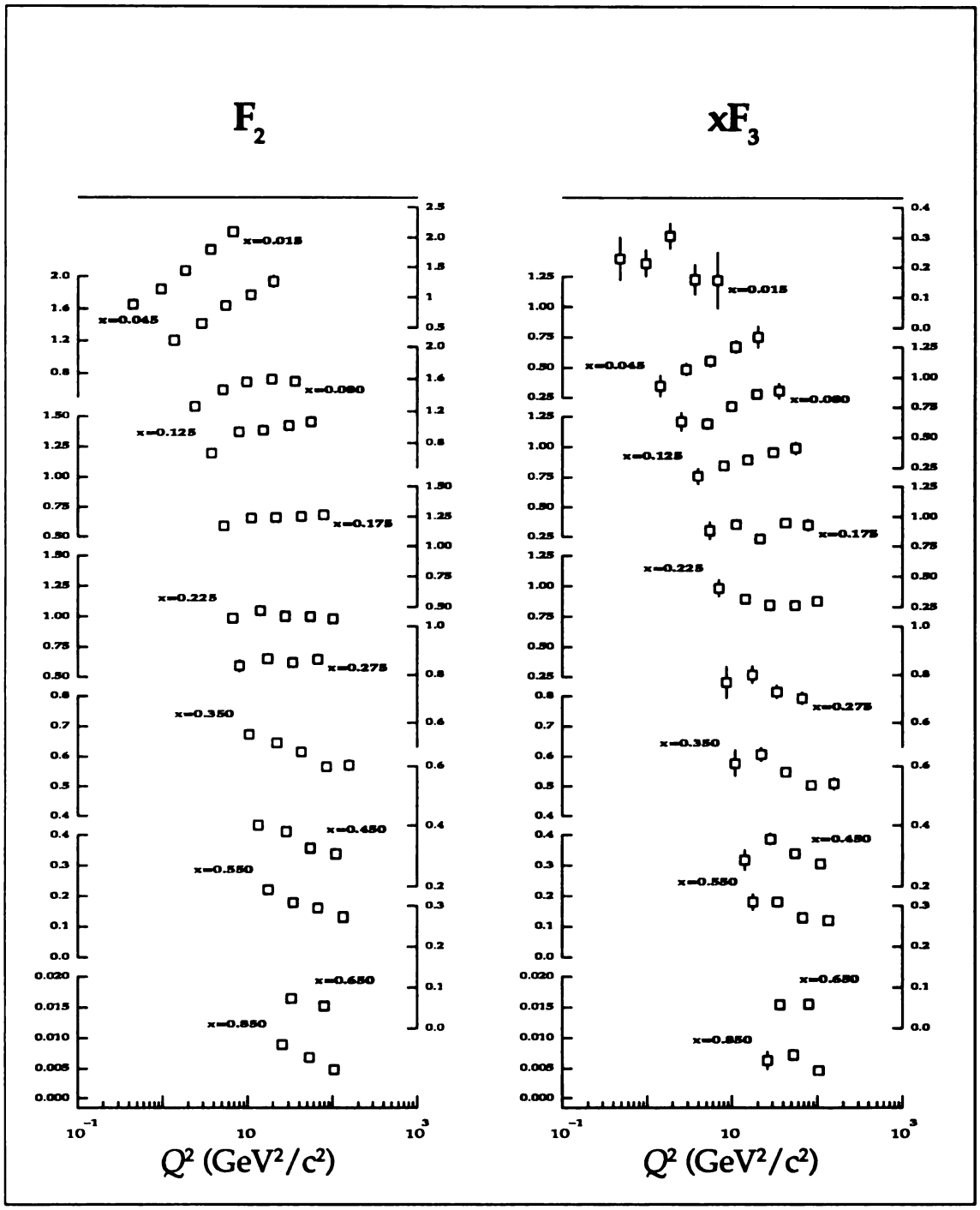

Figure 5.2. The FMMF Structure Functions. The figure plots the FMMF structure functions as a function of Q^2 for all x bins. Errors shown are statistical only.

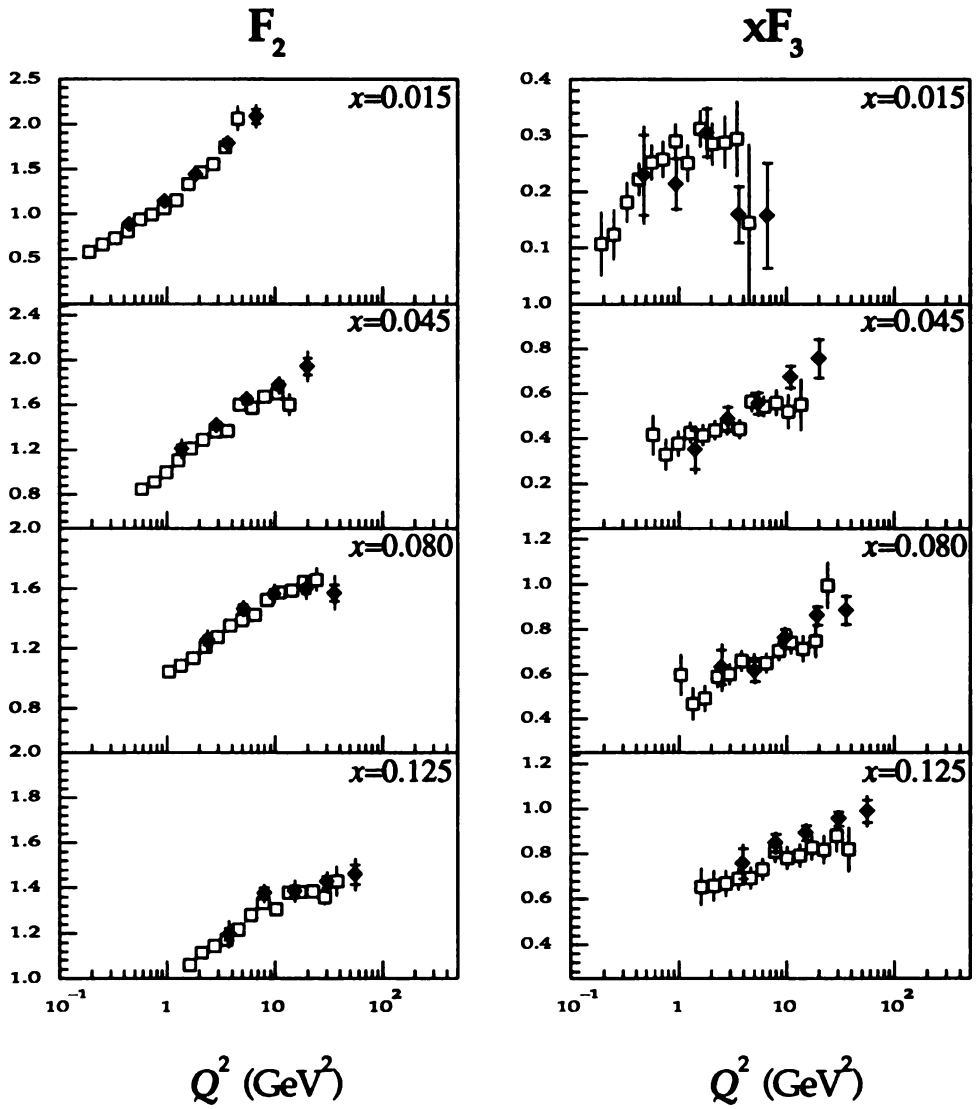

Figure 5.3. Comparison of FMMF and CDHSW Structure Functions. Shown are the FMMF structure functions (◆) and the CDHSW structure functions (□) plotted vs Q^2 for the various x bins. The error bars for the FMMF structure functions are the quadratic combination of the statistical, systematic and scale errors. The statistical errors are indicated by the cross bars. Note the logarithmic abscissa.

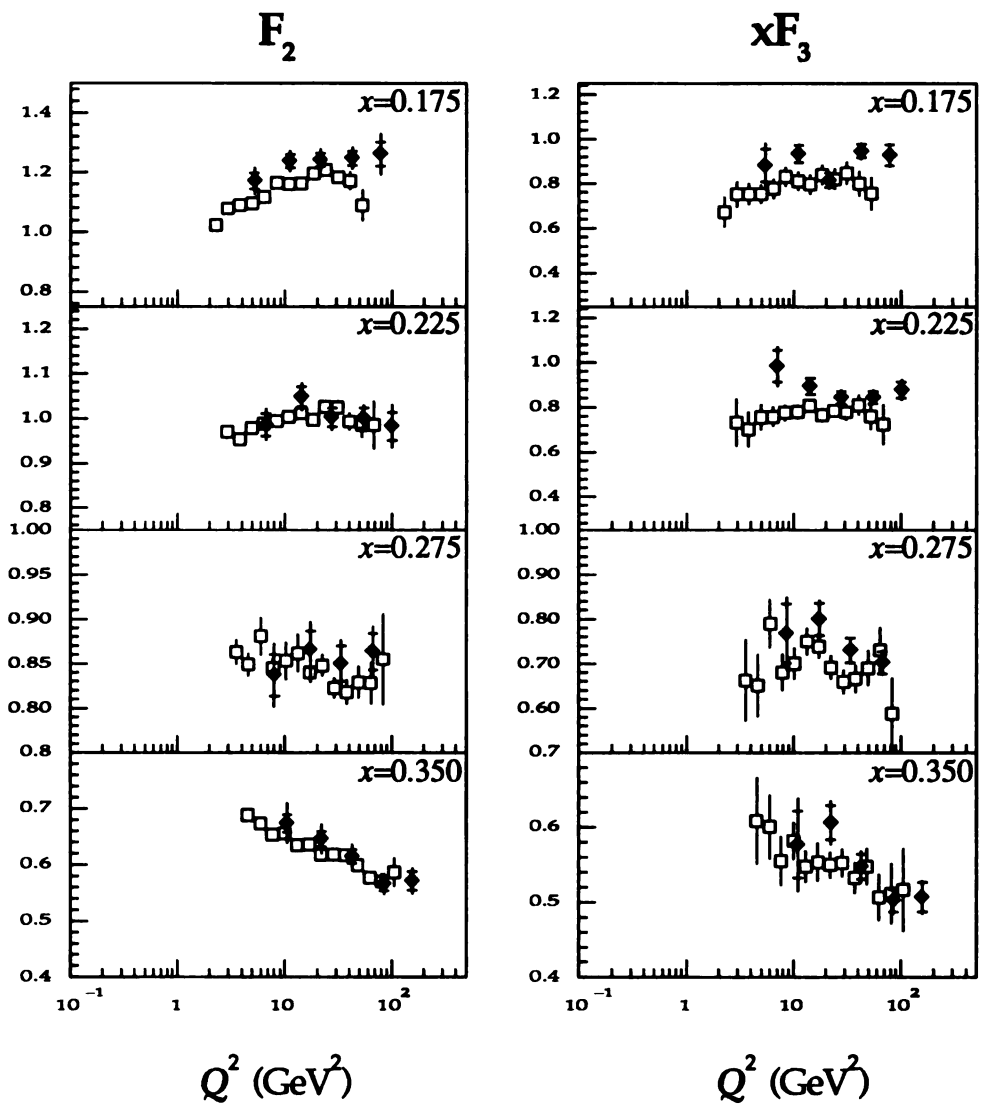

Figure 5.3 continued. Comparison of FMMF and CDHSW Structure Functions.

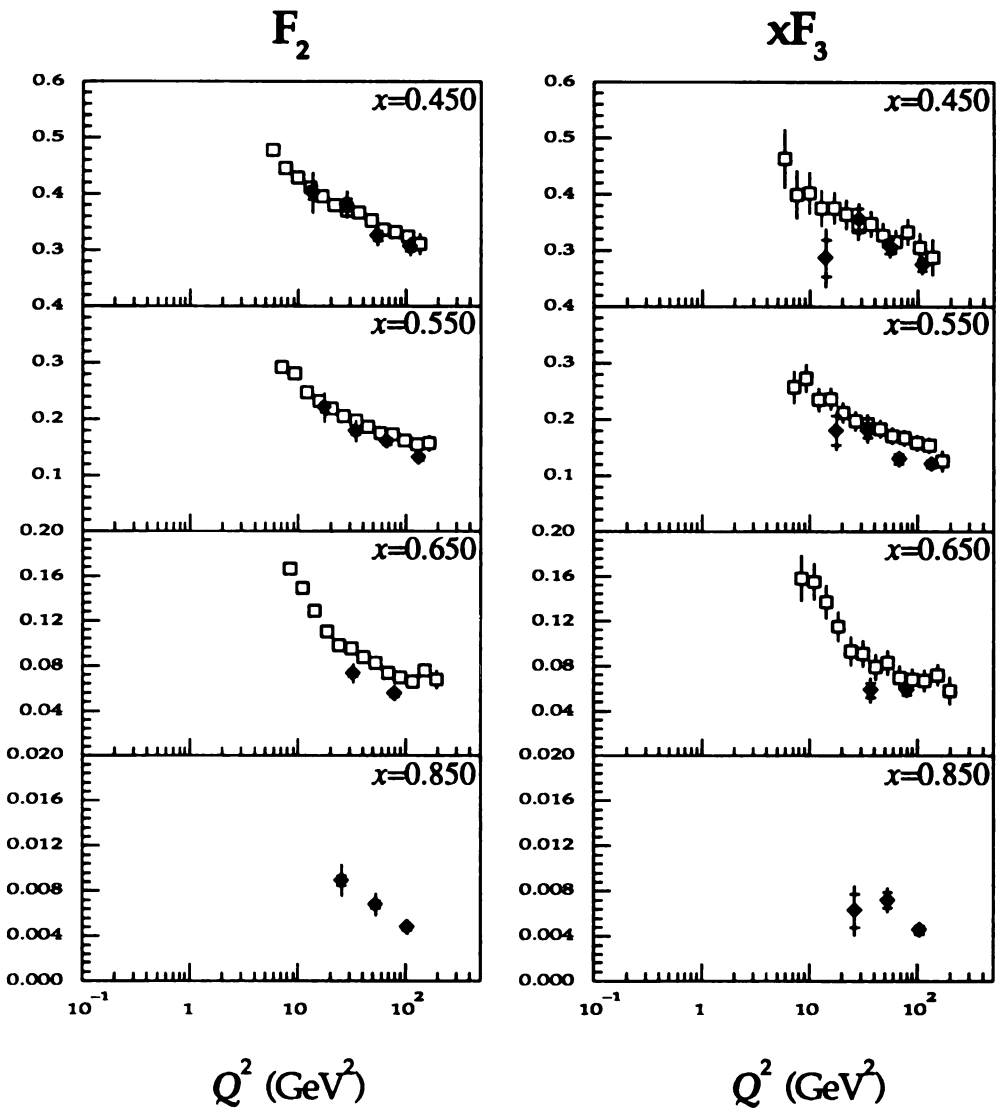

Figure 5.3 continued. Comparison of FMMF and CDHSW Structure Functions.

$$R(x,Q^2)=\frac{(1-x)^4}{\log\left(Q^2/\Lambda^2\right)}.$$

As one can see there is general agreement between the two experiments. In F_2 there is very good agreement in all the x bins. The CDHSW data with its much greater statistics and better acceptance (due to the magnetized calorimeter) is much more finely binned and in some regions probes higher Q^2 than the data of this experiment. For xF_3 the agreement between the two experiments is still good. The lack of anti-neutrino event statistics results in larger errors for the FMMF structure functions but, in general, the two data sets are consistent within their respective errors. In the x = 0.175 and x = 0.225 bins, the FMMF xF_3 data seems to be systematically above that of CDHSW but even in these bins the differences seem to be within 2 standard deviations.

5.2.3 CCFR

A comparison of the FMMF structure functions and those of CCFR (Quintas 1992) is presented in Figure 5.4. The CCFR data was taken at Fermilab in 1985 and 1987 using the Quad-Triplet Beam concurrently with the data taken by FMMF. The CCFR data set is roughly an order of magnitude larger than FMMF with 1,050,000 reconstructed, accepted neutrino events and 180,000 reconstructed, accepted anti-neutrino events. The CCFR detector was located upstream of the FMMF detector in Lab E. The CCFR detector is a more traditional design than the CDHSW apparatus. The CCFR detector consists of a large iron scintillator sampling calorimeter followed by a muon spectrometer. The CCFR detector is approximately 3 times more massive than FMMF and could be triggered multiple times per neutrino spill. This resulted in the larger CCFR data set. The CCFR structure function measurement was done in a more traditional manner. With their greater statistics, CCFR extracted the relative neutrino and anti-neutrino fluxes and used the known total neutrino cross section at low E_ν to normalize the neutrino flux and to measure the ratio of $\sigma^{\bar{\nu}N}/\sigma^{\nu N}$. The differential cross sections, $\frac{d^2\sigma^{\nu N,\bar{\nu}N}}{dx d\log Q^2}$, can be measured once the neutrino

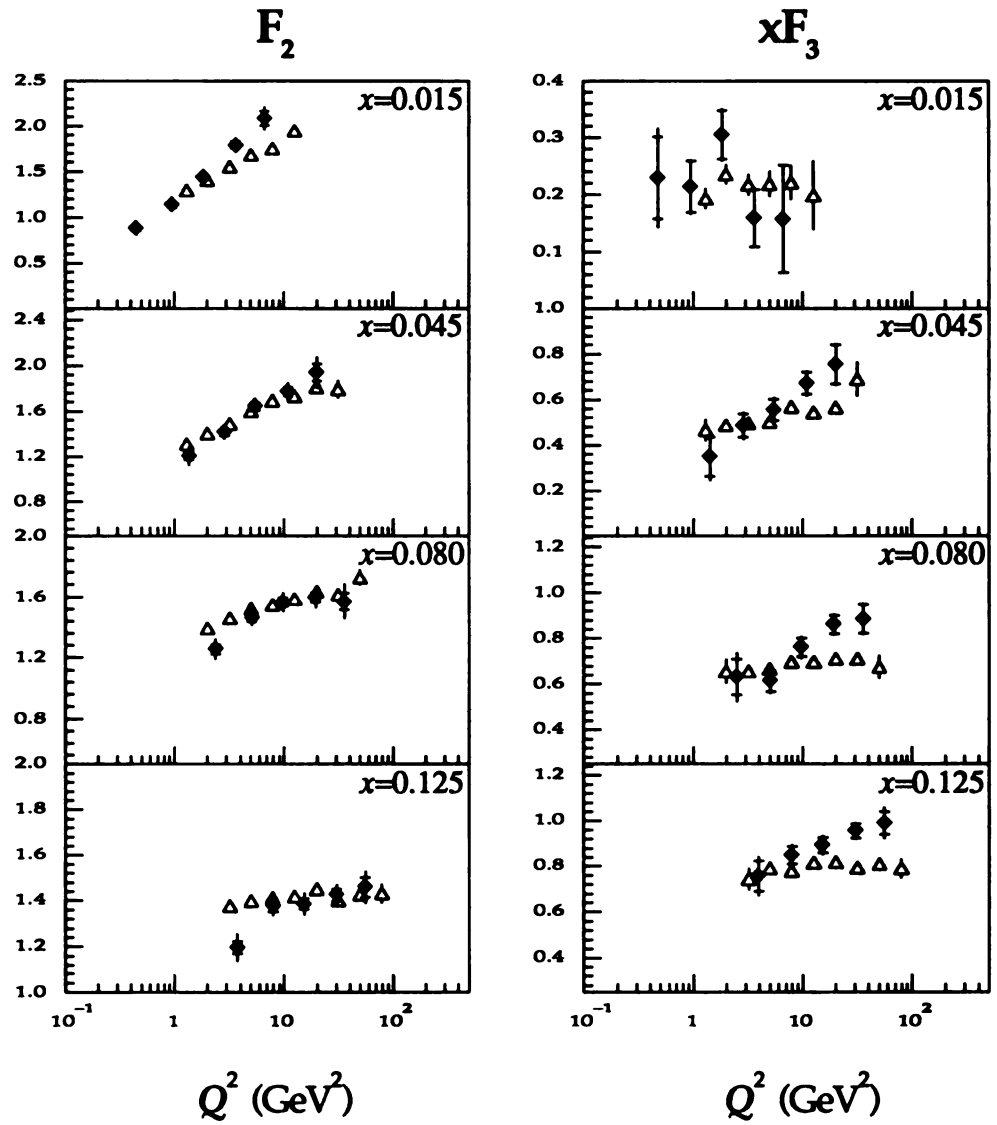

Figure 5.4. Comparison of FMMF and CCFR Structure Functions. Shown are the FMMF structure functions (◆) and the CCFR structure functions (△) plotted vs Q^2 for the various x bins. The error bars for the FMMF structure functions are the quadratic combination of the statistical, systematic and scale errors. The statistical errors are indicated by the cross bars. Note the logarithmic abscissa.

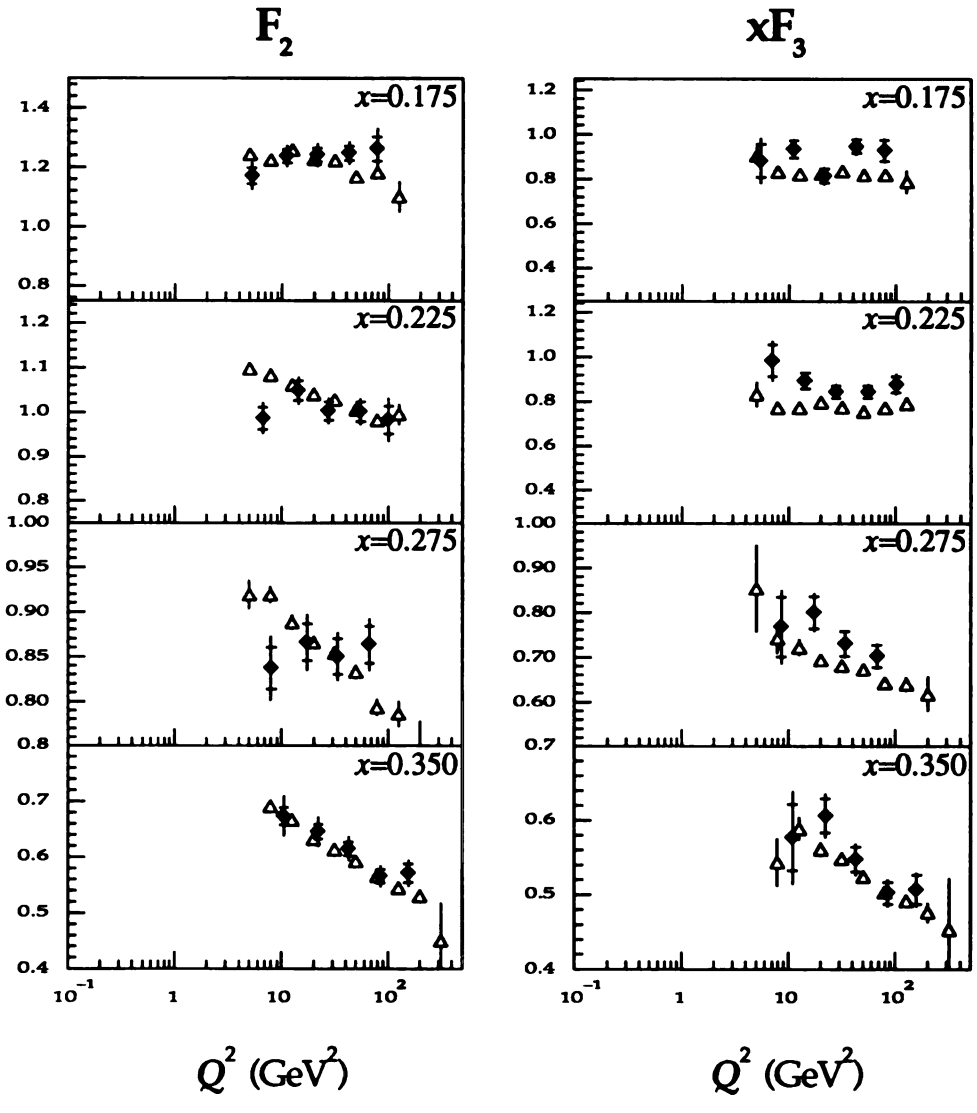

Figure 5.4 continued. Comparison of FMMF and CCFR Structure Functions.

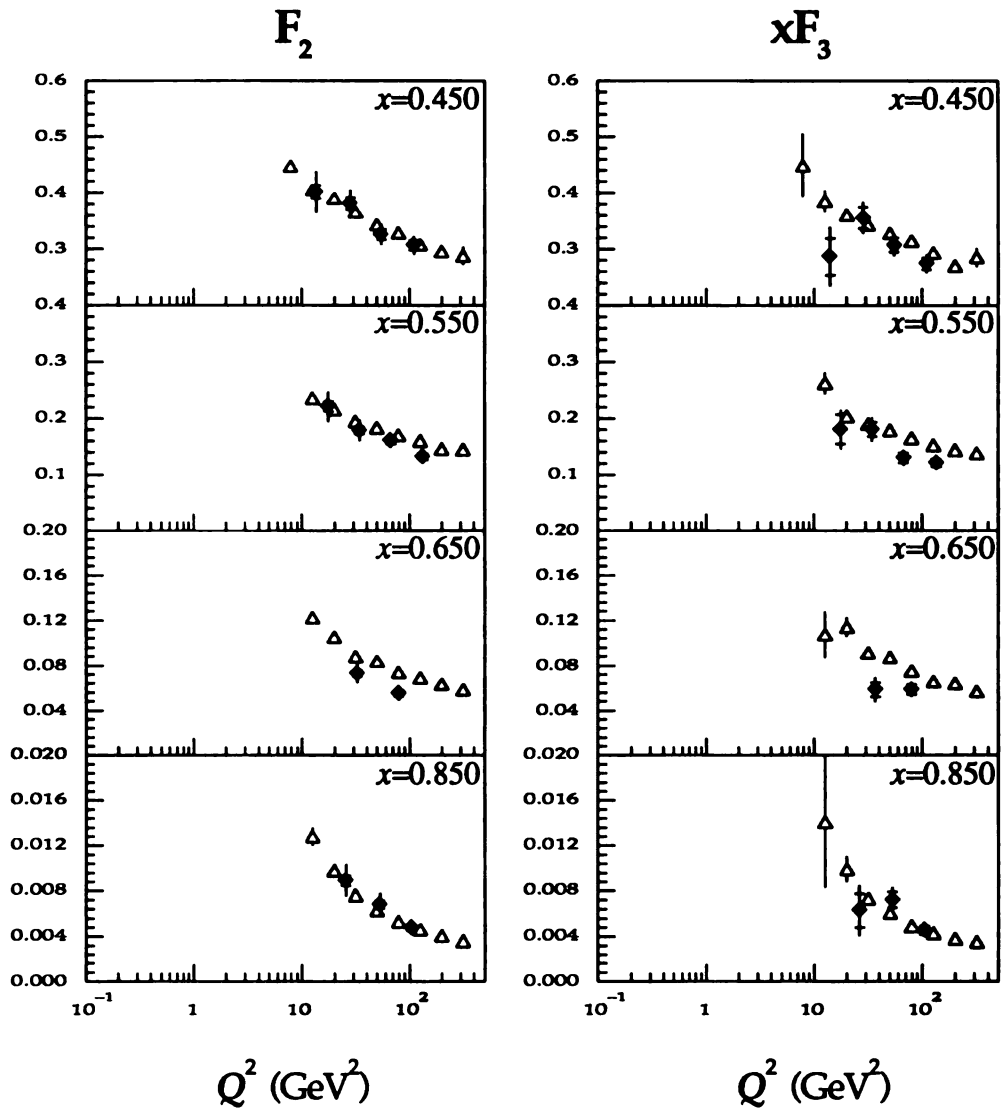

Figure 5.4 continued. Comparison of FMMF and CCFR Structure Functions.

and anti-neutrino fluxes are known. From the measured differential cross sections, CCFR extracts the structure functions. The other major difference between the CCFR and the FMMF analyses is that CCFR makes no correction for Fermi-Motion.

As one can see there is general agreement between the FMMF and CCFR structure functions. CCFR 's greater statistics result in their structure functions covering a greater range in Q^2 than those of FMMF. For F_2, there is general agreement between the two experiments. For xF_3, again there is general agreement but in the mid x bins, the FMMF structure functions seem to be systematically larger than those of CCFR.

5.3 Parton Distribution Function Fitting

The FMMF structure functions have been used as input for a parton distribution fitting program written by W.K. Tung (Private Communication, Morfín and Tung 1991). The fitting precedure uses a large package of routines that include Next-to-Leading Order (NLO) QCD and standard electroweak theory. The program allows the fitting of partons to the form:

$$p_i(x,Q_o^2) = Ax^{\alpha}(1-x)^{\beta}\log^{\gamma}\left(1-\frac{1}{x}\right),$$

where p_i is the probability that when probing with a probe of strength Q_o^2, one will find an ith parton in the interval $x \rightarrow x+dx$. The values of α, β, and γ can be varied for each quark or gluon distribution individually or correlations can be made as desired. The normalizations (based on A) are, where possible, fixed by sum rules. Where sum rules do not fix the normalization, the normalization then becomes another parameter in the fit. The parton distributions are then evolved to higher Q^2 using NLO QCD with the value of $\Lambda_{\overline{MS}}$, another free parameter of the fit. The standard χ^2 is then formed and minimized to determine the values of $\Lambda_{\overline{MS}}$, A_i, α_i, β_i, and γ_i.

For this analysis, the freedom the fit was allowed was sharply limited due to the limited data used as input. The factor, $\log^{\gamma}\left(1-\frac{1}{x}\right)$, was set to 1 for all distributions. The charm sea was assume to be zero. The other sea quark distributions were assumed to

have the same shape, which was simplified to the form $(1-x)^{\beta}$. The relative normalization of the strange sea to the up and down sea was set by previous measurements. The gluon distribution was fit to the same form as the sea distributions with the gluon normalization allowed to float. The valence quark distributions are fit to the form $x^{\alpha}(1-x)^{\beta}$. α was assumed to have the same value for both up and down valence quark distributions while for β no correlation between the values of β for the two distributions was required.

The fit for the PDF was done using the FMMF structure functions with $Q^2 > 16$ GeV^2 and $W^2 > 16$ GeV^2. Table 5.1 shows the final values obtained from the fit. Figures 5.5 and 5.6 shows a comparisons of the parton distributions obtained from fitting the FMMF data and those of HMRS-BCDMS (Harriman et al. 1990) at $Q^2 = 16$ GeV^2 and $Q^2 = 50$ GeV^2. There is general agreement between the FMMF parton distributions and the HMRS distributions but the FMMF PDF favor a lower average x distribution for the valance quarks and a harder gluon distribution. The FMMF gluon distribution has a much longer high x tail. In should be noted that the gluon distribution is not directly probed by neutrino–nucleon scattering and so the derived xG distribution must inferred from the evolution of the structure functions. The integrals of the FMMF valence quark distributions are larger than those of the HMRS. This due the fact that the FMMF xF_3 structure functions are larger than those of the other neutrino experiments.

5.4 Λ_{QCD} Fitting

As previously discussed, QCD makes a quantitative prediction about the Q^2 evolution of structure functions and parton distributions. The evolution of the structure functions is described by the Altarelli–Parisi equations (Altarelli and Parisi 1977). In this section we present a measurement of Λ_{QCD} using the evolution of xF_3.

A program originally written by Duke and Owens (Devoto et al. 1983) and modified by Oltman (1989) and other members of the CCFR collaboration was obtained from

Table 5.1

Results of Parton Distribution Fitting

	Parameter	Value
Overall Fit	$\Lambda_{\overline{MS}}$	176.9±9.3 MeV
	χ^2	67.0
	Degrees of Freedom	49
	χ^2 / DOF	1.37
Valence Distributions	α	0.810±0.030
Down Quark Valence	β	4.932±0.575
Up Quark Valence	β	3.518±0.141
Gluon	$\int xGdx$	0.413±0.051
	β	0.669±0.257
Sea Quark	β	8.609±0.781

Table 5.1. Results of Parton Distribution Fitting. The table shows the results of the PDF fitting program. The table is divided into 6 parts reflecting the portions of the fit for which a given set of parameters are relevant. The box titled "Overall Fit" shows the χ^2 of the fit and $\Lambda_{\overline{MS}}$ which controls the Q^2 evolution of the PDF. The other parts show parameters for the individual parton distribution functions at $Q_o^2 = 2.5\ GeV^2$

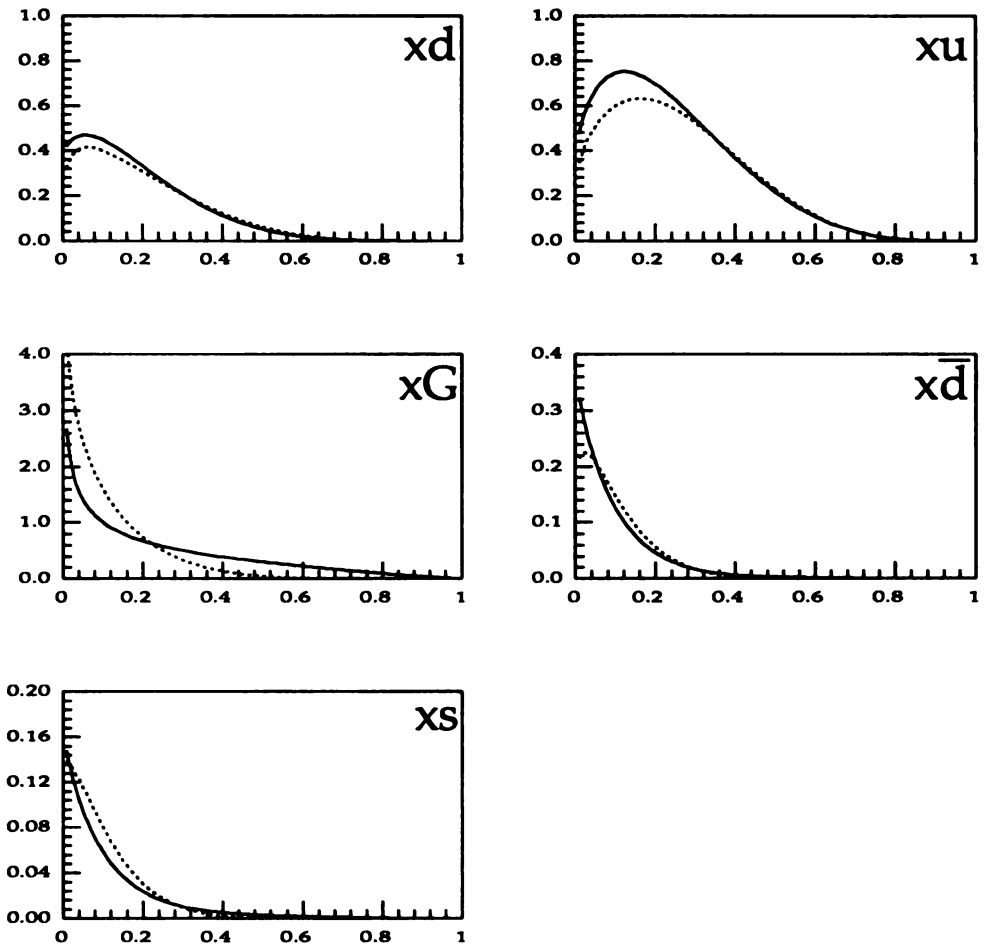

Figure 5.5. FMMF Parton Distribution Functions at Q^2= 16 GeV^2. The figure shows the FMMF PDF. The FMMF distributions are shown as the solid outlines. For comparison, the HMRS–BCDMS PDF are also shown as the dotted outlines. The top row shows the valence quark distributions. The center–left plot shows the gluon distributions. The center–right plot shows sea part of the valence quark distributions, $x\bar{d}$ ($\equiv x\bar{u}$). The bottom–left plot shows the strange sea distribution, $x\bar{s}$.

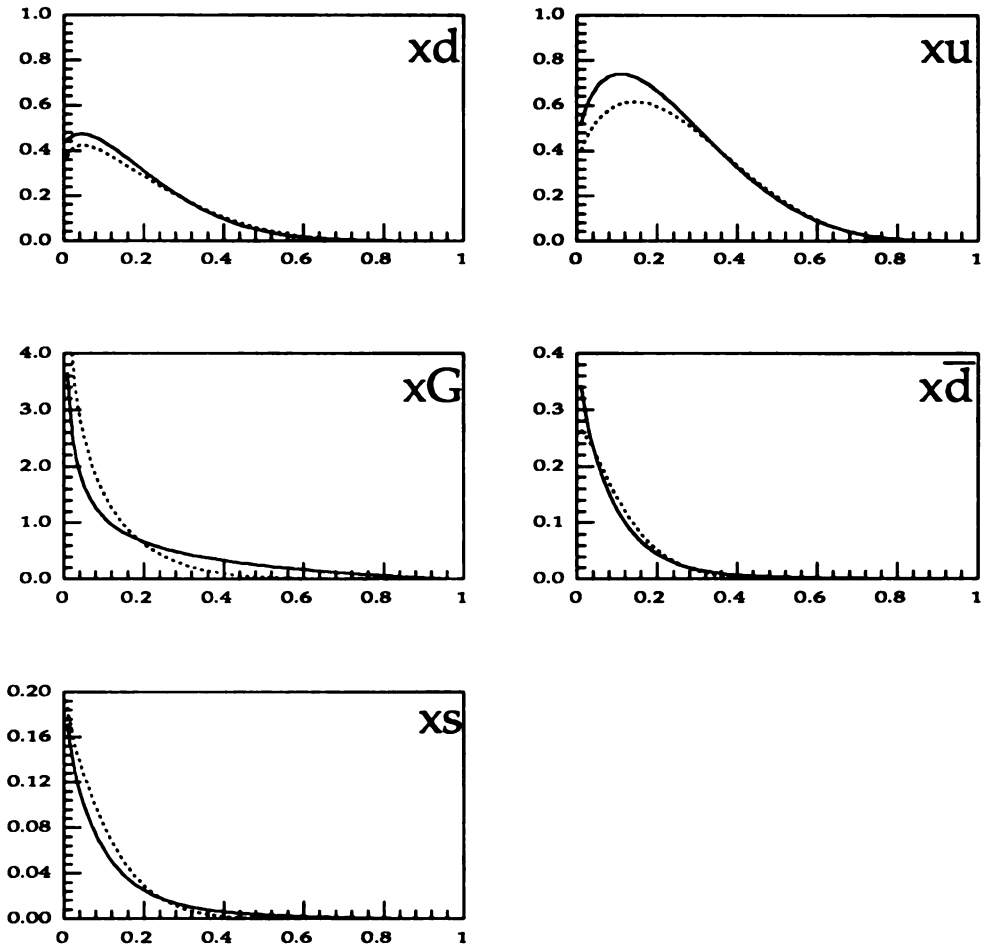

Figure 5.6, FMMF Parton Distribution Functions at Q^2= 50 GeV^2. The figure shows the FMMF PDF. The FMMF distributions are shown as the solid outlines. For comparison, the HMRS–BCDMS PDF are also shown as the dotted outlines. The top row shows the valence quark distributions. The center–left plot shows the gluon distributions. The center–right plot shows sea part of the valence quark distributions, $x\bar{d}$ ($\equiv x\bar{u}$). The bottom–left plot shows the strange sea distribution, $x\bar{s}$.

Paul Quintas (1992). The program was used to fit do leading order fits of the non-singlet evolution of the FMMF structure functions. The program fits the non-singlet structure function F_{NS} to the form,

$$F_{NS}(x) = Ax^{\alpha}(1-x)^{\beta}(1+\gamma x) + Bx^{\delta},$$

at a fixed $Q^2 = Q_o^2$. The Altarelli–Parisi equation (1.38a) is then regularized to obtain:

$$\frac{3\pi}{\alpha_s(t)}\frac{\partial F_{NS}(x,t)}{\partial t} =$$

$$[3 + 4\log(1-x)]F_{NS}(x,t) + 2\int_x^1 \frac{dy}{1-y}\left[(1-y^2)F_{NS}(x/y,t) - 2F_{NS}(x,t)\right],$$

where $t = \log(Q^2/\Lambda^2)$. Now the evolution of the non-singlet structure function is a direct function of t and can be measured. This method has the great advantage of not requiring knowledge of the gluon distribution but suffers from the larger errors associated with the statistical errors of xF_3. At higher x, one hopes that the contribution of the quantum sea will disappear and the relationship,

$$F_2 \cong xF_3$$

will hold and one could substitute F_2 for xF_3 above an x of 0.3 or so while doing the non-singlet fit.

The FMMF data has been used to fit for Λ. Three separate non-singlet fits have been preformed. The input structure functions which are treated as F_{NS} are:

- xF_3 *for* $0.0 < x < 0.7$
- xF_3 *for* $0.0 < x < 0.3$ and F_2 for $0.3 < x < 0.7$
- F_2 *for* $0.3 < x < 0.7$.

In all cases, the data was limited to $Q^2 > 15\ \text{GeV}^2$ and $W^2 > 10\ \text{GeV}^2$. For the errors used in the fitting, the statistical, systematic and scale error were combined in quadrature. The results of the three fits are shown in Table 5.2. Figures 5.7, 5.8 and 5.9 show the results of the fits.

The fit using only xF_3 returns,

$$\Lambda = 176.9 \pm 66.2 \text{ MeV}.$$

The large error is due the lack of precision of xF_3, especially at high x. The χ^2 for this fit is quite good at 25.4 for 26 degrees of freedom. This fit indicates that within the precision of the data the non-singlet evolution is as expected from QCD.

In the second fit, the xF_3 data above an x of 0.3 is replaced with that of F_2 and the fitting is done in the same manner. This fit returns,

$$\Lambda = 201.2 \pm 15.5 \text{ MeV}.$$

The much smaller error is due the greater precision of the F_2 structure functions. The χ^2 for this fit is 34.1 for 26 degrees of freedom. So while the error on Λ shrank, the overall fit is of a lesser quality. The probability of the xF_3 only fit is 49.6% while the probability for this fit is only 13.3%.

In the third fit, the same F_2 data that was used in the second fit is used but the xF_3 data is ignored. This fit returns,

$$\Lambda = 172.8 \pm 11.8 \text{ MeV}.$$

The χ^2 for this fit is 4.2 for 11 degrees of freedom with a very small error on the determined Λ.

5.5 Conclusions

The FMMF structure functions are a set of high statistics νN structure functions. As we have seen, the structure functions are in good agreement with the predictions of QCD. Comparisons between the FMMF structure functions and those of CDHSW and CCFR show general agreement. The FMMF structure functions have been used as input to a parton distribution fitting program and the fitted PDF have been presented. Finally a measurement of Λ_{QCD} from the Q^2 evolution of the non-singlet structure function has been presented which is consistent with the expectations of QCD.

The FMMF structure functions presented in this thesis are a valuable contribution to our overall knowledge of the structure of the nucleon.

Table 5.2

Results for Non-Singlet Λ_{QCD} Fitting

Structure Functions Used	Λ_{QCD}	χ^2/ DOF
xF_3 for $0.00 < x < 0.70$	176.9 ± 66.2 MeV	25.4/26
xF_3 for $0.00 < x < 0.30$ F_2 for $0.30 < x < 0.70$	201.2 ± 15.5 MeV	34.1/26
F_2 for $0.30 < x < 0.70$	172.8 ± 11.8 MeV	4.2/11

Table 5.2. Results for Non-Singlet Λ_{QCD} Fitting. The table shows the results of the fitting for non-singlet Λ_{QCD}. The first column shows the structure functions used as input for the fitting program. The input structure functions are treated as F_{NS} and the leading order Altarelli–Parisi equation is used to extract Λ_{QCD}. The second column shows the returned value of Λ_{QCD} and the estimated error from the fit. The third column shows the χ^2 of the fit.

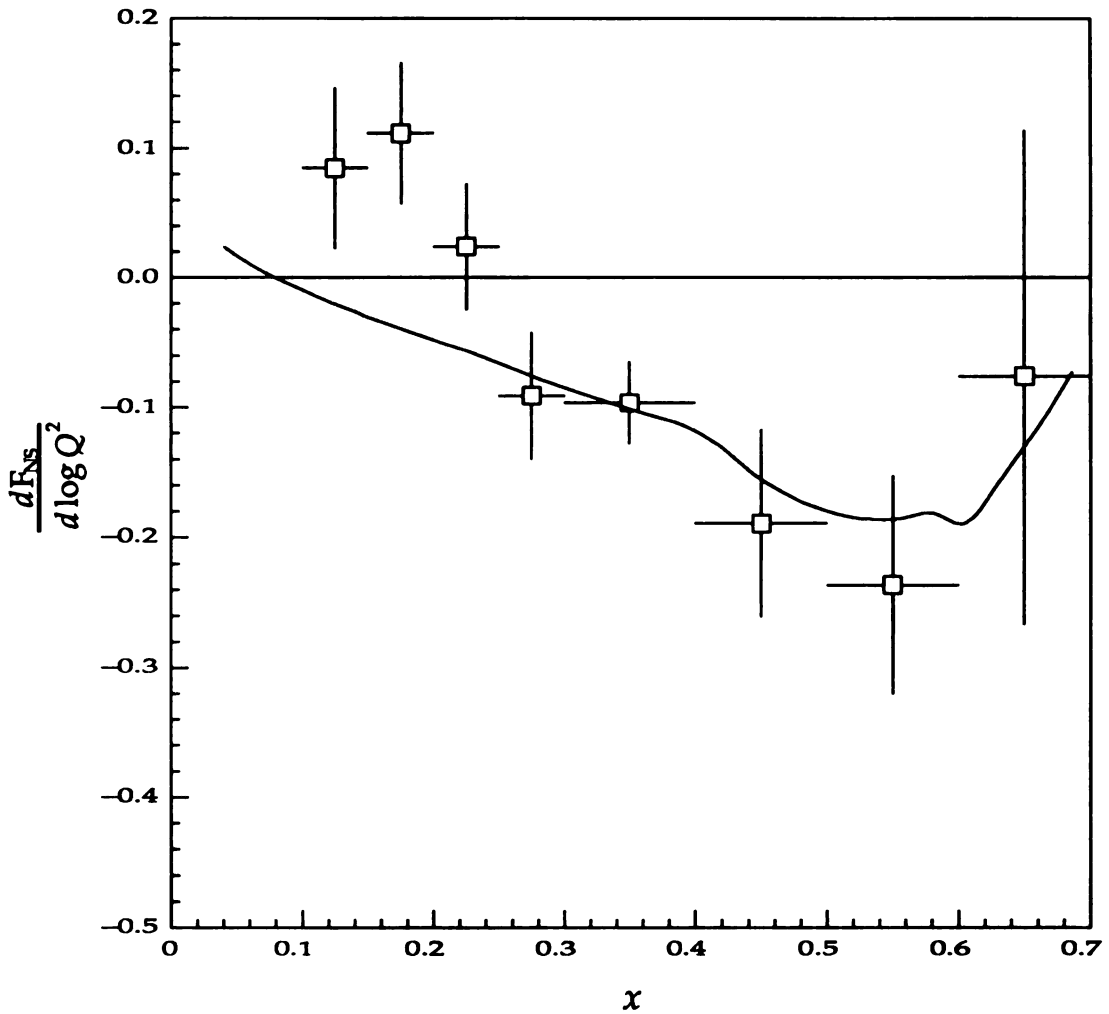

Figure 5.7. Result of Non-Singlet Fit using $F_{NS}=xF_3$ for $0.0 < x < 0.7$. Plotted is the fit of $\frac{dF_{NS}}{d\log Q^2}$ from the FMMF structure functions vs x. The line shows the value of $\frac{dF_{NS}}{d\log Q^2}$ as determined from the fit using the Duke and Owens fitting program.

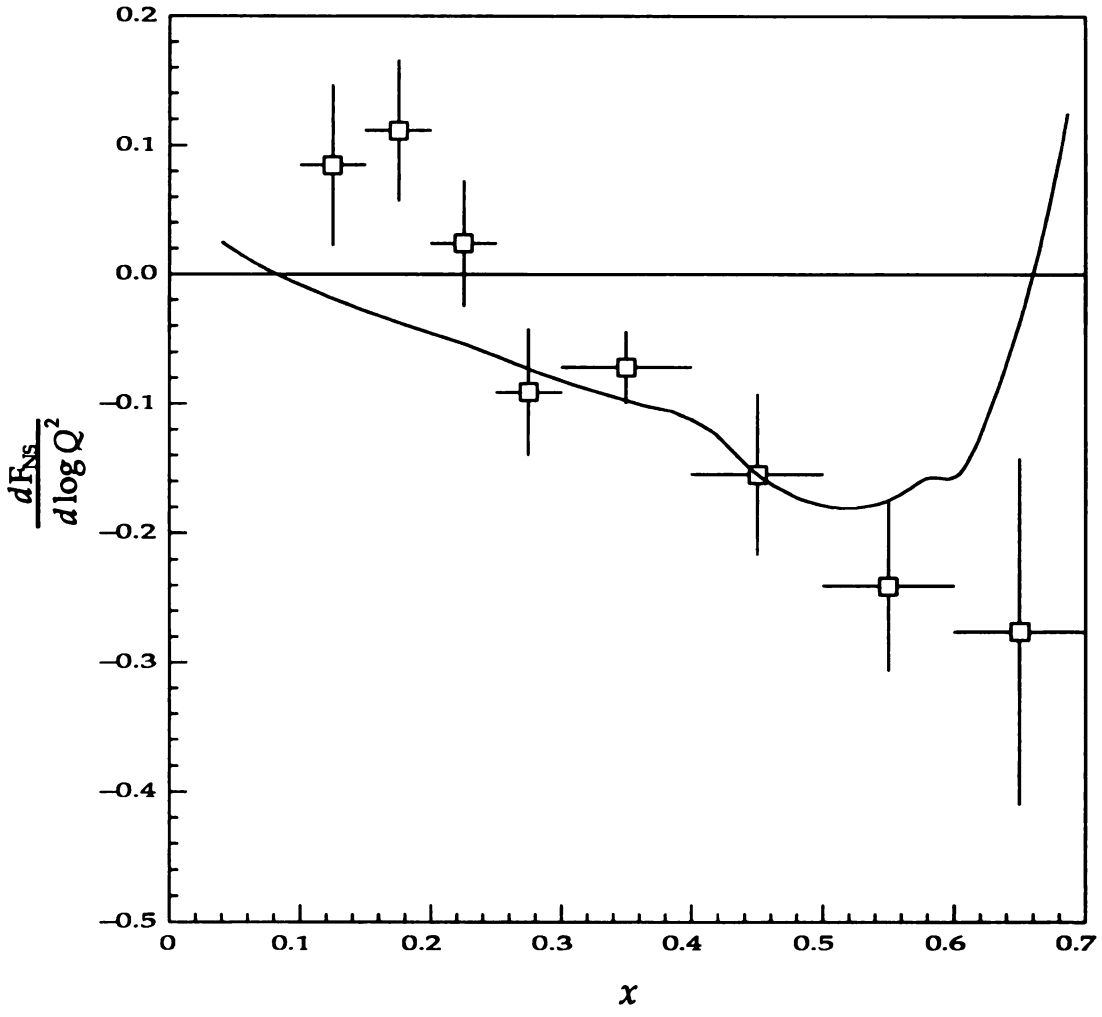

Figure 5.8. Result of Non-Singlet Fit using $F_{NS}=xF_3$ for $0.0 < x < 0.3$ and $F_{NS}=F_2$ for $0.3 < x < 0.7$. Plotted is the fit of $\frac{dF_{NS}}{d\log Q^2}$ from the FMMF structure functions vs x. The line shows the value of $\frac{dF_{NS}}{d\log Q^2}$ as determined from the fit using the Duke and Owens fitting program.

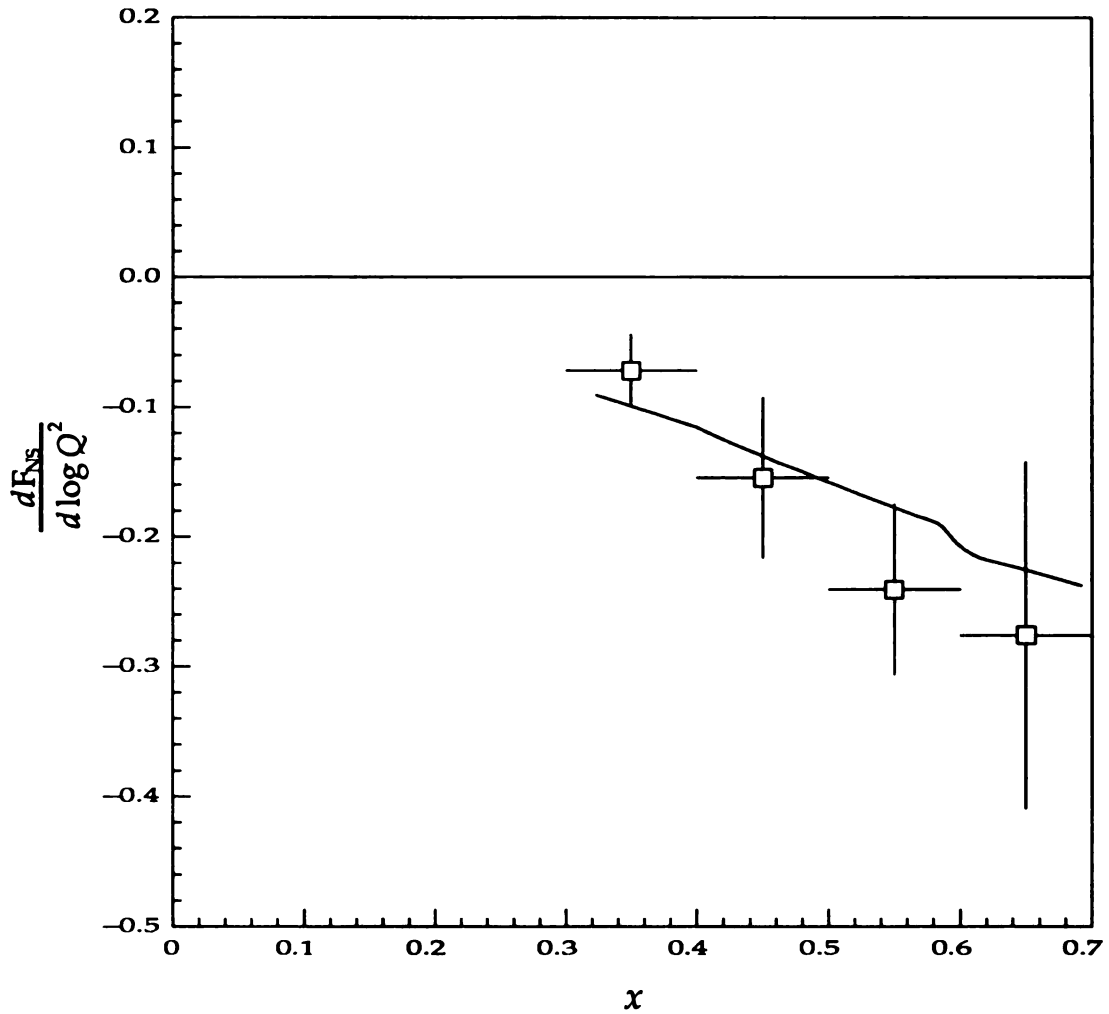

Figure 5.9. Result of Non-Singlet Fit using $F_{NS}=F_2$ for $0.3 < x < 0.7$. Plotted is the fit of $\frac{dF_{NS}}{d\log Q^2}$ from the FMMF structure functions vs x. The line shows the value of $\frac{dF_{NS}}{d\log Q^2}$ as determined from the fit using the Duke and Owens fitting program.

Appendix A

The FMMF Collaboration

Fermilab Experiments 594 and 733 are like most high energy physics experiments in that they involve large number of physicists in a collaboration that varies and evolves over time. The FMMF collaboration includes physicists from four institutions: Michigan State University, Fermi National Accelerator Laboratory, Massachusetts Institute of Technology and University of Florida. The University of Florida did not join the collaboration until 1984. Here we list the physicists involved in either E594 or E733.

The FMMF Collaboration

W. Cobau, M. Abolins, R. Brock, A. Cohen, J. Ernwein, E. Gallas,
R. Hatcher, D. Owen, G.J. Perkins, M. Tartaglia, J. Slate and H. Weerts
Michigan State University

D. Bogert, R. Burnstein, S. Fuess, G. Koizumi, J.G. Morfín and L. Stutte
Fermi National Accelerator Laboratory

J. Bofill, W. Busza, T. Eldridge, J.I. Friedman, M.C. Goodman,
H.W. Kendall, V. Kistiakowsky, T. Lyons, R. Magahiz, A. Mukherjee,
L.S. Osborne, R. Pitt, L. Rosenson, A. Sandacz, U. Schneekloth,
B. Strongin, F.E. Taylor, R. Verdier, J.S. Whitaker and G.P. Yeh
Massachusetts Institute of Technology

J.K. Walker, A. White and J. Womersley
University of Florida

Appendix B

Hadron Calibration

B.1 Introduction

Hadron calorimetry is extremely important in neutrino experiments. For charged current events, it provides one of the three standard measurables, the energy transfer, ν, (with the outgoing lepton energy and angle being the other two) and for neutral current events, only the properties of the hadron shower are observable. Exposures to the Quad-Triplet (QTB) Wide band beam required determination of ν over the wide energy range from 0–500 GeV. In addition, due to the long periods over which the QTB data was taken, stability over time (and over the detector) is essential.

For the QTB data, the analysis used the calorimetric information from both the flash chambers and the proportional planes. The results of the calorimetry using the flash chambers and proportional tubes were combined based on the experimentally measured resolutions.

The basic scheme for calorimetry using the flash chamber involves counting the number of hit cells. Corrections to the number of hit cells are made to account for variations in chamber response. The correct number of hit cells is then calibrated to determine a relationship between hits and ν.

Calorimetry with the proportional planes is similar in concept to that using the flash chambers. With the proportional planes, one sums the pulse height in the proportional planes and a calibration determines the relationship between pulse height and ν. Again, corrections to the pulse height are applied to account for variations in individual plane response.

In the cases of both the flash chambers and proportional planes, the final determination of ν involves many more details and complications than the simple sketchy outline provided above. The purpose of this appendix is to provide the reader with a detailed understanding of the process of defining the final calorimetry algorithms used in this analysis and the actual process of calibrating the large FMMF detector.

This appendix will discuss all aspects of the hadron calorimetry using the FMMF detector. The appendix is divided into 2 sections, the methods used to measure the hadron shower energy and scale determination. This appendix will focus on calorimetry in E733 although there will be some discussion of the algorithm used in E594.

This appendix is not for the faint of heart. The nitty gritty details of hadron calorimetry in the FMMF detector are discussed. It is hoped that this is a complete (and honest) discussion of the hadron calorimetry in E733.

B.2 Calorimetry

The FMMF target–calorimeter as discussed in Chapter 2 was constructed of two different types of detectors, flash chambers and proportional planes. Each of these detectors has its advantages and disadvantages. The flash chambers and proportional planes had very different characteristics and required very different methods for reconstructing the hadron energy. Any algorithm for reconstructing ν from the raw data must satisfy 2 requirements. The most important of these is that is possible to calibrate the algorithm and that the resolution of the algorithm be reasonable. It is essential to know the calibration to at least 5% and hopefully to better than 1%. A second requirement is that while the uncorrected response of the detector is non-uniform in position and over time, the algorithm's corrected response must be uniform temporally, spatially, and over the large range of energies available in the QTB. For example, an algorithm, for which the returned response to showers of a fixed energy fluctuated by ±20% (or even ±5%) over the duration of an exposure, is of limited value.

In this section, calorimetry using the flash chamber and proportional planes is discussed in detail with emphasis on how one obtains the uniformity of response and high energy calibration that is needed.

B.2.1 Flash Chamber

Because of the properties of flash chambers, there were many difficult problems in developing a hadron energy algorithm. This section will discuss the inherent problems in hadron calorimetry using flash chambers and the algorithms used in determining the energy deposited by a hadron shower in this thesis.

B.2.1.1 Properties of Flash Chambers

The most important aspects of the flash chambers for a hadron calorimetry algorithm are:

- The binary nature of the detector.
- The susceptibility of the detector to environmental effects.
- The extreme sensitivity to residual ionization.

The binary nature of the detector makes a hadron calorimetry algorithm difficult because the response is subject to saturation, which can be extreme at the highest energies. The susceptibility to environmental effects introduces time dependent effects which must be minimized. The sensitivity of the detector to residual ionization (from earlier events or cosmic rays) makes calibration problematic. These properties will be examined in detail below.

B.2.1.1.1 Saturation

The flash chamber is a binary detector. The term, binary detector, means that for a given cell, all that is known is whether a cell is on or off. A hit (or on) cell means that at least one ionizing particle traversed that particular cell. There is no additional information about how many particles actually traversed the cell. A hit could mean that the cell was traversed by a single minimum ionizing particle such as a muon or that it was traversed by a single highly ionizing particle such as a target nucleon fragment or that is

was traversed by several ionizing particles. Any type of detector can be subject to the effects of saturation, but a binary detector is extremely sensitive to saturation.

The standard method for hadron calorimetry is to simply add up the charge or light collected (possibly corrected for the variations in channel response) and the signal collected is proportional to the energy deposited in the detector. In a detector subject to saturation, one might envision that, in addition to correcting for the channel response, making saturation corrections that are dependent on the size of the signal. When doing hadron shower calorimetry with flash chambers, a large fraction of the hit cells in the core (or other part of the shower where there is dense energy deposition) of the shower are saturated. Correction for this saturation is the first challenge for a hadron calorimetry algorithm.

There are two tactics that one can use for correcting for saturation:

- A local method based on recognizing regions of saturation.
- A global method based on a non-linear calibration.

In a local method, one attempts to correct for saturation by recognizing, on a event by event basis, regions that are saturated and applying an appropriate correction to the response for that region. In a global method, one compensates for saturation effects by calibrating using a scale that takes into account shower saturation. One can also use a combination of the two methods (when the local corrections for saturation are not adequate.) Algorithms of both types have been developed for the flash chambers and are used in this thesis and will be discussed later in this appendix.

B.2.1.1.2 Detector and Environmental Effects

In a detector as large as the FMMF detector, it is inevitable that there will be variations in the response of flash chambers in different regions of the detector due to construction differences, electronic differences, gas composition variations and/or other factors. In addition, it is known from studies using cosmic ray muons that the response of the detector (to the muons) is subject to environmental effects such as humidity and

gas composition. These environmental effects can be rapid (on the time scale of a few hours or a day) when compared to the time span of an exposure (anywhere from 6 to 9 months) and are not necessarily uniform over the entire detector. These effects pose the second significant challenge to any calibration algorithm.

Since one can observe spatial and time dependent changes in the response of the detector using cosmic ray muons, one could envision using the response to cosmic ray muons to correct the detector response in a time and spatially dependent way. This has been done in one of the calorimetry algorithms using cosmic ray muons that were collected at the same time as the data.

While correcting the detector response using cosmic rays is appealing, there is no fundamental reason to believe that corrections based on isolated cosmic ray muons (which are minimum ionizing particles) will be the same as those for the many highly ionizing particles in the core of a hadron shower. For this reason, one might envision correcting the response of the detector to showers based on some observable shower property. The longitudinal transition profile of shower has been used to measure the response of parts of the detector in a time dependent way and these measured responses have then been used to correct the data.

Both the correction methods outlined above will be discussed below in the section on algorithms.

B.2.1.1.3 Residual Ionization

Residual ionization from closely spaced events is a major problem for calibration using the test beam. The problem occurs when two events closely spaced in time occur in the detector. Only one of the events need satisfy the trigger, but the second event leaves behind residual ionization that can cause additional hits that will add to the apparent energy deposited in the calorimeter. Because the second event does not need to satisfy the trigger, the trigger rate does not necessarily reflect this problem. In the neutrino beam, the problem of overlapping events is minimized because in the very rare case where two

neutrino interactions occur roughly simultaneously, the events will, in all probability, be spatially separated. In the test beam, overlapping events can cause major problems because the events, by their very nature, occur in only one region of the detector. High energy test beam events are the most problematic because high energy means large amounts of ionization. In addition, the higher energy beams had much higher rates of incident particles.

Spatially separated residual ionization is a relatively simple problem for the calorimetry algorithms. In the neutrino beam, one simply restricts the volume of the detector used for calorimetry based on the event topology. Both flash chamber calorimetry algorithms calculate the deposited energy in a limited volume. In the test beam, because the events overlap spatially, the problem is complicated and there are no simple solutions. This leads one to be cautious of all test beam results.

B.2.1.2 Flash Chamber Calorimetry Algorithms

There are two standard flash chamber calorimetry algorithms. Both of these algorithms are used in this analysis. The first of these algorithms is called SHOWER. This algorithm tries to correct for saturation on an event by event basis based on the shower topology and uses the response to cosmic ray muons to correct for the spatial and time dependent differences in detector response. This algorithm was written by S. Fuess for E594 (Fuess et al. 1982, Fuess et al. 1984). The scale for the E594 data was then refit by T. Mattison (1986) for each of the Narrow Band data settings. The E594 data was reanalyzed for this analysis, using the E733 muon finding and fitting package (appropriately modified) but the hadron scale information was retained and used as is, without the aid of the proportional planes. This algorithm is also used in various analyses in E733, but this analysis uses a new algorithm.

The second algorithm is based on simply correcting raw hits for response effects and then using a non-linear calibration. This algorithm is called EHFC. This routine is used for all the E733 data (1985 and 1987 exposures) and the result is then combined with the

proportional plane measurement.

Both these algorithms are described in detail below.

B.2.1.2.1 SHOWER

The SHOWER algorithm is based on the concept of correcting the shower for saturation and response effects by using the measured response of the flash chamber to cosmic ray muons and topological properties of the shower.

Figure B.1 shows the variations in response of the flash chambers to cosmic ray muons.

To make the corrections to showers, the response to muon is factored into two separate parts, efficiency and multiplicity. The quantity *EFFICIENCY* is defined as the probability that the flash chamber will have a hit within a small road centered around the point where a muon traversed the chamber (ideally the efficiency should be 1.0 but in reality efficiencies are in the range 0.5 to 0.9 with the average being between 0.65 and 0.75.) The second quantity *MULTIPLICITY* is defined as the average number of hits in the same small road when a muon traversed a chamber and caused at least one hit (ideally, the multiplicity should be 1.0 but multiplicities range from 1.1 to 2.2 with an average of about 1.4.) Multiplicity is due to electronics effects. The response, the average number of hits produced per minimum ionizing particle, is,

$$RESPONSE = EFFICIENCY \times MULTIPLICITY.$$

Tables of responses, efficiencies and multiplicities are made from the cosmic ray muons collected over the course of an exposure. The tables are divided into a master table and time dependent tables. There is one master table per exposure and it divides each chamber into ten cell bins. Thus each master table contains the average (over the exposure) response (or efficiency or multiplicity) for each of the ten cell bins in every chamber. The time dependent tables then break the exposure up into roughly day-long periods. The time dependent tables contain the corrections to the master table for each chamber. In the time dependent tables, the chambers are divided into four pieces, the

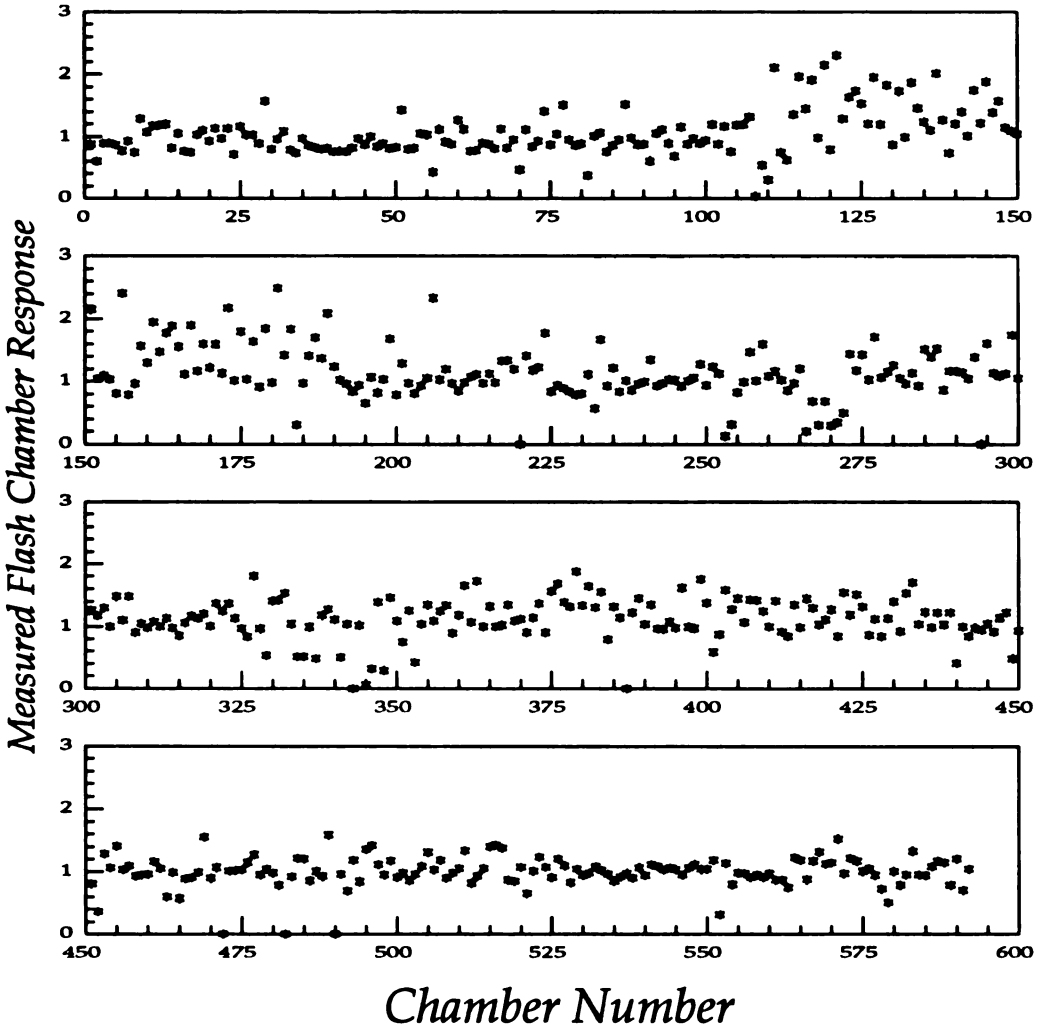

Figure B.1. Variation of Flash Chamber Response. The figure shows the variation in response of the flash chambers during one time period of the 1987 run. The response of the flash chambers was measured using cosmic ray muons. One defines response as,

$$RESPONSE = MULTIPLICITY \times EFFICIENCY.$$

Note that there are a number of dead chambers, i.e. those with $RESPONSE = 0.0$. Also note that response and the variation in response is dependent on the position in the detector. In particular, Chambers 1–108 show a lower average response and a smaller chamber to chamber variation in response.

outer two panels and the two halves of middle panel which are read out by the different amplifiers. This reflects the divisions of the chamber by gas supply and readout. The final time dependent value of the response, efficiency, or multiplicity is the product of the master table value for the ten cell bin and the correction factor for the appropriate section of the flash chamber.

SHOWER starts by binning all the hits in the event into the same ten cell bins discussed above for the master tables. The ten cell bins are first corrected for multiplicity in an attempt to eliminate electronic effects. A correction for efficiency and saturation is applied based on a probabilistic interpretation of the number of hits in the ten cell bin and measured efficiency. Both the multiplicity and efficiency corrections were originally derived by Stuart Fuess on a statistical basis and are highly non-linear. The multiplicity and efficiency corrections are shown in Figures B.2 and B.3.

After the corrections for multiplicity, efficiency and saturation, an additional correction is made for dead regions.

The corrected sparks are then summed in the shower region. The scale for the corrected hits was originally derived from test beam data taken in 1982 and then was adjusted by using the known E_ν vs radius relationship of the Di-Chromatic narrow band neutrino beam.

B.2.1.2.2 EHFC

For the QTB wide band beam, a second hadron calorimetry algorithm was invented. The algorithm corrected the data for non-uniformities in response of the detector using information derived from the neutrino beam. Corrections for saturation were made an intrinsic part of the calibration. The new algorithm is divided into two parts, the correction of the raw hits and the establishment of a calibration scale.

The correction of the raw hits is based on observed variations in the response of the detector. The response of the detector is measured using transition curves of neutrino showers selected to be in a narrow range of energies as measured by the proportional

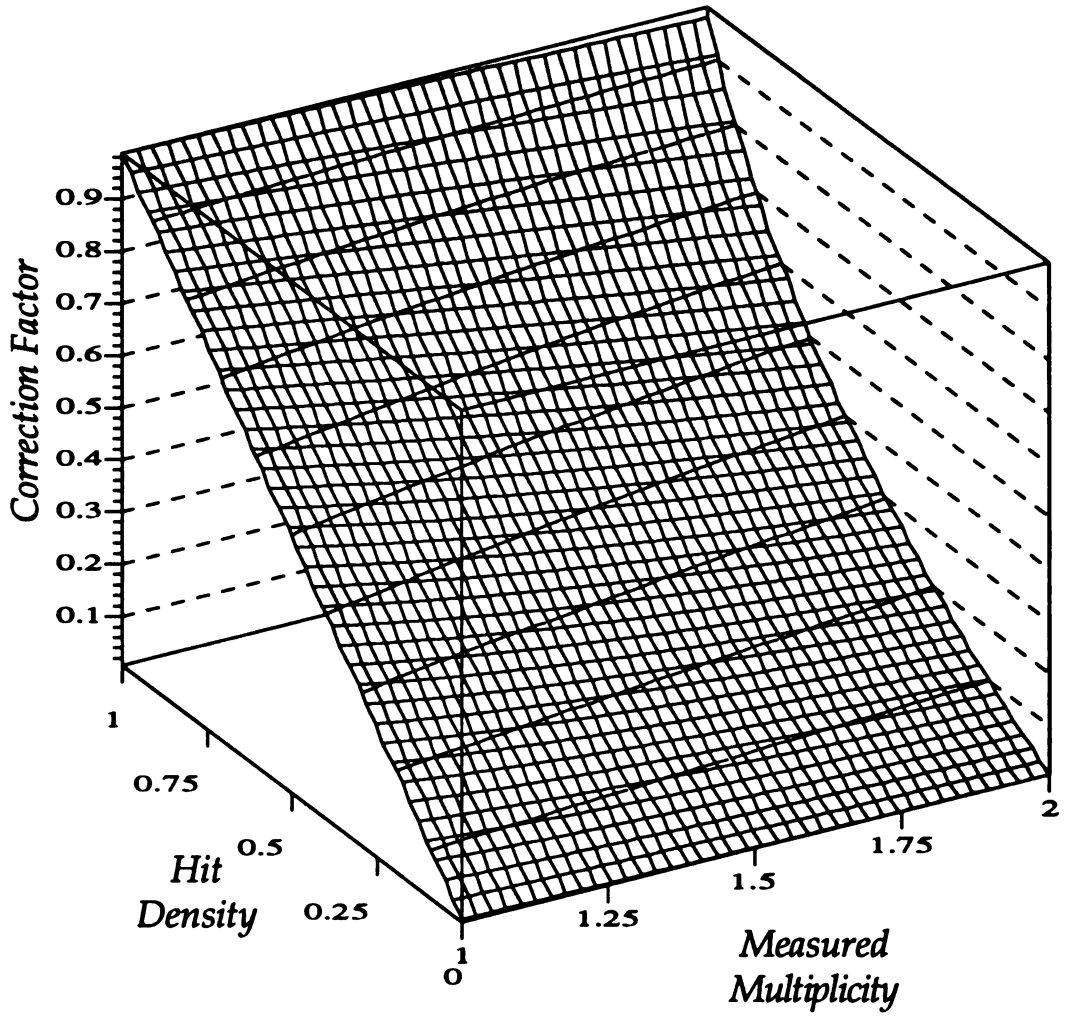

Figure B.2. Multiplicity Correction. The multiplicity correction applied by SHOWER as a function of multiplicity and the observed raw hit density. The number of multiplicity corrected hits is then calculated as the product of the multiplicity correction and the raw hits in the ten cell bin. The density of raw hits is defined as the raw hits divided by the total number of cells.

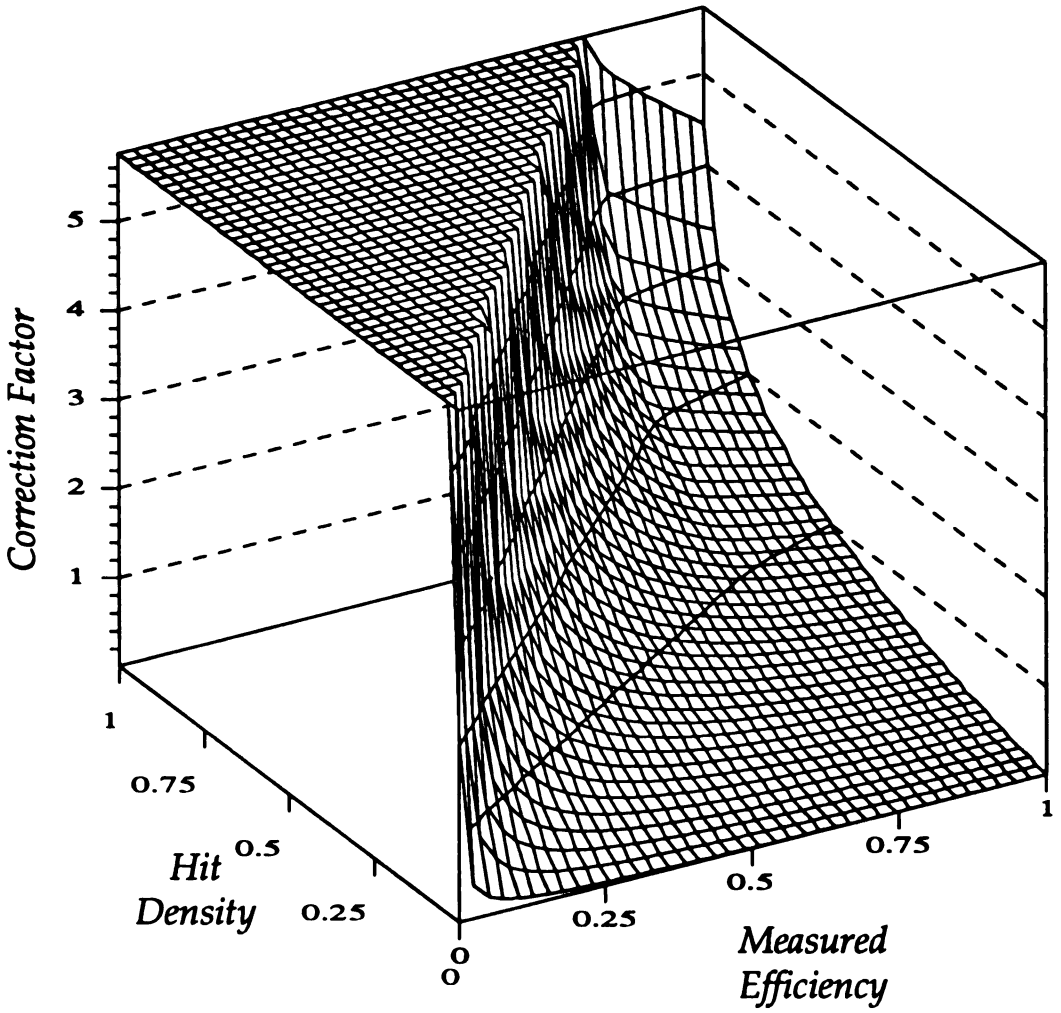

Figure B.3. Efficiency Correction. The figure shows the efficiency correction as a function of the bin efficiency and density of multiplicity corrected hits. The final number of corrected hits is the product of the efficiency correction and the number of multiplicity corrected hits.

planes. For this analysis, a transition curve describes the longitudinal development of a shower by measuring the energy deposited, $\frac{dE}{dz}$, as a function of z. The selection of the showers is not critical because the shower transition curves vary logarithmically with energy.

To calculate the response of a module, one constructs an average transition curve using many showers in a small energy range. For each of the showers, the vertex is found. The number of hits in the U, X or Y chambers of each module is determined. Then, based on the vertex position, one determines each module's position within the shower (see Figure B.4.) Based on where the shower starts (relative to a fixed module) and averaging over a large number of showers, one can measure the average transition curve for the selected showers using a single module. As an example, for all showers with a vertex in module 10, the average number of hits in module 13 gives the point in the transition curve three modules downstream of the vertex. Similarly, for showers having vertices in module 6, the average number of hits in module 13 gives the point seven modules downstream of the vertex. Using the events with vertices originating upstream of a given module, one can construct an average transition curve for each U, X, or Y module.

By comparing the transition curves measured by different modules, one can measure the relative difference in module response and then if one divides the data up into time bins, one can then determine the variation in response over time.

For the 1985 and 1987 data, showers between 40 and 60 GeV were selected using the proportional planes. The average transition curves for each U, X, or Y module were then obtained from those data. Examples of these transition curves are shown in Figure B.5. From these transition curves, the absolute variations in response was obtained. Once the absolute response for each module in each time period was determined, all the absolute responses were averaged and each module's relative response was determined. The relative module responses were used to correct the data and are shown in the figures that follow. Figure B.6 shows the variations in response over time for a three

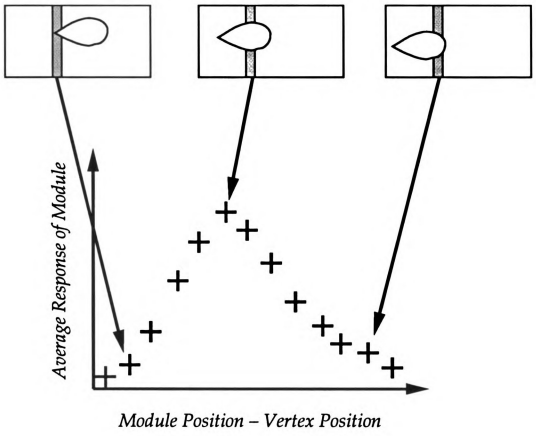

Figure B.4. Construction of Module Transition Curves. Shown is a schematic of how the module transition curves were constructed. One selects showers of similar energies throughout the detector. A fixed module, represented by the dark band above, samples different parts of the showers based on the position of the vertex as illustrated in the cartoons at the top of the figure. The position of the shower vertex determines which part of the shower is sampled for each event by the fixed module. Using many showers, one constructs an average transition curve measured by the fixed module. The arrows indicate which to part of the transition curves, each cartoon corresponds. The area under the curve measures the response of the module.

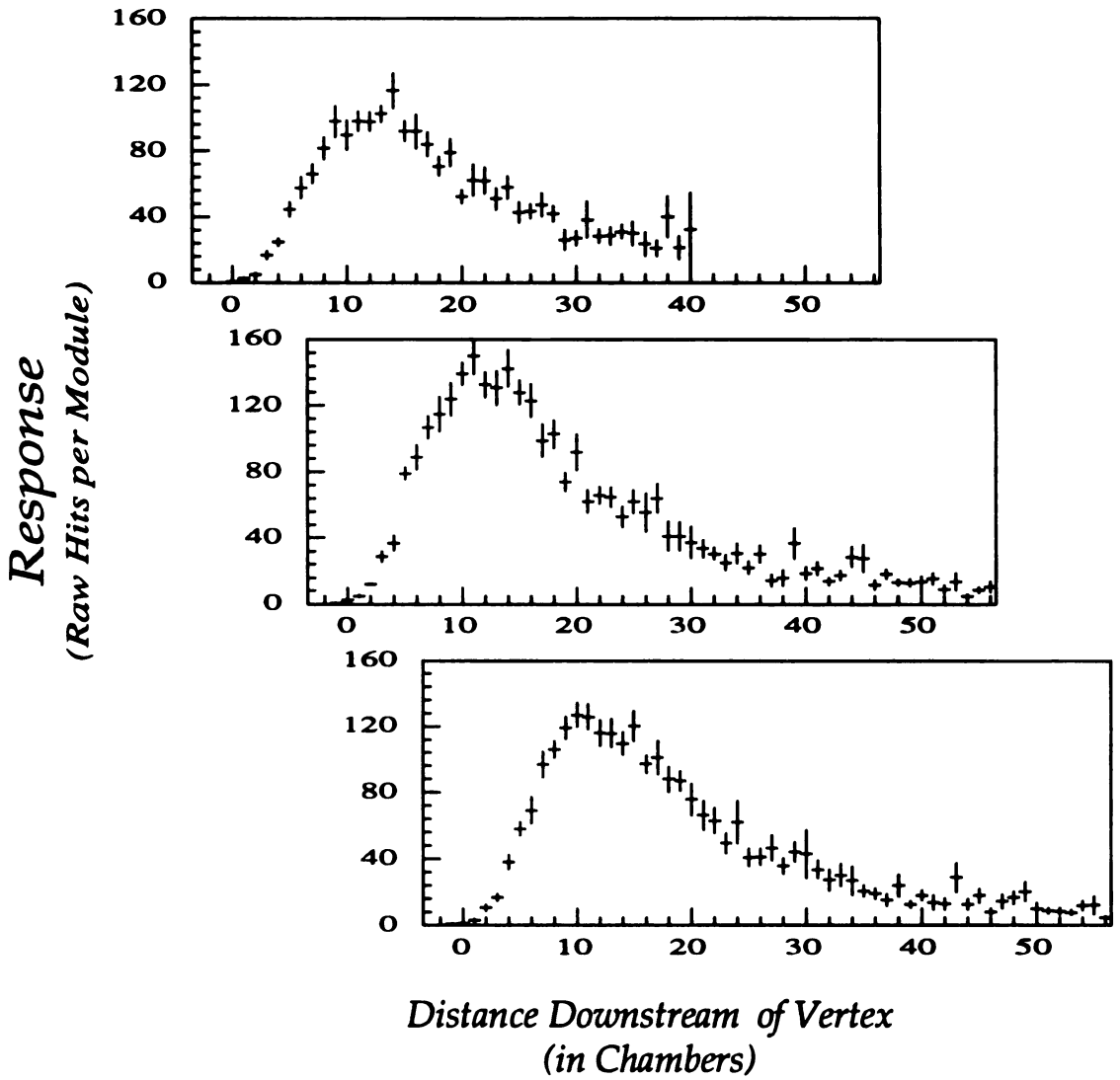

Figure B.5. Module Transition Curves. The figure shows some typical module transition curves for 3 different modules. Each module transition curve represents an average transition curve for 40–60 GeV showers as measured by a single module. One notes the difference in the responses of the modules shown.

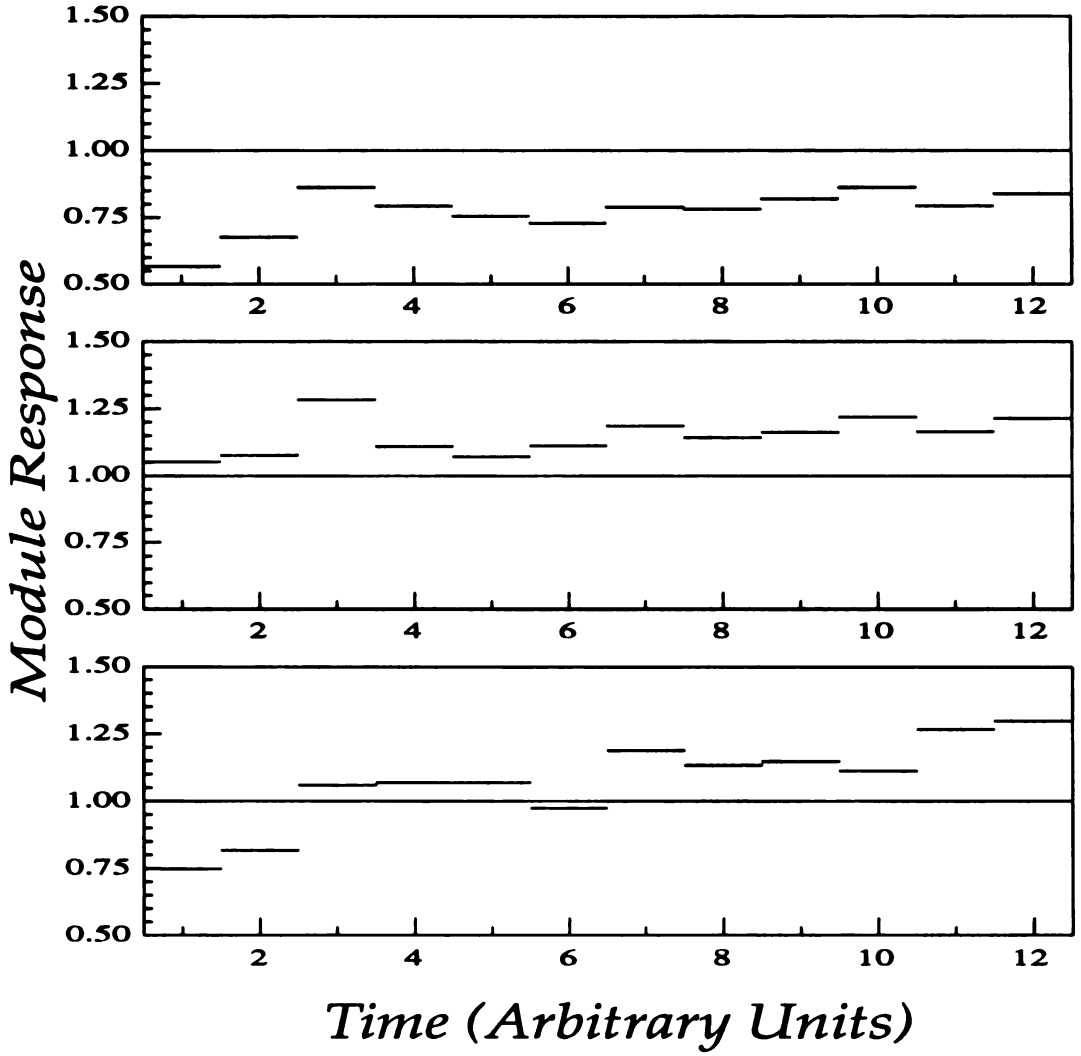

Figure B.6. Variations in Module Response as Measured by Transition Curves. The figure shows the variation in module response over time for typical modules as measured using the transition curves. The abscissa represents the duration of the 1987 nine month exposure in arbitrary units.

modules, as measured by using transition curves. As one can see, there are significant variations in the response of the shown modules over the course of an exposure. The variations in each module's response seem to follow the same pattern, starting low and then improving as the exposure progressed. The improvement in module response was due to the reduction in relative humidity in Lab C from the summer start of the 1987 exposure through the fall and into the winter. Figure B.7 shows the variation in module response over the detector. The measured response varied from 65 to 130% of the average response.

In the EHFC algorithm, one corrects the observed hits in each module based on the measured module responses. Figure B.8 shows the results of the corrections on 50 GeV test beam data. One uses the "corrected" hits in the shower region of the detector to measure the shower energy. A scale for the corrected hits was determined using the test beam and then adjusted using the neutrino data. The determination of the scale and the further adjustment using the neutrino data is discussed below.

B.2.2 Proportional Planes

The proportional planes system including electronics is explained in detail in other references (Tartaglia 1984 and Tartaglia et al. 1985) and was briefly described in Chapter 2. The most important aspects of the proportional plane system for the purposes of this thesis, are:

- They are analog devices.
- Gains were adjusted so that there would be no saturation in the energy range of the experiment.
- There were radioactive sources mounted on the planes to allow constant monitoring of the variations in gain of the individual channels.
- Environmental conditions were monitored continuously so as to correct for effects such as density variation of the gas mixture.
- Pedestals of the electronics noise were continuously monitored.

The properties of the proportional planes along with the continuous monitoring of conditions that could alter the response of the detector allows one to correct the data for

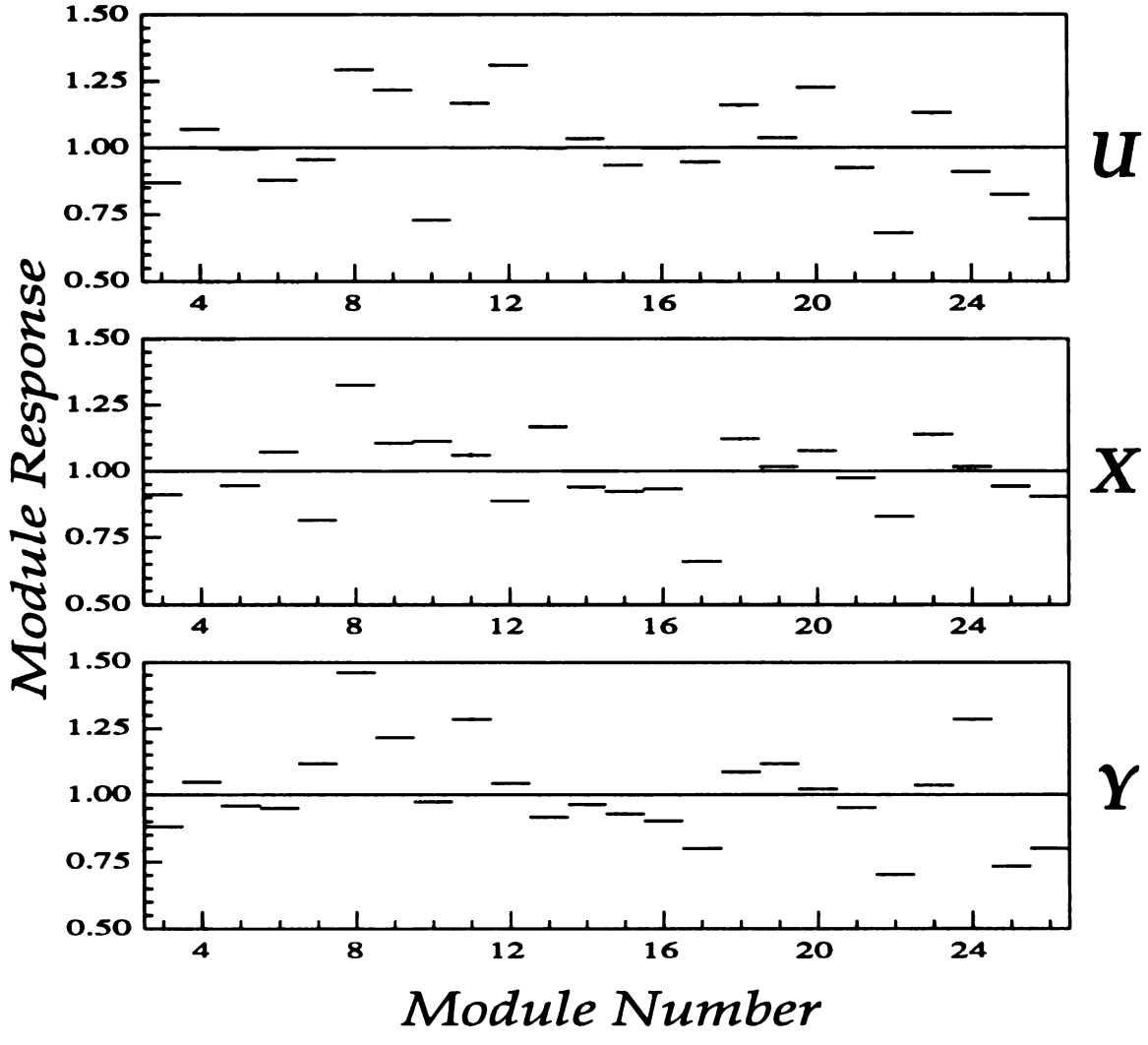

Figure B.7. Spatial Variations in Module Response. Shown is the variation in module response as a function of module number for each of the three flavors of flash chambers, U, X, and Y. Response was measured using the transition curve method. The data show are from one the 12 time slices used in the analysis of the 1987 data.

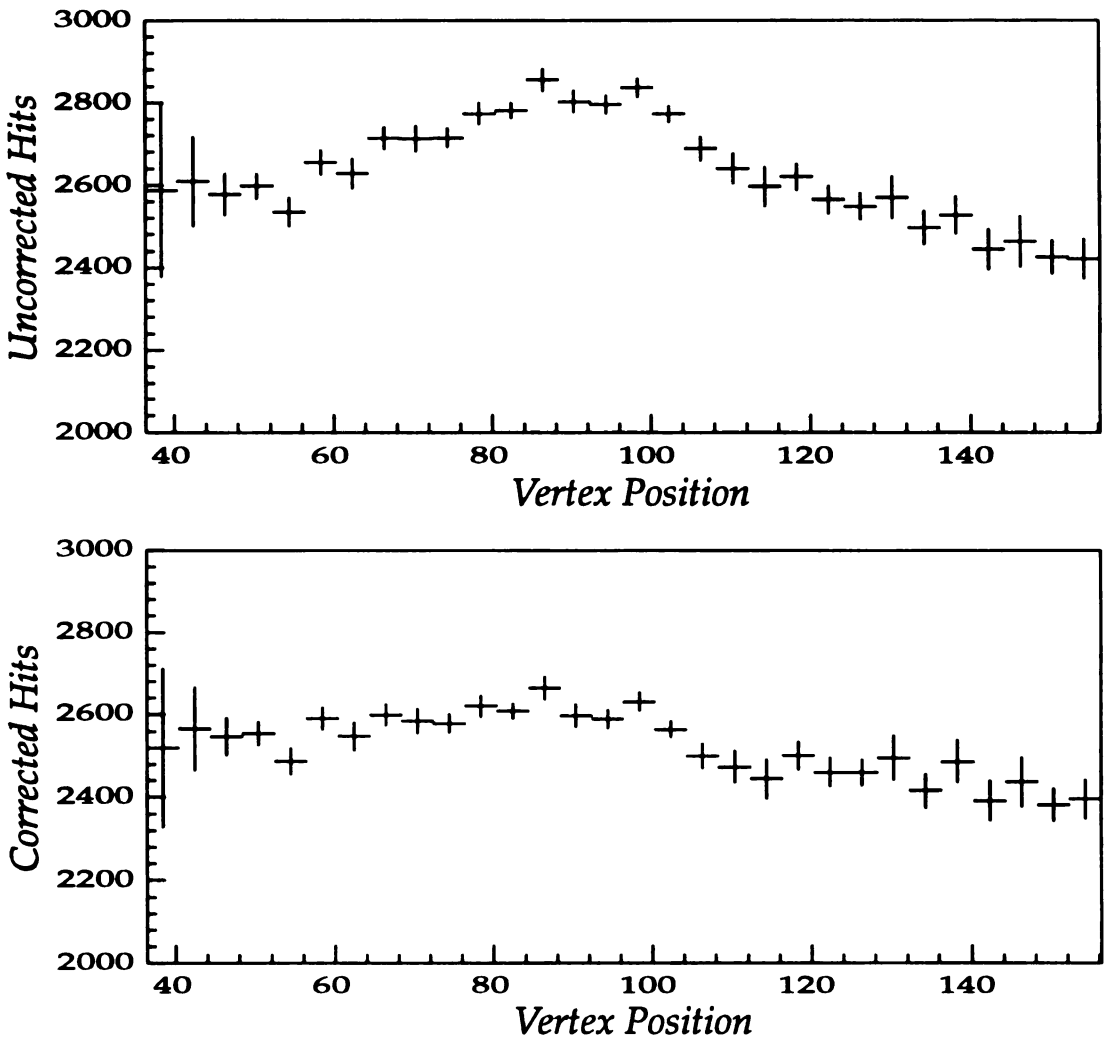

Figure B.8. Effects of Response Curve Corrections. The figures show the average number of hits versus vertex position (in flash chamber number) for 50 GeV test beam data. In the top plot, the average number of uncorrected hits is plotted versus vertex position. In the bottom plot, the average number of corrected hits is plotted versus vertex position. For the corrected hits, the hits in each module are corrected using the relative responses measured using the transition curves.

variations in the response. Let us examine how these corrections are made and how the final calorimetry algorithm for the proportional planes works in detail.

B.2.2.1 Monitoring

The first correction applied to the data from individual channels was pedestal subtraction. The pedestals were monitored by taking a random noise (pedestal) triggers at the start of every data tape (approximately every four hours). From the pedestal triggers, one calculated average noise for each channel which was subtracted from the pulse height for that channel.

The channel to channel variations in gain were monitored using the 22 KeV line of Cd-109. Special calibration triggers were taken between spills during normal neutrino data runs. Using the pedestal-subtracted pulse heights, the 22 KeV peak was found and the variation in the pulse height of the peaks was used to correct for the channel to channel variations in gains. The variation in gas gains over time can be compared to the change in gas density as calculated from the measured atmospheric pressure and gas temperature. It was found that the fractional variation in the gas gain was related to the fractional variation in the density by the relationship,

$$\frac{dM}{M} = -7.4\frac{d\rho}{\rho}$$

where M is the gain and ρ is the gas density (Tartaglia et. al 1985.)

In addition, the proportional planes were sensitive to variation in the composition of the gas mixture. The 90% Argon, 10% Methane (P-10) mixture was commercially supplied in large tankers. An exposure of 9 months in duration require 3 or more compressed gas tankers. The percentage of Methane varied slightly from tanker to tanker. Gas chromatography was used to analyze the composition of the gas and corrections were made to compensate for the variations in gas composition.

B.2.2.2 Calorimetry

Calorimetry using the proportional planes is straightforward. The corrected pulse height (i.e. pulse height with pedestal, gain and tanker corrections applied) for all channels of the planes in the shower volume are summed together and the summed corrected pulse height is then converted into a measure of the energy deposited by a scale determined using from an analysis of the hadron test beam data.

B.2.3 Corrections for Muon Energy Loss in Calorimeter

Muons, as they pass through matter, lose energy. This energy must be correctly accounted for to reconstruct the muon energy as we have seen in Chapter 2. In addition, in charged current events, one must correct for the energy deposited by the muon in the hadron shower. Two methods of making this correction are discussed in this section.

B.2.3.1 Explicit Elimination

Because of the extremely fine segmentation of the flash chambers, one might hope to eliminate the hits in the shower associated with the muon, and then use whichever calorimetry algorithm one likes best on the muon eliminated shower. The problem is determining which hits are associated only with the muon within the shower. For E594, muon elimination algorithms were used prior to the calorimetry algorithm. Details on the muon elimination algorithms can be found the theses of A. Mukherjee (1986) and T. Mattison (1986).

B.2.3.1 Statistical Subtraction

For the proportional planes, it is not possible to eliminate explicitly the energy left behind by the muon. This requires a "statistical" subtraction of the muon energy. The mean energy lost by the muon in the calorimeter is calculated using the Bethe-Bloch formula (Particle Data Group 1990) and then subtracted from the measured energy deposited in the calorimeter to give ν. This procedure was used for both the flash chamber and proportional plane measurements of ν in the QTB data.

B.3 Scale Determination

In principle, the scale determination is a straightforward exercise using hadron calibration data. One brings a mono-energetic hadron beam into the detector and then the response (in this context, response means the number of hits or summed pulse height due to the shower created by a incoming hadron) of the detector to the hadron beam determines the scale. In practice, it turns out, that for the desired precision and for some of the reasons mentioned above, one must do an additional adjustment to the scale using the neutrino data, which is described below.

In this section, we will discuss both of these determinations of the scales and their consistency.

B.3.1 Test Beam

During 1985 and 1987, the NH beamline was run almost constantly and provided test beams to the FMMF detector between neutrino pings, in the slow spill part of the Tevatron accelerator cycle. The NH (formerly NT) beamline transported a low intensity hadron beam to Lab C using a circuitous route. For many years, it was said, that the NH beamline was the longest and most optically complicated beam in the world. The beamline consisted of over 100 magnet elements and was over two miles in length. The beamline was capable of transporting hadron beams from 25 GeV to 400 GeV and was also capable of providing a muon beam. The momentum "bite" of the beam was approximately 2%.

The test beam trigger consisted of a scintillator telescope that required that particles satisfying the trigger pass through the last bending element and were therefore of the proper momentum. The signal from the scintillator telescope was delayed and combined with the standard PTH condition so that the timing of the PTH and test triggers were the same. The momentum of the test beam was determined using the recorded magnet current and the angle through which the beam was bent as defined by the scintillator

telescope.

B.3.1.1 Method

The test beam data were recorded on magnetic tape simultaneously with the neutrino data. Test beam data were then split off from the neutrino data and analyzed separately. Data with known problems (either detector or beam related) were rejected. The data was analyzed by first fitting and then eliminating the track from the incoming hadron. The vertex, muon finding and calorimeter energy reconstruction routines were then run on the event. Events were then required to pass a number of cuts to insure a clean sample. Some of the these requirements were:

- The fit of the incoming hadron track should agree with the known incident trajectory of the test beam.
- Incoming track must point back to last scintillator paddle.
- No muon may travel along the incident particle trajectory.
- Beam particle must interact between flash chambers 33 and 100.

After obtaining a clean sample, histograms were made of either the corrected raw hits or of the corrected pulse height. The means and width (root mean square, RMS) of the distributions were calculated. In addition, the distributions were fit to a Gaussian. The scale was then determined by fitting the relationship between the known beam energy and either corrected hits or corrected pulse height.

The flash chamber data is treated in the method outlined above but a separate scale for the corrected hits from each view was obtained. The final scale was a function of the hits in each view, where the obtained scale for each view was used and then the mean of the results from the three views was used as the EHFC result.

Once the scales were determined, they were used on the test beam data to test the consistency of the fits and to determine the resolutions of the different algorithms.

B.3.1.2 Results

The data used for scale determination were taken at five nominal energies, 25, 50, 70, 100 and 250 GeV. Three of the data sets (50, 100 and 250 GeV) are very large and were taken over extended periods of time. Histograms for the corrected raw hits (in each view) and the corrected pulse height for a single calibration point are shown in Figures B.9. As one can see, the distributions are very clean and nearly Gaussian with slight tails.

For the proportional planes, the mean corrected pulse height was fit to a straight line. Figure B.10 shows the results from each calibration point plotted versus beam energy along with a linear fit. The proportional planes show no signs of saturation.

For the flash chambers, the fit was more problematic due to the effects of saturation. Figure B.11 shows the results from each of the individual calibration points (for the three views) plotted versus energy. Even a cursory look at the data reveals the extreme effects of saturation. A quadratic (and even a cubic) was tried as the parameterization of the calibration data, but the fits were unsatisfactory. After trying a number of different functional forms, it was found empirically that the data was best described by a power law,

$$h_i = a_i + b_i E^c$$

h_i is the number of corrected hits in the i^{th} view, a_i and b_i differ between views but c is the same for all three views. The fit for the three different scales was done simultaneously. The calibrated results from each view are then combined in EHFC. A scale without a pedestal, (i.e. the values of a_i are forced to be zero) was also obtained. The result of the fit with a pedestal is shown in Figure B.11.

After the scales were determined, new distributions were made using the determined scales. The means and RMS's were calculated. Figure B.12 shows a set of these distributions using the determined scales. The test beam calibration procedure was found to be self-consistent.

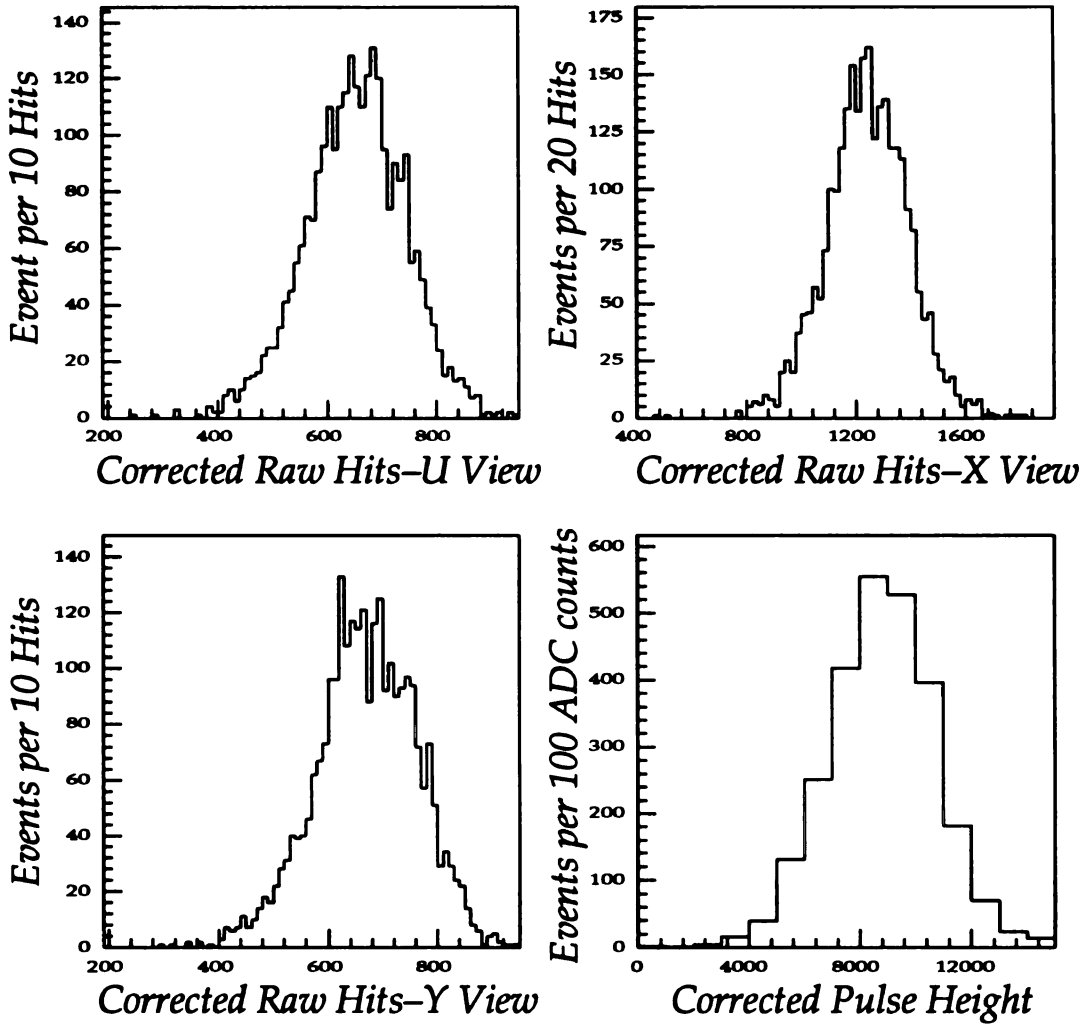

Figure B.9. Raw Test Beam Distributions. Shown are the response corrected raw hits and corrected pulse height distributions for the 50 GeV test beam setting. The bottom–right corner shows the pulse height distribution. The other three histograms show the correct raw hit distributions for U (top–left), X (top–right) and Y (bottom–left) views. Note that the X view has twice as many flash chambers as the U and Y views.

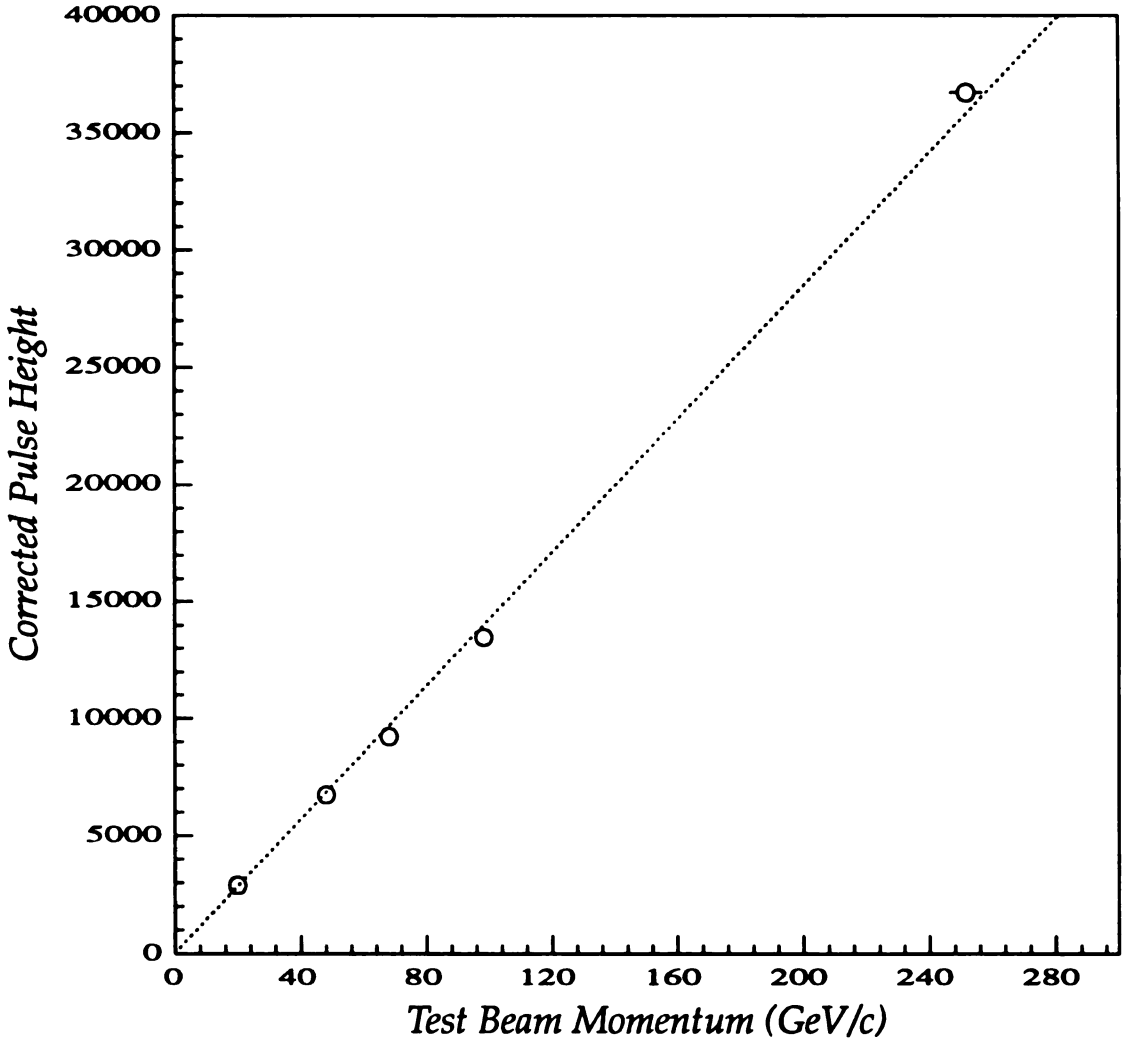

Figure B.10. Corrected Pulse Height vs. Test Beam Momentum. The figure shows the relationship between mean corrected pulse height and the momentum of the incident test beam. The dotted line is the result of a linear fit to the data.

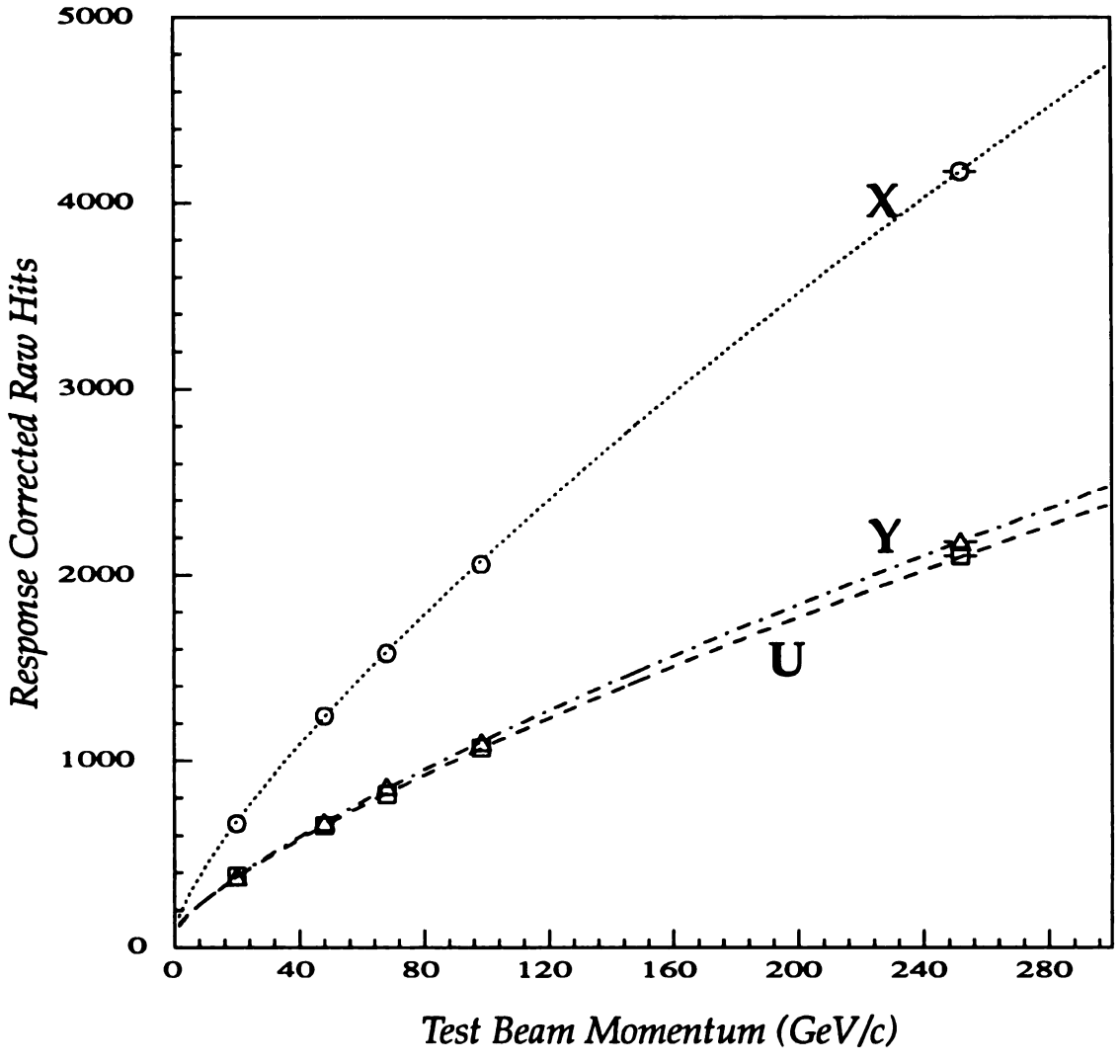

Figure B.11. Response Corrected Raw Hits vs. Test Beam Momentum. The figures shows the relationship between the mean corrected hits and the momentum of the incident test beam. The results for the three different flavors (U view–Squares; X view–Circles; Y view–Triangles) of the flash chambers are shown. The lines are the results of the fits discussed in the text.

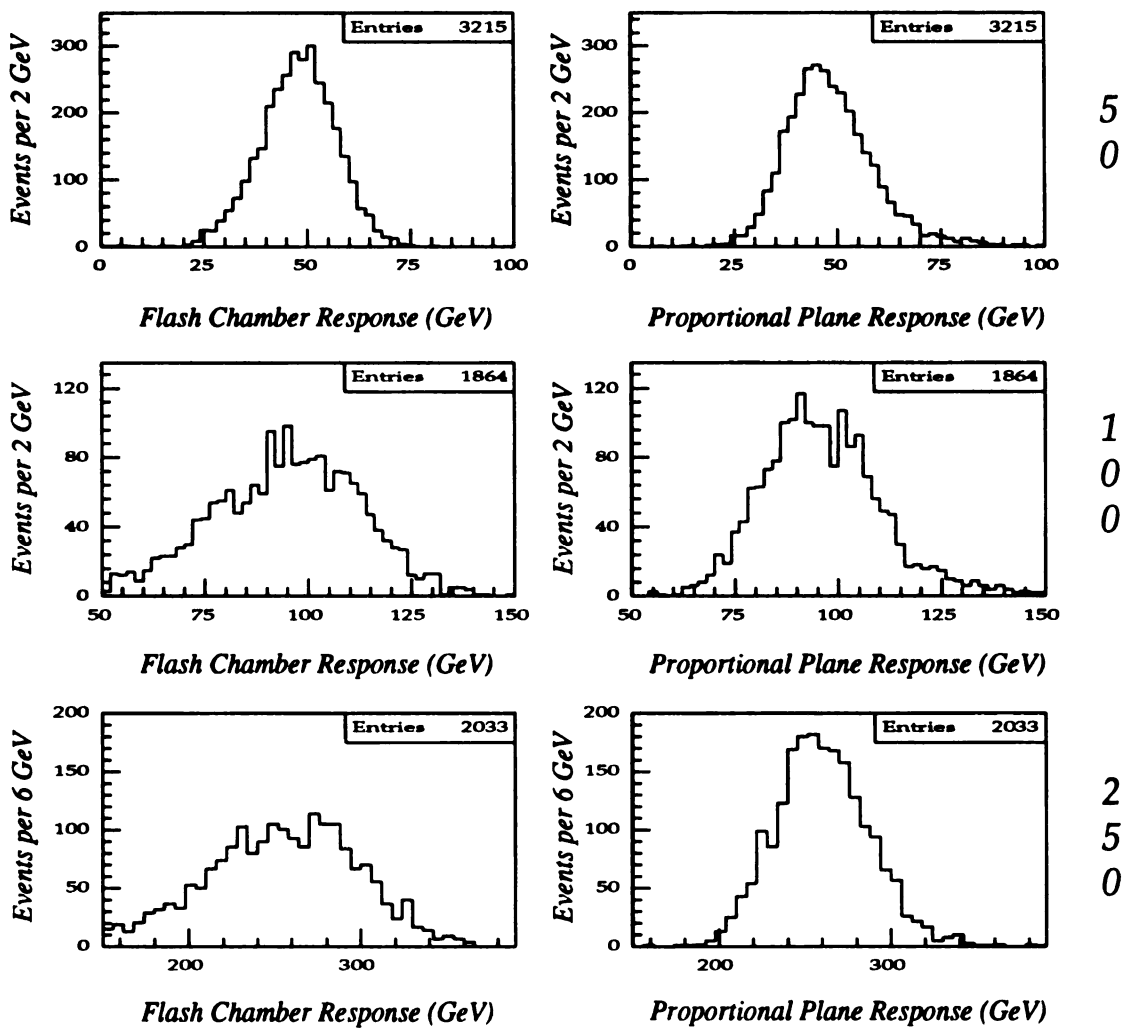

Figure B.12. Calibrated Test Beam Distributions. Shown are the calibrated distributions for both flash chambers and proportional planes for three test beam distributions. The left column shows the flash chamber results using the corrected raw hits algorithm. The right column shows the proportional plane results. The rows from top to bottom show the distributions for 50, 100, and 250 GeV incident test beams.

B.3.2 Neutrino Data

The scale determined using the test beam data was then applied to the neutrino data. It was immediately noticed that for EHFC, the test beam determined scale was inadequate, especially at high ν. In comparisons between 1987 neutrino data and Monte Carlo of the ν distribution (Figure B.13), the data were more sharply peaked then the Monte Carlo and at high ν, the number of events in the data was significantly below that predicted by the Monte Carlo.

There were also were significant problems in the y distribution, a quantity which is very sensitive to ν scale. The true y distribution for neutrino events is normally almost flat (there is a little $(1-y)^2$ behavior due to sea quarks) but the accepted y distribution shows the effects of both cuts and muon acceptance. At low y, events are rejected because accepted events are required to have $\nu > 10$ GeV. This requirement is trigger related and was discussed in Chapter 2. At high y, which corresponds to low muon energy, the effects of muon acceptance dominate. While this analysis has no explicit minimum E_μ requirement, it does require that a muon must traverse 550 cm in the calorimeter plus an additional 180 cm of iron in the spectrometer (resulting in a total mean energy loss to the muon of between 4 and 5 GeV) and, thus, there is an effective low E_μ cut. This effective low E_μ cut results in the lack of events at high y. Finally, the ratio of the E_μ and ν scales determines the mean of the accepted y distribution. If the ratio is not 1.0 as one expects and needs, the shape of the distribution will be skewed. The data/Monte Carlo comparison of the accepted y distributions using the EHFC scale is shown in Figure B.14. As one can see, the shape of the data distribution as compared to the Monte Carlo is significantly skewed.

This disagreement leads one to contemplate using the y distribution and the Monte Carlo to determine an adjustment to the hadron scale. This sort of adjustment is done using a complicated fitting algorithm using the Monte Carlo including the measured resolutions. Procedures of this type are standard in precision neutrino experiments

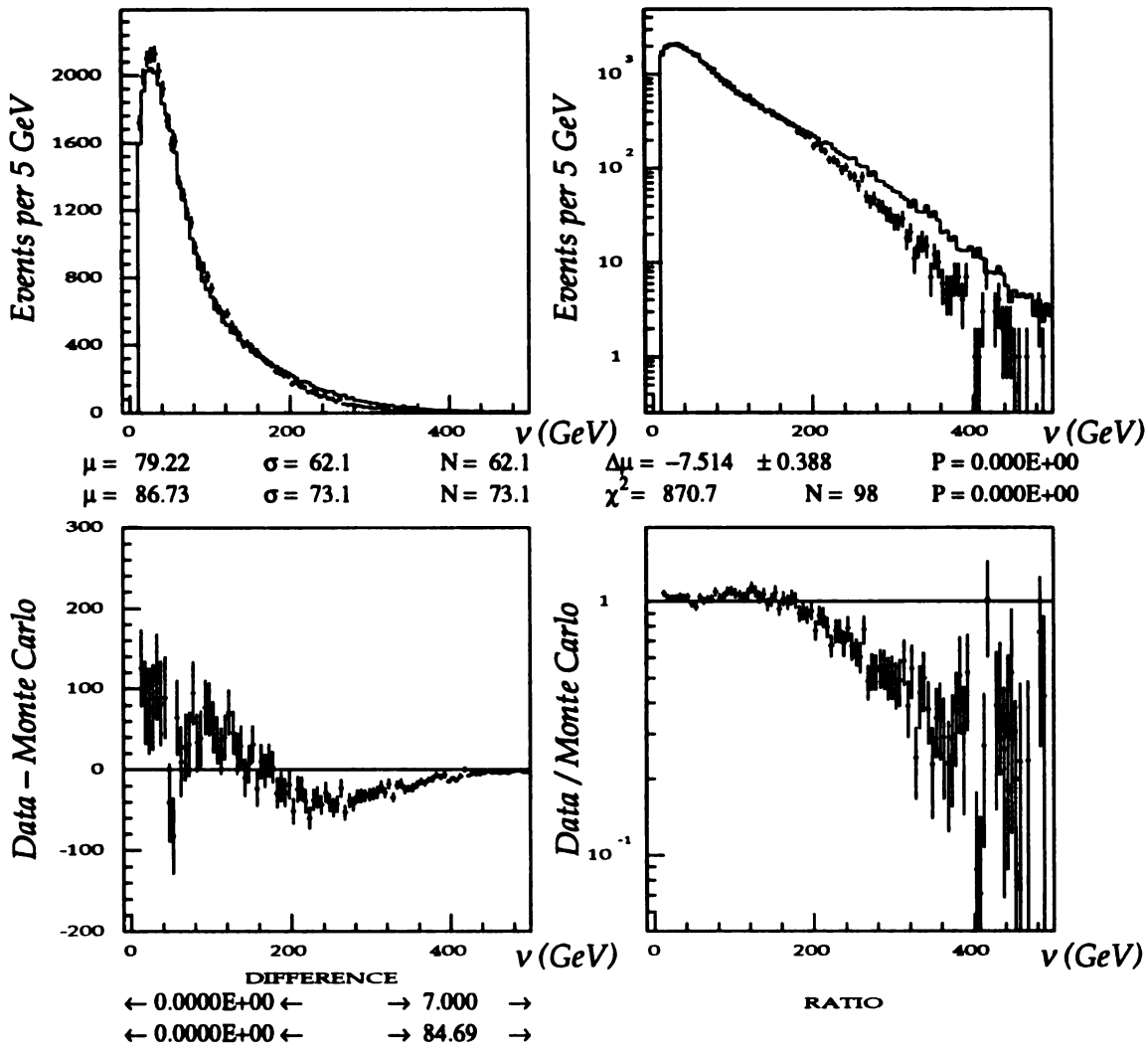

Figure B.13. Accepted ν Distribution–EHFC Scale. Shown is the comparison of the data and Monte Carlo ν distributions for the accepted neutrino events. ν is determined using the EHFC scale derived directly from the test beam data. The data is shown as the points with the error bars. Monte Carlo is shown as a solid outline. Upper–Left Corner shows Data and Monte Carlo distributions overlaid with a linear scale; Upper–Right Corner shows same overlay but with a logarithmic scale; Lower–Left Corner plots the quantity *DATA–MC*; Lower–Right Corner plots the ratio of the two distributions. The Monte Carlo is area normalized.

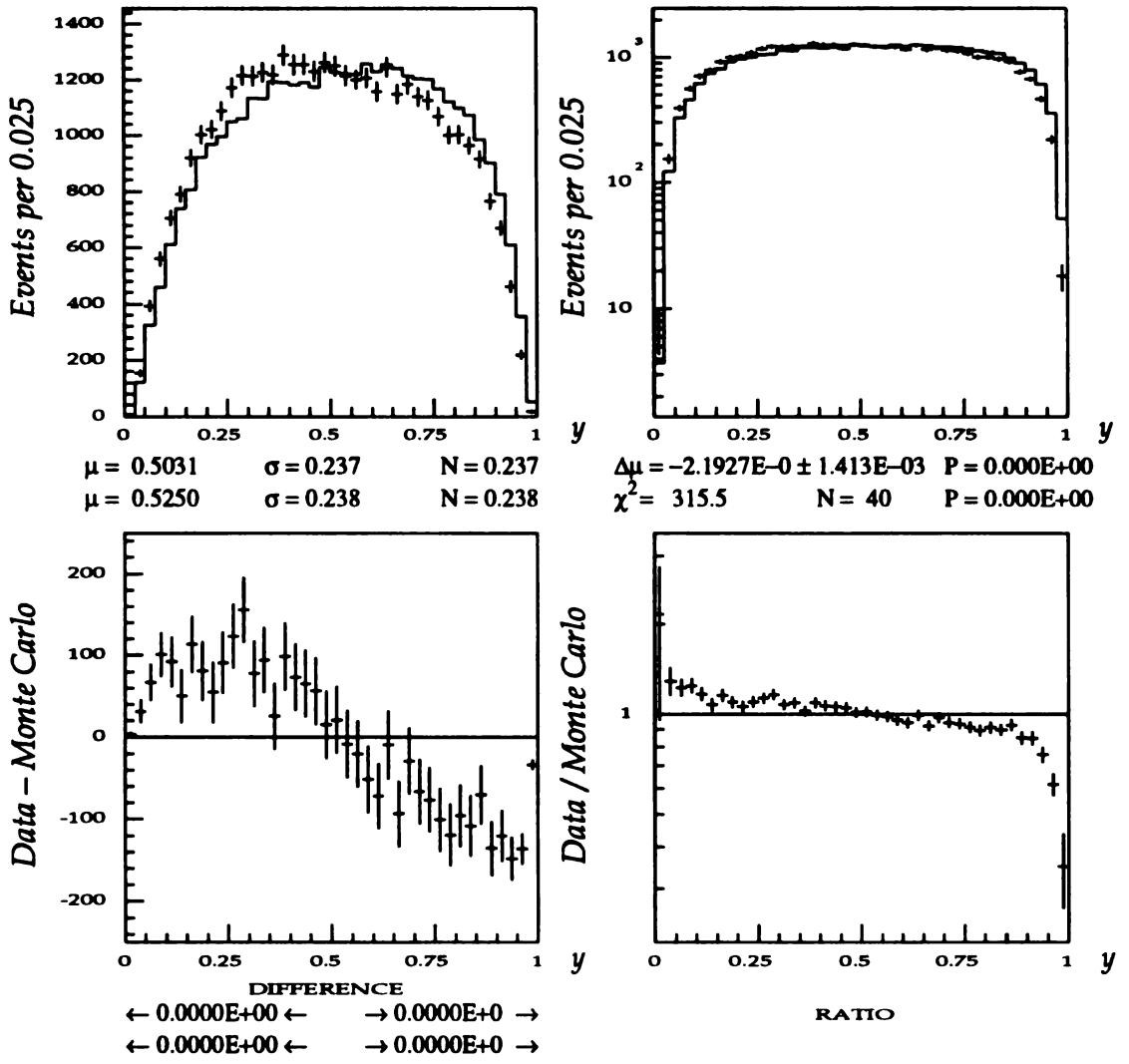

Figure B.14. Accepted y Distribution–EHFC Scale. Shown is the comparison of the data and Monte Carlo y distributions for the accepted neutrino events. ν is determined using the EHFC scale derived directly from the test beam data. The data is shown as the points with the error bars. Monte Carlo is shown as a solid outline. Upper–Left Corner shows Data and Monte Carlo distributions overlaid with a linear scale; Upper–Right Corner shows same overlay but with a logarithmic scale; Lower–Left Corner plots the quantity *DATA–MC*; Lower–Right Corner plots the ratio of the two distributions. The Monte Carlo is area normalized.

(see as an example, Oltman 1989.) In essence, a procedure of this type ties the hadron scale to the more precisely known muon energy scale. This procedure is explained in the following section and the results follow the discussion of the method.

B.3.2.1 Method

As has been shown before, there is a correlation between neutrino energy (E_ν) and radius (R) (See Figures 2.4 and 2.6). One can use this correlation and the known energy of the muon to determine the hadron scale. T. Mattison (1986) used a fit in the spirit of the one used in this analysis to determine the hadron scale along with the magnetic field of the 24' toroids for his analysis of E594.

The algorithm used for this analysis requires a Monte Carlo (preferably with a full simulation of the spectrometer, since the spectrometer sets the scale for ν in the analyzed data.) For all neutrino charged current events in both data and Monte Carlo data sets, on an event by event basis, one determines whether the neutrino was the product of the decay of a pion or a kaon. This is done by using a "separtrix". The separtrix divides the E_ν–R plane into pion and kaon halves. If a event falls in the pion half of the E_ν–R plane, it was assumed that the neutrino originated from the decay of a pion. Then the quantity,

$$\Delta = \left(\nu + E_\mu\right) - E_\nu(R)$$

was calculated, where E_μ is the reconstructed muon energy and $E_\nu(R)$ is the neutrino energy calculated from the E_ν vs. R relationship of the QTB beam and whether the interacting neutrino was the product of the decay of a pion or a kaon. The data were then binned in y and $\langle\Delta\rangle$ versus y was plotted separately for events of pion and kaon origin.

The fitting procedure adjusts the hadron scale in the data by minimizing the χ^2–like quantity,

$$\chi^2 = \sum_{\substack{y\,\text{bins} \\ \pi,K}} \frac{\left(\langle\Delta\rangle_{\text{data}} - \langle\Delta\rangle_{\text{MC}}\right)^2}{\sigma^2_{\text{data}} + \sigma^2_{\text{MC}}}.$$

In the data, ν is parameterized as,

$$\nu = a + b \cdot \nu_o + c \cdot \nu_o^2 - \delta$$

where ν_0 is the ν as originally determined from the test beam data and δ is the correction for the muon energy loss in the calorimeter and the average Δ was recalculated at each step. The minimization routine MINIUT (James and Roos 1989), was used to do the minimization. a, b and c were the free parameters in the fit.

B.3.2.2 Results

The results of the refitting of the EHFC scale are shown in Table B.1. The fitting program returns a scale that differs markedly from that found using the test beam data. The new scale has a significant pedestal, a 1% change in scale and a significant quadratic term. The quadratic term is positive indicating that the original EHFC scale may not have completely corrected for the effects of saturation.

Figures B.13 and B.14 showed the ν and y distributions for the 1987 data using the test beam derived EHFC scale. The scale derived from the test beam data seemed to be inadequate. After applying the results of refitting, the rescaled EHFC provides a much more satisfactory scale. Figure B.15 shows the integral ν distributions of data and Monte Carlo. The agreement is quite good between data and Monte Carlo. The extreme deficit at high ν is gone and the agreement at the peak is much more satisfactory. The y distribution shows the improvement in the scale even more dramatically. The y distribution comparison of data and Monte Carlo is shown in Figure B.16. There is now good agreement between data and Monte Carlo. For the original EHFC scale (shown in Figure B.14), the ratio plot (lower right-hand corner plot) was extremely skewed. For the new scale, the ratio plot is flat within errors.

All this is a bit puzzling. Why would the flash chamber scale as determined using the test data differ so dramatically from the scale determined using the neutrino beam? Clearly, the refitting makes the agreement between data and Monte Carlo improve greatly. The question that remains as to which scale is correct. The very nature of the algorithm used is to force the data's ν and y distributions to agree with those of the

Table B.1

Scale Refitting Results

Original Scale	Results of Refitting Procedure			
	Pedestal	Slope	Quadratic	χ^2
EHFC scale from Test Beam Calibration	+0.74	1.01	8.41×10^{-4}	172/97 DOF
1985 Proportional Plane Scale	–3.36	1.10	–	134/98 DOF
Prop Plane scale from Test Beam Calibration	+0.31	0.97	–	138/98 DOF

Table B.1. Scale Refitting Results. The table presents the results of the refitting of the v scales using the y fitting method described in the text. For the flash chamber EHFC scale the refit is to a quadratic. For the proportional planes, the refitting is linear only.

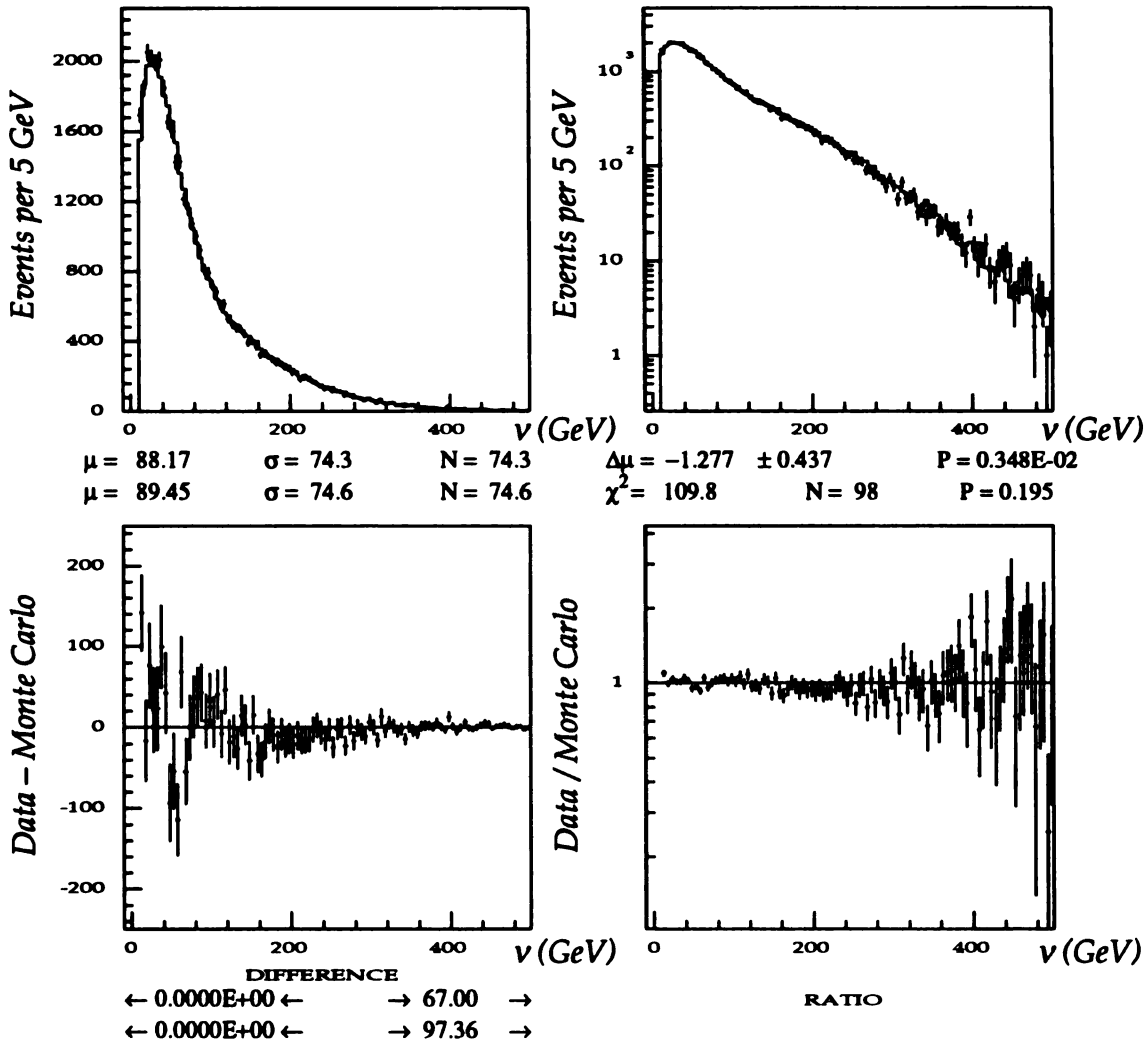

Figure B.15. Accepted ν Distribution–Rescaled EHFC Scale. The figure shows the comparison of the data and Monte Carlo ν distributions for the accepted neutrino events. ν is determined using the rescaled EHFC scale derived from refitting the test beam scale using the neutrino data as described in the text. The data is shown as the points with the error bars. Monte Carlo is shown as a solid outline. Upper–Left Corner shows Data and Monte Carlo distributions overlaid with a linear scale; Upper–Right Corner shows same distributions but with a logarithmic scale; Lower–Left Corner plots the quantity *DATA–MC*; Lower–Right Corner plots the ratio of the two distributions. The Monte Carlo is area normalized.

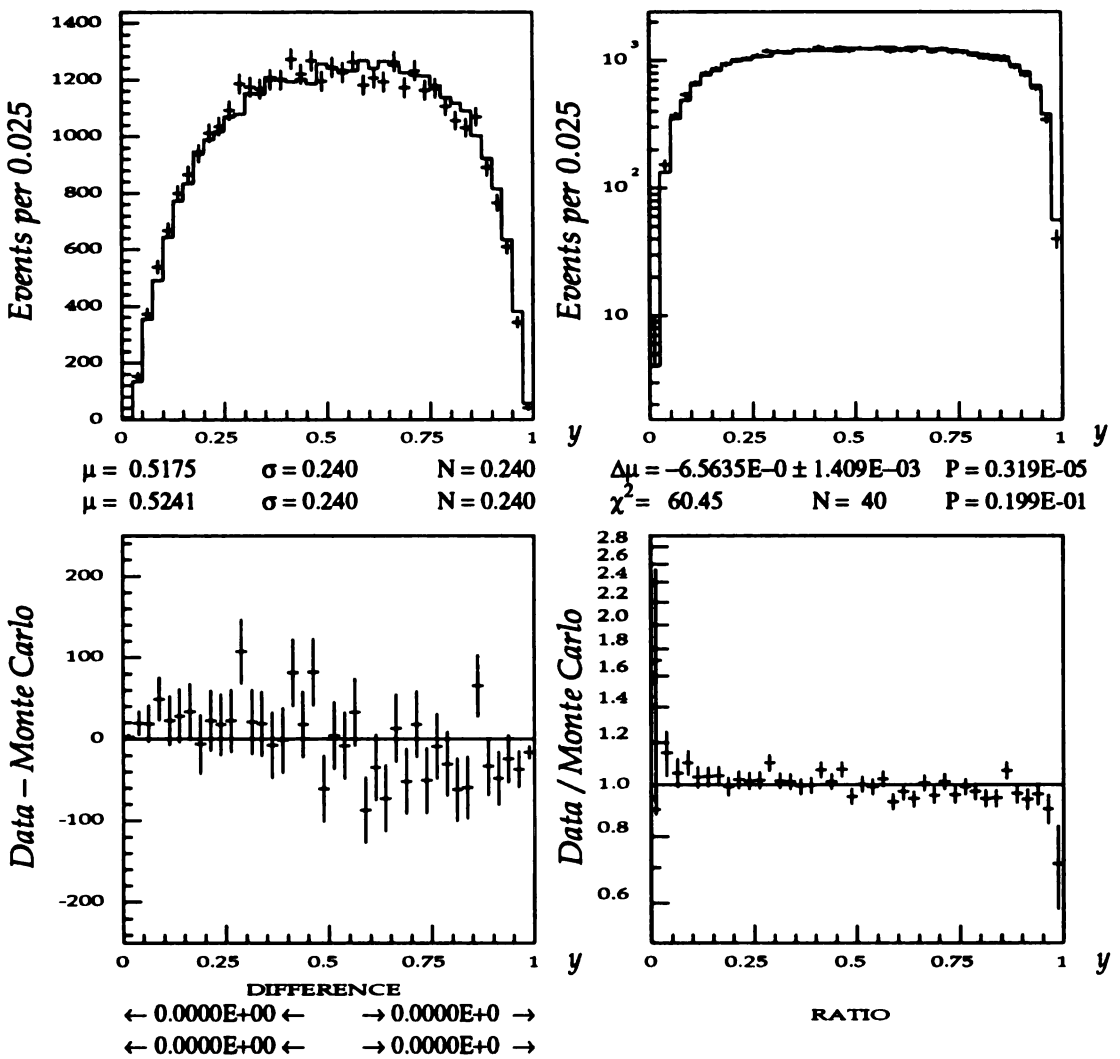

Figure B.16. Accepted y Distribution–Rescaled EHFC Scale. The figure shows the comparison of the data and Monte Carlo y distributions for the accepted neutrino events. y is determined using the rescaled EHFC scale derived from refitting the test beam scale using the neutrino data as described in the text. The data is shown as the points with the error bars. Monte Carlo is shown as a solid outline. Upper–Left Corner shows Data and Monte Carlo distributions overlaid with a linear scale; Upper–Right Corner shows same distributions but with a logarithmic scale; Lower–Left Corner plots the quantity *DATA–MC*; Lower–Right Corner plots the ratio of the two distributions. The Monte Carlo is area normalized.

Monte Carlo by modifying the ν scale. In the next section, we will examine the proportional plane results and the test beam data in order to try and resolve these inconsistences.

B.3.3 The Self Consistency of the Determined Scales

Now that we have ν scales that seem to give consistent results between the data and Monte Carlo, the inevitable question is whether either of the EHFC scales is to be believed? In this section, we will re-examine all the flash chamber data and compare the results with that obtained using the proportional planes. The re-examination of the EHFC data will include a re-analysis of the test beam data.

B.3.3.1 Proportional Plane Results

The calibration of the proportional planes using the test beam data was in many ways much more satisfying than that of the flash chambers As we have seen, there was a linear relationship between the corrected pulse height and the incident beam momentum. In addition, when applied to the neutrino data, the agreement between data and Monte Carlo was self-evident. Figures B.17 and B.18 show the ν and y distributions for the data using the EHPR scale obtained using the test beam data. In addition, Figures B.17 and B.18 show the Monte Carlo (with the proportional plane resolutions included) distributions overlaid. The agreement between data and Monte Carlo is more than satisfactory for both the ν and y distributions.

The excellent agreement between the data and Monte Carlo using the test beam proportional plane scale leads one to examine the effects of the scale fitting program on the EHPR scale. Figures B.19 and B.20 show the ν and y distributions using the rescaled EHPR resulting from the refit of the EHPR scale done in the same manner as the refitting of the EHFC scale. The data/Monte Carlo agreement using the rescaled EHPR is, if anything, slightly better than that of the original scale. This result gives one some confidence that at least the refitting for a new scale does converge on an appropriate scale.

As a further test, the 1985 proportional scale was used as input for the refitting

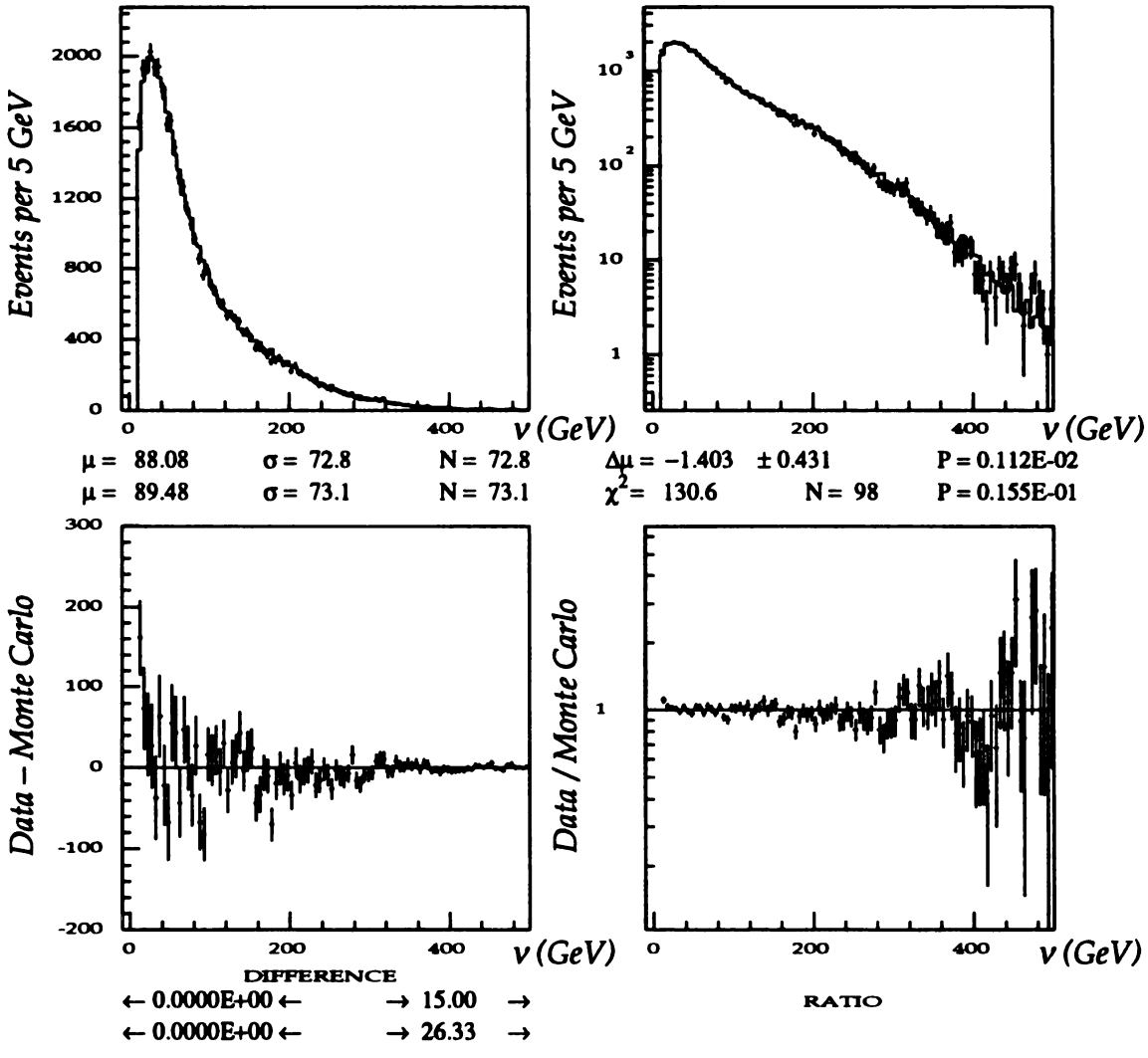

Figure B.17. Accepted ν Distribution–EHPR Scale. Shown is the comparison of the data and Monte Carlo ν distributions for the accepted neutrino events. ν is determined using the EHPR scale derived directly from the test beam data. The data is shown as the points with the error bars. Monte Carlo is shown as a solid outline. Upper–Left Corner shows Data and Monte Carlo distributions overlaid with a linear scale; Upper–Right Corner shows same overlay but with a logarithmic scale; Lower–Left Corner plots the quantity *DATA–MC*; Lower–Right Corner plots the ratio of the two distributions. The Monte Carlo is area normalized.

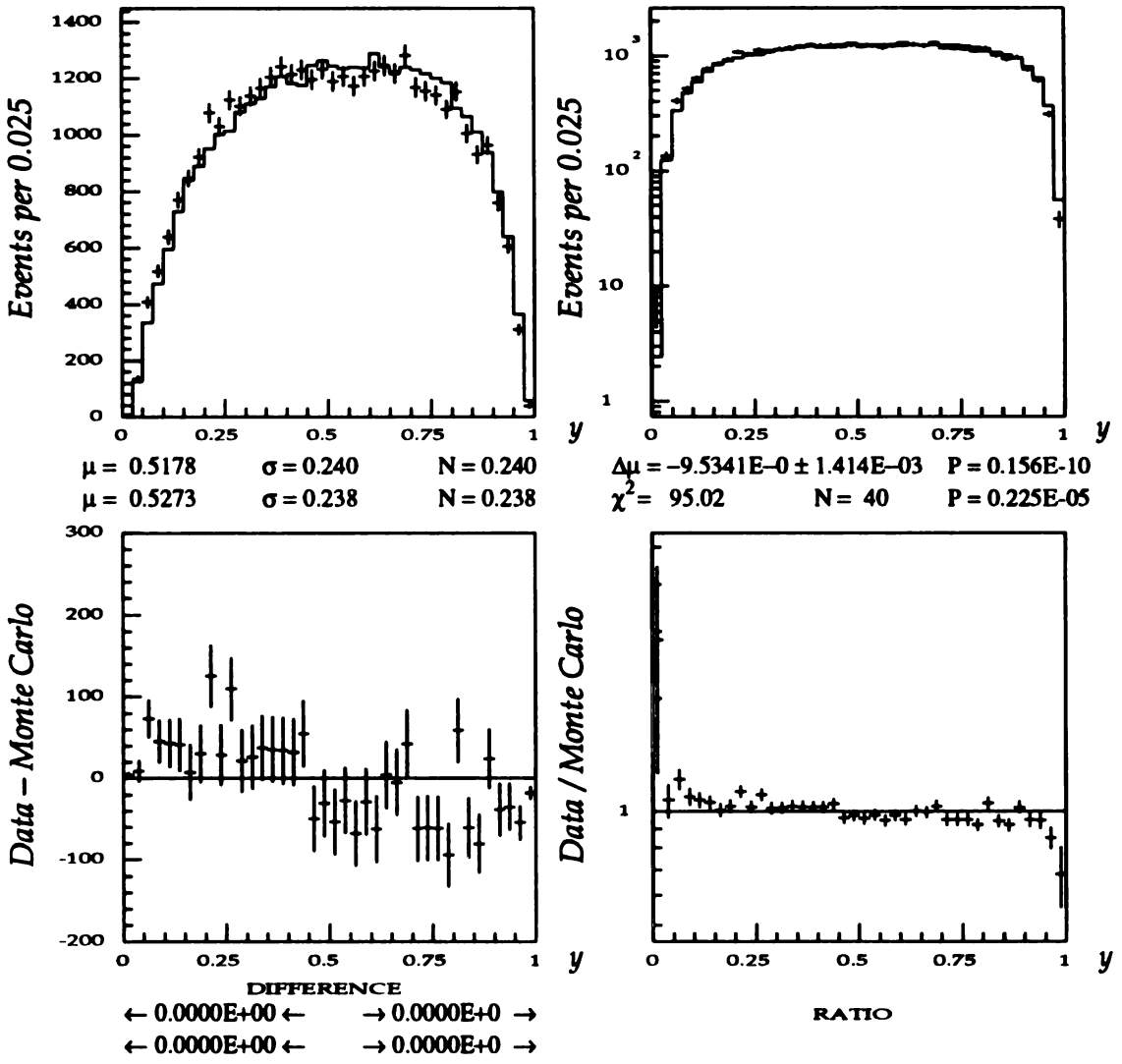

Figure B.18. Accepted y Distribution–EHPR Scale. Shown is the comparison of the data and Monte Carlo y distributions for the accepted neutrino events. ν is determined using the EHPR scale derived directly from the test beam data. The data is shown as the points with the error bars. Monte Carlo is shown as a solid outline. Upper–Left Corner shows Data and Monte Carlo distributions overlaid with a linear scale; Upper–Right Corner shows same overlay but with a logarithmic scale; Lower–Left Corner plots the quantity *DATA–MC*; Lower–Right Corner plots the ratio of the two distributions. The Monte Carlo is area normalized.

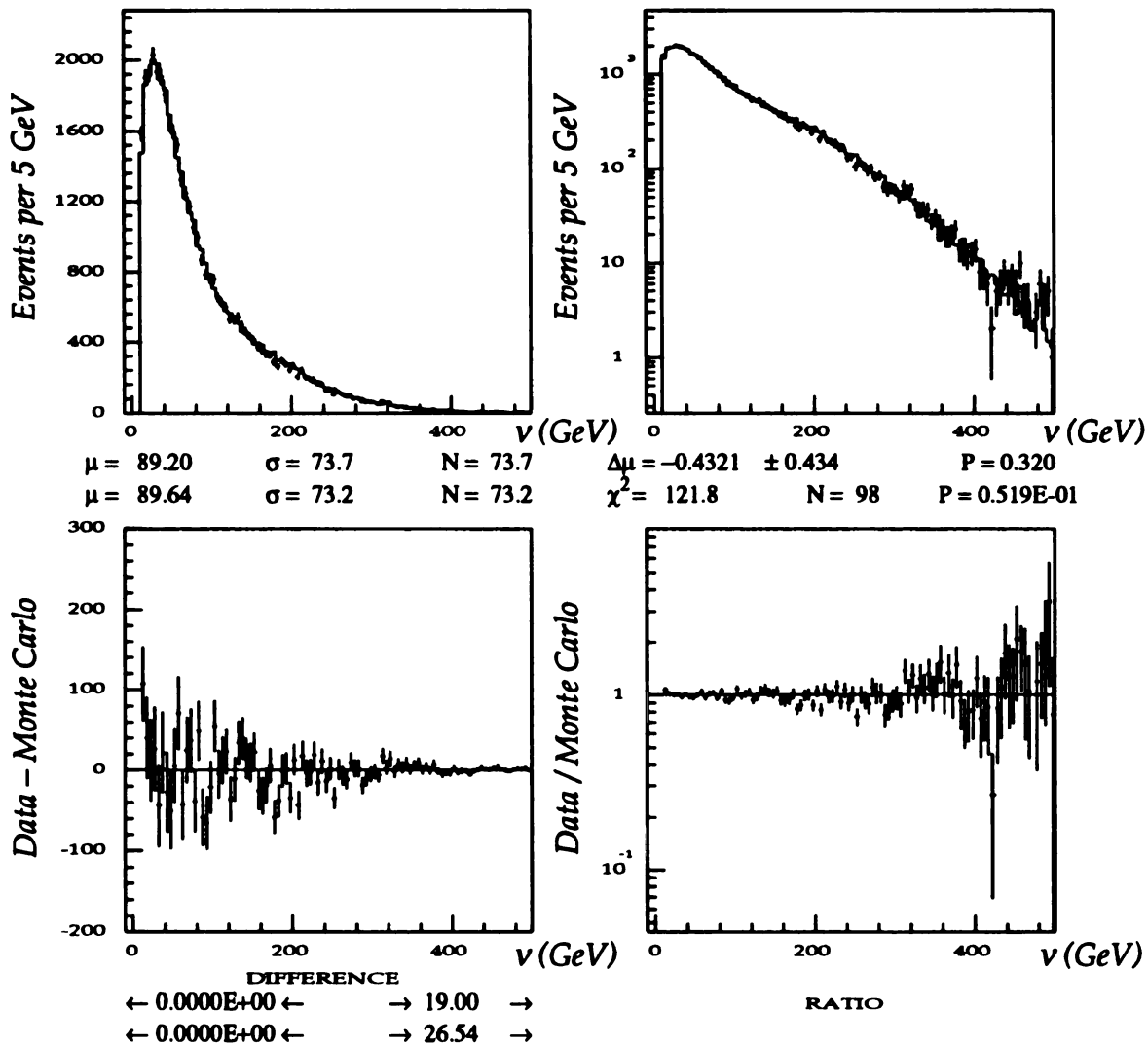

Figure B.19. Accepted ν Distribution–Rescaled EHPR Scale. The figure shows the comparison of the data and Monte Carlo ν distributions for the accepted neutrino events. ν is determined using the rescaled EHPR scale derived from refitting the test beam scale using the neutrino data as described in the text. The data is shown as the points with the error bars. Monte Carlo is shown as a solid outline. Upper–Left Corner shows Data and Monte Carlo distributions overlaid with a linear scale; Upper–Right Corner shows same distributions but with a logarithmic scale; Lower–Left Corner plots the quantity *DATA–MC*; Lower–Right Corner plots the ratio of the two distributions. The Monte Carlo is area normalized.

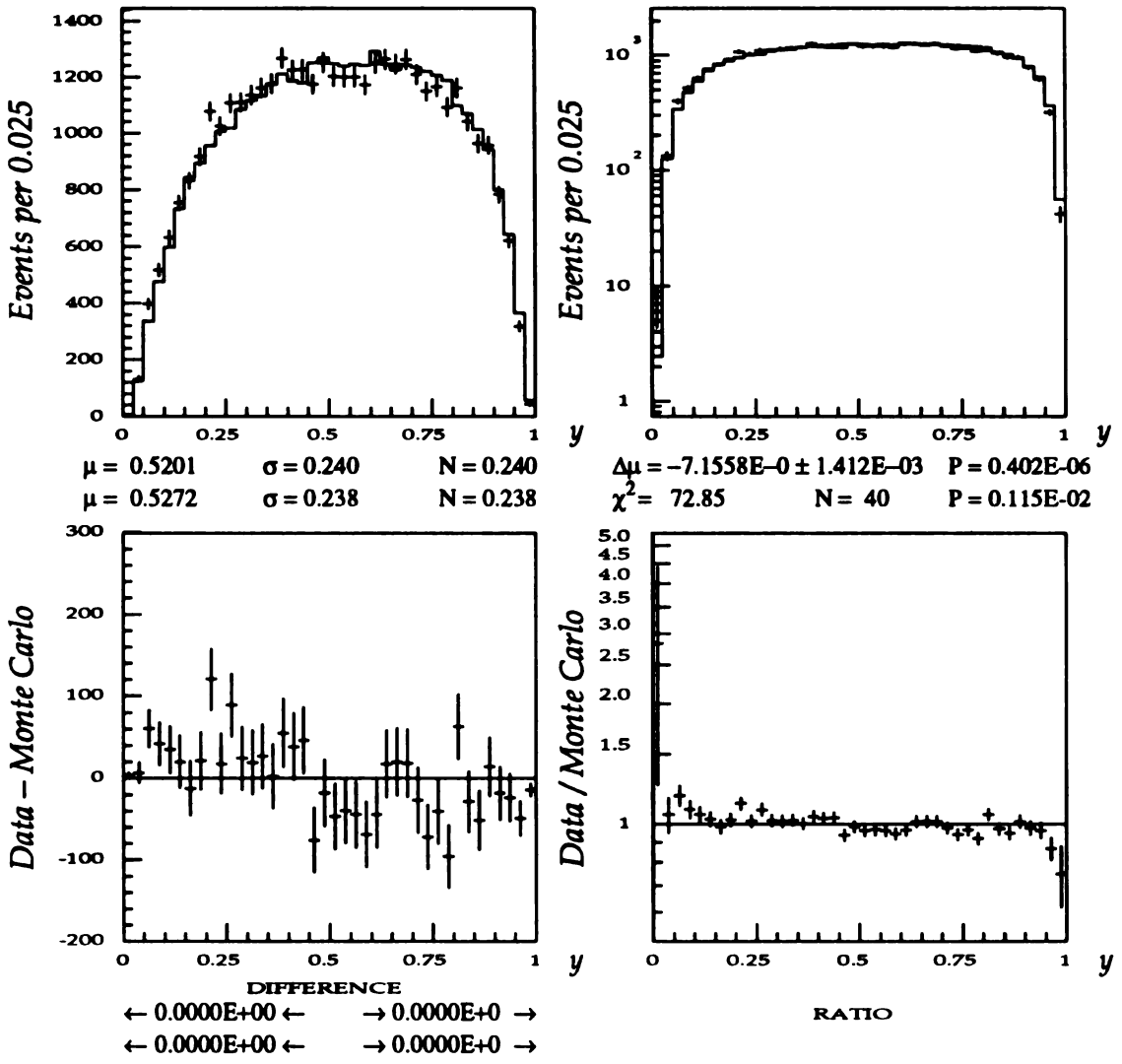

Figure B.20. Accepted y Distribution–Rescaled EHPR Scale. The figure shows the comparison of the data and Monte Carlo y distributions for accepted neutrino events. ν is determined using the rescaled EHPR scale derived from refitting the test beam scale using the neutrino data as described in the text. The data is shown as the points with the error bars. Monte Carlo is shown as a solid outline. Upper–Left Corner shows Data and Monte Carlo distributions overlaid with a linear scale; Upper–Right Corner shows same distributions but with a logarithmic scale; Lower–Left Corner plots the quantity *DATA–MC*; Lower–Right Corner plots the ratio of the two distributions. The Monte Carlo is area normalized.

program. Again, the v and y distributions for the data using the 1985 EHPR scale are shown in Figures B.21 and B.22 with the Monte Carlo overlaid. Using this scale, there is little agreement between data and Monte Carlo. The refitting of this scale results in a new scale which is used in Figures B.23 and B.24. Again, v and y distributions using the new scale for the data are compared with the Monte Carlo. There is again, good agreement between the data and Monte Carlo after the refitting.

An additional point lends additional confidence that the refitting procedure does result in the correct scale. The rescaling for the proportional planes was done as a linear function of the old scale. From the rescaling and the original scale's calibration of pulse height to energy, one can reconstruct the new pulse height scale calibration. These three different pulse height calibrations are the same within the estimated errors of the fits. Table B.1 contains the results for refitting of proportional plane scales in addition to those of the refitting EHFC. Table B.2 shows the final pulse height calibration for each of the three scales.

The proportional plane analysis leads one to draw two conclusions. The first conclusion is that, because the proportional plane scale from 1987 works so well, there does not seem to be any intrinsic problem with the test beam analysis. By this I do **not** mean that there is not a problem with the flash chamber data but that there is not some fundamental problem with the energy of the beam or the selection of events. The second conclusion is that, since, for the proportional planes, both the refitting of the scales and the test beam analysis return scales in good agreement, the refitting algorithm works and works well.

B.3.3.2 Re-Analysis of Test Beam Flash Chamber Results

The test beam was re-analyzed using the rescaled EHFC scale. The neutrino determined scale is completely inconsistent with the test beam data. In the extreme, the mean of the rescaled distribution for the nominal 250 GeV point is returned as being 309.7 GeV whereas the mean of the unrescaled distribution is 254.5 GeV. Obviously, the EHFC scales

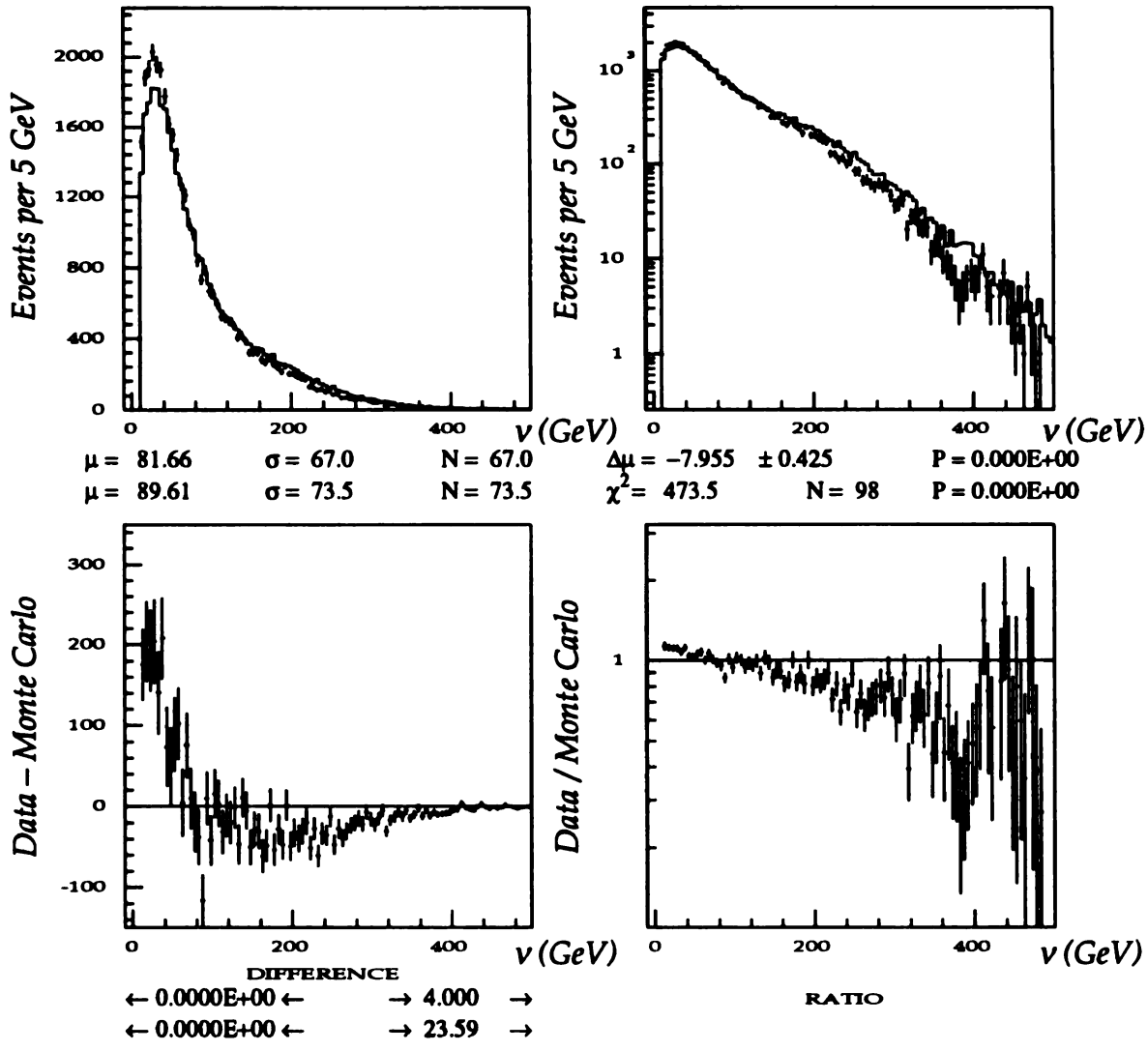

Figure B.21. Accepted ν Distribution–1985 EHPR Scale. Shown is the comparison of the data and Monte Carlo ν distributions for accepted neutrino events. ν is determined using the 1985 EHPR scale derived directly from the 1985 test beam data. The data is shown as the points with the error bars. Monte Carlo is shown as a solid outline. Upper–Left Corner shows Data and Monte Carlo distributions overlaid with a linear scale; Upper–Right Corner shows same overlay but with a logarithmic scale; Lower–Left Corner plots the quantity *DATA–MC*; Lower–Right Corner plots the ratio of the two distributions. The Monte Carlo is area normalized.

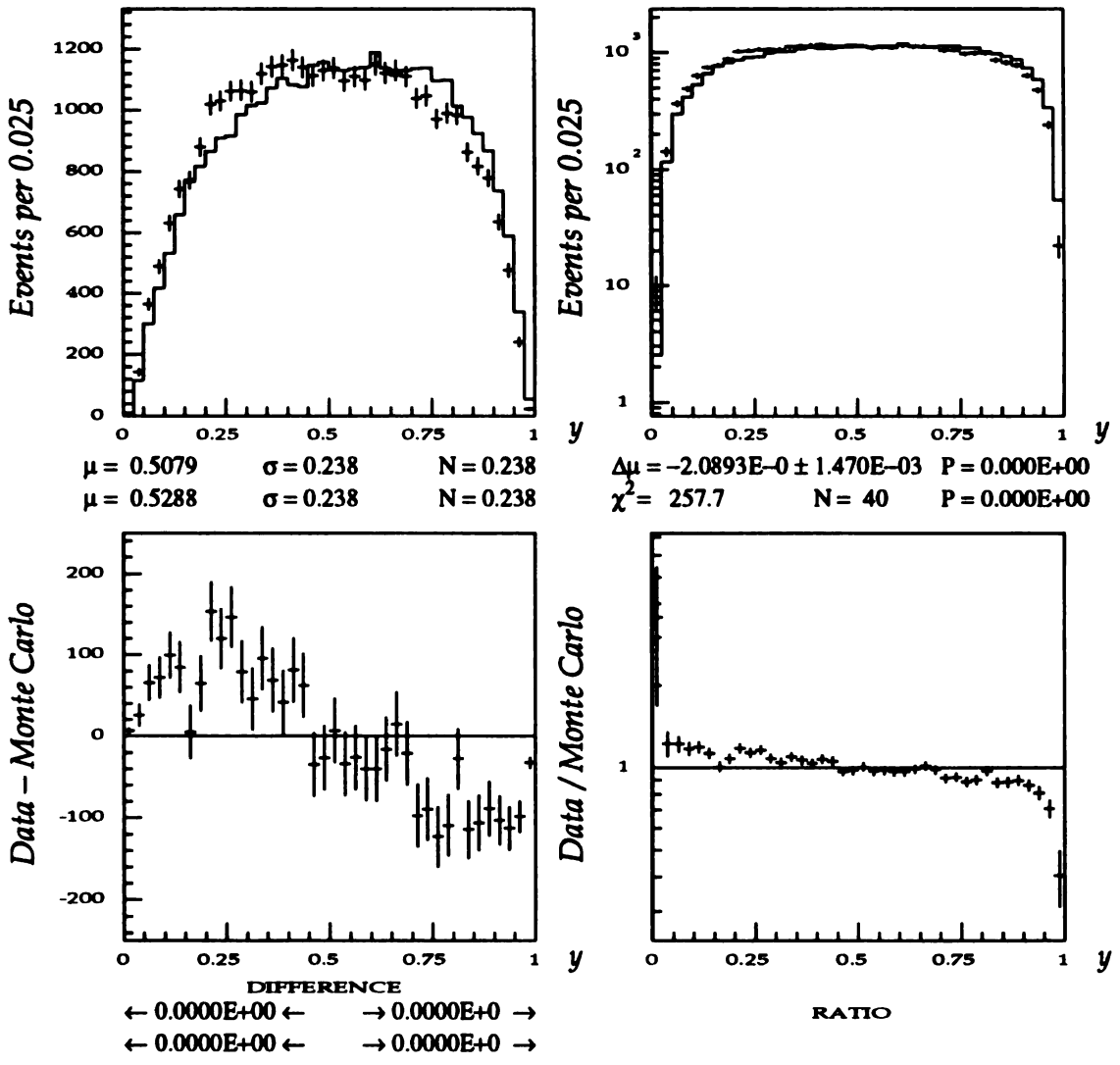

Figure B.22. Accepted y Distribution–1985 EHPR scale. Shown is the comparison of the data and Monte Carlo y distributions for accepted neutrino events. ν is determined using the 1985 EHPR scale derived directly from the 1985 test beam data. The data is shown as the points with the error bars. Monte Carlo is shown as a solid outline. Upper–Left Corner shows Data and Monte Carlo distributions overlaid with a linear scale; Upper–Right Corner shows same overlay but with a logarithmic scale; Lower–Left Corner plots the quantity *DATA–MC*; Lower–Right Corner plots the ratio of the two distributions. The Monte Carlo is area normalized.

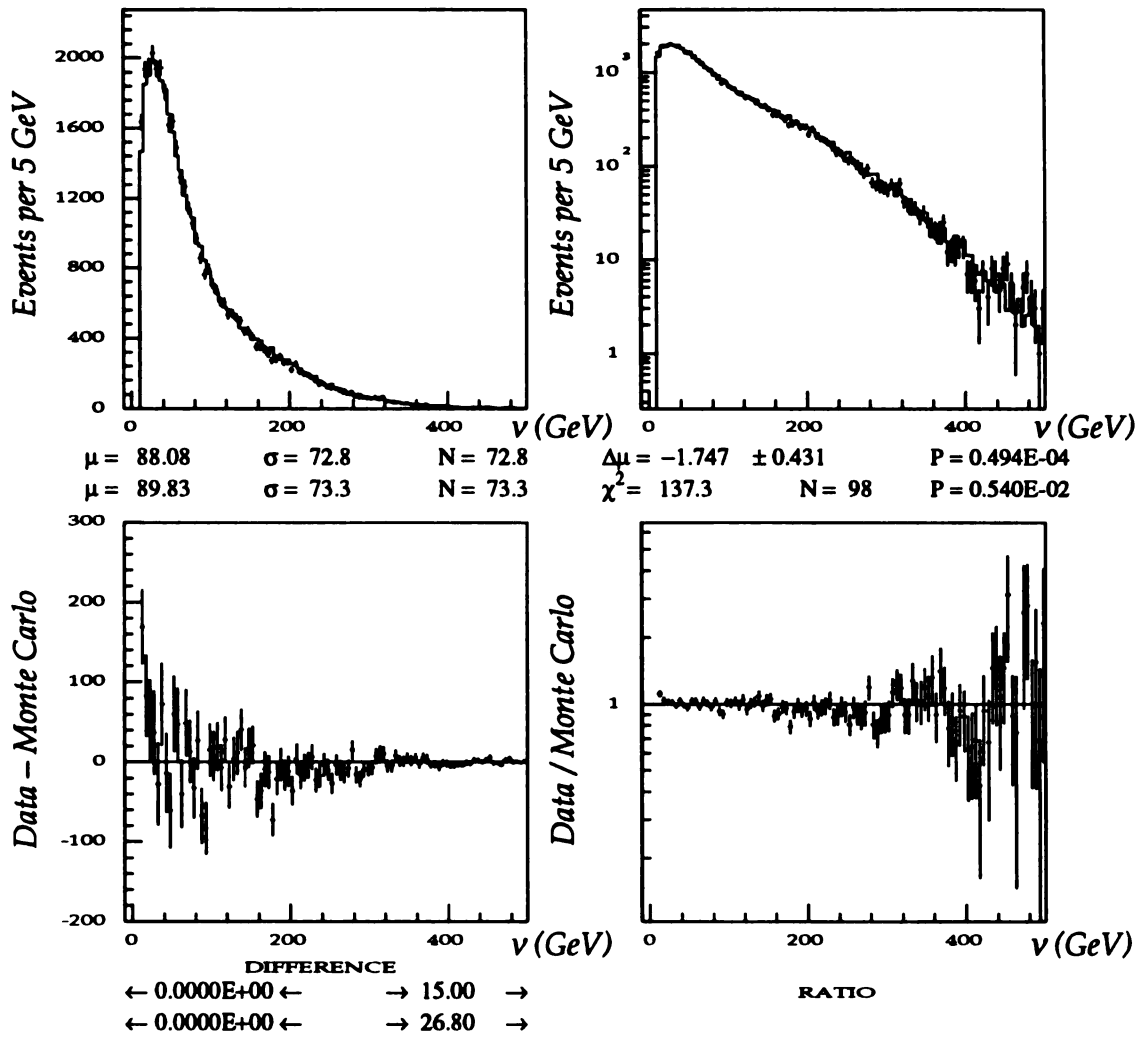

Figure B.23. Accepted ν Distribution–Rescaled 1985 EHPR Scale. The figure shows the comparison of data and Monte Carlo ν distributions for accepted neutrino events. ν is determined using the rescaled 1985 EHPR scale derived from refitting the 1985 test beam scale using the neutrino data as described in the text. The data is shown as the points with the error bars. Monte Carlo is shown as a solid outline. Upper–Left Corner shows the Data and Monte Carlo distributions overlaid with a linear scale; Upper–Right Corner shows same overlay but with a logarithmic scale; Lower–Left Corner plots the quantity *DATA–MC*; Lower–Right Corner plots the ratio of the two distributions. The Monte Carlo is area normalized.

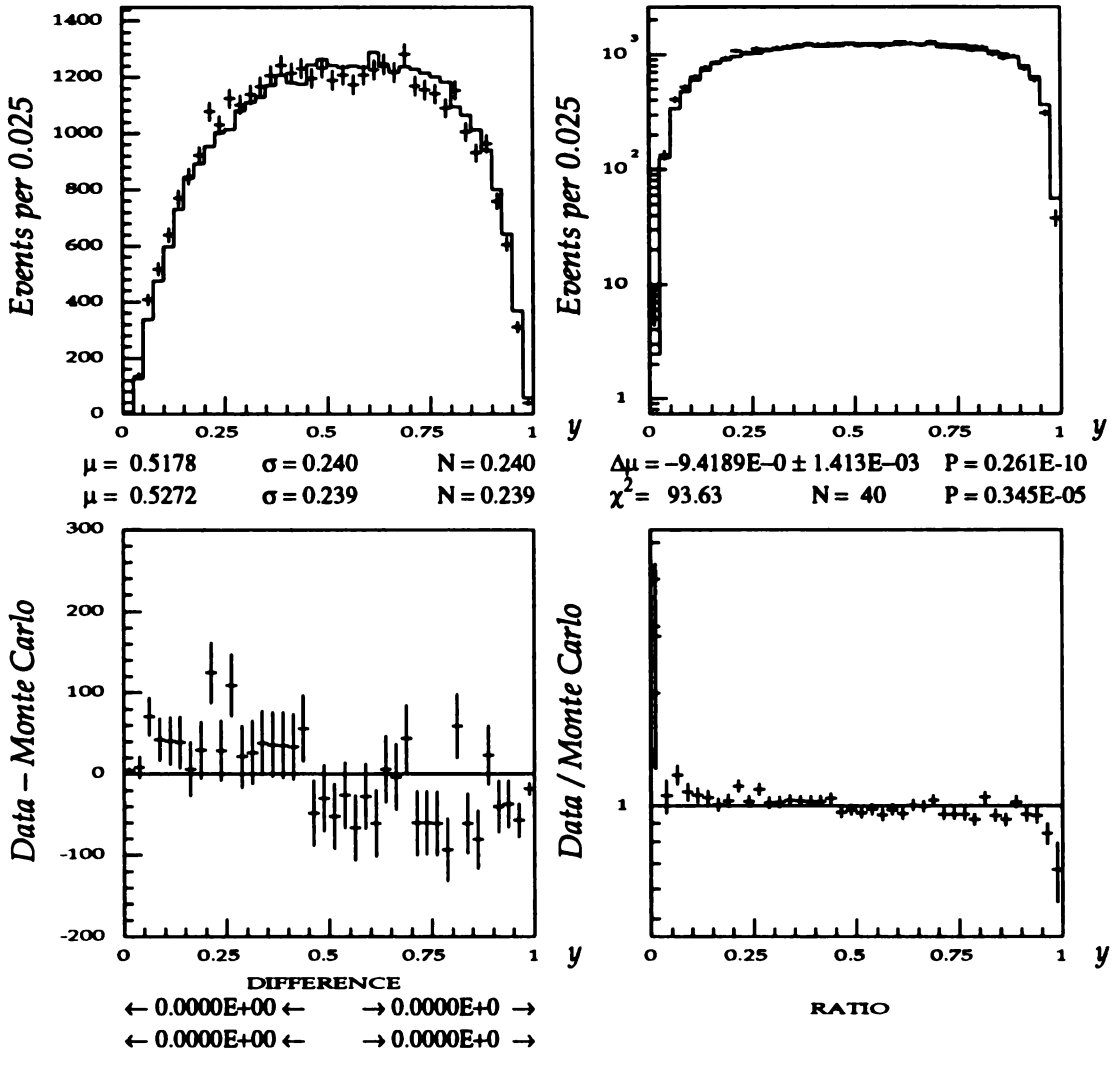

Figure B.24. Accepted y Distribution–Rescaled 1985 EHPR Scale. The figure shows the comparison of data and Monte Carlo y distributions for accepted neutrino events. ν is determined using the rescaled 1985 EHPR scale derived from refitting the 1985 test beam scale using the neutrino data as described in the text. The data is shown as the points with the error bars. Monte Carlo is shown as a solid outline. Upper–Left Corner shows the Data and Monte Carlo distributions overlaid with a linear scale; Upper–Right Corner shows same overlay but with a logarithmic scale; Lower–Left Corner plots the quantity *DATA–MC*; Lower–Right Corner plots the ratio of the two distributions. The Monte Carlo is area normalized.

Table B.2

Proportional Plane Refitting Results for Pulse Height

Scale	Pedestal	Slope
1985 Proportional Plane Scale	+2.76	6.36×10^{-3}
1985 Proportional Plane Rescaled	–0.33	6.93×10^{-3}
Prop Plane scale from Test Beam Calibration	-0.25	7.09×10^{-3}
1987 Proportional Plane Rescaled	+0.07	6.86×10^{-3}

Table B.2. Proportional Plane Refitting Results for Pulse Height. Presented are the calbration constants for the conversion of 1987 pulse height to GeV. Note that the calibration constants are very similar for the final three scales.

obtained using the two different methods are completely inconsistent.

B.3.3.2.1 Is There Any Reason to Believe the Test Beam Data?

From all of the above, one must answer that there seems to be little reason to believe the test beam calibration results for the flash chambers. The proportional plane calibration gives a self-consistent picture. The refitting of the proportional plane scales showed that the refitting algorithm worked correctly. The comparisons between the neutrino data and Monte Carlo showed that:

- There are no significant problems with the Monte Carlo.
- The test beam determined scales worked for the proportional planes but not EHFC.
- The rescaled EHFC provided excellent agreement between data and Monte Carlo.

All in all, it seem that one should have ignored the test beam data in the calibration of the flash chambers.

But, why does the test beam data give the wrong scale? As discussed in Chapter 2, there are a number of experimental problems with flash chambers. The two largest are saturation and memory. From the re-analysis of the test beam data using the rescaled EHFC, saturation is not the problem with the test beam data. Using the scale obtained from the neutrino beam, ehfc returns that the test beam energy is larger than the known incident beam momentum. This is the opposite of saturation. The problem is the flash chamber memory. Because flash chambers are constructed of a non-conducting material (i.e. plastic) it is possible for static charge to collect on the inside walls of cells. For a conductor, this charge recombines; however with an insulator, the residual charge can be long lived. This problem was probably exacerbated when there were large amounts of charge deposited at high rates in the same location. This is exactly the unavoidable condition present for high energy test beam running. At high energies, trigger rates of hundreds of Hertz were common and the high energy showers deposited large amounts of charge in the same flash chambers repeatedly. This was probably the cause of the

immense difficulties of calibrating the flash chamber using the test beam.

B.4 Conclusions

In the end, the rescaled EHFC scale was used in conjunction with the EHPR scale derived from the test beam data for the analysis of the neutrino data. These two scales are consistent with each other and provide very good agreement between data and Monte Carlo.

Together, the combination of EHFC and EHPR provides a scale that has good high energy resolution, that exhibits uniformity over the entire volume of the target–calorimeter and that was unvarying over the long span of the QTB runs.

Appendix C

The Physical Cross Section

C.1 Introduction

The simple cross section outlined in Chapter 1 makes a number of simplifications that are not adequate for a complete, physically correct extraction of structure functions. The discussion in Chapter 1 makes two major simplifications: next-to-leading order Electroweak corrections to the simple Feynman diagram shown in Chapter 1 are ignored and charm mass threshold effects are not included.The next-to-leading order Electroweak corrections go by the common name "radiative corrections." One commonly models the charm mass threshold effect using the "Slow Rescaling Model."

These corrections are important for this analysis because of the greater statistical precision of the extracted structure functions. The extracted structure functions have been corrected for both next-to-leading order Electroweak effects and for charm mass threshold. This appendix discusses these corrections.

C.2 Radiative Corrections

There are two next-to-leading order Feynman diagrams of importance to this analysis. The first of these diagrams involves the exchange of a photon (or Z boson) between the outgoing muon and either of the quark legs. This diagram is called the Box diagram. The second diagram involves the emission of photon by the muon. Figure C.1 shows both of these diagrams.

This section discusses the calculation of each of these radiative corrections and their effects on the structure function extraction.

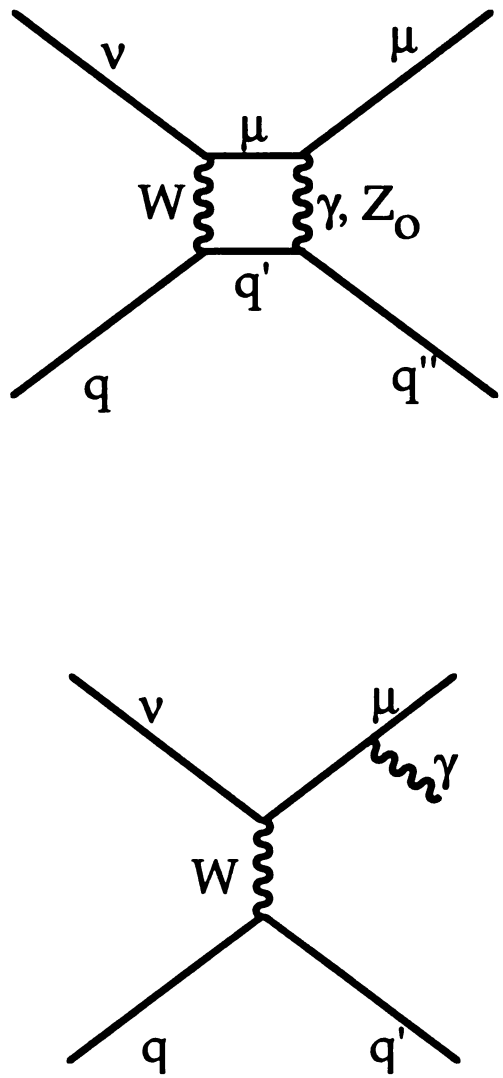

Figure C.1. Feynman Diagrams for Radiative Corrections. Shown are the two next-to-leading order Electroweak Feynman diagrams for neutrino–quark scattering. The top diagram is the "Box Diagram" involving the exchange of an additional photon between the muon leg and one of the quark legs. The bottom diagram is the "Final State Radiation" diagram for the process $\nu q \rightarrow \mu \gamma q'$.

C.2.1 Box Diagram

The exchange of a photon between the muon leg and one of the quark legs results in an enhancement of the bare (leading order) cross section for neutrinos. (Because the effect of the exchange of a Z_0 is smaller by the ratio of G_{Fermi}/α, one can neglect its contribution.) This diagram has been calculated as a correction to the bare cross section. The standard method of expressing the results of this calculation is as a factor of the bare cross section, i.e.

$$\sigma_{\text{corrected}} = K\sigma_{\text{bare}}. \tag{C.1}$$

Wheater and Llewellyn-Smith (1982) have calculated the value of K for the case of νd and $\bar{\nu}u$ scattering. νd scattering contributes the majority of the cross section to neutrino–nucleon scattering. Whereas, $\bar{\nu}u$ scattering is the most important process in anti-neutrino–nucleon scattering. For the case of νd scattering, Wheater and Llewellyn-Smith calculate that

$$K_{\nu d} = 1+\frac{\alpha}{\pi}\left\{\left[\log\left(\frac{M_W^2}{s_d}\right)+\frac{9}{4}\right]-\frac{1}{9}\left[\frac{2}{3}\log\left(\frac{s_d}{m_d^2}\right)+\frac{1}{6}\left(\pi^2-\frac{19}{4}\right)\right]\right\}. \tag{C.2}$$

Where,

$$s_d \equiv 2p_\nu \cdot p_d = 2ME_\nu x. \tag{C.3}$$

Now to examine the size of the correction, let's evaluate the expression C.2 at a typical E_ν and x. If we use E_ν=150 GeV, and x=0.25, then s_d≈70 GeV^2. Evaluating C.2 with M_W=80 GeV and m_d=50 MeV, we get

$$\begin{aligned} K_{\nu d} &= 1+\frac{\alpha}{\pi}\left\{[4.5+2.25]-\frac{1}{9}\left[\frac{2}{3}10.2+\frac{1}{6}5.12\right]\right\} \\ &= 1+0.00232\{6.75-0.85\} \\ &= 1.0137 \end{aligned}$$

This means that the νd cross section is 1.4% larger than the bare cross section calculated from leading-order electroweak theory at the chosen energy. The correction shrinks as the s_d grows because the first term in the correction shrinks while the second term

grows, thus resulting in a smaller value of K_{vd}. Equation C.2 can also be used for $\bar{\nu}\bar{d}$ and if one substitutes the s quark mass for the d quark mass, C.2 should also hold for neutrino scattering off the strange sea.

Sirlin and Marciano (1981) have also calculated K_{vd}. Their result differs slightly from that of Llewellyn-Smith and Wheater in that their result is smaller by $\frac{\alpha}{4\pi}$ (or the $\frac{9}{4}$ term, in Equation C.3, goes to 2). One finds that using the Sirlin and Marciano formula results in a value of K_{vd}=1.0131 for the values used in the calculation above.

For the case of $\bar{\nu}$u, Wheater and Llewellyn-Smith find,

$$K_{\bar{\nu}u} = 1+\frac{\alpha}{\pi}\left\{\left[\log\left(\frac{M_W^2}{s_u}\right)+\frac{3}{2}\right]-\frac{4}{9}\left[\frac{2}{3}\log\left(\frac{s_u}{m_u^2}\right)+\frac{1}{6}\left(\pi^2-\frac{43}{4}\right)\right]\right\}. \quad \text{(C.4)}$$

Evaluating this expression in the same manner as we evaluated the expression for K_{vd}, one finds,

$$\begin{aligned} K_{\bar{\nu}u} &= 1+\frac{\alpha}{\pi}\left\{[4.5+1.5]-\frac{4}{9}\left[\frac{2}{3}10.2+\frac{1}{6}(-0.88)\right]\right\} \\ &= 1+0.00232\{6.0-2.97\} \\ &= 1.0070 \end{aligned}$$

This correction is a little smaller then that for νd.

Sirlin and Marciano have not made the calculation for the $\bar{\nu}$u case. For consistency, we have chosen to use only the calculations of Wheater and Llewellyn-Smith. Figure C.2 shows the corrections to the bare cross sections as a function of s_{quark} for the four relevant cases.

C.2.2 Final State Radiation

The second diagram of Figure C.1 involves the emission of a photon by the outgoing muon. In principle, this diagram represents a different interaction, $\nu q \rightarrow \mu\gamma q'$ than the bare cross section interaction, $\nu q \rightarrow \mu q'$. The cross sections measured in our experiment are for the process $\nu N \rightarrow \mu X$, which is the combination of these interactions.

The fact that the second diagram in Figure C.1 is divergent adds an additional

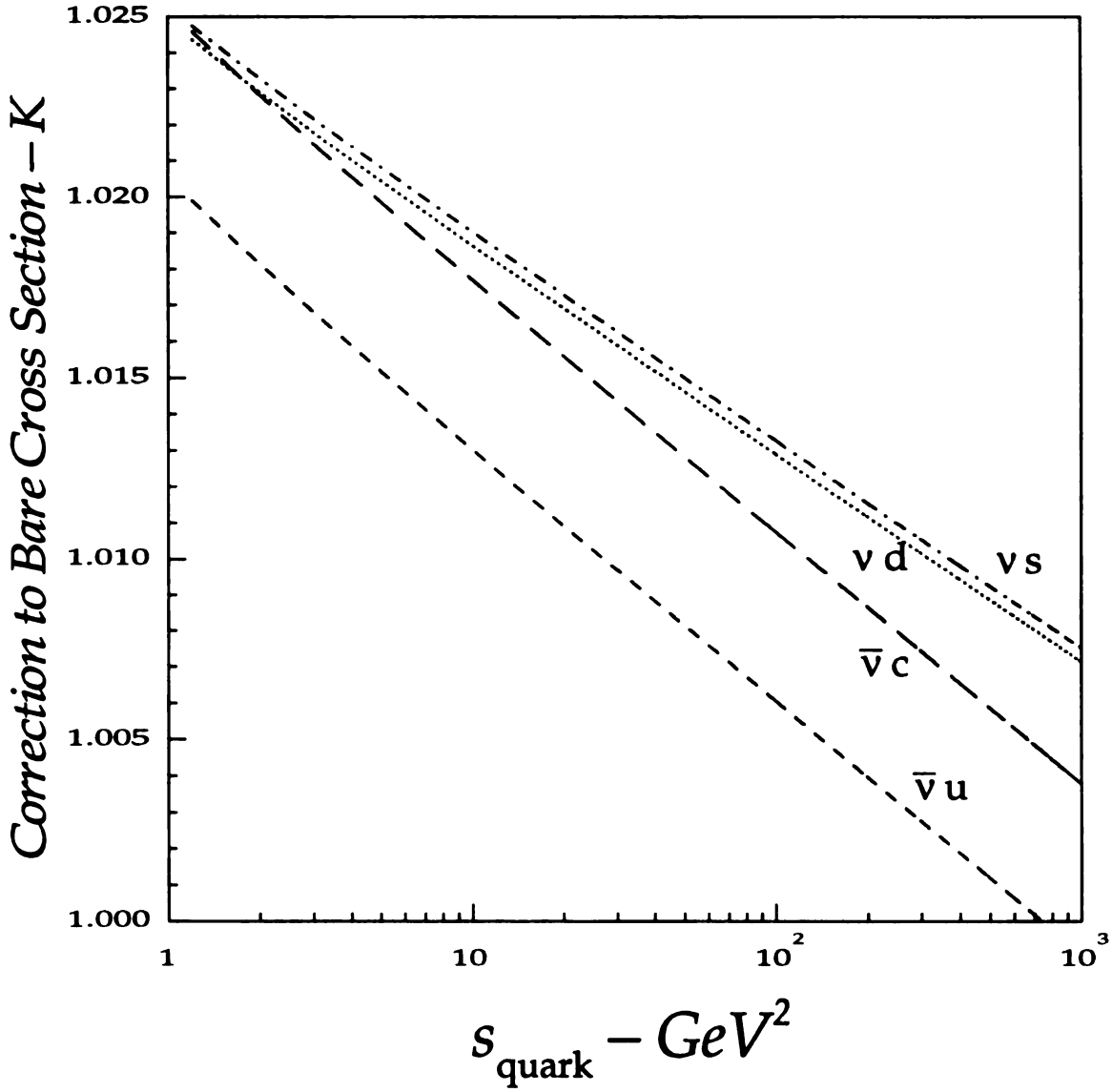

Figure C.2. Box Diagram Corrections to the Leading Order Neutrino–Quark Cross Sections. The figure shows the corrections to the bare cross section as a function of s_{quark} due to the exchange of an extra photon. The corrections are from a calculation by Wheater and Llewellyn-Smith. The dotted line is the correction to νd scattering, the small dashed line to $\bar{\nu}$u, the dashed–dotted to νs, and the large dashed line to $\bar{\nu}$c.

complication. The outgoing muon will emit an infinite number of infinitely small photons thus the cross section for the process, $\nu q \rightarrow \mu \gamma q'$, is infinite.

In principle, the radiation of photons by the quark legs should also be including in the next-to-leading order corrections to the cross section but one can argue that radiation of photons by the quarks is just another part of the physics underlying the structure functions and thus should just be included as part of the structure functions. This analysis uses this approach.

de Rújula et al. (1979) have calculated the leading log corrections to the bare cross section due to radiation of photons by the muon. The correction takes the form of a correction to the bare cross section. In this case, "bare cross section" means the cross section calculated as if the muon charge was turned off. The relationship between the observed and bare differential cross sections, in terms of the outgoing muon's final energy, E_μ and the muon three-space angle, Ω, calculated by de Rújula et al. is,

$$\frac{d\sigma_{\text{observed}}}{dE_\mu d\Omega} = \frac{d\sigma_{\text{bare}}}{dE_\mu d\Omega} + \frac{\alpha}{2\pi}\log\left[\frac{s(1-y+xy)^2}{\mu^2}\right] I \qquad \text{(C.5a)}$$

where,

$$I = \int_0^1 dz \frac{1+z^2}{1-z}\left[\frac{1}{z}\theta(z - z_{\min})\frac{d\sigma_{\text{bare}}}{dE'_\mu d\Omega}\bigg|_{E'_\mu = E_\mu/z} - \frac{d\sigma_{\text{bare}}}{dE_\mu d\Omega}\right] \qquad \text{(C.5b)}$$

and

$$z_{\min} = \left[E_\mu / E_\nu\right]\left[1 + E_\nu\left(1-\cos\theta_\mu\right)/m_p\right]. \qquad \text{(C.5c)}$$

The term $s(1-y+xy)^2$ is the square of the center of momentum energy of the muon. μ is the mass of the muon, θ_μ is the standard lepton scattering angle and z is defined by $E'_\mu = E_\mu / z$. This complicated expression can be thought of as the decrease in the observed cross section due to the radiation of photons by muons with energy E_μ and the increase in the observed cross section due to muons of the same angle but higher energy radiating photons. The variable z relates the photon energy to muon energy by,

$$E_\gamma = E'_\mu - E_\mu = E'_\mu(1-z).$$

The θ function and z_{min} enforce the kinematic limit on the maximum energy loss by the muon while maintaining the same trajectory.

Equation C.5 can be thought of as an effective radiator of a strength involving α, a kinematic logarithm and an integral over the bare cross section. Using the interpretation of an effective radiator, the effects of the muon radiation can easily be included in a Monte Carlo by generating photons with the correct spectrum and normalization and removing the photon energy from the muon and adding it to the hadron system.

The end result of the final state radiation is an effective smearing. The observed cross section differs from the bare cross section. For each event, energy is apparently transferred to the hadron system from the muon system. This results in an enhancement of the observed cross section at high y and low x. The high y enhancement results from the shifting of every event to a higher apparent y due to the final state radiation. The shift in energy decreases the observed Q^2 (while E_ν and θ_μ remain constant, E_μ decreases) and increases the observed ν, resulting in a smaller apparent x for every event.

It is also important to note that in the leading log approximation, the total cross section remains unchanged.

C.3 Slow Rescaling Model

For the process $\nu d \rightarrow \mu^+ q$, there are two possible flavors (neglecting the possibility of top quark production) for q. The outgoing quark may be either a u or c quark. At high energy transfers, where ν is much greater than the rest mass of the charm quark, the process $\nu d \rightarrow \mu^+ c$ is Cabibbo suppressed while $\nu d \rightarrow \mu^+ u$ is Cabibbo favored. In contrast, at low energy transfers, where ν is significantly lower than the rest mass of the charm quark, the process $\nu^+ d \rightarrow \mu c$ is completely suppressed due to the charm mass threshold and all νd charged-current scattering results in the creation of a u quark. The "slow rescaling" model incorporates a threshold for the production of charm.

The slow rescaling model substitutes the quantity ξ for x in the calculation of the cross section for processes producing a c quark. The slow rescaling model defines ξ as,

$$\xi = x + \frac{m_c^2}{2ME_\nu y}. \qquad \text{(C.6)}$$

ξ is then used to calculate the cross section for the production of charm.

Let's look at the specific case of νd scattering. The bare differential cross section for νd scattering is simply,

$$\frac{d^2\sigma^{\nu d}}{dxdy} = \frac{G_F^2 s}{2\pi} \mathrm{d}(x,Q^2), \qquad \text{(C.7)}$$

neglecting the propagator term. In the slow rescaling model, one replaces the simple $\mathrm{d}(x,Q^2)$ in equation C.7 by,

$$\mathrm{d}(x,Q^2) \rightarrow \cos^2\theta_c\, \mathrm{d}(x,Q^2) + \left(1 - y + \frac{xy}{\xi^2}\right) \sin^2\theta_c\, \mathrm{d}(\xi,Q^2). \qquad \text{(C.8)}$$

Expression C.8 can be generalized for νs scattering by replacing the d parton distribution functions by s parton distribution functions and using the appropriate K-M matrix elements instead of the Cabibbo factors. For values of ξ greater than 1.0, all charm production is suppressed and the second term in expression C.8 is set to zero.

C.4 Application

The three corrections for simple bare cross section discussed above were included in the Monte Carlo. Inclusion in the Monte Carlo simplifies the calculation of the corrections. The alternative to inclusion in the Monte Carlo is calculation of the corrections for each x, y bin. In reality, this correction would have to be done by Monte Carlo to include the effects of acceptance and would add an additional layer of complication to the analysis.

Both the slow rescaling and the box diagram correction were included in the calculation of the cross section and the throwing of the Monte Carlo events.

The final state radiation correction was implemented as alluded to above. After

the bare event kinematics were determined, final state photons were thrown and the energy transferred from the muon to the hadron system. Photons were generated with a spectrum,

$$\frac{dN}{dk} = \frac{1+(1-k)^2}{k}\frac{\alpha}{2\pi}\log\left[\frac{s(1-y+xy)^2}{\mu^2}\right], \qquad \text{(C.9)}$$

where k is defined by $E_\gamma = kE_\mu$. The spectrum of photons is the same as that in Equation C.5. The spectrum is cutoff by the kinematics of the photon emission as defined by $k_{max} = (1 - z_{min})$ where z_{min} was defined equation in C.5c. The mean energy radiated is,

$$\langle E_\gamma \rangle = E_\mu \int_0^{k_{max}} k dk \frac{dN}{dk} \approx E_\mu \frac{2\alpha}{3\pi}\log\left[\frac{s(1-y+xy)^2}{\mu^2}\right]. \qquad \text{(C.10)}$$

The average energy lost due to final state radiation is about 1% of the muon energy. A quick calculation of the integral, $N = \int_{k_o}^{k_{max}} \frac{dN}{dk} dk$, for the number of photons emitted in the range $k_0 \rightarrow k_{max}$ and then setting it equal to $N = 1$, yields that $k_0 < 10^{-17}$. From this calculation, one sees that while the number of soft photons emitted is infinite, their total energy is negligible. For this reason, we throw only one photon in the Monte Carlo but we require that its energy be above k_0. The energy of the single photon is removed from the muon and transferred to the hadron system.

C.5 Conclusions

Radiative corrections and slow rescaling corrections have been made to both the measured cross sections and the structure functions. All these corrections have been include in the Monte Carlo to keep the analysis of the data reasonably straight forward, if not simple.

Additional corrections to the simple model were described in Chapters 3 and 4. These corrections include Fermi-motion and non-isoscalarity corrections.

Appendix D

Systematic Error Analysis

D.1 Introduction

It is essential to have an understanding of the systematic errors associated with the measured differential cross sections and structure function discussed in Chapter 4. While causes of systematic errors in the extracted cross sections and structure functions are well understood, their determination is not straight-forward. This appendix outlines the procedure used to calculate the systematic errors for both the differential cross sections and the structure functions.

D.2 Procedure

Systematic errors arise from two sources. The first source is measurement biases. The second source is an incomplete knowledge of the (for lack of a better word) acceptance. In this context, acceptance refers to the effects of the various resolutions, the trigger, the pattern recognition programs, the analysis cuts, and the geometric acceptance of the detector and has a simple meaning. Acceptance is simply the ratio of the number of events in some bin that are reconstructed and pass all cuts to the true number of events in that bin. This section discusses the methods used to estimate the systematic errors arising from these sources. The systematic errors from the two sources are then added in quadrature.

D.2.1 Calculation of Systematic Errors from Measurement Biases

From the procedures used to calibrate the detector, one can determine the uncertainties in the scales used to measure events. Based on the estimated uncertainties in the

scales, one must then calculate the uncertainties in the quantities derived from the measured events.

A commonly used method for estimating systematic uncertainties is to vary the scales by one standard deviation and use variations in the derived quantity as an estimate of the systematic error. This method has the virtue of being extremely simple to implement but is susceptible to statistical variations.

This analysis uses an alternative method. The calibration constants used in event measurement are varied based on the estimates of their uncertainties. The cross section and structure function analyses are then repeated for each of the variations in the scales. This results in an ensemble of experiments from which the systematic errors in both the differential cross sections and structure functions can then be measured. This method can also provide the functional variation in a derived quantity as a function of the variation in a scale. When all the scales were varied simultaneously, the ensemble of experiments can also account for the correlations and anti-correlations between the variations in the different scales.

D.2.1.1 The Method in Detail

The variation in the scale parameters can be done in many different ways but to allow for the simplest interpretation of the ensemble, the parameters were varied using a Gaussian of the appropriate width. The Gaussian was divided into N slices of equal probability and the mean value of each slice was used as the variation in the scale (See Figure D.1.) If more than one parameter was being varied, a matrix of variations was formed so that all possible combinations were included in the ensemble.

For each combination of variations in the scale parameters, the entire data set was reanalyzed. In each bin, for each member of the ensemble, the value of the quantity of interest was calculated. The RMS of the derived quantity for ensemble was then calculated. The systematic error was chosen to be simply this ensemble RMS.

The ensemble gives more information than is available from simply varying a

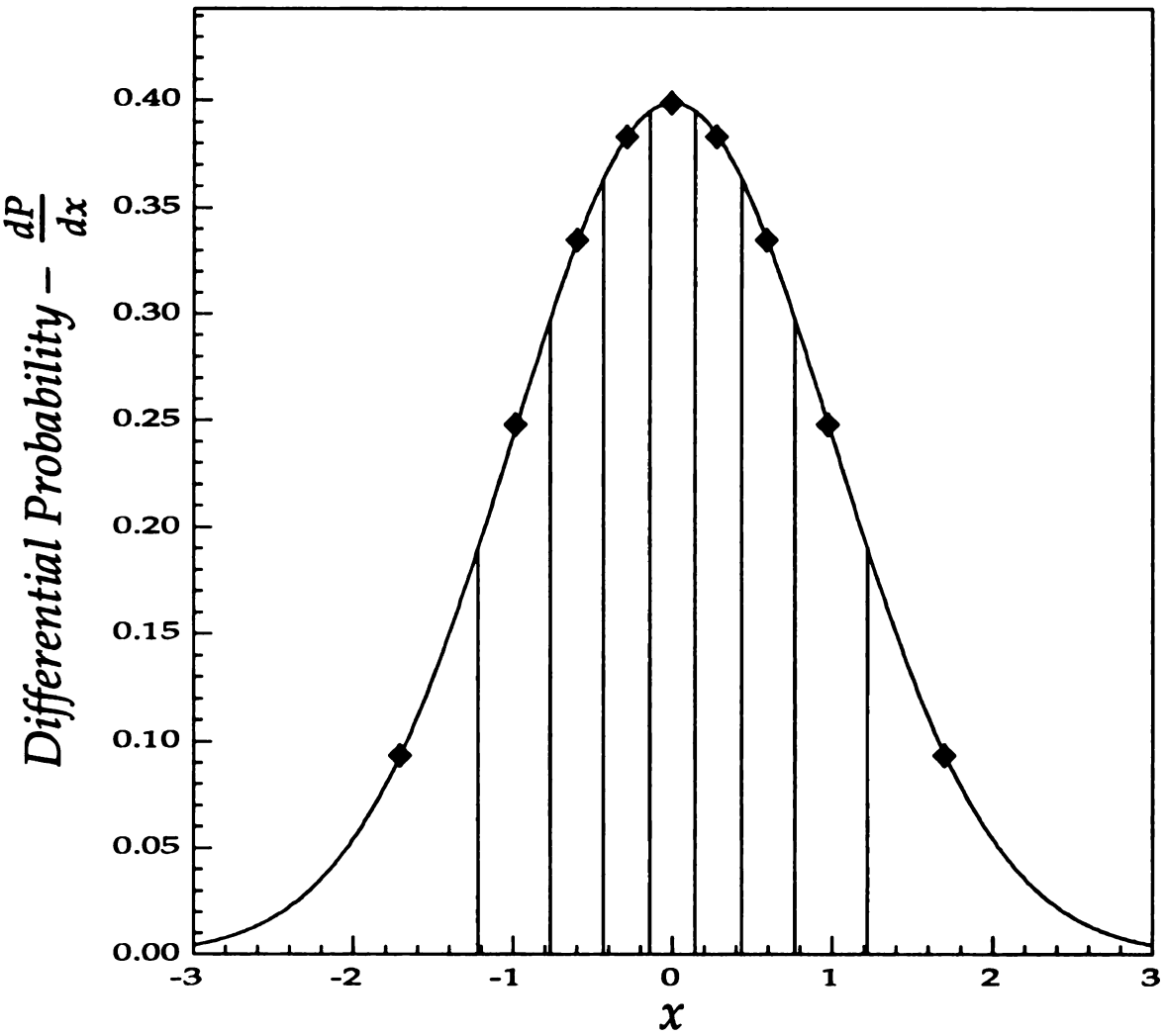

Figure D.1. Division of a Gaussian for Systematic Error Measurement. The Figure shows a Gaussian divided into 9 slices of equal area (i.e. equal probability.) The mean of each slice is shown by the black diamonds (◆.) The binning is chosen so that for one bin the average is 0 and so that there are the maximum divisions possible. The number of divisions are limited by computer resources.

single scale by one standard deviation. The dependance of the uncertainty on each scale can be easily obtained. It is also possible, if desired to include correlations between the scale errors.

D.2.1.2 Scale Errors

In doing the detailed calibrations necessary for a structure function analysis, one determines both the event measurement scales and the uncertainties in the event measurement scales. This section discusses the magnitude of the uncertainties and how uncertainties were estimated. These uncertainties are also discussed in both Chapter 2 and Appendix B.

As discuss before, there are three measurables used in the event reconstruction for this analysis, θ_μ, E_μ and ν. Let us examine the scale uncertainties in each of these in turn.

D.2.2.2.1 θ_μ

θ_μ is extremely important in the event reconstruction. For small angles, one finds,

$$Q^2 \approx \left(\nu + E_\mu\right) E_\mu \theta_\mu^2 .$$

As one can see, Q^2 is proportional to θ_μ^2. For this reason, a bias in θ_μ would result in a large systematic error.

One might imagine that mis-alignment of the calorimeter elements could result in a bias in θ_μ. To determine if there is an alignment problem, the data's muon slope distributions in the two orthogonal views were compared with the same distributions from the Monte Carlo simulation. The agreement between the data and the Monte Carlo is excellent but the means of the data and Monte Carlo distributions differed slightly (~0.1 milliradians). These differences were then used as the input to a simple Monte Carlo to estimate the induced bias due to the possible mis-alignment. The Monte Carlo study showed that there in no induced bias just a small increase in the θ_μ resolution (<10% of the resolution quoted in Chapter 2). This result is not surprising because of the

muon trajectory's azimuthally symmetry about the beam axis (i.e. there is no prefered ϕ_μ). and because θ_μ is the result of the combination of the muon slope measurements in the 3 different views of the flash chambers. The azimuthal symmetry cancels out any alignment bias by for a given θ_μ by averaging over all ϕ_μ.

The question now becomes what are the other possible sources of bias in θ_μ.

Another possible source of a θ_μ bias is a bias induced by the procedure that fits the muon slopes. The comparison of the muon slope distributions previously discussed argues strongly against a bias due to the fitting procedure since the data and Monte Carlo orthoginal slope distributions agree very well.

A bias in θ_μ could result from the uncertainties in the length and/or width of the FMMF detector. The physical size of the detector defines the θ_μ scale. The uncertainty in the θ_μ scale is proportional to the uncertainty in detector size.

Since there is no evidence that there is any bias in θ_μ due to the muon finding and fitting routines, this leaves the uncertainty in the θ_μ scale as the largest possible source of a θ_μ bias known. To estimate the possible bias in the θ_μ scale, one conservatively estimates that the length of the detector is known to 1.0 cm over the roughly 20 m length of the detector. This results in an estimate in the fractional uncertainty in θ_μ of,

$$\frac{\sigma(\theta_\mu)}{\theta_\mu} = 5.0\times10^{-4},$$

due entirely to the uncertainty in the θ_μ scale. This uncertainty is negligible and is thus not included in the systematic error analysis.

D.2.2.2.2 E_μ

The uncertainty in the E_μ scale is due primarily to uncertainties in the knowledge of the magnetic field of the iron toroids in the muon spectrometer and in particular the field of the 24' toroids. The uncertainty in E_μ is determined by expanding the fitting of the calibration scales using the neutrino beams, E_ν versus radius structure as detailed in Appendix B. In the expansion, a multiplicative factor of the measured E_μ is included as

part of the fit. This fitting procedure results in only a slight modification of the E_μ scale but the estimated error in the fitting is approximately ±2%, which is used here.

D.2.2.2.3 ν

The two largest sources of uncertainty in ν are: improper elimination of noise in the calorimeter and errors in the calibration of the calorimeter. These two sources of uncertainty would result in two different types of variation in the hadron calibration scales. The uncertainty in the noise elimination and in the extrapolation of the calibration to low energies could result in a constant offset or pedestal in the calibrated ν. The uncertainty in the calibration could also result in ν scale error.

From the fitting procedure described in Appendix B, one can again estimate the uncertainty in the scales. Again, using the errors estimated by the fitting program, one finds that the uncertainty in the ν pedestal is ±1 GeV and the uncertainty in the ν scale is ±2%.

D.2.1.3 The Final Ensemble

The final ensemble used to measure the systematic errors is described in this section.

The ensemble used to measure the systematic error could be derived from either the Data Sample or the Monte Carlo Sample. The systematic errors presented in Chapter 4 are derived from an analysis of the ensemble derived from the Monte Carlo. The same procedure and variation were used with the data with similar results for the systematic errors. The results for the Monte Carlo are used because of the greater statistics of the Monte Carlo sample.

The final ensemble consists of 9^3 (or 729) different sets of calibration constants. The calibration constants varied were the E_μ scale, ν scale and the ν pedestal. The variation in E_μ and ν took the forms,

$$E_\mu \rightarrow \alpha_\mu E_\mu \qquad \text{(D.1)}$$

$$\nu \rightarrow \delta_\nu + \beta_\nu \nu. \qquad \text{(D.2)}$$

Table D.1 shows the variations chosen for each of the calibration constants. The final size of the ensemble was dictated by computer memory limitations. The odd number of bins allowed the 0 bin to correspond to no variation.

Figures D.2 shows the ensemble structure functions for three bins allowing the reader to gain a feeling for the dependance of the systematic errors due to possible measurement biases on the calibration constants.

D.2.2 Acceptance Uncertainties

In making comparisons between the data and the Monte Carlo, one finds that there are a number of small discrepancies. From these differences, one may estimate the uncertainties in the knowledge of the acceptance. Based on the iron distributions shown in Figure 3.11, one calculates the uncertainty in knowledge of the acceptance as 1.3% of the acceptance. This error is applied to all bins.

D.3 Results

The results of the systematic error analysis are presented with the measured differential cross sections and structure functions in Chapter 4. As mentioned before, the systematic errors are a quadratic combination of the errors associated with measurement biases and with acceptance uncertainies.

Table D.1

Variation in Calibration Constants

Bin	α_μ	β_ν	δ_ν
–1	0.96591	0.96591	–1.7046 GeV
–2	0.98049	0.98049	–0.9756 GeV
–3	0.98816	0.98816	–0.5922 GeV
–4	0.99434	0.99434	–0.2832 GeV
0	1.00000	1.00000	0.0000 GeV
+1	1.00566	1.00566	+0.2832 GeV
+2	1.01184	1.01184	+0.5922 GeV
+3	1.01951	1.01951	+0.9756 GeV
+4	1.03409	1.03409	+1.7046 GeV

Table D.1. Variations in Calibration Constants. The table lists the variations in the calibration constants. α_μ, β_ν, and δ_ν are defined by Equations D.1 and D.2. For a discussion of the variation of the calibration constants, see the text.

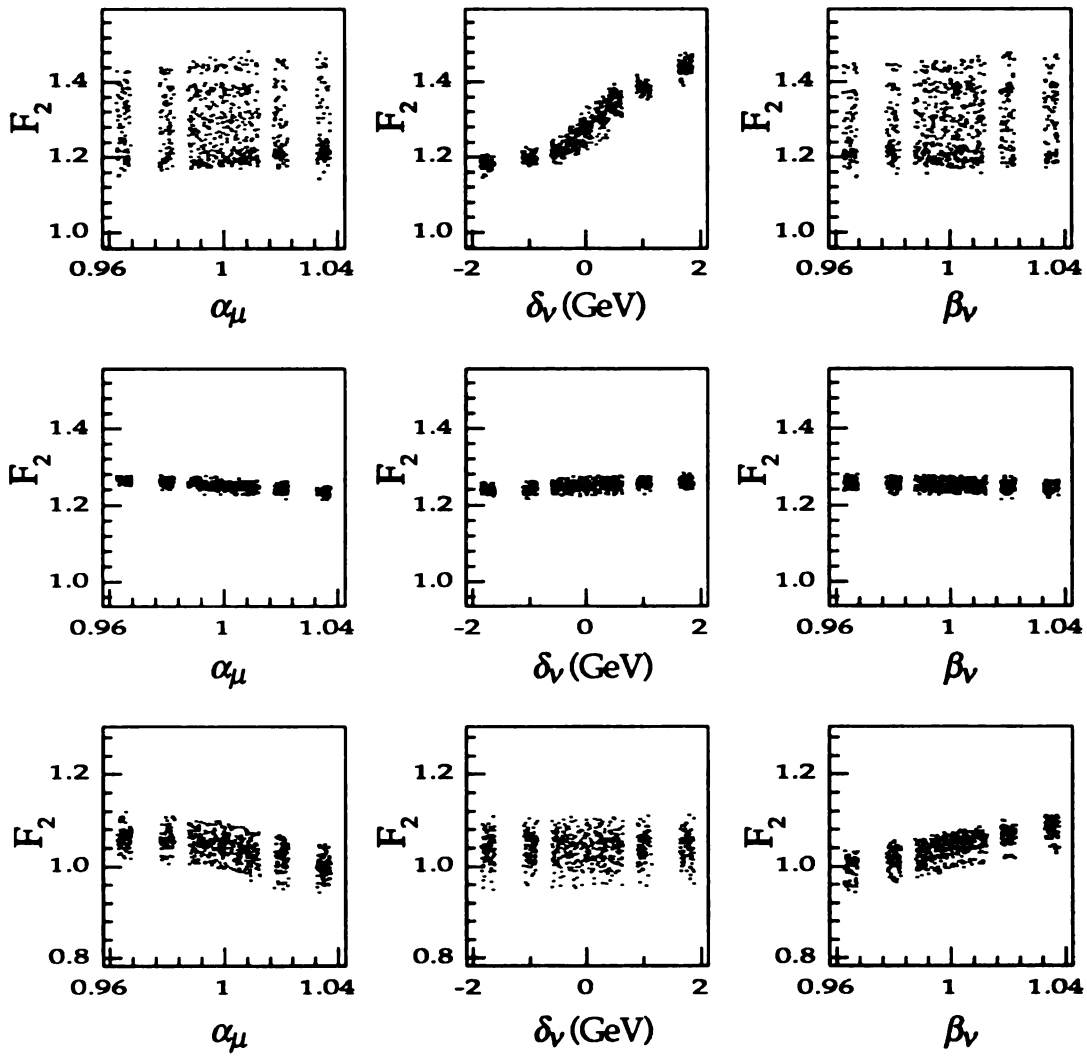

Figure D.2. Ensembles of Structure Functions. Shown are scatter plots of F_2 as a function of the varied calibration constants, α_μ, β_ν, and δ_ν. The rows show F_2 for three different x,Q^2 bins. The columns show the dependance of F_2 on (from left to right) α_μ, β_ν, and δ_ν. The top row shows a bin which is very sensitive to δ_ν. The middle row shows a bin with a relatively small systematic uncertainty. The bin of the bottom row shows an anti-correlation between α_μ and β_μ. The variations in the calibration constants was done at the discrete values shown in Table D.1. The horizontal widths of the variations in the calibration constants shown in the plots are an artifact of the plotting procedure.

Appendix E

Alternative Structure Functions

E.1 Introduction

A number of assumptions have been made in the extraction of the structure functions presented in Chapter 4. Two of these assumptions have been modified and different sets of structure functions have been extracted. These structure function are described and tabulated in this appendix.

E.2 Structure Functions with Non-Linear Cross Section

The standard assumption is that $\sigma_{\text{total}}^{\nu N}$ is a linear function of E_ν. This assumption was used in Chapter 4. The value used for $\frac{\sigma}{E}$ was the average the results from the world's three high statistics νN scattering experiments. The CCFR collaboration (Quintas 1992) have measured the increase in the neutrino–nucleon cross section as a function of the energy of the neutrino and fit $\frac{\sigma}{E}$ to the form $A(1-BE)$. It was found that, for the neutrino data, B = (0.4±0.3)% per 100 GeV which is consistent with a linear increase in the cross section. For the anti-neutrino data, it was found that B = (3.3±0.7)% per 100 GeV. It should be noted that an additional increase in the cross section as a function of E_ν beyond the expected linear increase is not unexpected as the suppression of the production of charm should decrease as E_ν increases.

The entire structure function extraction process has been repeated using the values for A presented in Chapter 4 but including the CCFR measured values of B for both the neutrino and anti-neutrino total cross sections. This set of structure function is tabulated in Table E.1.

E.3 Structure Functions without Slow Rescaling Correction

The slow rescaling model of the suppression of charm production is a very simple and intuitive approach to the problem. While the slow rescaling model is adequate for leading order QCD modeling, for next-to-leading order QCD calculations, the charm suppression is simply another part of the QCD of the parton distributions (W.K. Tung Private Communication). For this reason, the structure function analysis has been repeated with the slow rescaling corrections to the Monte Carlo cross section turned off. This set of structure functions is presented in Table E.2.

Table E.1

Structure Functions Using CCFR Cross Section

x	Q^2	F_2	F_2 Statistical Error	F_2 Systematic Error	F_2 Scale Error	xF_3	xF_3 Statistical Error	xF_3 Systematic Error	xF_3 Scale Error	$\bar{\nu}$	ν
0.015	0.404	0.8909	0.0295	0.0695	0.0044	0.2166	0.0723	0.0361	0.0095	188	809
0.015	0.958	1.1550	0.0287	0.0482	0.0056	0.1986	0.0455	0.0133	0.0082	317	1351
0.015	1.845	1.4711	0.0326	0.0569	0.0070	0.2813	0.0437	0.0135	0.0092	358	1932
0.015	3.645	1.8637	0.0420	0.0627	0.0087	0.1045	0.0522	0.0068	0.0109	224	2209
0.015	6.714	2.2139	0.0877	0.1042	0.0103	0.0550	0.1026	0.0081	0.0121	66	1077
0.045	2.141	1.2218	0.0355	0.0777	0.0060	0.3325	0.0878	0.0365	0.0132	267	1030
0.045	2.880	1.4349	0.0327	0.0509	0.0072	0.4707	0.0512	0.0332	0.0104	303	1763
0.045	5.515	1.6772	0.0360	0.0687	0.0084	0.5315	0.0484	0.0263	0.0109	329	2326
0.045	10.98	1.8226	0.0418	0.0687	0.0092	0.6358	0.0513	0.0232	0.0112	179	2506
0.045	20.15	2.0324	0.0806	0.1201	0.0102	0.6931	0.0943	0.0263	0.0120	38	1240

Table E.1. Structure Functions Using CCFR Cross Section. Tabulated are structure functions extracted from the FMMF data using the CCFR total cross sections in x, Q^2 bins. (Q^2 is presented in units of GeV^2.) In addition the statistical, systematic and scale errors are tabulated. The final two columns indicate the number of anti-neutrino and neutrino events in the x, Q^2 bin. Please see the text for details on the extraction of the structure functions and the determinations of the errors.

Table E.1 continued

Structure Functions Using CCFR Cross Section

x	Q^2	F_2	F_2 Statistical Error	F_2 Systematic Error	F_2 Scale Error	xF_3	xF_3 Statistical Error	xF_3 Systematic Error	xF_3 Scale Error	$\bar{\nu}$	ν
0.080	3.034	1.2731	0.0314	0.0604	0.0064	0.6146	0.0786	0.0531	0.0140	311	1472
0.080	5.120	1.4850	0.0295	0.0456	0.0075	0.6013	0.0458	0.0276	0.0108	395	2399
0.080	9.807	1.5942	0.0300	0.0540	0.0082	0.7428	0.0405	0.0275	0.0107	364	3123
0.080	19.47	1.6411	0.0339	0.0621	0.0086	0.8359	0.0420	0.0206	0.0106	147	3201
0.080	35.82	1.6333	0.0581	0.1062	0.0087	0.8528	0.0680	0.0207	0.0102	37	1474
0.125	4.736	1.2104	0.0272	0.0535	0.0061	0.7415	0.0683	0.0261	0.0132	314	1794
0.125	7.989	1.3946	0.0253	0.0329	0.0072	0.8372	0.0404	0.0211	0.0108	365	2849
0.125	15.31	1.4091	0.0247	0.0428	0.0075	0.8816	0.0332	0.0255	0.0098	340	3469
0.125	30.52	1.4584	0.0272	0.0377	0.0080	0.9409	0.0333	0.0189	0.0097	127	3606
0.125	55.96	1.5085	0.0459	0.0581	0.0083	0.9701	0.0537	0.0480	0.0097	28	1725
0.175	7.416	1.1862	0.0278	0.0361	0.0059	0.8659	0.0754	0.0400	0.0146	305	1648
0.175	11.17	1.2541	0.0240	0.0256	0.0066	0.9243	0.0386	0.0175	0.0100	275	2614
0.175	21.45	1.2608	0.0241	0.0306	0.0067	0.8051	0.0322	0.0212	0.0087	271	2936
0.175	42.76	1.2722	0.0256	0.0283	0.0071	0.9376	0.0313	0.0229	0.0086	95	3065
0.175	78.33	1.3003	0.0426	0.0585	0.0073	0.9147	0.0499	0.0198	0.0085	29	1479

Table E.1 continued

Structure Functions Using CCFR Cross Section

x	Q^2	F_2	F_2 Statistical Error	F_2 Systematic Error	F_2 Scale Error	xF_3	xF_3 Statistical Error	xF_3 Systematic Error	xF_3 Scale Error	$\bar{\nu}$	ν
0.225	8.842	0.9995	0.0257	0.0248	0.0051	0.9715	0.0715	0.0261	0.0130	227	1436
0.225	14.33	1.0606	0.0226	0.0204	0.0057	0.8867	0.0373	0.0114	0.0089	209	2130
0.225	27.65	1.0158	0.0212	0.0198	0.0057	0.8390	0.0285	0.0131	0.0075	166	2415
0.225	54.94	1.0190	0.0225	0.0200	0.0059	0.8402	0.0275	0.0108	0.0071	60	2447
0.225	100.7	1.0059	0.0327	0.0379	0.0060	0.8771	0.0382	0.0271	0.0070	17	1194
0.275	10.50	0.8480	0.0239	0.0269	0.0043	0.7568	0.0667	0.0260	0.0106	181	1192
0.275	17.42	0.8773	0.0210	0.0234	0.0047	0.7937	0.0364	0.0210	0.0078	158	1719
0.275	33.75	0.8625	0.0202	0.0180	0.0048	0.7255	0.0279	0.0094	0.0065	133	1956
0.275	67.09	0.8787	0.0213	0.0200	0.0050	0.6982	0.0261	0.0103	0.0061	56	1995
0.350	11.76	0.6836	0.0158	0.0327	0.0034	0.5683	0.0451	0.0268	0.0088	288	1711
0.350	22.15	0.6541	0.0133	0.0237	0.0035	0.6032	0.0229	0.0174	0.0057	243	2338
0.350	42.84	0.6233	0.0124	0.0182	0.0035	0.5452	0.0168	0.0123	0.0046	174	2601
0.350	85.23	0.5740	0.0123	0.0145	0.0034	0.5017	0.0150	0.0096	0.0040	61	2573
0.350	156.7	0.5847	0.0177	0.0159	0.0035	0.5075	0.0207	0.0102	0.0041	14	1288

Table E.1 continued

Structure Functions Using CCFR Cross Section

x	Q^2	F_2	F_2 Statistical Error	F_2 Systematic Error	F_2 Scale Error	xF_3	xF_3 Statistical Error	xF_3 Systematic Error	xF_3 Scale Error	$\bar{\nu}$	ν
0.450	16.26	0.4059	0.0122	0.0342	0.0020	0.2805	0.0335	0.0355	0.0045	175	1078
0.450	28.38	0.3853	0.0106	0.0220	0.0021	0.3529	0.0190	0.0200	0.0034	152	1345
0.450	54.93	0.3298	0.0091	0.0159	0.0019	0.3055	0.0127	0.0151	0.0025	84	1427
0.450	110.0	0.3099	0.0091	0.0136	0.0018	0.2733	0.0111	0.0118	0.0022	40	1376
0.550	17.68	0.2236	0.0092	0.0246	0.0011	0.1768	0.0264	0.0219	0.0027	98	553
0.550	34.36	0.1806	0.0067	0.0178	0.0010	0.1784	0.0129	0.0161	0.0018	79	766
0.550	67.35	0.1628	0.0062	0.0110	0.0009	0.1285	0.0087	0.0105	0.0012	62	735
0.550	134.5	0.1334	0.0056	0.0096	0.0008	0.1207	0.0068	0.0082	0.0009	17	720
0.650	25.15	0.0743	0.0028	0.0080	0.0004	0.0576	0.0062	0.0087	0.0007	101	718
0.650	79.56	0.0561	0.0029	0.0055	0.0003	0.0584	0.0043	0.0044	0.0005	24	410
0.850	24.16	0.0090	0.0005	0.0014	0.0000	0.0061	0.0015	0.0015	0.0001	83	427
0.850	52.95	0.0069	0.0003	0.0009	0.0000	0.0071	0.0007	0.0008	0.0001	46	449
0.850	104.3	0.0049	0.0003	0.0005	0.0000	0.0046	0.0004	0.0004	0.0000	38	402

Table E.2

Structure Functions Without Slow Rescaling Correction

x	Q^2	F_2	F_2 Statistical Error	F_2 Systematic Error	F_2 Scale Error	xF_3	xF_3 Statistical Error	xF_3 Systematic Error	xF_3 Scale Error	$\bar{\nu}$	ν
0.015	0.404	0.8788	0.0291	0.0689	0.0040	0.2289	0.0717	0.0368	0.0088	188	809
0.015	0.957	1.1348	0.0281	0.0475	0.0051	0.2131	0.0449	0.0136	0.0076	317	1351
0.015	1.844	1.4395	0.0317	0.0556	0.0064	0.3049	0.0428	0.0141	0.0084	358	1932
0.015	3.642	1.7933	0.0399	0.0605	0.0078	0.1590	0.0499	0.0074	0.0098	224	2209
0.015	6.714	2.0880	0.0803	0.0986	0.0091	0.1566	0.0940	0.0097	0.0106	66	1077
0.045	2.140	1.2061	0.0349	0.0769	0.0055	0.3493	0.0871	0.0371	0.0122	267	1030
0.045	2.877	1.4127	0.0320	0.0504	0.0065	0.4862	0.0506	0.0333	0.0096	303	1763
0.045	5.512	1.6411	0.0350	0.0671	0.0076	0.5544	0.0474	0.0270	0.0100	329	2326
0.045	10.97	1.7685	0.0399	0.0665	0.0083	0.6722	0.0492	0.0242	0.0102	179	2506
0.045	20.15	1.9398	0.0743	0.1144	0.0092	0.7547	0.0869	0.0292	0.0107	38	1240

Table E.2. Structure Functions Without Slow Rescaling Correction. Tabulated are structure functions extracted from the FMMF data without correction for Slow Rescaling in x, Q^2 bins. (Q^2 is presented in units of GeV^2.) In addition the statistical, systematic and scale errors are tabulated. The final two columns indicate the number of anti-neutrino and neutrino events in the x, Q^2 bin. Please see the text for details on the extraction of the structure functions and the determinations of the errors.

Table E.2 continued

Structure Functions Without Slow Rescaling Correction

x	Q^2	F_2	F_2 Statistical Error	F_2 Systematic Error	F_2 Scale Error	xF_3	xF_3 Statistical Error	xF_3 Systematic Error	xF_3 Scale Error	$\bar{\nu}$	ν
0.080	3.032	1.2561	0.0309	0.0600	0.0058	0.6311	0.0780	0.0534	0.0130	311	1472
0.080	5.114	1.4636	0.0290	0.0451	0.0068	0.6149	0.0453	0.0277	0.0100	395	2399
0.080	9.802	1.5642	0.0292	0.0529	0.0075	0.7616	0.0397	0.0278	0.0099	364	3123
0.080	19.45	1.5971	0.0325	0.0603	0.0079	0.8616	0.0404	0.0213	0.0097	147	3201
0.080	35.82	1.5699	0.0539	0.1011	0.0079	0.8870	0.0630	0.0231	0.0092	37	1474
0.125	4.738	1.1958	0.0267	0.0530	0.0056	0.7566	0.0678	0.0265	0.0122	314	1794
0.125	7.981	1.3749	0.0248	0.0324	0.0066	0.8481	0.0400	0.0213	0.0100	365	2849
0.125	15.30	1.3854	0.0241	0.0418	0.0069	0.8928	0.0326	0.0257	0.0091	340	3469
0.125	30.49	1.4257	0.0261	0.0367	0.0073	0.9557	0.0322	0.0191	0.0089	127	3606
0.125	55.96	1.4585	0.0429	0.0567	0.0075	0.9907	0.0502	0.0478	0.0088	28	1725
0.175	7.411	1.1705	0.0273	0.0357	0.0054	0.8813	0.0749	0.0400	0.0135	305	1648
0.175	11.15	1.2368	0.0236	0.0254	0.0061	0.9331	0.0383	0.0174	0.0092	275	2614
0.175	21.44	1.2411	0.0236	0.0301	0.0061	0.8141	0.0317	0.0211	0.0080	271	2936
0.175	42.71	1.2468	0.0247	0.0277	0.0065	0.9457	0.0303	0.0226	0.0079	95	3065
0.175	78.33	1.2613	0.0399	0.0560	0.0066	0.9273	0.0467	0.0210	0.0077	29	1479

Table E.2 continued

Structure Functions Without Slow Rescaling Correction

x	Q^2	F_2	F_2 Statistical Error	F_2 Systematic Error	F_2 Scale Error	xF_3	xF_3 Statistical Error	xF_3 Systematic Error	xF_3 Scale Error	$\bar{\nu}$	ν
0.225	8.835	0.9860	0.0253	0.0247	0.0046	0.9829	0.0710	0.0263	0.0121	227	1436
0.225	14.31	1.0476	0.0222	0.0202	0.0052	0.8931	0.0370	0.0114	0.0082	209	2130
0.225	27.64	1.0021	0.0207	0.0194	0.0052	0.8441	0.0281	0.0131	0.0069	166	2415
0.225	54.88	1.0010	0.0218	0.0194	0.0054	0.8433	0.0268	0.0108	0.0066	60	2447
0.225	100.7	0.9826	0.0311	0.0369	0.0055	0.8772	0.0364	0.0272	0.0064	17	1194
0.275	10.51	0.8369	0.0235	0.0267	0.0039	0.7676	0.0663	0.0261	0.0099	181	1192
0.275	17.40	0.8658	0.0206	0.0232	0.0043	0.7998	0.0361	0.0211	0.0072	158	1719
0.275	33.73	0.8500	0.0197	0.0177	0.0044	0.7295	0.0275	0.0094	0.0060	133	1956
0.275	67.02	0.8633	0.0206	0.0195	0.0046	0.7023	0.0254	0.0104	0.0056	56	1995
0.350	11.75	0.6742	0.0155	0.0324	0.0031	0.5771	0.0447	0.0271	0.0081	288	1711
0.350	22.12	0.6460	0.0131	0.0234	0.0032	0.6066	0.0228	0.0176	0.0053	243	2338
0.350	42.82	0.6152	0.0121	0.0181	0.0032	0.5475	0.0167	0.0124	0.0043	174	2601
0.350	85.15	0.5661	0.0120	0.0143	0.0031	0.5025	0.0146	0.0097	0.0037	61	2573
0.350	156.7	0.5716	0.0169	0.0154	0.0032	0.5073	0.0198	0.0102	0.0037	14	1288

Table E.2 continued

Structure Functions Without Slow Rescaling Correction

x	Q^2	F_2	F_2 Statistical Error	F_2 Systematic Error	F_2 Scale Error	xF_3	xF_3 Statistical Error	xF_3 Systematic Error	xF_3 Scale Error	$\bar{\nu}$	ν
0.450	16.27	0.3976	0.0119	0.0329	0.0018	0.2848	0.0329	0.0354	0.0042	175	1078
0.450	28.32	0.3767	0.0103	0.0213	0.0019	0.3519	0.0186	0.0197	0.0032	152	1345
0.450	54.84	0.3232	0.0088	0.0155	0.0017	0.3047	0.0125	0.0149	0.0023	84	1427
0.450	109.8	0.3043	0.0088	0.0133	0.0017	0.2720	0.0108	0.0116	0.0020	40	1376
0.550	17.63	0.2186	0.0090	0.0236	0.0010	0.1805	0.0259	0.0221	0.0025	98	553
0.550	34.28	0.1765	0.0065	0.0171	0.0009	0.1789	0.0127	0.0159	0.0016	79	766
0.550	67.26	0.1594	0.0061	0.0107	0.0008	0.1288	0.0086	0.0103	0.0011	62	735
0.550	134.3	0.1312	0.0055	0.0093	0.0007	0.1201	0.0067	0.0081	0.0009	17	720
0.650	20.71	0.0791	0.0044	0.0107	0.0004	0.0707	0.0141	0.0094	0.0010	52	312
0.650	40.47	0.0685	0.0036	0.0056	0.0003	0.0559	0.0068	0.0086	0.0006	49	406
0.650	79.44	0.0551	0.0029	0.0053	0.0003	0.0584	0.0043	0.0043	0.0004	24	410
0.850	23.99	0.0089	0.0004	0.0013	0.0000	0.0066	0.0015	0.0016	0.0001	83	427
0.850	52.85	0.0068	0.0003	0.0009	0.0000	0.0073	0.0007	0.0008	0.0001	46	449
0.850	104.2	0.0048	0.0003	0.0005	0.0000	0.0046	0.0004	0.0005	0.0000	38	402

List of References

J.V. Allaby et al., CHARM Collaboration, *Total cross sections of charged-current neutrino and anti-neutrino interactions on isoscalar nuclei*, Zeitschrift für Physik, C38, pgs. 403–410, 1988.

G. Alterelli and G. Parisi, *Asymptotic Freedom in Parton Language*, Nuclear Physics B126, pg 229, 1977.

H.W. Atherton et al., *Precise Measurements of Particle Production by 400 GeV/c Protons on Beryllium Targets*, CERN Report 80-7, 22 August 1980.

P.S. Auchincloss et al., *Measurement of the inclusive charged-current cross sections for neutrino and anti-neutrino scattering on isoscalar nucleons*, Zeitschrift für Physik, C41, pgs 411–431, 1990.

P. Berge et al. *Total neutrino and anti-neutrino charged current cross section measurements in 100, 160, and 200 GeV narrow band beams*, Zeitschrift für Physik, C35, pgs 443–452, 1987.

P. Berge et al., *A measurement of differential cross-sections and nucleon structure functions in charged-current neutrino interactions on iron*, Zeitschrift für Physik, C49, pgs 187–223, 1991.

J.D. Bjorken and E.A. Paschos, *Inelastic Electron–Proton and γ–Proton Scattering and the Structure of the Nucleon*, Physical Review 185, pgs 1975–1982, 1969.

R. Brock, *Dimuon Measurements and the Strange-Quark Sea*, Physical Review Letters, 44, pgs 1027–1030, 1980.

R. Brock et al., *Massive Fine Grained Detector for Neutrino-Nucleon Scattering*, NIM, in preparation.

A. Bodek and J.L. Ritchie, *Fermi-motion effects in deep-inelastic lepton scattering from nuclear targets*, Physical Review, D23, pgs 1070–1091, 1981.

A.J. Buras and K.J.F. Gaemers, *Simple Parametrizations of Parton Distributions with Q^2 Dependance Given by Asymptotic Freedom*, Nuclear Physics, B132, pgs 249–267, 1978.

J. Bofill Abadia, *Upper Limit for ν_μ Oscillation Into ν_τ in a Dichromatic Beam*, PhD Thesis, Massachusetts Institute of Technology, 1984.

D. Bogert et al., *The Operation of a Large Flash Chamber Neutrino Detector at Fermilab*, IEEE Transaction in Nuclear Science, 29 (1982), pgs 363–367.

C.G. Callan and D.J. Gross, *High Energy Electroproduction and the Constitution of the Electric Current*, Physical Review Letters 22, pgs 156–159, 1969.

D.C. Carey, K.L. Brown, and Ch. Iselin, *DECAY TURTLE*, Fermilab Program Note: PM0031, March, 1982.

T.P. Cheng and L.F. Li, *Gauge theory of elementary particle physics*, Oxford University Press, New York, 1984.

F.E. Close, *An Introduction to Quarks and Partons*, Academic Press, London, 1979.

P.D.B. Collins and A.D. Martin, *Hadron Interactions*, Adam Hilger Ltd, Bristol, England, 1984.

S. Dasu et al. *Precision Measurement of* $R = \sigma_L / \sigma_T$ *and* F_2 *in Deep-Inelastic Electron Scattering*, Physical Review Letters, 61, pgs 1061–1064.

A. Devoto et al. *Direct analysis of scaling violations in large* Q^2 *deep-inelastic neutrino and muon scattering*, Physical Review D27, pgs 508–522, 1983.

M. Diemoz, F. Ferroni and E. Longo, *Nucleon Structure Functions From Neutrino Scattering*, Physics Reports, 130, pgs 293–380, 1986.

D.A. Edwards and F.J. Sciulli, *A Second Generation Narrow Band Neutrino Beam*, Fermi National Accelerator Laboratory Technical Memo 660, May 1976.

R.P. Feynman, *Very High-Energy Collisions of Hadrons*, Physical Review Letters, 23, pgs 1415–1418, 1969.

J.I. Friedman and H.W. Kendall, *Deep Inelastic Electron Scattering*, Annual Review of Nuclear Physics, pgs 203–251, 1972.

S. Fuess et al., *Calorimetry with Flash Chambers*, Proceedings of the Gas Calorimetry Workshop at Fermilab, pg 241, 1982.

S. Fuess et al., *Neutral Current x Distributions*, Proceedings of the XIth International Conference on Neutrino Physics and Astrophysics, Nordkirchen, West Germany, pg 486, 1984.

E. Gallas, *Search for Massive Neutral Particles in the Tevatron Wide Band Neutrino Beam*, PhD Thesis, Michigan State University, 1992.

M. Gell-Mann, *A Schematic Model of Baryons and Mesons*, Physics Letters, 8, pgs 214–213, 1964.

D. Griffiths, *Introduction to Elementary Particles*, John Wiley & Sons, Inc., New York, 1987.

R. Hatcher, *Multimuon Final States in Neutrino–Nucleon Scattering*, PhD Thesis, Michigan State University, 1993.

F. Halzen and A.D. Martin, *Quarks and Leptons: An Introductory Course in Modern Particle Physics*, John Wiley & Sons, Inc., New York, 1984.

P.N. Harriman, A.D. Martin, W.J. Stirling and R. Roberts, *Parton Distributions Extracted from Data on Deep Inelastic Lepton Scattering*, Physical Review D42, pgs 798–810, 1990.

F. James and M. Roos, *MINUIT, Functional Minimization and Error Analysis*, CERN Computer Division Long Write-Up, 12 September 1989.

E. Leader and E. Predazzi, *An Introductions to Gauge Theories and the 'New Physics'*, Cambridge University Press, Cambridge, England, 1982.

A.J. Malensek, *Empirical Formula For Thick Target Particle Production*, Fermilab Internal Note: FN-341, 12 October 1981.

T.S. Mattison, *Comparison of Charged and Neutral Current Structure Functions*, PhD. Thesis, Massachusetts Institute of Technology, 1986.

T.S. Mattison et al., *Nucleon Neutral Current Structure Functions*, Physical Review, D42, pgs 1311–1330, 1990.

S.R. Mishra and F. Sciulli, *Deep Inelastic Lepton–Nucleon Scattering*, Annual Review of Nuclear and Particle Science, 39, pgs 259–310, 1989.

S.R. Mishra and F. Sciulli, *Do present deep inelastic scattering data demonstrate* $R = R_{QCD}$*?*, Physics Letters B, Volume 244, pgs 341–346.

J.G. Morfín and W.K. Tung, *Distributions from a QCD global analysis of deep inelastic scattering and lepton pair production*, Zeitschrift für Physik, C52 pgs 13–30, 1991.

A. Mukherjee, *Azimuthal Energy Flow in Deep Inelastic Neutrino Scattering*, PhD Thesis, Massachusetts Institute of Technology, 1986.

E. Oltman, *Nucleon Structure Functions from High Energy Neutrino and Antineutrino Interactions in Iron*, PhD Thesis, Columbia University, 1989.

A. Pais, *Inward Bound: Of Matter and Forces in the Physical World*, Oxford University Press, New York, 1986.

Particle Data Group, *Review of Particle Properties*, Physics Letters, B239, 1990.

G.J. Perkins, *A Measurement of the Ratio of Neutral Current to Charged Current Deep Inelastic* ν_μ *Scattering Interactions in a Fine Grain Detector at FNAL*, PhD thesis, Michigan State University, 1992.

C. Quigg, *Gauge Theories of the Strong, Weak and Electromagnetic Interactions*, The Benjamin–Cummings Publishing Company, Advanced Book Program, Reading Massachusetts, 1983.

P.Z. Quintas, *Nucleon Structure Functions at the Fermilab Tevatron With a Measurement of* $\Lambda_{\overline{MS}}$, PhD Thesis, Columbia University, 1992.

R.G. Roberts, *The Structure of the Proton*, Cambridge University Press, New York, 1990.

A. de Rújula et al., *Radiative Corrections to High-Energy Neutrino Scattering*. Nuclear Physics B154, pgs 394–426, 1979.

A. Sirlin and W.J. Marciano, *Radiative Corrections to* $\nu_\mu + N \rightarrow \mu^- + X$ *and Their Effect on the Determination of* ρ^2 *and* $\sin^2\theta_w$, Nuclear Physics, B189, pgs 442–460, 1981.

J.A. Slate, *A Comparison of Neutral to Charged Current Neutrino-Nucleon Interactions in a Wide Band Beam at Fermilab*, PhD Thesis, Michigan State University, 1985.

B. Strongin, *Opposite Sign Dimuon Production in High Energy Neutrino-Nucleon Interactions*, PhD Thesis, Massachusetts Institute of Technology, 1989.

L. Stutte, *NCenter Wide Band Neutrino Beam*, Fermi National Accelerator Laboratory Technical Memo 1305, 26 March 1985.

M. Tartaglia, *A Measurement of the Elastic Scattering Cross Section,* $\nu_\mu + e^- \rightarrow \nu_\mu + e^-$, PhD Thesis, MIT, 1984.

M. Tartaglia et al., *Proceedings of Gas Sampling Calorimetry Workshop II*, pgs 259–290, 1985.

A. VanGinnekin, *Energy Loss and Angular Characteristics of High Energy Electromagnetic Processes*, Nuclear Instruments and Methods in Physics Research, A251, pgs 21–39, 1986.

J.F. Wheater and C.H. Llewellyn Smith, *Electroweak Radiative Corrections to Neutrino and Electron Scattering and the Value of* $\sin^2\theta_w$, Nuclear Physics B208, pgs 27–76, 1982.

G. Zweig, *An* SU(3) *Model for Strong Interaction Symmetry and Its Breaking*, CERN Preprint TH-412, February 1964, unpublished.